

SPHERICAL PERIODIC MESOPOROUS  
ORGANOSILICAS (sph-PMOs):  
SYNTHESES, CHARACTERISATION AND  
APPLICATION IN CHROMATOGRAPHY

DISSERTATION

Zur Erlangung des Doktorgrades  
des Fachbereichs 08 Chemie und Biologie  
der Justus-Liebig-Universität Giessen

vorgelegt von  
Vivian Rebbin  
aus Hamburg

Giessen 2006

Die vorliegende Arbeit entstand in der Zeit von Mai 2001 bis Dezember 2006 am Institut für Anorganische und Analytische Chemie der Justus-Liebig-Universität Giessen in der Arbeitsgruppe von Prof. Dr. Michael Fröba.

Gutachter: Prof. Dr. Michael Fröba

Gutachter: Prof. Dr. Siegfried Schindler

*Wenn Du ein Schiff bauen willst,  
dann trommle nicht Männer zusammen,  
um Holz zu beschaffen, Aufgaben zu vergeben  
und die Arbeit einzuteilen,*

*sondern lehre sie die Sehnsucht nach dem weiten, endlosen Meer.*

(Antoine de Saint-Exupéry)

Für meine Eltern

## Contents

<b>1</b>	<b>Introduction</b>	<b>1</b>
<b>1.1</b>	<b>Ordered mesoporous silica materials</b>	<b>2</b>
<b>1.2</b>	<b>Organic-inorganic hybrid materials</b>	<b>5</b>
1.2.1	Post-synthetic functionalisation of pristine silicas (“grafting”)	6
1.2.2	Co-condensation	7
1.2.3	Periodic mesoporous organosilicas (PMOs)	9
1.2.3.1	Synthesis of PMOs with ionic surfactants (alkyltrialkylammonium- and cetylpyridinium halides)	10
1.2.3.2	Synthesis of PMOs with non-ionic surfactants	17
1.2.3.3	PMOs synthesised with tris-/multi-silylated precursors	21
1.2.3.4	PMOs and other organic-inorganic hybrid materials synthesised with mixtures of different (organo)silica precursors	22
<b>1.3</b>	<b>Spherical (organically modified) mesoporous silica particles</b>	<b>24</b>
<b>1.4</b>	<b>Spherical periodic mesoporous organosilica particles (sph-PMOs)</b>	<b>28</b>
<b>1.5</b>	<b>Aim of this work</b>	<b>29</b>
<b>2</b>	<b>Characterisation methods</b>	<b>32</b>
<b>2.1</b>	<b>Powder X-ray diffraction (P-XRD)</b>	<b>32</b>
<b>2.2</b>	<b>Nitrogen physisorption</b>	<b>32</b>
<b>2.3</b>	<b>Raman spectroscopy</b>	<b>34</b>
2.3.1	Microreactor experiments	34
2.3.1.1	Micromachining and reactor assembly	34
2.3.1.3	Measurements of the adsorption solvents	35
2.3.2	Raman spectroscopic measurements of powder samples	36
<b>2.4</b>	<b>Nuclear magnetic resonance spectroscopy (NMR)</b>	<b>36</b>
<b>2.5</b>	<b>UV/Vis spectroscopy</b>	<b>37</b>
<b>2.6</b>	<b>Optical microscopy (OM)</b>	<b>37</b>
<b>2.7</b>	<b>Scanning electron microscopy (SEM)</b>	<b>37</b>
<b>2.8</b>	<b>Transmission electron microscopy (TEM)</b>	<b>37</b>
<b>2.9</b>	<b>Atomic force microscopy (AFM)</b>	<b>38</b>
<b>2.10</b>	<b>Thermogravimetric analysis combined with mass spectrometry (TG/MS)</b>	<b>38</b>

<b>2.11</b>	<b>Laser diffraction</b>	<b>38</b>
2.11.1	Fundamentals	38
2.11.2	Instrumental parameters	42
<b>2.12</b>	<b><i>In situ</i> small angle X-ray scattering (SAXS)</b>	<b>43</b>
2.12.1	Experimental setup	43
2.12.2	Instrumental parameters	44
<b>2.13</b>	<b>High performance liquid chromatography (HPLC)</b>	<b>45</b>
2.13.1	Chromatographic fundamentals	45
2.13.2	Choice of the elution solvent	49
2.13.3	Filling of the HPLC columns	50
2.13.4	Instrumental parameters	50
<b>2.14</b>	<b>Atomic absorption spectroscopy (AAS)</b>	<b>50</b>
<b>3</b>	<b>Syntheses and characterisation</b>	<b>51</b>
<b>3.1</b>	<b>Samples for heavy metal adsorption: Ethane- and amine-bridged PMOs</b>	<b>51</b>
3.1.1	Synthesis	51
3.1.2	Results	52
3.1.3	Influence of different synthesis parameters	57
3.1.4	Discussion and conclusion	64
<b>3.2</b>	<b>Spherical ethane-bridged particles with an average particle diameter of 500 nm</b>	<b>70</b>
3.2.1	Synthesis	70
3.2.2	Results	70
3.2.2.1	Comparison of the materials synthesised with different surfactants	70
3.2.2.2	Influence of different synthesis parameters	76
3.2.3	Conclusion	81
<b>3.3</b>	<b>Spherical ethane- and phenylene-bridged particles in the size range of 10 – 300 µm</b>	<b>83</b>
3.3.1	Synthesis of spherical ethane-bridged PMOs in the size range of 25-300 µm	83
3.3.2	Synthesis of spherical phenylene-bridged PMOs in the size range of 10-300 µm	83
3.3.3	Results and discussion	83

3.3.3.1	Characterisation of ethane-bridged and phenylene-bridged PMO spheres	83
3.3.3.2	Influence of different synthesis parameters	90
3.3.3.2.1	Ethane-bridged PMO spheres	91
3.3.3.2.2	Phenylene-bridged PMO spheres	95
3.3.4	Conclusion	97
<b>3.4</b>	<b>Spherical phenylene-bridged PMOs in the size range of 5 – 10 µm</b>	<b>100</b>
3.4.1	Synthesis	100
3.4.2	Results	101
3.4.2.1	Comparison of the phenylene-bridged spheres and Nucleosil 50-10	101
3.4.2.2	Influence of different synthesis parameters	108
3.4.3	Conclusion	113
<b>4</b>	<b>Formation mechanism studies</b>	<b>116</b>
<b>4.1</b>	<b><i>In situ</i> small angle X-ray scattering (SAXS) experiments</b>	<b>116</b>
<b>4.2</b>	<b>Experimental</b>	<b>120</b>
4.2.1	Synthesis of 2d hexagonal ordered phenylene-bridged PMOs	120
4.2.1.1	Structure-directing agent: Pluronic <sup>®</sup> P123	120
4.2.1.2	Structure directing agent: Brij <sup>®</sup> 76	121
<b>4.3</b>	<b>Results and discussion</b>	<b>121</b>
4.3.1	Phenylene-bridged PMOs with Pluronic <sup>®</sup> P123 as SDA	121
4.3.2	Phenylene-bridged PMOs with Brij <sup>®</sup> 76 as SDA	127
<b>4.4</b>	<b>Conclusion</b>	<b>131</b>
<b>5</b>	<b>Copper adsorption experiments</b>	<b>132</b>
<b>5.1</b>	<b>Adsorption of heavy metal ions on organic-inorganic hybrid silica materials</b>	<b>132</b>
<b>5.2</b>	<b>Experimental</b>	<b>135</b>
<b>5.3</b>	<b>Results and discussion</b>	<b>136</b>
5.3.1	Comparison of the adsorber materials	136
5.3.2	Adsorption experiments	139
5.3.2.1	Concentration-dependent Cu <sup>2+</sup> adsorption	139
5.3.2.2	Time-dependent Cu <sup>2+</sup> adsorption	141
<b>5.4</b>	<b>Conclusion</b>	<b>142</b>

<b>6</b>	<b>Solvent vapour adsorption</b>	<b>146</b>
<b>6.1</b>	<b>Solvent sorption experiments</b>	<b>146</b>
<b>6.2</b>	<b>Characteristics of the applied PMO spheres</b>	<b>147</b>
<b>6.3</b>	<b>Results and discussion</b>	<b>147</b>
<b>6.4</b>	<b>Conclusion</b>	<b>154</b>
<b>7</b>	<b>Chromatography on spherical phenylene-bridged PMOs</b>	<b>156</b>
<b>7.1</b>	<b>Chromatography on (functionalised) spherical mesoporous silica particles</b>	<b>156</b>
<b>7.2</b>	<b>Chromatography on spherical periodic mesoporous organosilicas</b>	<b>160</b>
<b>7.3</b>	<b>Experimental</b>	<b>161</b>
7.3.1	Sieving procedure	161
7.3.2	Characteristics of the applied materials	163
<b>7.4</b>	<b>Chromatographic experiments</b>	<b>164</b>
7.4.1	Separation of benzene, naphthalene, biphenyl and phenanthrene	164
7.4.2	Separation of aspartam, BHT and sorbic acid	170
7.4.3	Separation of caffeine, coumarin and vanillin	173
<b>7.5</b>	<b>Conclusion of the separation experiments</b>	<b>178</b>
<b>8</b>	<b>Summary</b>	<b>181</b>
<b>9</b>	<b>Zusammenfassung (German Summary)</b>	<b>186</b>
<b>10</b>	<b>References</b>	<b>193</b>
	<b>Appendix I</b>	<b>203</b>
A.I.1	Applied organosilica precursors	203
A.I.2	Applied structure-directing agents	204

	<b>Appendix II</b>	<b>205</b>
A.II.1	Molar ratios of ethane- and amine-bridged samples synthesised with OTAC as SDA	205
A.II.2	Molar ratios of ethane- and amine-bridged materials synthesised with CTAC as SDA	207
A.II.3	Nitrogen physisorption data of the samples synthesised with different OTAC concentrations	209
A.II.4	Variation of the aging temperature and the aging time	210
A.II.5	Variation of the hydrothermal treatment temperature	212
A.II.6	Nitrogen physisorption data of the ethane- and amine-bridged PMOs synthesised with CTAC as SDA	213
	<b>Appendix III</b>	<b>214</b>
A.III.1	Spherical ethane-bridged particles with an average particle diameter of 500 nm	214
A.III.2	Nitrogen physisorption data of the samples synthesised with different ethanol concentrations	215
	<b>Appendix IV</b>	<b>216</b>
A.IV.1	Molar ratios of the ethane-bridged spheres in the size range of 25 – 300 $\mu\text{m}$	216
A.IV.2	Molar ratios of the phenylene-bridged spheres in the size range of 10 – 300 $\mu\text{m}$	218
A.IV.3	Ethane-bridged PMOs synthesised with different stirring rates	219
A.IV.4	Ethane-bridged samples synthesised with different pH values	221
A.IV.5	Ethane-bridged samples synthesised with different co-surfactants	222
A.IV.9	Phenylene-bridged PMOs synthesised at different pH values	223
A.IV.10	Phenylene-bridged PMOs synthesised with different shaking intensities	224
	<b>Appendix V</b>	<b>225</b>
A.V.1	Spherical phenylene-bridged PMOs in the size range of 5 to 10 $\mu\text{m}$	225
A.V.2	Investigations of the hydrothermal treatment procedure	227
A.V.3	Phenylene-bridged spherical PMOs synthesised at different pH values	228
A.V.4	Phenylene-bridged spherical PMOs synthesised with different ethanol concentrations	229

A.V.5	Phenylene-bridged samples synthesised with different contents of both SDAs	230
-------	--	-----

<b>Appendix VI</b>	<b>231</b>
--------------------	------------

A.VI.1	Molar ratios of the phenylene-bridged samples synthesised with Pluronic <sup>®</sup> P123 as SDA	231
A.VI.2	Molar ratios of the phenylene-bridged samples synthesised with Brij <sup>®</sup> 76 as SDA	231

<b>Appendix VII</b>	<b>233</b>
---------------------	------------

A.VII.1	Experimental details of the Cu <sup>2+</sup> adsorption experiments	233
A.VII.2	Results of the copper adsorption experiments	236
A.VII.3	Results of the washing procedure	238

<b>Appendix VIII</b>	<b>241</b>
----------------------	------------

A.VIII.1	UV/Vis spectra of the components of the three test mixtures applied for chromatographic tests	241
A.VIII.2	The Elutropic Series	244

<b>Appendix IX: Hazardous Chemicals</b>	<b>246</b>
---	------------

<b>Appendix X: Abbreviations</b>	<b>249</b>
----------------------------------	------------

<b>Appendix A: Thanks</b>	<b>253</b>
---------------------------	------------

<b>Appendix B: Full list of publications</b>	<b>256</b>
--	------------

<b>Appendix C: Curriculum vitae</b>	<b>260</b>
-------------------------------------	------------

## 1 Introduction

The discovery of porous solids with high specific surface areas has established a wide field of research concerning the application of these porous materials in catalysis, adsorption, chromatography, sensor-technology and gas storage or gas separation. The discovery of the mesoporous silica materials, the so-called M41S materials, by the Mobil Oil group in 1992 enabled the synthesis of materials with narrow pore size distributions, high specific surface areas and a high ordering of the mesopores but X-ray amorphous pore walls.<sup>[1,2]</sup> The ordered pore systems are already known from the microporous crystalline zeolites but in contrast to the typical pore size of the zeolite materials of about 1.5 nm the new materials exhibited pore diameters between 2 and 15 nm. The new concept of the synthesis procedure of these materials was the application of supramolecular aggregates of ionic surfactant molecules as structure-directing agents (SDAs). These aggregates in the form of a liquid crystalline phase lead to the assembly of an ordered mesostructured composite during the condensation of the silica precursors under basic conditions. The mesoporous materials were obtained by subsequent removal of the surfactant from the inorganic composite by calcination or solvent extraction.

These pure silica materials have been used for a variety of applications such as host/guest chemistry in order to form nanoparticles of definite sizes to study magnetic and optical properties.<sup>[3,4]</sup> The application of host/guest compounds in catalysis is also a field of interest. The high loading with particles in the nanometer size range that could be achieved because of the high specific surface areas of the host materials offer high catalytic activity of the composite depending on the incorporated species.<sup>[5,6]</sup> Pristine silica materials have also been used as stationary phases in chromatography.<sup>[7]</sup> In order to expand the field of applications organic functionalities on the surface of these materials were necessary. Three possibilities of incorporating organic functions into the mesoporous materials have been used in a wide range of variations up to now. Grafting organic molecules onto the surface in an additional single reaction, co-condensation reactions of silicon alkoxides with terminal trialkoxysilanes and the synthesis of periodic mesoporous organosilicas are widely used to adjust the materials' properties.<sup>[8]</sup>


The most established representatives of these solids are the members of the M41S family, the MCM-41 silica with a 2d hexagonal pore arrangement (space group:  $p6mm$ ), the MCM-48 silica with a cubic arrangement of the mesopores (space group:  $Ia\bar{3}d$ ) and the MCM-50 silica which consists of lamellar layers (space group:  $p2$ ) (see Figure 1.1).

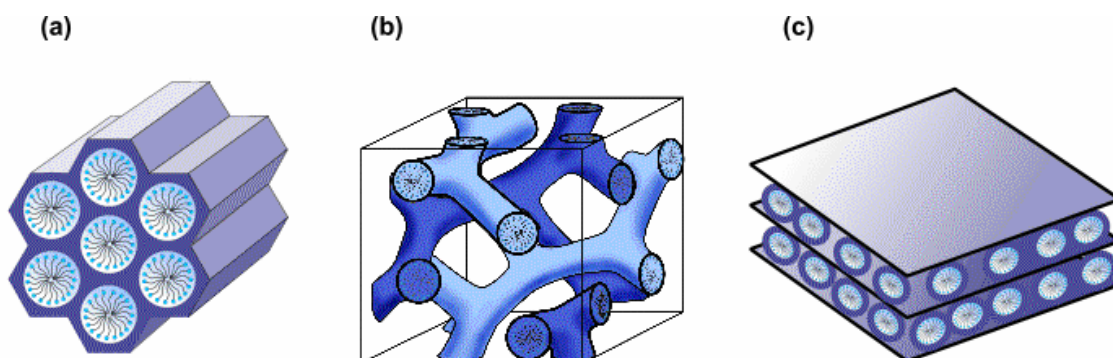


**Figure 1.1:** Structures of the mesoporous 2d hexagonal MCM-41 silica (a); the cubic MCM-48 silica (b) and the lamellar MCM-50 silica (c). <sup>[1,2]</sup>

The formation of the single mesophases depends on the structure of the surfactant as well as on the concentration and the synthesis temperature. The formation of each structure can be explained with the concept of the effective ion pair packing parameter  $g = V/a_0 \cdot l$ , where  $V$  is the total volume of the surfactant chains plus any co-solvent organic molecules between the chains,  $a_0$  being the effective headgroup area at the micelle surface, and  $l$  being the kinetic surfactant tail length or the curvature elastic energy.<sup>[9]</sup> This concept was designed for the description of surfactant organisation in amphiphilic liquid crystal arrays. Table 1.1 shows the expected mesophase sequence as a function of the packing parameter  $g$  in classical micelle chemistry.

**Table 1.1:** Expected mesophase sequence as a function of the packing parameter  $g$ .

$g$	mesophase	 <p>Decreasing curvature of the micelles</p>
$\frac{1}{3}$	cubic ( $Pm\bar{3}n$ )	
$\frac{1}{2}$	hexagonal ( $p6mm$ )	
$\frac{1}{2}-\frac{2}{3}$	cubic ( $Ia\bar{3}d$ )	
1	lamellar ( $p2$ )	

Investigations concerning the formation mechanisms of these composite materials had gained much attention and two different mechanisms are found to be involved. One possibility is the true liquid crystal templating (TLCT) mechanism. In this case the concentration of the surfactant is so high that under the prevailing conditions (temperature, pH value) a lyotropic liquid crystalline phase is formed without requiring the addition of the silica source.<sup>[10]</sup> Alternatively, the liquid crystalline phase is formed even at lower concentration of the surfactant when there is a cooperative self-assembly between the surfactant molecules and the already added inorganic species, which leads to a liquid crystalline phase with hexagonal, cubic or lamellar arrangement.<sup>[11]</sup>

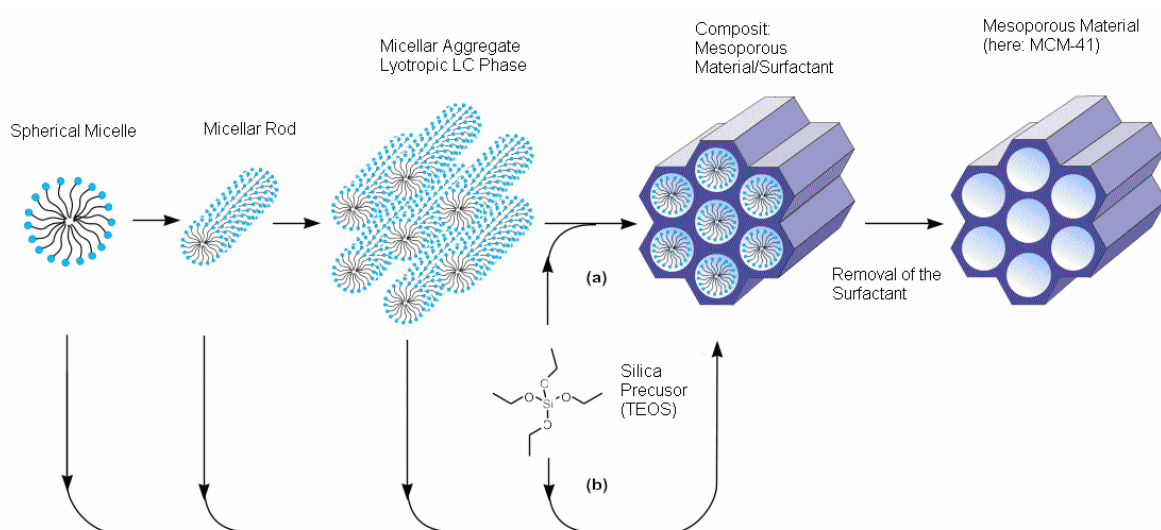


**Figure 1.2:** Formation process of the mesoporous materials by the “real” liquid crystalline template mechanism (a) and the cooperative liquid crystalline template mechanism (b).<sup>[10]</sup>

The synthesis of the materials from the M41S family inspired many research groups in developing new synthesis pathways for mesoporous materials. An alternative route is the synthesis of the so-called SBA-n silica materials, which were attained under acidic conditions.<sup>[9]</sup> A new aspect of this procedure was the application of non-ionic triblock copolymers with the formula  $\text{PEO}_x\text{PPO}_y\text{PEO}_x$  (PEO: polyethylene oxide, PPO: polypropylene oxide) as SDAs instead of the ionic surfactant molecules chosen for the synthesis of the M41S phases and thus, the possibility of increasing the pore diameters up to 30 nm.<sup>[12]</sup>

The fundamental requirements for the formation of ordered mesoporous materials in general are attractive interactions between the SDA and the silica source to ensure the embedding of the SDA without phase separation occurring. Figure 1.3 represents the different attractive interactions between the inorganic components with the headgroups of the SDA according to

a suggestion made by Huo et al.<sup>[13, 14]</sup> These interactions are classified as described in the following part:

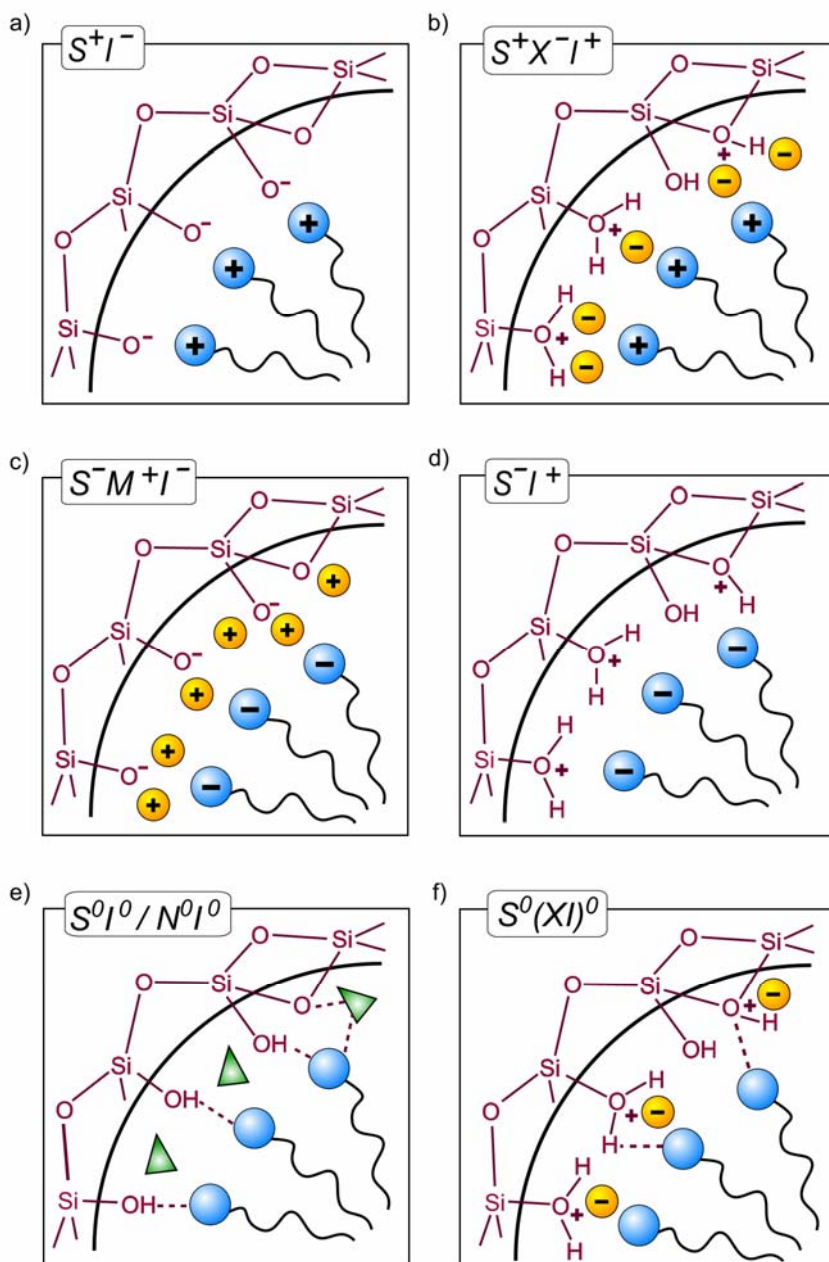


**Figure 1.3:** Scheme of the different interactions between the surfactant headgroup and the silica species under different pH values in the synthesis mixture: electrostatic interactions:  $S^+I^-$ ;  $S^+X^-I^+$ ;  $S^-X^+I^-$ ;  $S^-I^+$  and hydrogen bonding interactions:  $S^0I^0/N^0I^0$  and  $S^0(XI)^0$  (for further details see text).

A reaction under basic conditions with the inorganic species present as anions and cationic quaternary ammonium surfactants present as SDA follows a pathway described by  $S^+I^-$  with

$S^+$  being the positive charged surfactant molecule and  $I^-$  the negative charged inorganic species (a). If the syntheses take place under acidic conditions (below the isoelectric point of the Si-OH-bearing inorganic species of  $\approx 2$ ) attractive interactions between the positive charged inorganic species and the cationic quaternary ammonium surfactant molecules can only be produced by incorporation of a mediator ion (halides in most cases) in this process named  $S^+X^-I^+$  (b). For reactions containing anionic surfactant molecules acting as SDA two further pathways are described dependent on the pH value of the solution. For syntheses under basic conditions a mediator ion is needed in order to produce attractive interactions between the anionic surfactant molecules and the anionic inorganic species present in the solution

( $S^-X^+I^-$ ) (c). During reactions under acidic conditions direct attractive interactions between the positive charged inorganic species and the anionic surfactant molecules take place and lead to a  $S^-I^+$  pathway (d). In all four cases (a – d) electrostatic interactions dominate the formation process. In contrast to the formation pathways guided by attractive electrostatic interactions a hydrogen bonding mediated formation of the mesophase can take place. The non-ionic SDAs like long chain alkylamines ( $S^0$ ),<sup>[15]</sup> polyethylene oxide surfactants<sup>[16]</sup> or triblock copolymers such as  $PEO_xPPO_yPEO_x$ <sup>[12]</sup> ( $N^0$ ) interact with non-ionic silica species ( $S^0I^0$  or  $N^0I^0$ ) or ion pairs ( $S^0(XI)^0$ ).

All synthesis routes described above are classified as “soft matter templating” synthesis routes. Instead of the typical SDAs “hard” templates such as inorganic porous solids can be used in order to obtain mesoporous materials. This mechanism is called “hard matter templating”. The pores of these inorganic solids are filled with an (in)organic precursor, which is then transformed under appropriate conditions. The resulting solid is a negative image of the hard template. After removal of the original porous material the “negative replica” remained with a high specific surface area and a pore diameter dependent on the template. As exotemplates mesoporous silicas like MCM-48 or SBA-15 silica materials are used. This procedure was first applied by Ryoo et al. for the synthesis of mesoporous carbons, the so-called CMK-n materials.<sup>[17]</sup>

## 1.2 Organic-inorganic hybrid materials

The combination of organic and inorganic units within the same material is of particularly interest for materials scientists because the variety of the functionalities in the organic

chemistry combined with the thermal stability of the inorganic solids provides new opportunities concerning application especially in chromatography or heterogeneous catalysis. The properties of these materials differ from those of the individual isolated components. The surface of these materials can be functionalised in order to “tune” the polarity or to form new reaction centres. Three pathways for the synthesis of ordered organic-inorganic hybrid silica materials are available. The first is a post synthetic modification of the pore surface of a pure mesoporous silica material with organic units (“grafting”), the second is the simultaneous condensation of silica and organosilica precursors in presence of a SDA and the third is the incorporation of organic functionalities into the pore wall network by hydrolysis and condensation of bisilylated organosilica precursors with the formula  $(\text{RO})_3\text{Si-R}'\text{-Si}(\text{OR})_3$

(R: short alkyl chain; R': any organic function) in presence of a SDA as well (Chapter 1.2.3: Periodic mesoporous organosilicas, PMOs).

### 1.2.1 Post-synthetic functionalisation of pristine silicas (“grafting”)

The modification of the pore surface of pristine silica materials can be achieved by the grafting process. In a post synthetic treatment primarily organic molecules such as organosilanes with the formula  $(\text{R}'\text{O})_3\text{Si-R}$  but also chlorosilanes ( $\text{ClSiR}_3$ ), long chain alcohols or silazanes ( $\text{HN}(\text{SiR}_3)_3$ ) react with the free silanol functions on the inner surface of the material.

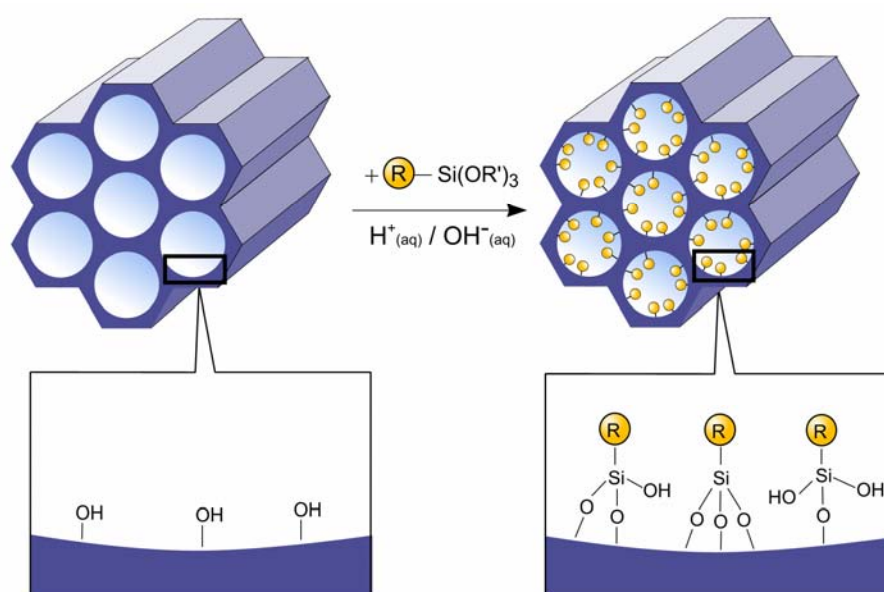


**Figure 1.4:** Schematic illustration of the “grafting” process.<sup>[8]</sup>

Materials with a variety of organic functionalities on the surface can be synthesised just by variation of the organic residue  $R'$ . It is advantageous that the order of the mesostructure of the starting material is not affected by this procedure but relating to the resulting hybrid materials this grafting procedure exhibits a lot of disadvantages. The grafting of organic functionalities onto the pore surface leads to a reduction of the specific surface areas and the pore diameters of the material. A complete functionalisation is impossible; many free silanol functions remain on the surface. If the organosilanes react preferentially at the pore openings during the initial state of the grafting process the diameter of the pore is reduced and thus, the diffusion of further organosilanes into the pore network is interfered. This effect is increasing with increasing size of the organosilanes. Even a complete blockage of the pores is possible if the organic functionality of the organosilane is voluminous ("pore-blocking effect").

These materials are applied for photochemical reactions, acidic, basic, oxidative or chiral catalysis as well as enzyme-immobilisation and biocatalysis. A good overview is given by Hoffmann et al.<sup>[8]</sup>

The grafting procedure is also of great interest for the synthesis of functionalised separation materials for chromatographic applications. The classic reversed phases (RP) are synthesised by grafting a hydrocarbon chain onto the surface of a pure silica material as described above. In case of separation materials an incomplete post synthetic grafting process causes problems, because the adsorption behaviour of the stationary phase is influenced by the coexistence of hydrocarbon chains and silanol functions on the surface. This "combination" of the normal (silanol functionalities) and a typical reversed phase (grafted hydrocarbon chains or hydrocarbon chains with organic functionalities on the material's surface) is not usable for separation. In order to avoid remaining free silanol functions on the surface the materials are endcapped, which means a reaction with trimethylchlorosilane follows the grafting process. The low number of free silanol functions remaining after the endcapping process does not influence the separation quality of the material. The pore sizes, typically between 10 and 30 nm, wide enough for a material with an acceptable inner surface and pore diameter after grafting the organic functionalities onto the pore surface.

### 1.2.2 Co-condensation

An alternative method of incorporating organic functionalities into mesoporous silica materials is the co-condensation method. Materials are synthesised by the condensation of a silica precursor (tetraethyl orthosilicate, TEOS or tetramethyl orthosilicate, TMOS) with

terminal trialkoxysilanes ( $(R'O)_3\text{-Si R}$ ) in presence of a SDA and the resulting materials exhibit organic residues covalently linked with the pore walls as illustrated in Figure 1.5.

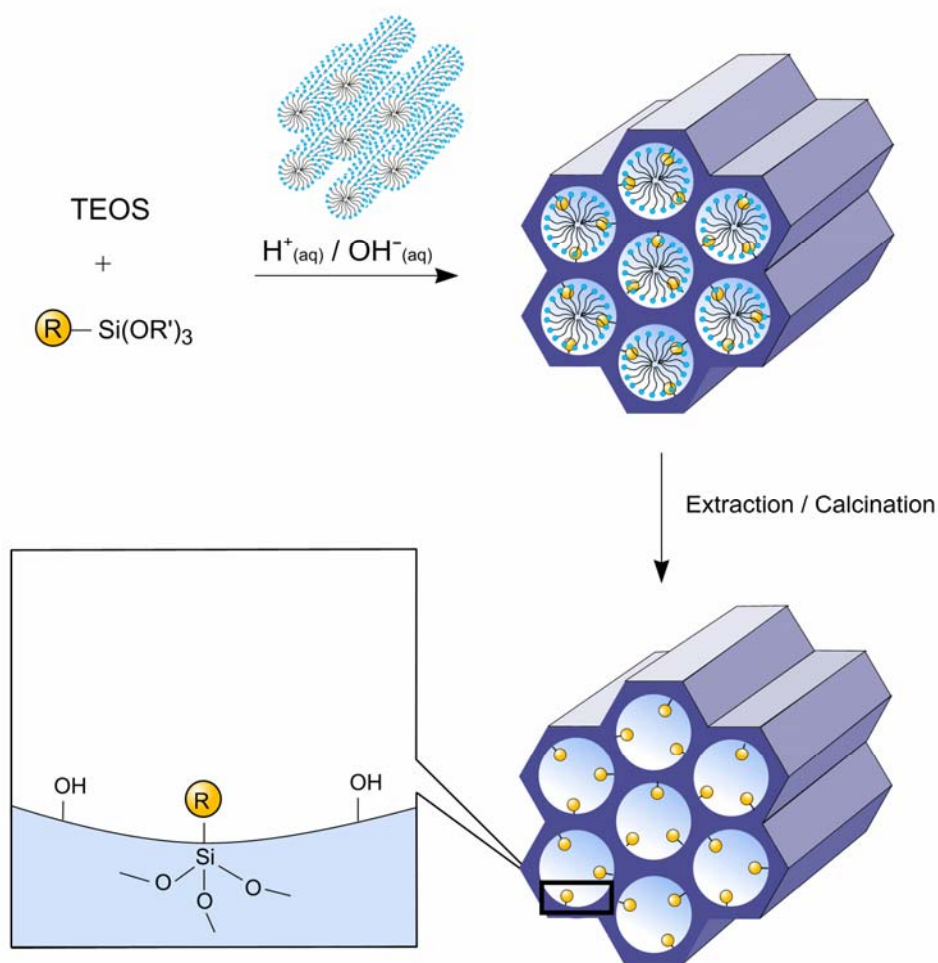


**Figure 1.5:** Schematic illustration of the co-condensation of TEOS with a terminal organically modified precursor (R: organic function).<sup>[8]</sup>

By using SDAs that are normally used for the synthesis of ordered mesoporous silica materials such as MCM-n or SBA-n silicas ordered organically modified materials with organic functionalities protruding into the pores can be obtained by the addition of terminal trialkoxysilanes. Thus, the pore blocking effect is reduced due to the incorporation of the organic functionalities into the network. The distribution of the organic functionalities is more homogeneous than it is when using the grafting process but this synthesis procedure possesses a lot of disadvantages as well. With increasing concentration of the terminal trialkoxysilane in the reaction solution the structural order of the material degrades. Normally, concentrations higher than 40 mol % lead to completely non-ordered materials. Furthermore, the hydrolysis

and condensation rates of the structurally different precursors favour homocondensation reactions of both precursors with increasing amount of the terminal alkoxy silane in the reaction solution due to the positive inductive effect (+I) of the organic function and thus, the different reactivity at a certain pH values. Thus, a high loading and a homogeneous distribution of the organic functionalities in the materials are hardly achievable. In addition, the removal of the SDA from the pores of these materials can only be accomplished by solvent extraction because at calcination temperatures around 500 °C the organic functionalities in the silica network decompose.

Since the first publications dealing with the synthesis of organic-inorganic hybrid silica materials via the co-condensation reaction a wide range of organic functions such as alkyl, thiol-, amino-, cyano-/isocyano-, vinyl-/allyl-, organophosphin-, alkoxy-, or aromatic groups has been introduced up to now. As already mentioned above, the careful removal of the surfactant is of high importance because of the low thermal stability of these materials. These solids as well as the materials synthesised via the grafting pathway exhibit interesting properties concerning catalysis, adsorption or as reaction centre for further functionalisation. Because of the inferior importance for this work no further details concerning these materials are given at this point. For further information see reference [8].

### 1.2.3 Periodic mesoporous organosilicas (PMOs)

The synthesis of organic-inorganic hybrid materials by hydrolysis and condensation of an organosilica precursor with the general formula  $(R'O)_3\text{-Si-R-Si-(OR)}_3$  has already been known from the sol-gel chemistry.<sup>[18,19]</sup> In contrast to the hybrid materials synthesised via post synthetic treatment or co-condensation reactions the organic functions are directly incorporated into the pore wall network by two covalent bonds. Thus, the distribution of the organic moieties is, in contrast to the materials described above, completely homogeneous. These materials which are obtained as aerogels or xerogels exhibit high inner surfaces up to 1800 m<sup>2</sup>/g, usually a disordered pore system and broad pore size distributions.

The application of the concept of the structure-directed synthesis of mesoporous materials by SDAs for the reaction with bisilylated organosilica precursors instead of tetraalkoxysilanes enabled the synthesis of a new class of materials: the periodic mesoporous organosilicas (PMOs). The organic functionalities are directly and homogeneously incorporated into the pore wall network and these materials exhibit a high ordering of the mesopores, high specific surface areas and narrow pore size distributions.

By using this concept for the synthesis of ordered organic-inorganic hybrid materials pore blocking effects caused by organic functionalities on the pore wall surface can be avoided. The thermal and mechanical stability of the resulting material depends on the incorporated organic functionality. From the practicability of tuning the materials' properties just by variation of the organic bridge in the organosilica precursor great attention arose for these materials concerning application in catalysis, adsorption, chromatography, nanoelectronics or drug release systems.

#### 1.2.3.1 Synthesis of PMOs with ionic surfactants (alkyltrialkylammonium- and cetylpyridinium halides)

The most frequently used surfactants for the synthesis of mesoporous silicas and organosilicas are long chain alkyltrialkylammonium halides (chloride and bromide) mostly with an octadecyl chain (octadecyltrimethylammonium chloride/bromide, OTAC/OTAB) or hexadecyl chain (hexadecyltrimethylammonium chloride/bromide, CTAC/CTAB) or cetylpyridinium halides (chloride and bromide) (CPB/CPC). Under certain conditions depending on pH value, temperature and solvent concentrations in presence of a bisilylated organosilica precursor, these surfactants form a lyotropic liquid crystalline phase. Hydrolysis and condensation of the organosilica precursor lead to the periodically ordered mesoporous hybrid material, which exhibits uniform pore diameters after removal of the surfactant (see Figure 1.6).

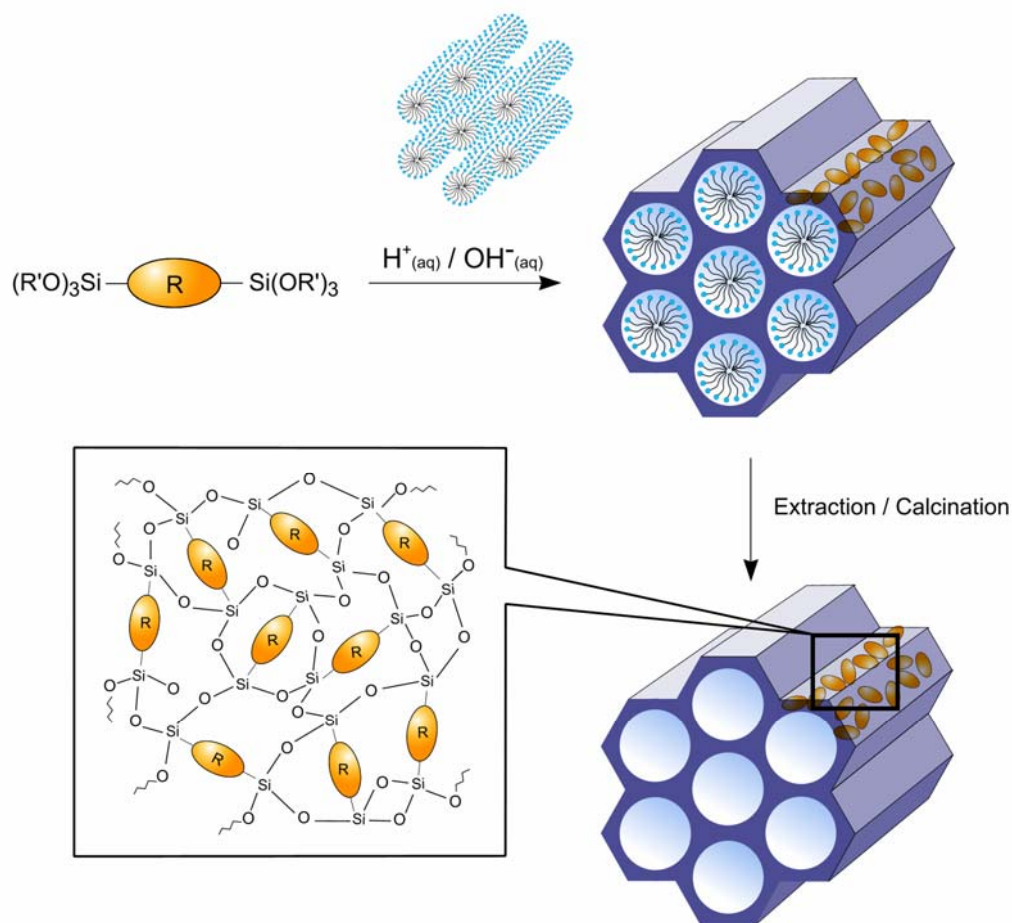


**Figure 1.6:** Schematic illustration of the synthesis of a periodic mesoporous organosilica material.<sup>[8]</sup>

In 1999, three independently working groups introduced these new materials nearly at the same time.<sup>[20-22]</sup> An overview of all organosilica precursors that have successfully been applied for the synthesis of PMO materials is given in Figure 1.7.

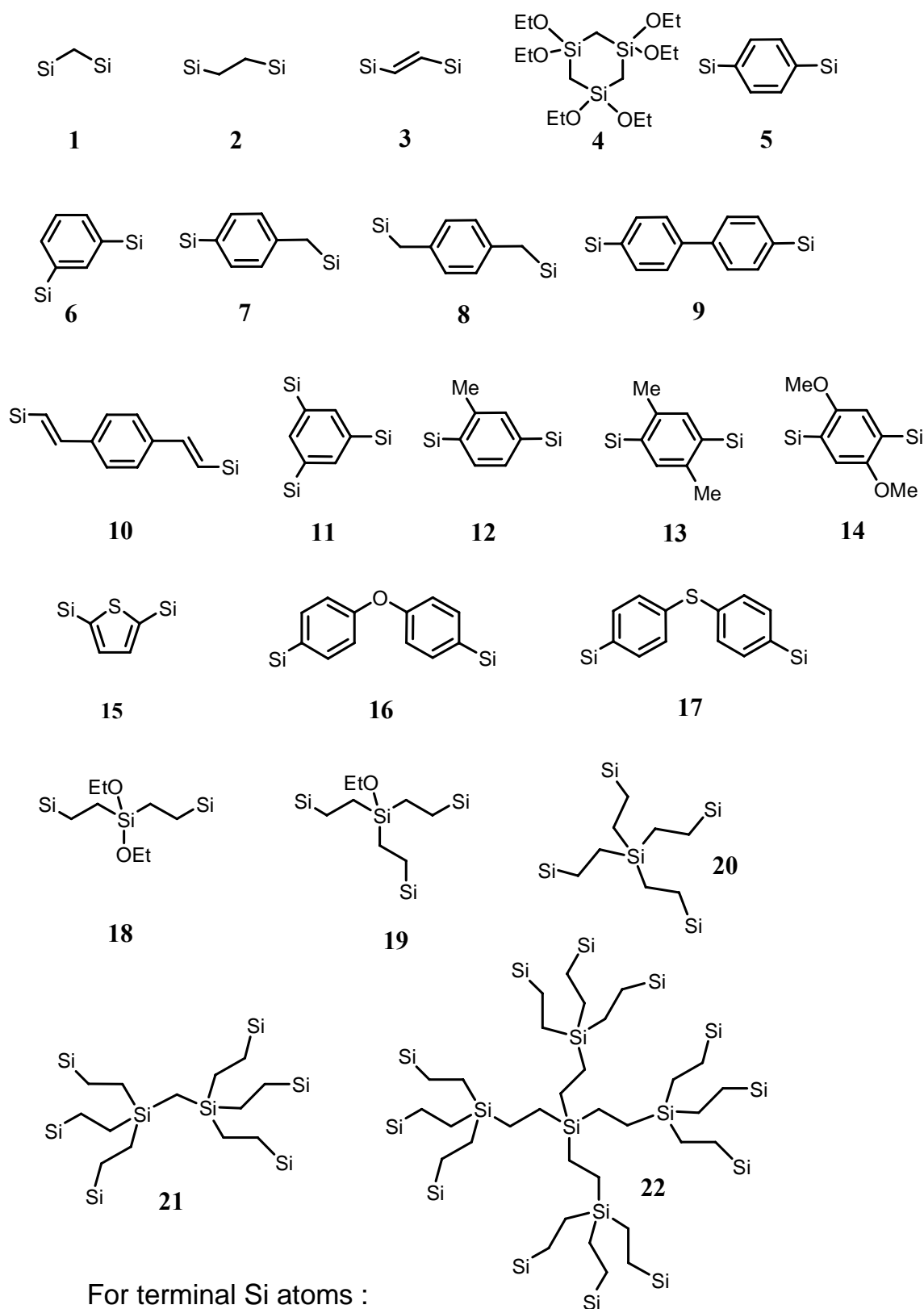


**Figure 1.7:** Overview of the organosilica precursors that have successfully been used for the synthesis of PMOs.<sup>[8]</sup>

*a) Aliphatic PMOs*

The first publications dealing with the synthesis of periodic mesoporous organosilica materials describe the incorporation of aliphatic bridges. Inagaki et al. first synthesised a 2d hexagonal and a 3d hexagonal ordered material with OTAC as SDA and 1,2-bis(trimethoxysilyl)ethane (BTME) (**2**) as organosilica precursor under basic conditions.<sup>[20]</sup> The symmetry of the pore arrangement depended on the component ratios of the single substances in the reaction solution. The existence of the Si-C bonds after the complete reaction and extraction procedure was proved by <sup>29</sup>Si MAS NMR spectroscopy. In the same year Ozin et al. reported the synthesis of a 2d hexagonal ordered material synthesised with the unsaturated spacer 1,2-bis(triethoxysilyl)ethylene (**3**) with CTAB as SDA under basic conditions.<sup>[21]</sup> A bromination reaction of the PMO material was carried out in order to prove the accessibility of the double bond in the solid. Similar results were obtained by Melde et al.<sup>[22]</sup>

A more recent report of a 2d hexagonal long-range ordered ethane-bridged material synthesised with BTME (**2**) as organosilica precursor and OTAC as SDA under basic reaction conditions was given by Nakajima et al.<sup>[23]</sup>

In 2000, Guan et al.<sup>[24]</sup> and Sayari et al.<sup>[25]</sup> first published a synthesis of an ethane-bridged PMO material with a cubic symmetry (space group:  $Pm\bar{3}n$ ) that is analogous to the pure mesoporous silica SBA-1. The phase transition from hexagonal to cubic was achieved by changing the surfactant from OTAC to CTAC. Further studies concerning the influence of the alkyl chain length of the surfactant between C<sub>10</sub> and C<sub>18</sub> on the resulting mesostructure of the ethane-bridged material were carried out by the authors.<sup>[26]</sup> Two different synthesis procedures were compared, in the first case the last step of the synthesis procedure was just an aging step at room temperature while in the second case a hydrothermal treatment at 95 °C was comprised. In most cases the materials exhibited 2d hexagonal mesostructures with increasing pore diameters for increasing alkyl chain lengths of the SDA. Only the material synthesised with CTAC (see above) combined with the hydrothermal treatment procedure exhibited a cubic structure (space group:  $Pm\bar{3}n$ ).

The incorporation of a methylene bridge (**1**) was described by Asefa et al.<sup>[27]</sup> The 2d hexagonal ordered material was synthesised under basic conditions and showed a transformation from the methylene bridge to a terminal methyl group at temperatures above 400 °C due to the cleaving of a Si-C bond, a proton exchange from a silanol group to a neighbouring Si-CH<sub>2</sub> group, and the formation of a new Si-O-Si bridge.

Ethane-bridged materials were also obtained under acidic synthesis conditions using CPB as SDA.<sup>[28]</sup> But only a poor ordering of the mesopores was observed and evidence for the stability of the materials was missing.

All examples described above show that the incorporation of aliphatic alkyl chains into PMO materials is limited to an alkyl chain length of only two carbon atoms. Syntheses with organosilica precursors containing aliphatic groups with more than two carbon atoms only led to non-ordered materials, which leads to the assumption that the rigidity of the organic moiety plays an important role for mesostructure formation.

#### *b) Aromatic PMOs*

The synthesis of aromatic PMOs was first described by Yoshina-Ishii et al. in 1999.<sup>[29]</sup> 1,4-bis(triethoxysilyl)benzene (BTEB) (**5**) and 2,5-bis(triethoxysilyl)thiophene (BTET) (**15**) were used as organosilica precursors and CTAC as SDA under mild basic conditions (base: ammonia). Interestingly, the presence of ammonia led to cleavage of nearly every Si-C bond in the PMO material. Only the synthesis under mild acidic conditions with CPB as SDA led to well ordered solids with a high degree of structural integrity of the organic moieties but even under these synthesis conditions a cleavage of the Si-C bonds could not be avoided completely.

New organosilica precursors 1,4-bis(triethoxysilyl)-2-methylbenzene (**12**), 1,4-bis(triethoxysilyl)-2,5-dimethylbenzene (**13**) and 1,4-bis(triethoxysilyl)-2,5-dimethoxybenzene (**14**) were synthesised by Temtsin et al.<sup>[30]</sup> by Grignard reaction of the respective brominated compounds with chlorotriethoxysilane. PMO materials involving these new organosilica precursors were prepared using CPC as SDA under acidic conditions and ammonium fluoride as a catalyst. The resulting materials exhibited a 2d hexagonal arrangement of mesopores with mesopores diameter of 2.3 nm. An interesting fact was in this case the low thermal stability (360 °C) compared to other aromatic PMOs ( $\approx$  450 °C).

#### *c) PMOs with crystal-like pore walls*

In the last few years some research groups synthesised PMO materials with a high crystal-like organisation of the organic functionalities in the pore walls additional to the high ordering of the mesopores. This means that the mass centres of the molecules and the inversion centres of the organic bridges show a long-range order. Because of the free rotation of the Si-C bond around the molecular longitudinal axis the organic bridges have altering orientations in relation to the bordering silica layers. Thus, the organic moieties do not possess any strict

translational symmetry. A schematic illustration of the formation mechanism of these new materials is shown in Figure 1.8.

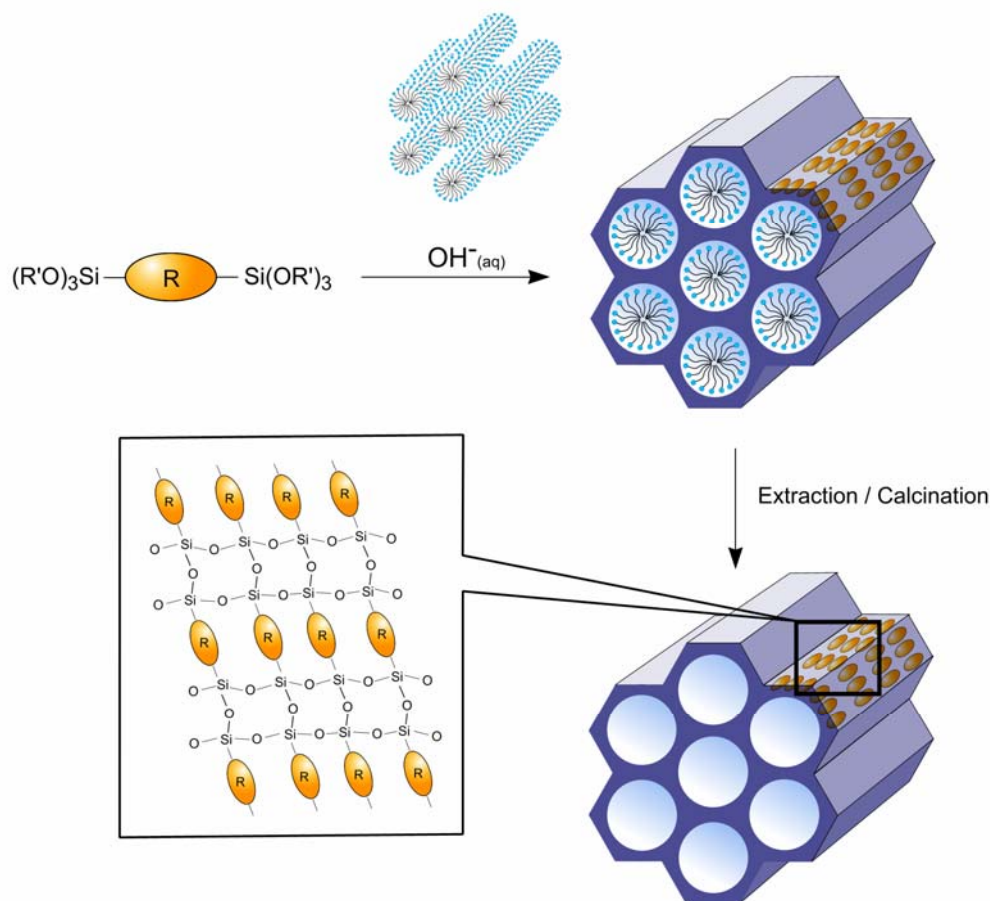


**Figure 1.8:** Schematic illustration of the synthesis of PMOs with high ordering of mesopores combined with a periodicity of organic functionalities in the pore walls.<sup>[8]</sup>

First investigations concerning the synthesis of PMOs with a high ordering of organic units in the pore walls were published by Inagaki et al. in 2002.<sup>[31]</sup> This work deals with the synthesis of phenylene-bridged PMOs with OTAC as SDA under basic conditions which show in the XRD pattern, additional to the reflections of the 2d hexagonal mesophase ( $p6mm$ ) in the low angle region, four reflections (100, 200, 300, 400) in the wide angle range ( $2\theta > 10^\circ$ ) that showed the existence of a periodicity of 0.76 nm on the molecular scale. This organisation of the single organic bridges could be evidenced by high resolution transmission electron microscopy (HRTEM) investigations which show many lattice fringes along the pore axis with the same distance of 0.76 nm. A model of the pore wall structure is presented in Figure

1.9 a and b. The thermal stability of the product is much higher (up to 500 °C) than it is for PMOs without this periodicity of the organic functionalities on the molecular scale.

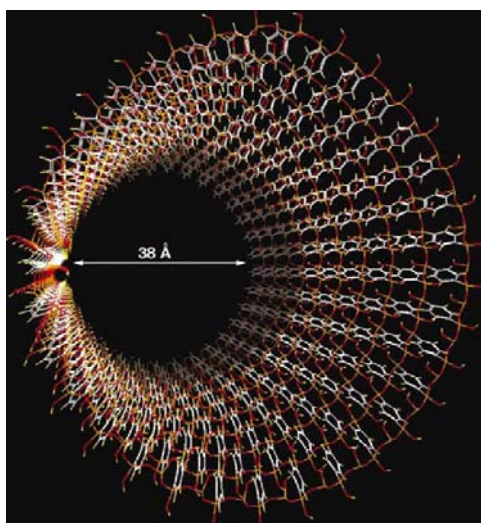


**Figure 1.9 a:** Model of a pore surface. The surface is completely saturated with silanol functions.<sup>[31]</sup>

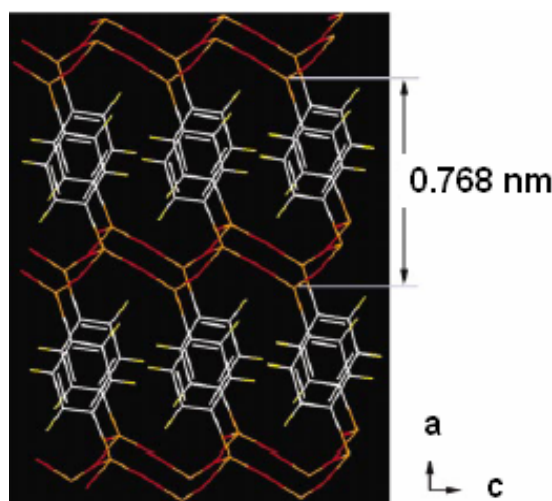


**Figure 1.9 b:** pore wall section. The aromatic units in the wall show the periodicity of exact one molecule.<sup>[31]</sup>

Similar results concerning periodicity of the organic groups in the pore walls on the molecular scale were obtained by Bion et al.,<sup>[32]</sup> who varied the SDA chain length and thus the pore diameter.

The synthesis of another PMO material with an aromatic system incorporated into the pore walls with a molecular scale periodicity was published by the same group.<sup>[33]</sup> The organosilica precursor 4,4'-bis(triethoxysilyl)biphenyl (BTEBP) (**9**) was used in presence of OTAC as SDA under basic conditions. Due to the lower structural order this material showed one reflection in the low angle region ( $2\theta < 10^\circ$ ) of the XRD pattern but five additional reflections could be observed in the wide angle region. These five reflections could be indexed as 100, 200, 300, 400 and 500 and were attributed to the arrangement of biphenylene units on the molecular level (1.16 nm). The crystal-like arrangement of organic functionalities in the pore wall, which was interpreted from the powder X-ray diffraction, was proved by HRTEM, as described above.

The synthesis of a new interesting material with crystal-like arrangement of organic moieties in the pore walls was accomplished by Sayari and Wang.<sup>[34]</sup> A new organosilica precursor with a highly conjugated unit, 1,4-bis[(*E*)-2-(triethoxysilyl)vinyl]benzene (BTEVB) (**10**), was used in a synthesis with OTAC as SDA under basic conditions. For the first time an organic bridge with a conjugation extending beyond the benzene unit was applied. The unsaturated

units in this material offer opportunities for further functionalisation of this new material and thus, the chance to synthesise chiral PMOs. Cornelius et al.<sup>[35]</sup> synthesised 1,4-divinylbenzene-bridged PMOs in order to investigate the possibility of further functionalisation by post-synthetic hydroboration for the formation of chiral diols and cycloaddition reactions.

The synthesis of a materials by application of 1,3-bis(triethoxysilyl)benzene (**6**) as organosilica source with OTAC as SDA under basic conditions presented by Kapoor et al.<sup>[36]</sup> demonstrate that the crystal-like arrangement of organic moieties in the pore walls is not restricted to symmetrically substituted precursors.

The formation process of these materials was investigated by Morell et al. in an *in situ* small and wide angle X-ray scattering study in order to obtain information about the formation of the mesophase and the ordering of molecules in the pore walls.<sup>[37]</sup> The synthesis of a biphenylene-bridged material was reproduced and during the hydrothermal treatment of the reaction solution XRD patterns were measured every minute. The analysis of the data leads to the conclusion that both ordering processes occur simultaneously.

### 1.2.3.2 Synthesis of PMOs with non-ionic surfactants

#### *a) PMOs with large pores*

After the successful synthesis of PMOs with pore diameters limited to a range between 2 and 5 nm by the use of the ionic alkylammonium surfactants (alkyl chain lengths: C<sub>8</sub> – C<sub>22</sub>) much effort was spent on the synthesis of PMO materials with larger pores that might be interesting for application in catalysis, sorption, separation or host/guest chemistry. Larger pore diameters could be obtained by the usage of triblock copolymers such as Pluronic<sup>®</sup> P123 (PEO<sub>20</sub>PPO<sub>70</sub>PEO<sub>20</sub>), Pluronic<sup>®</sup> F127 (PEO<sub>106</sub>PPO<sub>70</sub>PEO<sub>106</sub>) or B50-6600 (PEO<sub>39</sub>PBO<sub>47</sub>PEO<sub>39</sub>) as SDAs under acidic conditions which has still been applied for the syntheses of pristine mesoporous silica materials like the SBA-15 (space group: *p6mm*), SBA-16 (*Im $\bar{3}m$* ) and FDU-1 (*Fm $\bar{3}m$* ).<sup>[38-41]</sup> With triblock copolymers the pore diameters could be expanded up to 30 nm.

The first synthesis of PMOs with large pores was published by Muth et al. in 2001.<sup>[42]</sup> With BTME (**2**) as organosilica precursor and Pluronic<sup>®</sup> P123 as SDA in acidic medium an ethane-bridged material with a pore diameter of 6.5 nm and a specific surface area of 913 m<sup>2</sup>/g was obtained. Similar synthesis conditions were chosen by Burleigh et al. who were also able to increase the pore diameter up to 20 nm by the addition of different amounts of the swelling

agent 1,3,5-trimethylbenzene (TMB) to the reaction solution with a pore structure changing from wormlike to a hexagonal arrangement of spherical pores.<sup>[43]</sup>

As described by Guo et al., the degree of order of the materials structured with these non-ionic triblock copolymers could be influenced by the addition of inorganic salts to the reaction solution because these salts play important roles as mediator ions during the formation process of the material. As a result a 2d hexagonal ordered ethane-bridged PMO material was obtained by the addition of NaCl to the reaction solution.<sup>[44]</sup>

The influence of the organosilica precursor/SDA ratio and the pH value of the reaction solution on the structure and the morphology of the resulting materials was investigated by Bao et al.<sup>[45-47]</sup> Optimal synthesis conditions led to 2d hexagonal ordered materials without the addition of an inorganic salt. Ethane-bridged monolithic materials (pore diameter: 7.7 nm, BET surface: 957 m<sup>2</sup>/g) were obtained via the TLCT-mechanism from a lyotropic crystalline phase consisting of P123, water and BTME.<sup>[48]</sup> A 2d hexagonal ordered ethane-bridged material of extreme thermal stability was synthesised using the triblock copolymer poly(ethyleneoxide)-poly(DL-lactic acid-co-glycolic acid)-poly(ethyleneoxide) (PEO<sub>16</sub>(L<sub>28</sub>G3)PEO<sub>16</sub>; LGE53) as SDA.<sup>[49]</sup>

The application of Pluronic<sup>®</sup> P123 as SDA normally leads to 2d hexagonal ordered materials. By the application of Pluronic<sup>®</sup> F127 or B50-6600 cubic PMO materials could be obtained as well, which was shown by Guo et al. who were able to synthesise an ethane-bridged material with the cubic  $Im\bar{3}m$  symmetry (pore diameter: 9.8 nm, BET surface: 989 m<sup>2</sup>/g).<sup>[50]</sup> In this case the addition of K<sub>2</sub>SO<sub>4</sub> to the synthesis solution was necessary in order to obtain ordered materials; otherwise the synthesis resulted in amorphous gels. Matos et al. presented a synthesis with the more hydrophobic B50-6600 as SDA and BTME (**2**) as organosilica source.<sup>[51]</sup> This material exhibited a cubic structure similar to the pure mesoporous silica phase FDU-1 (space group:  $Im\bar{3}m$ ). The synthesis of a cubic structured material synthesised with BTME (**2**) as organosilica precursor and F127 as SDA with the addition of KCl was published by Zhao et al. This material exhibited a cage-like pore network (pore diameter: 5.6 nm) with  $Fm\bar{3}m$  symmetry.<sup>[52]</sup>

Most of the PMO materials with large pores which result from the application of a triblock copolymer under acidic reaction conditions are ethane-bridged materials, which do not offer interesting properties due to the saturated aliphatic character of the organic moiety. Only few publications are presented up to now dealing with the synthesis of PMO materials with more complex organic bridges.

A 2d hexagonal ordered phenylene-bridged material with a pore diameter of 7.4 nm and a specific surface area of 1029 m<sup>2</sup>/g synthesised with Pluronic<sup>®</sup> 123 as SDA was first presented by Goto and Inagaki. In contrast to the phenylene-bridged materials synthesised with OTAC under basic conditions, no molecular periodicity of the organic bridges could be observed for the material with large pores.<sup>[53]</sup> This material exhibited a thermal stability up to 550 °C. The integration of an unsaturated aliphatic bridge was accomplished by applying 1,2-bis(triethoxysilyl)ethene (**3**) as organosilica source and the addition of butanol to the reaction solution.<sup>[54]</sup> The unsaturated unit was brominated in a following reaction. About 30 % of all ethene units were brominated during this post synthetic treatment. In 2005, Morell et al.<sup>[55]</sup> succeeded in synthesising a thiophene-bridged PMO material with large pores (pore diameter: 5.6 nm). In contrast to publications dealing with this organosilica precursor BTET (**15**) <sup>29</sup>Si MAS NMR spectroscopic investigations showed that only 4 % of the Si-C bonds were cleaved during the reaction and extraction procedures.

#### *b) PMOs with small pores*

A further synthesis pathway of PMOs with small pores was introduced in 2002 for the first time. Non-ionic polyoxyethylenealkylether such as polyoxyethylene-(10)-cethylether (Brij<sup>®</sup> 56) or polyoxyethylene-(10)-stearylether (Brij<sup>®</sup> 76) were used in an acidic reaction medium, therewith following the pathway S<sup>+</sup>X<sup>-</sup>T<sup>+</sup>. The synthesis of PMOs under acidic conditions usually leads to higher hydrolysis and condensation rates due to the +I effect of the organic function and thus leads to thicker pore walls. The pore diameters are limited to 5.5 nm; specific surface areas around 1000 m<sup>2</sup>/g are obtained under these synthesis conditions.

Burleigh et al. synthesised ethane-bridged PMOs with Brij<sup>®</sup> 56 and Brij<sup>®</sup> 76 in reaction solutions with different pH values.<sup>[56]</sup> Samples synthesised with Brij<sup>®</sup> 76 as SDA exhibited a 2d hexagonal mesostructure (*p6mm*) with pore diameters between 4.3 and 4.5 nm while the samples synthesised with Brij<sup>®</sup> 56 as SDA showed only a poor ordering and corresponding smaller pore diameters between 3.6 and 3.9 nm due to the shorter chain length of the SDA. The degree of order and the symmetry of the mesostructure proved to be almost independent of the acid concentration. In contrast the ethane-bridged PMOs synthesised with CTAC as SDA under acidic conditions showed a low degree of structural order. Changes of the pH value significantly affected the resulting mesostructure. Further investigations concerning the synthesis of methylene-, ethane-, ethene- and phenylene-bridged PMOs synthesised with Brij<sup>®</sup> 76 as SDA were carried out by Burleigh et al.<sup>[57]</sup> These materials exhibited a higher

thermal and mechanical stability than the equivalent pristine silica materials.<sup>[58]</sup> Highly ordered ethane-bridged materials synthesised with Brij<sup>®</sup>-surfactants were also obtained by Hamoudi and Kaliaguine<sup>[59]</sup> and Sayari et al.<sup>[60]</sup> Sayari and coworkers were also able to synthesise well ordered ethene- and phenylene-bridged PMOs with the aid of Brij<sup>®</sup>-surfactants.<sup>[54,61]</sup> Nearly 50 % of the C=C bonds of the ethene-bridged material were accessible as tested by bromination experiments. In contrast to the 2d hexagonal ordered materials synthesised with alkyltrimethylammonium surfactants under basic conditions no periodicity of the organic units on the molecular scale was observed for the 2d hexagonal structured materials synthesised with Brij<sup>®</sup>-surfactants under acidic conditions as concluded from the absence of reflections in the wide angle region of the corresponding XRD patterns. According to the authors, Fourier transform TEM images indicated a new arrangement of the organic moieties not parallel to the pore axis but including an angle of 57 °.

Two completely new materials were presented by Hunkeler and Ozin.<sup>[62,63]</sup> The organosilica precursors bis-4-(triethoxysilyl)phenylether (**16**) and bis-4-(triethoxysilyl)phenylsulfide (**17**) were applied in combination with Brij<sup>®</sup> 76 as SDA and NaCl. The 4-phenylenether-bridged material showed a wormlike structure while the 4-phenylsulfide-bridged material exhibited only a poor ordering of pores. Pore diameters between 2 and 3 nm and specific surface areas between 430 and 640 m<sup>2</sup>/g were obtained. Both materials offered thermal stabilities up to 500 °C.

The synthesis of materials containing arylmethylene bridges from the organosilica precursors of the type 1,4-(CH<sub>2</sub>)<sub>n</sub>C<sub>6</sub>H<sub>4</sub> (n = 0-2), (**5**), (**7**), (**8**) with the aid of Brij<sup>®</sup>-surfactants and NaCl was first introduced by Hunkeler and Ozin.<sup>[63]</sup> The phenylene-bridged material was already known but the 4-benzyl-bridged and the *p*-xylene-bridged material were introduced for the first time. All products exhibited a 2d hexagonal mesostructure and pore diameters between 2 and 3 nm. The thermal stability decreased with increasing number of methylene groups in the order **5** > **7** > **8**.

A synthesis pathway with Brij<sup>®</sup> 76 as SDA and BTME (**2**) as organosilica precursor but under neutral reaction conditions was published by Zhang et al.<sup>[64]</sup> The formation of the 2d hexagonal mesostructure under neutral synthesis conditions needed to be catalysed by the addition of small amounts of fluoride ions to the reaction solution. Due to the neutral reaction conditions the addition of sodium fluoride or bivalent inorganic salts was necessary in order to obtain structured materials.

Kapoor and Inagaki worked with a mixture of OTAC and Brij<sup>®</sup> 30 (C<sub>12</sub>H<sub>25</sub>(EO)<sub>4</sub>OH) as SDAs under basic conditions.<sup>[65]</sup> With the organosilica precursor BTME (**2**) a highly ordered ethane-

bridged material with a cubic symmetry ( $Pm\bar{3}n$ ), a pore diameter of 2.8 nm and a specific surface area of over 700 m<sup>2</sup>/g was obtained.

### 1.2.3.3 PMOs synthesised with tris-/multi-silylated precursors

PMO materials that are synthesised by hydrolysis and condensation of bissilylated organosilica precursors in presence of a SDA could be considered as ordered mesoporous materials, in which in the ideal case, a quarter of the Si-O-Si units are replaced by Si-R-Si units. The general formula for such materials would be  $R_{0.5}SiO_{1.5}$ . Unlike the bivalent oxygen atoms the applied organic bridges can form bonds to more than two silicon atoms. By realising this idea the structure of the PMOs can be extended by the use of mixtures of mono-, bis- and trissilylated or multisilylated organosilica precursors. The mechanical and thermal stability of these materials might be increased due to the cross-linking properties of tris- and multisilylated organosilica precursors. The use of these materials for industrial applications such as catalytic reactions or petrochemical processes requires temperatures normally above 500 °C, which excepts the usage of the PMO materials from such applications. But the thermal stability of the “usual” PMO materials might be high enough for the use in catalysis of organic- or biocatalysis reactions.

In 2002, the first synthesis of a PMO material synthesised from a trissilylated precursor was published by Kuroki et al.<sup>[66]</sup> In a typical reaction the organosilica precursor 1,3,5-tris(triethoxysilyl)benzene (**11**) was used and the result was a mesoporous material with small pores but high thermal stability (600 °C).

Another interesting material was presented by Landskron et al.<sup>[67]</sup> 1,1,3,3,5,5-hexaethoxy-1,3,5-trisilacyclohexane (**4**) was incorporated into a typical synthesis procedure and the resulting product exhibited connected  $[Si(CH_2)_3]$  ring structures. The pore diameter was 2.2 nm and thus, still in the mesopore range. The decomposition of the material started at about 600 °C.

The periodic mesoporous dendrisilicas were introduced by Landskron and Ozin in 2004.<sup>[68]</sup> Different dendrimer building blocks (see Figure 1.7 (**20**), (**21**), (**22**)) with alkoxysilyl functionalities were used in different synthesis procedures with OTAC or triblock copolymers as SDA. No decomposition of the organosilica network was observed up to 600 °C under nitrogen atmosphere. The mesostructure as well as the Si-C bond remain intact up to this temperature.

The synthesis of a new class of bifunctional PMO material formed from single source precursors was published by Hunks and Ozin.<sup>[69]</sup> Siloxane-, disilsesquioxane (DT<sup>2</sup> type, formed from **18**) and trisilsesquioxane (MT<sup>3</sup>-type, formed from **19**) units were used with a non-ionic triblock copolymer as SDA in order to obtain high connected networks. PMOs that are built from bissilylated precursors are of the T<sup>2</sup> type. The organosiloxane compounds are classified according to the number of oxygen atoms grouped around the silicon core. Four siloxane bridges per silicon atom could be realised named mono- (M), di- (D), tri- (T) and tetra-substitution (Q)). The resulting 2d hexagonal ordered materials exhibited pore diameters of 6.2 nm (DT<sup>2</sup>) and 5.8 nm (MT<sup>3</sup>), respectively but a low thermal stability (stable up to 250 °C).

#### 1.2.3.4 PMOs and other organic-inorganic hybrid materials synthesised with mixtures of different (organo)silica precursors

As one can see from Figure 1.7 the number of organosilica precursors that were successfully transferred into PMO materials is relatively low. The successful reaction to a highly ordered PMO material depends on the structural properties of the organosilica precursor. The most important criteria for a successful synthesis is the rigidity of the organic bridge. High conformational flexibilities present in long chain aliphatic bridges lead to a collapse of the structure. However, the class of the PMO materials can be extended by co-condensation reaction of different mixtures of precursors that are normally used for the synthesis of bi- or multifunctional PMO materials. Three different synthesis pathways for these materials are described in the literature.

- a) mixtures of TEOS/TMOS and bis/multisilylated precursors
- b) mixtures of mono- and bissilylated precursors
- c) mixtures of bissilylated precursors

These three pathways establish new fields of organosilica materials. The synthesis pathway a) allows the incorporation of large organic molecules into the pore wall framework. The high TEOS/TMOS concentrations added to relatively low amounts of the organosilica precursor permits the formation of a highly ordered structure. The disadvantage is the low amount of organic bridges in the materials. A list of precursors used in such co-condensation reactions is given in Figure 1.10. The co-condensation with TEOS or short organosilica precursors like

BTME with these organosilica precursors offered the possibility of incorporating active sites for the adsorption of heavy metal ions (**25**, **26**),<sup>[70-72]</sup> for an organic switching function<sup>[73]</sup> (**24**) or high catalytic activity (**23**).<sup>[74]</sup> The incorporation of the precursors (**27**), (**28**), (**29**) or (**30**) leads to chiral groups in the PMO framework.

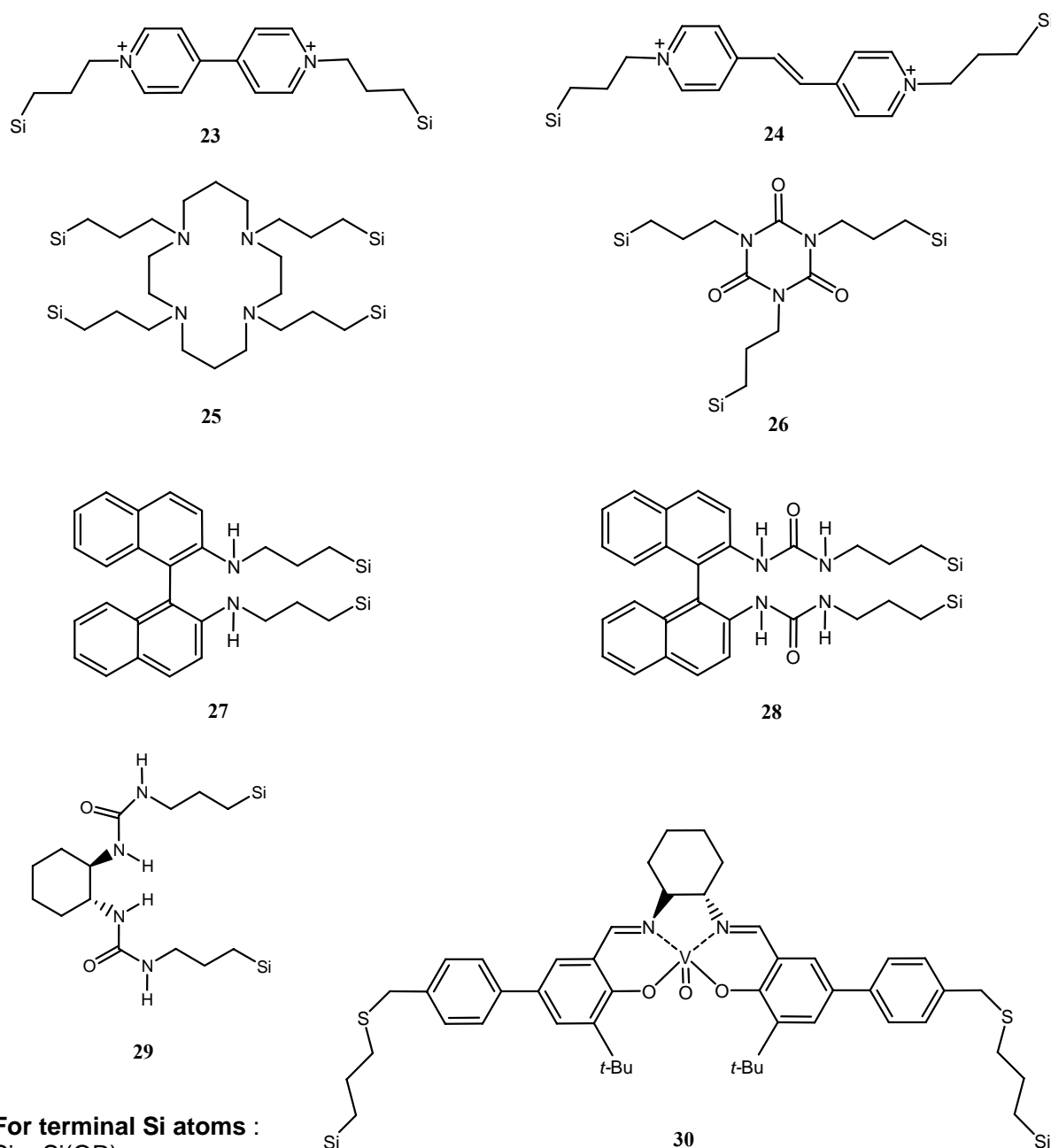


**Figure 1.10:** Overview of the complex organosilica precursors that were successfully incorporated in PMO materials via the co-condensation pathway with TEOS/TMOS.<sup>[8]</sup>

Materials synthesised via the pathway b) exhibit organic functionalities protruding into the pores which might be interesting for further reactions at the terminal functionalities.<sup>[75-78]</sup>

Materials synthesised via the pathway c) allow the tuning of the surface polarity to some extent and might be useful for new adsorption materials. The disadvantage of both synthesis pathways a) and b) is, as described in chapter 1.2.2, the homocondensation caused by the +I effect of the organic functions and thus, the different electron densities at the silicon atoms, which influence the hydrolysis and condensation. An overview of the different co-condensation reactions following the pathways a), b) and c) is given by Hoffmann et al.<sup>[8]</sup> Recently, a synthesis of a 2d hexagonal structured material containing phenylene- and thiophene-bridges has been published by Morell et al.<sup>[79]</sup> For the first time it was possible to synthesise materials that show always the same quality of the mesostructure independent on the organosilica precursor ratio.

### 1.3 Spherical (organically modified) mesoporous silica particles

From the discovery of the high ordered mesoporous materials and the possibility of functionalisation by grafting or co-condensation great attention arose concerning a synthesis of materials with a definite morphology. Monodisperse spherical particles were of great interest because of their potential application in chromatography or drug release.

Since 1956, when spherical silica particles were first synthesised, much effort was spent on the synthesis of spherical silica particles with variable sizes.<sup>[80]</sup> In these syntheses a silica precursor (tetraalkyl orthosilicate with alkyl being methyl, ethyl, propyl, butyl or pentyl) was hydrolysed and condensed in a mixture of water, ethanol as a co-solvent and ammonia. In 1968, Stöber et al. reproduced these syntheses and made different experiments concerning the particle size and shape in dependence on the co-solvent concentration, the pH value, the reaction time, the stirring procedure and the interactions between the applied silica source and the co-solvent or co-solvent mixtures (methanol, ethanol, 1-propanol, 2-propanol, 1-butanol, 1-pentanol).<sup>[81]</sup> The resulting particles showed sizes between 50 nm and 2 µm but high particle sizes led in most cases to a broad particle size distribution. Stöber et al. supposed the presence of ammonia and the resulting pH value to be responsible for the particle shape but a clear explanation about the formation of the spheres in the reaction solution was not given.

The discovery of the mesoporous materials in 1992 (described above) established a new idea for the so-called Stöber particles. In 1997, the Stöber synthesis was modified by the Unger group by adding an *n*-alkyltrialkoxysilane as SDA to a typical Stöber solution consisting of water, ethanol, ammonia and TEOS.<sup>[82-84]</sup> These experiments led to spherical porous silica

particles with particle diameters of 500 nm, high specific surface areas ( $\approx 1000 \text{ m}^2/\text{g}$ ), narrow pore size distributions but a relatively low structural order proved by only one reflection in the X-ray diffraction pattern. At nearly the same time, Huo et al. published a synthesis of mesoporous silica spheres in acidic medium.<sup>[85]</sup> The properties of these spheres were nearly the same except for the particle diameter. The spheres synthesised in acidic medium exhibited a particle diameter of up to 1  $\mu\text{m}$ . In 1998, Büchel et al. presented a synthesis of partly porous spherical particles.<sup>[86]</sup> The core was synthesised according to the procedure described by Stöber et al.<sup>[81]</sup> After finishing the synthesis of the core a growing process followed. The seeds were stirred in a solution containing water, ammonia, the silica source and a surfactant<sup>[82]</sup> in order to produce a porous shell as described by Giesche et al.<sup>[87]</sup> for the first time. The resulting particles consisted of non-porous cores of 420 nm in diameter and porous shells of only 75 nm thickness. These particles exhibited of course lower specific surface areas than other mesoporous materials but surface areas up to  $350 \text{ m}^2/\text{g}$  and pore diameters up to 3.8 nm could be obtained. The synthesis of completely porous particles in the size range synthesised with CTAB as SDA was published by the same authors.<sup>[88]</sup>

In the same year another synthesis pathway for mesoporous silica spheres was introduced by Qi et al.<sup>[89]</sup> A mixture of CTAB and the non-ionic surfactant Brij<sup>®</sup> 56 combined with TEOS as silica source was used for liquid crystal templating under acidic conditions but without the addition of a co-solvent. The resulting particles reveal a particle diameter of 2 - 6  $\mu\text{m}$  and all characteristic properties of the ordered mesoporous materials.

From that time the development of new spherical materials was carried out by several research groups. In 1999, the Unger group first published cubic ordered spheres (space group:  $Ia\bar{3}d$ )<sup>[90]</sup> and 2d hexagonal ordered spheres (space group:  $p6mm$ ).<sup>[91]</sup> Both materials were synthesised via the modified Stöber reaction. But in both cases the size of the particles was below 2  $\mu\text{m}$ . Even the incorporation of metal atoms like aluminium or titanium into the framework could be achieved.<sup>[92]</sup> The synthesis containing the non-ionic Triton X as SDA and sodium silicate as silica source led to spherical but agglomerated particles in the size range of 0.3 – 10  $\mu\text{m}$ .<sup>[93]</sup> The first review dealing with the synthesis and the application of spherical mesoporous silica particles was published by Unger et al. in 2000.<sup>[94]</sup>

The synthesis of the so-called MSU-1 material by Bossière et al. expanded the field of mesoporous spherical particles.<sup>[95,96]</sup> The reaction was accomplished under acidic conditions with the non-ionic surfactant Tergitol 15S12 PEO and with the addition of sodium fluoride as a catalyst. For the first time it was possible to synthesise spherical mesoporous silica particles with a narrow particle size distribution in the size range of 5 to 15 nm, which is in the particle

size range for application in HPLC. The agglomeration, which is one of the most important problems during the syntheses procedures of the particles, was reduced to a high extent by ultrasonic treatment of the calcined particles.

In 2001, many results concerning small mesoporous silica spheres (1 - 2  $\mu\text{m}$ ) or large mesoporous spheres (30 - 100  $\mu\text{m}$ ) were published but a particle size of 3 - 10  $\mu\text{m}$  could not be obtained.<sup>[97-101]</sup> Particle sizes of 2 – 3 nm were obtained by Chan et al.<sup>[102]</sup> In a typical synthesis CTAB was used as SDA and TEOS and monomethyltriethoxysilane as silica sources under acidic synthesis conditions.

An interesting but completely different synthesis pathway was developed by Oh et al.<sup>[103]</sup> The original solution was an oil/water/oil ( $\text{O}_\text{A}/\text{W}/\text{O}_\text{B}$ ) emulsion consisting of *n*-hexane/water/decanol with TEOS as silica source. Hydroxypropyl cellulose (HPC) was added into the decanol phase, polyethylene glycol (PEG) to the water phase. Both substances helped to stabilise the emulsion. The resulting material contained mesopores as well as macropores. The size and the shape of the particles depend on the HPC concentration in the  $\text{O}_\text{B}$  phase while the PEG influences the formation of macropores. The specific surface areas were relatively low ( $\approx 300 \text{ m}^2/\text{g}$ ) due to the high pore diameter. Unfortunately, no data concerning the pore sizes was given.

Another interesting synthesis way was described by Martin et al.<sup>[104]</sup> Commercial spherical mesoporous silica spheres were obtained from Merck (Lichrospher 100) and stirred in an alkaline solution consisting of water, sodium hydroxide and CTAB. Then the solution was heated up to 110 °C for 24 hours under autogenous pressure. As a result microspheres were obtained which showed nearly the same size as the original material. Lichrospher 100 was X-ray-amorphous while the new material showed a well-defined 2d hexagonal arrangement of pores. The nitrogen physisorption isotherms differ also to a high extent. The Lichrospher 100 showed a capillary condensation step over a wide  $p/p_0$  range and a resulting broad pore size distribution while the isotherm of the new material exhibited a sharp capillary condensation step and thus, a narrow pore size distribution. This transformation was called pseudomorphism by the authors which is already known from the mineralogy. In a following publication the phase transition from spherical MCM-41 to spherical MCM-48 was described by application of the same synthesis strategy.<sup>[105]</sup>

Further investigations were published by Rao et al.<sup>[106]</sup> The synthesis of 5 - 10  $\mu\text{m}$  spherical particles was accomplished by a vibrating orifice aerosol generator (VOAG) and is based on evaporation-driven surfactant templating in microdroplets. By applying different SDAs (CTAB, Brij<sup>®</sup> 58) the particle size could be varied between 5 and 10  $\mu\text{m}$ .

In 2003, Kosuge et al. presented a synthesis pathway in acidic medium with the possibility of varying the particle size distribution to a high extent.<sup>[107]</sup> The solution consisted of TEOS, octylamine (SDA), hydrochloric acid and ethanol. Nearly monodisperse particle sizes between 20 and 300  $\mu\text{m}$  were obtained by varying the stirring speed between 400 and 1000 rotations per minute (rpm).

Spherical SBA-15 silica particles of 5  $\mu\text{m}$  in diameter were synthesised by Ma et al.<sup>[108]</sup> These particles exhibited the optimal size for chromatographic applications and the typical characteristics for mesoporous materials. In contrast to the synthesis of the SBA-15 silica that was often described in the literature a co-surfactant (CTAB) and a co-solvent (ethanol) were added to the synthesis solution of the SBA-15.

In 2004, spherical particles have been obtained by Yano et al. with a reaction mixture similar to the original modified Stöber reaction first published by the Unger group.<sup>[109]</sup> But instead of ammonia sodium hydroxide was added in order to increase the pH value into the basic region. These results disprove the statement made by Stöber et al.<sup>[81]</sup> concerning the function of ammonia as a morphological catalyst. A substitution of ammonia by sodium hydroxide also led to well-defined monodisperse spherical particles which exhibited all characteristics for ordered mesoporous materials. Even the size of the particles (0.5 - 1  $\mu\text{m}$ ) is typical for Stöber particles.

From all publications dealing with the synthesis of spherical Stöber particles one can conclude that particle diameters above 2  $\mu\text{m}$  could not be achieved under such synthesis conditions. But Lind et al. developed a new way of synthesising large Stöber particles.<sup>[110]</sup> The original material (particle diameter:  $\sim 500$  nm) was agglomerated to large particles with a mean diameter of 25  $\mu\text{m}$  by spray drying technique. The large particles showed two different forms of porosity: the porosity of the MCM-41 or MCM-48 silica particles (intra particle porosity) and the porosity between the single small particles (inter particle porosity) which established new fields of application such as size exclusion chromatography. A high density packing of these particles into a column offered a third form of porosity additional to the bimodal diameter distribution of the large spheres: the porosity between the large particles (inter particle porosity).

Some investigations concerning organically modified mesoporous silica spheres have been published yet. In 2003, Huh et al. presented spherical particles (particle diameter: 0.5 - 1  $\mu\text{m}$ ) functionalised with 3-[2-(2-aminomethylamino)ethylamino]propyl (AEP) groups or alternatively 3-cyanopropyl (CP) groups by co-condensation reactions of TEOS and

AEP-trimethoxysilane or alternatively CP-triethoxysilane in the presence of CTAB as SDA under basic conditions.<sup>[111]</sup>

Sadasivan et al. first synthesised spherical mesoporous silica particles via a co-condensation reaction of TEOS and 3-mercaptopropyltriethoxysilane (MPTS), 3-aminopropyltriethoxysilane (APTS) or allyltriethoxysilane with CTAB as SDA under basic conditions.<sup>[112]</sup> But the low particle diameter of 100 nm is not suitable for application in chromatography. Only slightly larger particles (300 nm) were synthesised by Ganesan et al. using the same substances.<sup>[113]</sup> A synthesis of mercaptopropyl-functionalised silica spheres via the co-condensation reaction with octylamine or dodecylamine as SDA under mild acidic conditions was accomplished by Kosuge et al.<sup>[107]</sup> Similar results but with Igepal Ca-720 ((C<sub>8</sub>H<sub>17</sub>)-(C<sub>6</sub>H<sub>4</sub>)-(OCH<sub>2</sub>CH<sub>2</sub>)<sub>10</sub>OH) as SDA were published by Beaudet et al.<sup>[114]</sup> Particles with diameters between 5 and 10 nm could be obtained by this synthesis procedure.

The co-condensation of TEOS with [3-(methacryloxy)propyl]trimethoxysilane led to alcohol-functionalised silica spheres as described by Ding et al. but no data concerning the morphology was shown by the authors.<sup>[115]</sup>

Polydisperse mesoporous metal containing silica spheres were synthesised by Hampsey et al. in a spray drying process in order to obtain new catalytic active materials.<sup>[116]</sup>

As one can conclude from these publications many different ways of synthesising spherical mesoporous silica particles have been developed up to now. The morphology of the materials was investigated by varying different synthesis parameters but different opinions exist concerning the synthesis parameters which are responsible for the spherical morphology.

#### 1.4 Spherical periodic mesoporous organosilica particles (sph-PMOs)

Only few results concerning spherical PMO particles have been published yet. In 2004, Kapoor et al. synthesised spherical phenylene-bridged PMO particles.<sup>[117]</sup> These particles exhibited small sizes between 0.6 and 1 µm, small pore diameters between 1.8 and 2 nm and a poor ordering of mesopores. The mild alkaline reaction conditions caused by the addition of ammonia instead of sodium hydroxide initialised a particle growing procedure similar to the original<sup>[81]</sup> or the modified Stöber reaction.<sup>[88]</sup>

Ethane-bridged spherical particles were introduced by Kim et al. in 2004.<sup>[118]</sup> These particles were synthesised with CTAC as SDA and BTME as organosilica source in basic reaction medium (NaOH). No co-surfactant or co-solvent was used. The hydrothermal treatment was

accomplished by microwave heating. The resulting particles were well ordered monodisperse mesoporous spheres with a particle diameter of 1  $\mu\text{m}$  and a 3.2 nm.

An additional publication dealing with spherical PMOs was presented by Xia et al.<sup>[119]</sup> Xia et al. synthesised PMOs spheres by hydrolysis and condensation of 1,2-bis(triethoxysilyl)ethene in presence of dodecyltrimethylammonium bromide as SDA under basic conditions without the addition of a co-surfactant or co-solvent. Particle diameters between 3 and 14  $\mu\text{m}$  were obtained. The control of the particle size was accomplished by the ratio  $\text{H}_2\text{O}$ /surfactant but also by the pH value to a certain degree. The materials showed high specific surface areas between 780 and 1000  $\text{m}^2/\text{g}$  and pore sizes around 2 nm. The bromination of the C=C double bond provided the accessibility of the C=C double bond in the pore walls.

Spherical particles via the co-condensation pathway were synthesised by Zhu et al.<sup>[120]</sup> BTME and phenyltrimethoxysilane (PTMS) were applied as organosilica sources in presence of P123 and CTAB as SDAs and ethanol as a co-solvent under acidic synthesis conditions. Particles in the size range of 2 to 8  $\mu\text{m}$  were obtained with specific surface areas between 600 and 700  $\text{m}^2/\text{g}$  and pore diameters between 2.8 and 3.7 nm.

As one can conclude from this chapter only few results have been published concerning the synthesis procedures for spherical periodic mesoporous silica materials. Thus, the synthesis, characterisation and application of spherical PMOs with different organic moieties incorporated in the pore wall framework will be an interesting field of research.

### 1.5 Aim of this work

The main aim of this work was the synthesis of monodisperse spherical periodic mesoporous organosilicas in different size ranges with different organic moieties within the pore wall framework. Three different size ranges should be obtained by different synthesis pathways.

For the application in high performance liquid chromatography spherical PMO particles in the size range of 3 to 10  $\mu\text{m}$ , which is the usually applied particle diameter for separation materials in high performance liquid chromatography, had to be synthesised and tested in a chromatographic system. Test mixtures of different polarity should be separated with different elution solvents. Comparisons of each experiment with analogous experiments on a commercial silica material should be carried out and an estimation with respect to the separation quality had to be given.

In further experiments particles with a mean diameter of around 100  $\mu\text{m}$  had to be synthesised. In addition, vapour adsorption properties of monodisperse spherical PMOs with a mean particle diameter of 80  $\mu\text{m}$  and different organic moieties incorporated in the pore wall network had to be carried out. In different test series the adsorption of benzene and ethanol on each material in dependence of the temperature in the range of 20 to 120  $^{\circ}\text{C}$  had to be investigated.

Furthermore, a synthesis of monodisperse spherical mesoporous particles in the size range between 0.5 – 1  $\mu\text{m}$  should be developed. A possible application for such materials is a use in capillary electrochromatography which was in this case not investigated.

The second aspect was the synthesis and characterisation of PMO powders containing heteroatoms in the organic bridge. These materials had to be investigated with respect to their heavy metal adsorption capacity in order to develop new materials for wastewater treatment or soil remediation.

A study on the formation mechanism of already known periodic mesoporous organosilicas by *in situ* measuring techniques should complete the work about the syntheses, characterisation and application of periodic mesoporous organosilicas. *In situ* small angle X-ray scattering measurements offer the possibility of observing the evolution of the single reflections from the XRD patterns during the complete synthesis procedure. For these experiments highly ordered PMO materials had to be chosen due to a relatively large number of higher ordering reflections in the small angle region. By regarding the evolution of these higher ordering reflections during the complete synthesis procedure conclusions about eventually occurring phase transitions during the formation process of the resulting material should be drawn. In order to obtain representative and reproducible results a setup had to be developed that enables a dynamic experiment which allows the data acquisition during the complete synthesis procedure.

Thus, the results of this work are divided into four parts. The first deals with the synthesis and characterisation of all synthesised samples (chapter 3) starting with the samples containing the nitrogen atom in the organic bridge which should be used for copper adsorption experiments. In the following part of chapter 3 the synthesis and characterisation of the spherical particles first in the size range of 0.5 – 1  $\mu\text{m}$ , then the spheres in the range of 10 – 300  $\mu\text{m}$  and at least the particles in the range of 3 – 10  $\mu\text{m}$  were described according to the importance of the samples concerning the main focus that was set on chromatography. In chapter 4 *in situ* studies of the formation mechanism of 2d hexagonal ordered phenylene-bridged PMOs are described. Chapter 5 deals with the copper adsorption experiments of the powder samples

containing a heteroatom. The adsorption of solvents on PMO spheres filled in a microreactor is described in chapter 6 and in chapter 7 results of the chromatographic experiments are presented.

A short description of the sample names as well as the applied organosilica precursors and structure-directing agents is given in Appendix I.

## 2 Characterisation methods

### 2.1 Powder X-ray Diffraction (P-XRD)

Powder X-ray diffraction (P-XRD) patterns were recorded with a Bruker AXS D8 Advance diffractometer at room temperature using filtered Cu-K $\alpha$  radiation in  $\theta/\theta$  geometry. The diffractometer was equipped with variable slits on the tube and detector side and a secondary monochromator. The data were collected in a step scan mode of  $\Delta 2\theta = 0.01^\circ$  and a counting time of 4 s per step as standard configuration.

### 2.2 Nitrogen Physisorption

Physisorption is based on the weak bond of an inert gas particle on a surface with adsorption heats of 5 – 10 kJ/mol. In the case of the mesoporous materials the binding force is of a van-der-Waals-type in contrast to the microporous material with adsorption heats of up to 25 kJ/mol which are extended in the chemisorption area. Different types and hysteresis loops can appear. Figure 2.1 shows the characteristic types of the isotherms. Type I is typical for a microporous material with a high specific surface area; type II is characteristic for a non-porous or macroporous substance. Isotherms of type III are undesirable and appear if interaction between the adsorbents and the surface is too weak. Their occurrence can in most cases be avoided by choosing a different kind of adsorbents. Mesoporous materials with a narrow pore size distribution show type IV isotherms. Type V is, like type III unwanted and occurs if the adsorbent-surface interaction is too weak. Type IV is a sequence of type II isotherms and is caused by consecutive monolayer adsorption on uniform non-porous substances.

While measuring adsorption isotherms hysteresis loops can occur due to the capillary condensation. The four characteristic hysteresis loops are depicted in Figure 2.2. The hysteresis loop H1 is attributed to a mesoporous material with a narrow pore size distribution. H2 is characteristic for a mesoporous substance with a broader pore size distribution or non-cylindrical pores. Larger slit pores cause hysteresis loops of type H3, microporous slit pores lead to type H4 hysteresis loops.

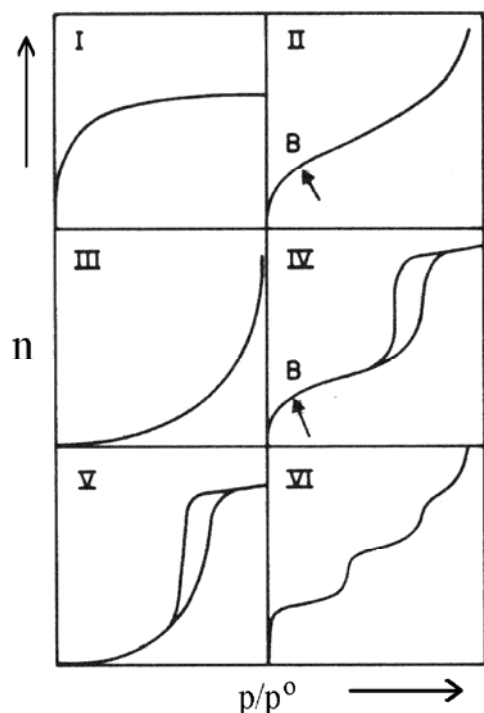


**Figure 2.1:** Diagram of the characteristic types of isotherms.<sup>[122]</sup>

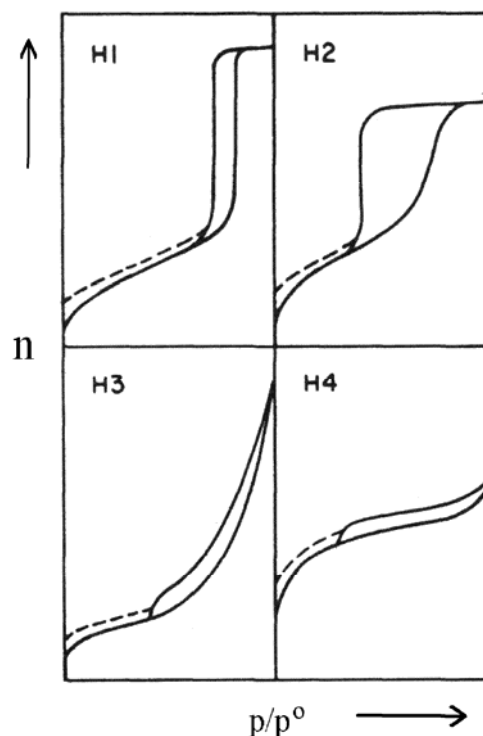


**Figure 2.2:** Overview of the characteristic types of hysteresis loops.<sup>[122]</sup>

Nitrogen physisorption measurements were carried out with a Quantachrome Autosorb 1 or alternatively a Quantachrome Autosorb 6 at 77 K. Specific surface areas and pore diameters were determined by nitrogen adsorption/desorption investigations. In our case nitrogen was used as adsorptive. Before each measurement the sample was outgassed for 24 hours in vacuum at 100 °C. Specific surface areas were calculated applying the theoretic equation of Brunauer, Emmet and Teller (BET) for the relative pressures between 0.05 and 0.1 – 0.3 depending on the number of data points that were appropriate for a linear fit.<sup>[123]</sup> Pore size distributions of the amine- and ethane-bridged samples were calculated by Barret-Joyner-Halenda (BJH) formula using the desorption branch of the nitrogen physisorption isotherms.<sup>[124]</sup> Although the calculation with the BJH formula does not lead to exact results for pore diameters below 3 nm this method was chosen because of the large organic unit of the organosilica precursor *N,N*-[bis(trimethoxysilyl)propyl]amine. The application of the non-local density theory (NLDT) (adsorption branch) was not applied in this case because no fitting kernel exists for such large organic units. The pore sizes of the ethane- and phenylene-bridged materials were calculated using the NLDT theory. All determinations were made assuming cylindrical pore geometry in a silica matrix. The calculated pore sizes can not be determined exactly due to the organic units in the pore walls which are neglected for the

calculation but the resulting values are more satisfying due to a smaller deviation from the real values. Micropore volume and mesopore volume could be separated by the t-method as well as the micropore surface of the materials. All calculations were carried out with the Autosorb software 1.51. (June 2005).

## 2.3 Raman Spectroscopy

### 2.3.1 Microreactor experiments

#### 2.3.1.1 Micromachining and reactor assembly

An array of seven microchannels, each 200  $\mu\text{m}$  wide and 100  $\mu\text{m}$  deep, was machined by micromilling with a rotation tool into a brass plate of 5 mm thickness. At the downstream end of these 200  $\mu\text{m}$  channels, the brass plate contained a recess into which the separately micromachined retainer structure was inserted. This retainer structure was manufactured by microcutting in brass and comprised two high aspect ratio microchannels of only 40  $\mu\text{m}$  width and 100  $\mu\text{m}$  depth, separated by a ridge of 60  $\mu\text{m}$  width, for each of the seven 200  $\mu\text{m}$  channels (Figure 2.3 a). To enable optical access for *in situ* measurements, a glass plate sealed by a polymeric gasket covered the microchannel array. The microstructured plate was fixed on a stainless steel base providing fluidic connections with standard fittings. The temperature of the reactor channel array was monitored by two thermocouples located just below the brass plate, and was electronically controlled via an electrical heater cartridge with integrated thermocouple inserted in the steel base block.

The 200  $\mu\text{m}$  channels were loaded with spherical PMO material by injecting a suspension of a mixture of ethane-bridged and phenylene-bridged PMO microspheres in ethanol into the assembled reactor via the fluidic inlet. The ethanol was then driven out by heating and flushing with nitrogen gas. The 40  $\mu\text{m}$  channel retainer structures reliably immobilised the PMO microspheres inside the 200  $\mu\text{m}$  channels (see Figure 2.3 b).

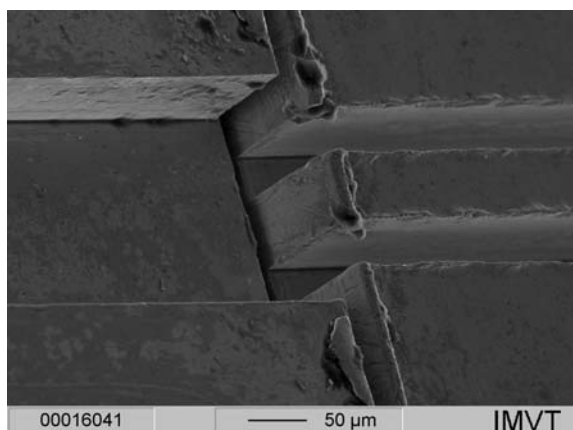


**Figure 2.3 a:** Scanning electron micrograph of a microchannel outlet (left) and the comb-shaped retainer structure (right).

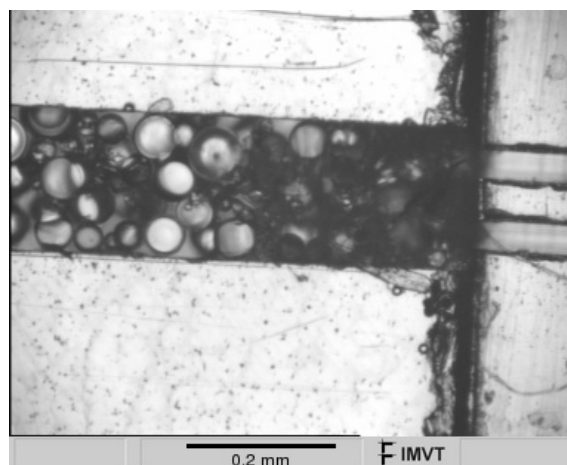


**Figure 2.3 b:** Optical microscopic image of PMO spheres incorporated inside a microchannel.

### 2.3.1.2 Measurements of the adsorption solvents

Figure 2.4 depicts schematically the set-up used for the temperature-dependent measurements of the adsorption of a solvent by a mixture of ethane-bridged and phenylene-bridged PMO microspheres at adsorption-desorption equilibrium. Nitrogen gas was led through a flask with the solvent at 20 °C. The outlet of the flask was connected to the inlet of the reactor which was kept at a constant temperature in the range between 20 and 140 °C. The nitrogen gas enriched with the solvent vapour was led over the two types of microspheres inside the reactor channel.

To monitor the adsorption of vapour by individual PMO microspheres at different temperatures micro-Raman measurements were performed in back-scattering geometry using a Jobin-Yvon microscope system. Excitation light (514.5 nm) of an air-cooled Ar<sup>+</sup> laser was coupled via optical fibres into the microscope system and focussed onto an individual PMO sphere inside the 200 μm channels. The laser power on the sample was less than 20 mW to avoid laser-induced annealing. The scattered light was collected via the same microscope objective. Elastically scattered laser light was rejected by a Kaiser Optics holographic Notch filter before coupling the Raman scattered light into the spectrometer system (Acton Research Corporation SpectraPro 500). A liquid nitrogen cooled ISA CCD2000 CCD camera detected the spectra. Typical recording times for a spectrum were 6 min. At each temperature, it was assured that the adsorption of the solvent vapour by the PMO microsphere under study was in the steady state.

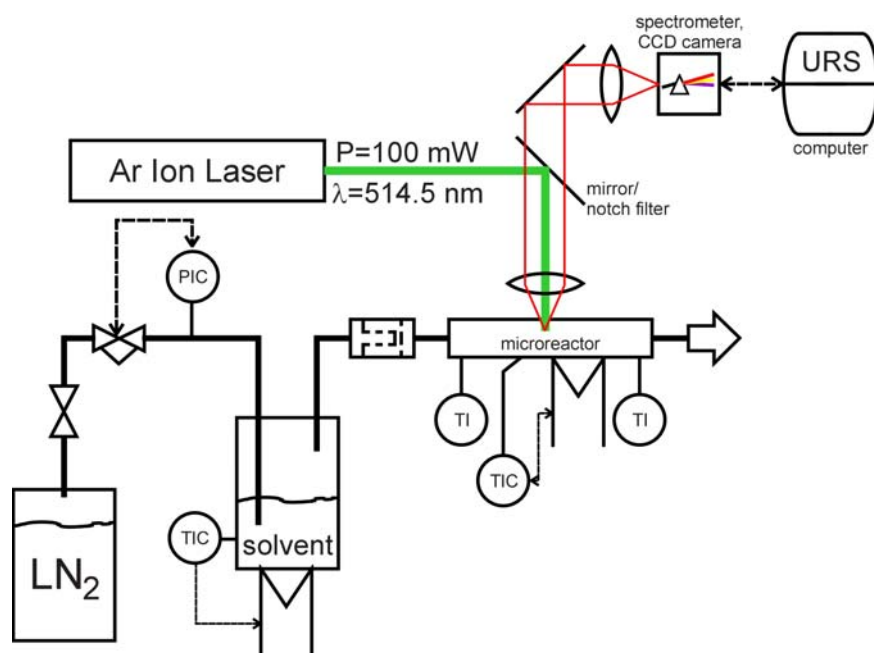


**Figure 2.4:** Experimental set-up for the *in situ* adsorption measurements of solvents by the PMO microspheres.

### 2.3.2 Raman spectroscopic measurements of powder samples

Raman spectra of PMO powder samples were recorded with the same instrument as described in chapter 2.3.1.1. The Ar-ion laser line 514.5 nm was used for excitation. The power on the sample was 20 mW, and the spectral resolution was  $1 \text{ cm}^{-1}$ .

## 2.4 Nuclear Magnetic Resonance Spectroscopy (NMR)

The  $^{29}\text{Si}$ -MAS-NMR spectra were recorded with a Bruker MSL-400 spectrometer. The samples were spun at 3.5 kHz. Further experimental parameters are p/2 pulse width of 6 ms, recycle delay of 300 s, 1500 scans. In order to obtain data about the relative number of different silicon sites in the material, the spectra were recorded without cross polarisation.

The  $^2\text{H}$ -NMR spectra were recorded with a Bruker 200 DBX-spectrometer and were spun at 30.7 MHz. As a standard sodium-trimethylsilylpropionate-2,2,3,3- $d_4$  was measured. After normalisation of the signals the number of deuterium atoms/g substance and for the porous material the number of atoms/ $\text{nm}^2$  could be specified.

## **2.5 UV/Vis Spectrometry**

The UV/Vis spectra were recorded with an Agilent HP8452A Diode-Array-Spectrometer. The range of the wavelength was 190-820 nm. 10 mg of the samples were dissolved in 10 mL cyclohexane and the solution was measured in a bulb with footprint of 1 cm<sup>2</sup>. Samples with high absorption were diluted again with cyclohexane.

## **2.6 Optical Microscopy**

For optical microscopic investigations the samples were suspended in 2-propanol and the suspension was dispersed on a microscope slide. The dry powder was then investigated with an Olympus BX 50 optical microscope. Images were recorded using the ExwaveHAD digital colour video camera by SONY. Images were edited with AnalySIS 3.0 by Soft Imaging System GmbH.

## **2.7 Scanning Electron Microscopy (SEM)**

For scanning electron microscopic measurements the powders were suspended in 2-propanol and the suspension was dropped onto a microscope slide. After evaporation of the solvent an adhesive round carbon foil with 1 cm in diameter was pressed onto the powder on the microscope slide. The powder particles were glued to the foil and the foil was sputtered with platinum for 90 s. Scanning electron micrographs were recorded with a HREM EDX Leo Gemini 982.

## **2.8 Transmission Electron Microscopy (TEM)**

For transmission electron microscopic investigations the powders were crushed in ethanol and the ground material was dispersed on a holey copper grid. Transmission electron micrographs were obtained with a Philips CM-ST 30 microscope operating at 300 keV.

## **2.9 Atomic force microscopy (AFM)**

Atomic force micrographs were recorded with a Quesant Electronic Q-Scope 250 Atomic Force Microscope. The samples were measured in the non-contact mode with a scan rate of 300 Hz and a resolution of 300 dpi.

## **2.10 Thermogravimetric Analysis (TG/MS)**

Thermogravimetric measurements were carried out with a Netzsch STA 409C/MS. The thermobalance was connected via a capillary system 403/4 to a Balzers QMS 421 quadrupole mass spectrometer. Heating rates of 10 K/min or 5 K/min in an air stream were applied. In case of the amine-bridged materials all TG/MS measurements were recorded in an argon/O<sub>2</sub> stream (4:1; v:v).

## **2.11 Laser diffraction**

### **2.11.1 Fundamentals**

In the laser diffraction technique the angular distribution of light scattered from a dilute particle dispersion is measured. A simple setup is illustrated in Figure 2.5. The basic physical principle is light scattering at the edges of particles. After focussing the light in the centre of a multielement-detector the scattering effect leads to signals on the non-centred elements of the detector. The optical setup is referred to the Fourier-optics.<sup>[125]</sup>

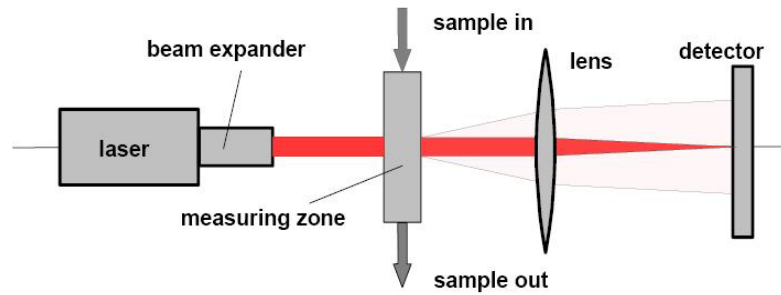


**Figure 2.5:** Illustration of the setup for laser diffraction measurements.<sup>[126]</sup>

After widening, the monochromatic wave of the laser light reaches the measuring zone. The through-passing and the scattered light are focussed by a lens system. In general one can say that the smaller the particles are the larger are the resulting diffraction angles. Hence, the focal length determines the measuring range. Diffraction at small angles can only be recognised by the system if the scattered light is not focussed to the central elements where all the unscattered light is collected (see Figure 2.6).<sup>[126]</sup>

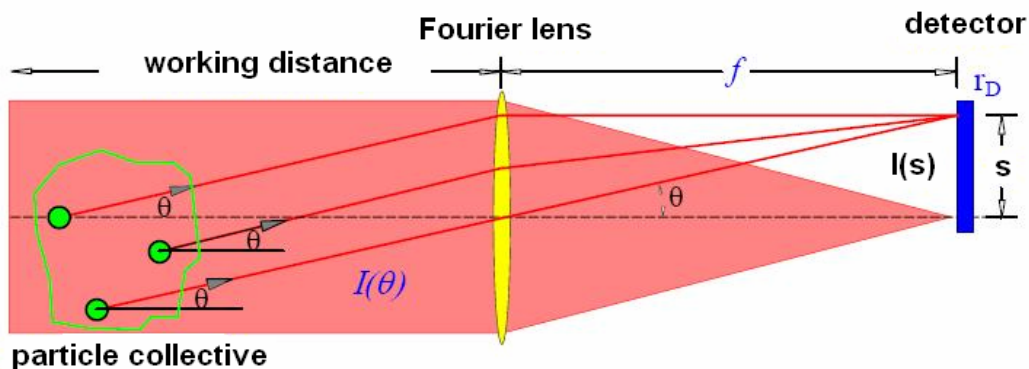


**Figure 2.6:** Particle size analysis in the parallel laser beam.<sup>[126]</sup>

For a more detailed consideration it should be said that light can be scattered, diffracted and absorbed by the disperse particles.<sup>[127]</sup> Scattered light depends on the form, the size and the composition of the particles and consists of reflected and refracted light. The diffraction is independent of the composition of the particles. It arises from edge phenomena and is only dependent on the geometric shadow caused by each particle. Absorption is again dependent on the size and the composition and occurs when light is converted into heat or electrical energy by interaction with the particles. An illustration of the scattering at a single particle is given in Figure 2.7.

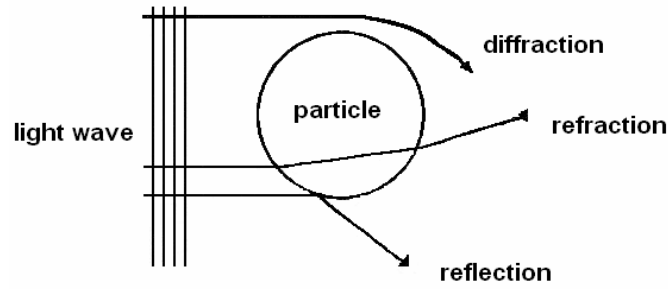


**Figure 2.7:** Scattering at a single particle.<sup>[128]</sup>

The loss of intensity of the original intensity ( $I_0$ ) is influenced by the scattering angle  $\theta$ , the refraction index  $n$ , the wavelength of the light wave  $\lambda$  and the particle diameter  $d_p$ .

$$\frac{I}{I_0} = f(\theta, n, \lambda, d_p) \quad (2.1)$$

The ratio of the particle perimeter and the wave length  $\lambda$  is the so-called Mie-parameter  $\alpha$ .

$$\alpha = \frac{\pi * d_p}{\lambda} \quad (2.2)$$

There are three possibilities for the determination of the particle size distribution that are dependent on the Mie-parameter or the particle size.

$\alpha \ll 1$ ;  $d_p \ll \lambda$       Region of Rayleigh scattering

(corresponds to particle diameters around 0.02  $\mu\text{m}$  for the application of wave lengths of the visible light of around 0.5  $\mu\text{m}$ )

$0.1 < \alpha < 10$ ;  $d_p \approx \lambda$       Region of Mie scattering

(corresponds to particle diameters around 0.2 – 2  $\mu\text{m}$ )

$\alpha \gg 1$ ;  $d_p \gg \lambda$       Region of Fraunhofer scattering

(corresponds to particle diameters above 2  $\mu\text{m}$ )

In the region of Rayleigh scattering the light scattering distribution is dominated by refraction. Diffraction and reflection hardly appear. The intensity of the scattering light is proportional to the sixth power of the particle diameter.<sup>[129]</sup> The region of Rayleigh scattering could not be acquired by Laser scattering instruments.

In the region of Mie scattering diffraction, absorption and reflection occur (see Figure 2.3) and thus, the complex refractive index is necessary in order to determine the particle size distribution. The influence of the composition is described by the complex refractive index  $m$ :

$$m = n - ik \quad (2.3)$$

with  $i$  being  $\sqrt{-1}$  and  $k$  being the imaginary component of the refractive index that is related to the absorption coefficient of the material. The imaginary component of the refractive index is zero for non-absorbing materials. Both, the real as well as the imaginary part of the complex refractive index are dependent on the wavelength. Scattering arises due to the differences in the refractive index of the particles and the surrounding medium. Thus, in order to use a scattering model for the calculation of the particle size distribution that produced a scattering pattern, it is necessary to know the complex refractive index of the particles as well as of the surrounding medium.<sup>[126]</sup> The intensity of scattering light is proportional to the fourth power of the particle diameter.<sup>[129]</sup> A calculation via the Mie theory is possible for particle sizes above  $0.1 \mu\text{m}$ .

In the scope of the geometric optics (Fraunhofer) the scattering at particles with diameters significantly larger than the wavelength of the laser is dominated by diffraction while reflection and refraction can be disregarded. In the region of Fraunhofer diffraction a circular intensity distribution around the optical axis is observed when parallel laser light impinges on a particle or particle collective due to the small scattering angles. A typical diffraction pattern is shown in Figure 2.8.

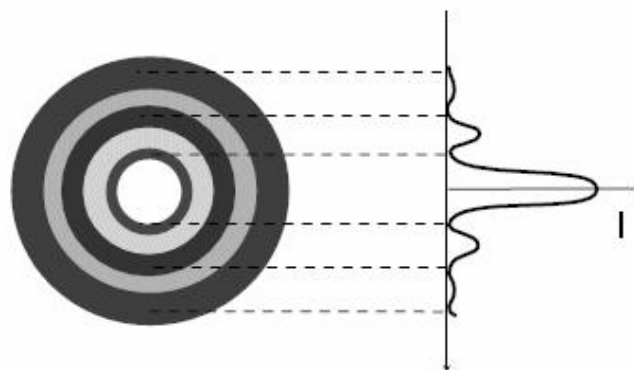


**Figure 2.8:** Fraunhofer diffraction circles: Diffraction pattern of a spherical particle ( $I$  being the intensity).<sup>[129]</sup>

The maxima and minima of the intensity distributions are determined by the particle size. The intensity is determined by the number of scattering particles in the sample. Therefore, the diffraction pattern is characteristic for the particle size distribution.

$$I(s, d_p) = I_0 * \left( \frac{2 * J_1(x)}{x} \right)^2 \quad (2.4)$$

With x being:

$$x = \frac{\pi * d_p * s}{\lambda * f} \quad (2.5)$$

and  $J_1$  being the Besselfunction of first type and first order and s the distance from the optical axis.

The particle size is inversely proportional to the diffraction angle and thus to the radius of the Fraunhofer circles. The light intensity of the diffraction circles is a measure for the amount of particles in the corresponding size. The particle size distribution can be calculated from the intensity distribution over the scattering angle  $\theta$  and accordingly the distance from the optical axis (s).

$$I(s) = \int_{d_p \min}^{d_p \max} N_{ges} * q_0(d_p) * I(s, d_p) dd \quad (2.6)$$

with  $N_{ges}$  being the total number of particles.

An approximation of this equation can be obtained by the so-called numeric quadrature.

### 2.11.2 Instrumental parameters

The particle size of the spherical phenylene-bridged PMOs (for synthesis see chapter 3.4) as well as of Nucleosil 50-10 (for further information see chapter 3.4) was determined using a Beckmann Coulter LS 13320. The calculation of the particle size distribution was carried out applying the Fraunhofer theory.

## 2.12 Small Angle X-ray Scattering (SAXS)

### 2.12.1 Experimental setup

The experimental setup was developed by Flodström et al. and a schematic illustration is depicted in Figure 2.9.<sup>[37,121]</sup> In our case the pump volume was 26 mL/min. The diameter of the capillary was 1.5 mm with 10  $\mu\text{m}$  glass thickness. Photographs of the experimental setup at beamline A2 are shown in Figure 2.10. Figure 2.10 a shows the reaction vessel with the contact thermometer and the tubing that were linked with the capillary. Figure 2.9 b and c show the capillary directly placed in the beam.

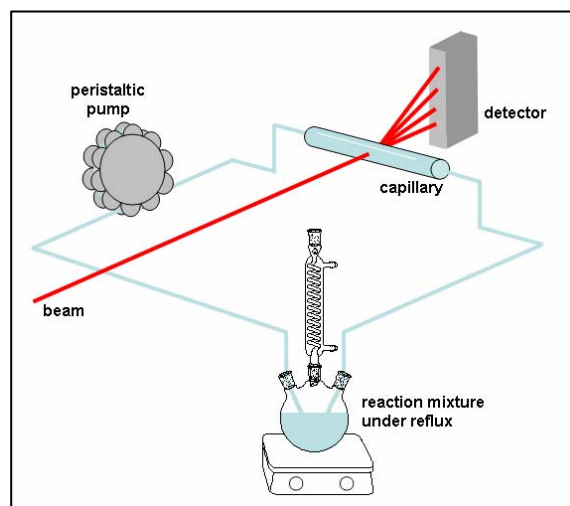


**Figure 2.9:** Schematic illustration of the experimental setup at beamline A2.



**Figure 2.10 a:** Experimental setup: Four neck flask with the reflux condenser, the tubing connecting the capillary with the reaction vessel.

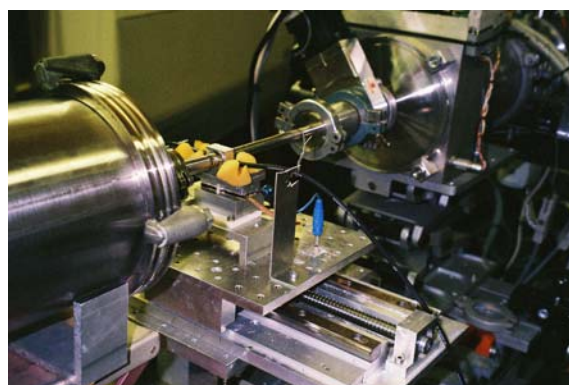
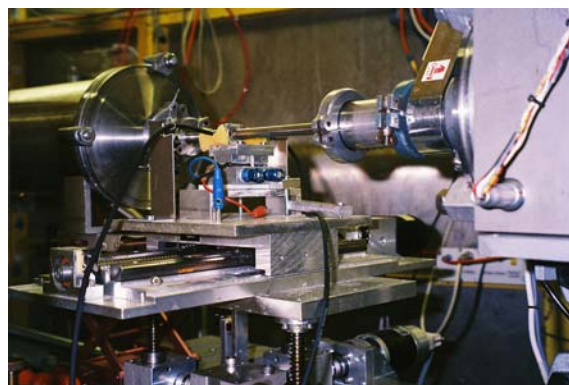


**Figure 2.10 b and c:** Capillary placed in the beam.

### 2.12.2 Instrumental parameters

*In situ* SAXS experiments were carried out at the soft condensed matter beamline A2 at Hasylab at the “Deutsches Synchrotronlabor” (DESY) in Hamburg. The wave length of the X-ray beam was 0.15 nm. All data were collected with a linear detector. The measurements were carried out in a flow-through capillary with an inner diameter of 1.5 mm and a glass thickness of 10  $\mu\text{m}$ . The capillary was connected to the reaction vessel by norprene tubings which are chosen due to the high resistance to extreme pH values. The reaction vessel, a four neck bottle was placed in an oil bath on a magnet stirrer that was able to hold a certain temperature. The calibration of the small angle region was accomplished with a rat tandom tail in order to allocate the channel numbers to  $s$  values ( $s = 1/d$ ;  $d$  = d-spacing).

## 2.13 High Performance Liquid Chromatography (HPLC)

### 2.13.1 Chromatographic fundamentals<sup>[130,131]</sup>

The high performance liquid chromatography is a special variation of the liquid chromatography. In most cases the stationary phase is a solid material. Compared to the gaschromatography the advantage of the HPLC technique is the possibility of separating substances that possess a boiling point that is too high to be reached for evaporation in a gaschromatograph. Compared to the liquid chromatography the HPLC technique is much more effective because the linear velocity  $u$  (see Van Deemter equation 7.2) can be influenced by the variation of the solvent pressure on the column. Thus, the minimum of the Van Deemter curve (Figure 2.11) can be found by optimising the column pressure when all parameters that influence the single parts of the Van Deemter equation are in the optimal range.

High performance liquid chromatography depends on the interaction of sample analytes with the stationary phase (packing) and the mobile phase to effect a separation. The separation properties of a chromatographic system is characterised by the Van Deemter equation (7.2), the peak width, the plate number and the resolution of the single peaks.

The effectivity of a chromatographic system can be characterised by the plate number ( $N$ ). The plate number is the necessary number of ideal mass transfer processes that offer a separation of the same quality like the chromatographic system. In most cases the plate height HETP (height equivalent to one theoretical plate) instead of the plate number is used. The HETP is calculated by:

$$\text{HETP} = L/N \quad (2.7)$$

with  $L$  being the length of the separation distance (in most cases: the length of the column). The quality of the chromatographic system increases with decreasing HETP. The correlation between the plate height and the flow velocity is the Van Deemter equation.

$$\text{HETP} = A + B/u + C * u \quad (2.8)$$

This correlation as well as the single terms of the Van Deemter equation is illustrated in Figure 2.11.

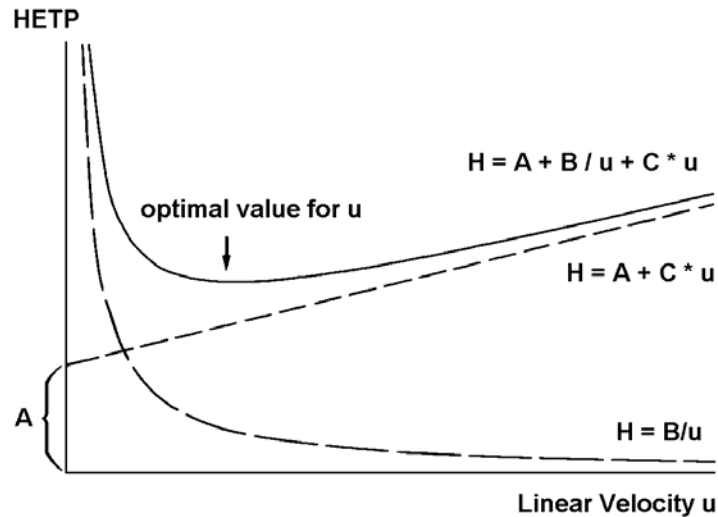


**Figure 2.11:** Illustration of the complete the Van Deemter equation as well as of the single terms.

The individual terms  $A$ ,  $B$  and  $C$  describe different influences on the peak broadening. The term  $A$  considers the Eddy-Diffusion which is also called multipath term. The Eddy-Diffusion  $A$  is described by the following equation:

$$A = 2 * \lambda * d_p \quad (2.9)$$

With  $\lambda$  being a factor for the statistical inhomogeneity of the column packing, and  $d_p$  being the mean particle diameter. From the Eddy-Diffusion term one can conclude that the particle diameter is of essential importance for the separation quality. On the one hand, large particle diameters (above  $10 \mu\text{m}$ ) lead to a significant increase of the Eddy-Diffusion and thus, to peak broadening. On the other hand, particle diameters below  $3 \mu\text{m}$  lead to an increase of the back pressure in the column and thus, to an increase of the temperature caused by friction. The influence of the Eddy-Diffusion on the peak shape is illustrated in Figure 2.12.

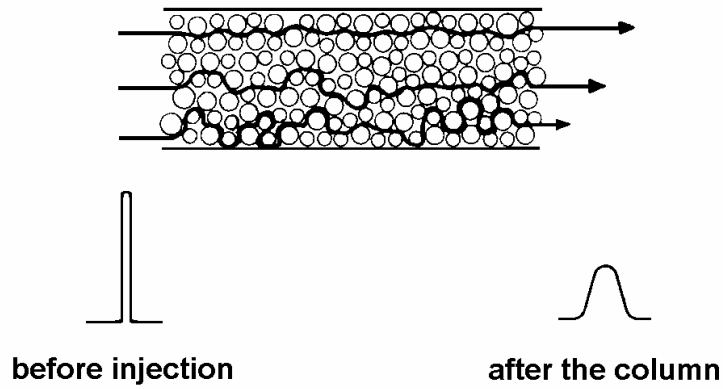


**Figure 2.12:** Illustration of the peak broadening caused by the Eddy-Diffusion.

The term B of the van Deemter equation includes the longitudinal diffusion. The term B of the longitudinal diffusion can be calculated as follows:

$$B = 2 * \gamma * D_m \quad (2.10)$$

with  $\gamma$  being the porosity and  $D_m$  being the diffusion coefficient of the substance in the mobile phase.  $D_m$  is calculated by the following equation:

$$D_m = \frac{7.4 * 10^{-12} * T * \sqrt{\Psi M}}{\eta * V_s} \quad (2.11)$$

with M being the molar mass,  $V_s$  the molar volume of the analyte,  $\eta$  the viscosity of the mobile phase, T the temperature and  $\psi$  being a constant dependent on the solvent (for macromolecules another factor is needed due to the molecule size).

Another interesting correlation is given with the permeability K of the column, which is a characteristic value for the quality of the packing. The permeability depends on the column length L, the flow velocity u, and the pressure difference between the inlet and the end of the column ( $\Delta p$ ):

$$K = \frac{u * L}{\Delta p} \quad (2.12)$$

The specific permeability  $K^0$  is additionally dependent on the viscosity of the solvent and the porosity of the stationary phase:

$$K^0 = K * \eta * \gamma \quad (2.13)$$

For commercial HPLC columns the term B is only of minor importance. The longitudinal diffusion only increases when small particles of the stationary phase are combined with a relatively low flow velocity and high diffusion coefficients of the substances. It should be mentioned that the porosity of the particles plays an important role for the longitudinal diffusion. Thus, an increase of the porosity (deep pore networks with high specific surface areas of the stationary phase) might influence the term B.

The term C characterises the delay of the mass transfer of the single analytes between the stationary and the mobile phase. All species need a certain period of time to equilibrate between stationary and mobile phase. With high flow rates, if species exhibit a strong affinity for the stationary phase, the species molecules that do not enter the stationary phase can move far ahead and band broadening will occur. Therefore the mass transfer factor is directly proportional to the mobile phase velocity  $u$ . The term C can be calculated as follows:

$$C = \frac{8 * k' * d_p^2}{\pi^2 * (1 + k')^2 * D_s} \quad (2.14)$$

With  $k'$  being the mass distribution coefficient between the stationary and the mobile phase ( $k' = k * V_s/V_m$ ,  $k'$ : distribution coefficient of the analyte,  $V_s$ : volume of the stationary phase,  $V_m$ : volume of the mobile phase),  $d_p$  the particle diameter and  $D_s$  being the diffusion coefficient of the analyte in the stationary phase. As one can see from equation 8 the resistance of mass transfer increases with increasing particle diameter.

From the Van Deemter equation one can conclude the necessary properties for a new material for HPLC. The particle diameter should be in the range of 3 to 10  $\mu\text{m}$ . A deep pore network might cause problems such as peak broadening or long retention times. The flow velocity should be tuned to that point the plate height reaches its minimum.

For characterisation of a HPLC column the empiric Van Deemter equation, the Knox equation, is commonly used.

$$h = A * v^{0.33} + B/v + C * v \quad (2.15)$$

In this case the Van Deemter equation consists of non-dimensional values with  $h$  being the reduced plate height ( $h = \text{HETP}/d_p$ ), and the reduced flow velocity  $v$  ( $v = d_p * u/D_m$ ). The terms A, B and C can be calculated from the measurements (a high number of  $h(v)$  values is necessary).

The peak symmetries as well as the retention times and the peak widths are calculated as described in Figure 2.13.

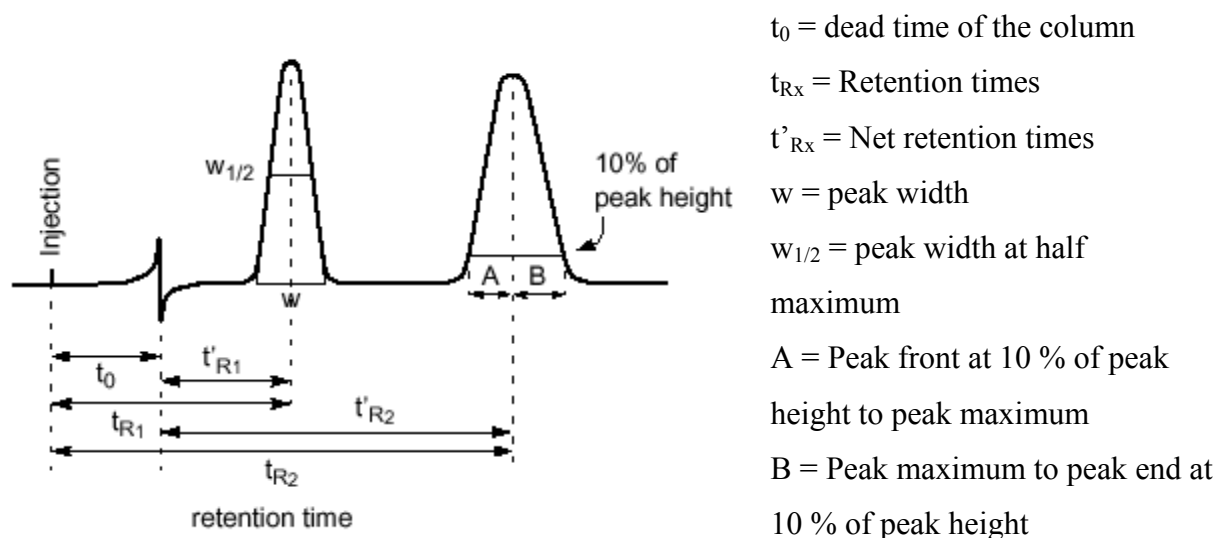


**Figure 2.13:** Schematic explanation of the peak constants.<sup>[130]</sup>

### 2.13.2 Choice of the elution solvent

In order to find the elution solvent, which should be applied for separation of the single substances the  $\log K_{OW}$  values can give first hints whether the chosen substances are hydrophilic or hydrophobic. The  $\log K_{OW}$  is calculated by the following equation:

$$K_{OW} = c(\text{octanol})/c(\text{H}_2\text{O}) \quad (2.16)$$

with  $c(\text{octanol})$  being the concentration of the substance in octanol and  $c(\text{H}_2\text{O})$  being the concentration in water when solving the substance in the two-phase system octanol/water.

This system is normally chosen because these substances simulate the cell/membrane water system and the assimilation of different substances in the organism through the cell membrane/water layer could be estimated as well as the accumulation of substances in the organism.

### 2.13.3 Filling of the HPLC columns

2.5 g of the sieved material (particle diameter between 5 and 20  $\mu\text{m}$ ) was in a mixture of carbon tetrachloride/dioxane (24:24; v:v). Under a pressure of 400 bar the suspension was filled into a stainless steel column (inner diameter: 4 mm; column length: 250 mm). 500 mL *n*-hexane of HPLC quality were then pressed through the column in order to achieve a continuous packing and to remove residues of carbon tetrachloride and dioxane. The same procedure was carried out for another column that was filled with Nucleosil 50-10 that was used as a reference material for the HPLC experiments. At the end of the procedure 1.0 g of the respective material was in each column.

### 2.13.4 Instrumental parameters

HPLC measurements were recorded with a Dionex system consisting of Dionex P680 HPLC pump, a Dionex UVD 170U detector with variable wavelength and a Shodex RI-101 refractive index detector. The sample was injected over a Rheodyne 7125 with a 20  $\mu\text{L}$  sample loop. The data was collected using Chromeleon by Dionex.

## 2.14 Atomic Absorption Spectroscopy (AAS)

Atomic absorption spectroscopic measurements were acquired using a SpectrAAs 220 FS Atomic Absorption Spectrometer from Varian. The samples were measured using a SPS 5 Sample Preparation System (Varian). The absorption of copper was measured at a wavelength of 324.8 nm.

### 3 Syntheses and characterisation

The organosilica precursors which were used for all experiments were 1,2-bis(trimethoxysilyl)ethane (BTME), 1,2-bis(triethoxysilyl)ethane (BTEE), 1,4-bis(triethoxysilyl)benzene (BTEB) and *N,N*-[bis(trimethoxysilyl)propyl]amine (BTMPA). Samples synthesised with BTME or BTEE are called “ethane-bridged samples”, with BTEB “phenylene-bridged samples” and with BTMPA “amine-bridged samples” in the following chapters. Samples synthesised with mixtures of two different precursors as used in the following chapter 3.1 are called “ethane- and amine-bridged samples” due to the mixture of BTME and BTMPA that was applied.

#### 3.1 Samples for heavy metal adsorption: Ethane-and amine-bridged PMOs

Amine-bridged PMOs were synthesised in order to develop adsorption materials for the adsorption of heavy metal ions. The synthesis of an ethane-bridged material already published by Sayari et al.<sup>[25]</sup> was chosen and different amounts of the amine-bridged precursor *N,N*-bis(trimethoxysilyl)propyl]amine (BTMPA) were added to the reaction solution. The resulting hybrid materials exhibited secondary amine functionalities incorporated in the pore wall network. Samples were synthesised with different surfactants (OTAC, CTAC) and different surfactant concentrations as well as with different aging times and temperatures. The temperature of the hydrothermal treatment was varied in order to obtain the optimal synthesis conditions. All samples were investigated with P-XRD, nitrogen physisorption and TEM. SEM, TG/MS and <sup>29</sup>Si MAS NMR measurements were carried out for selected samples.

##### 3.1.1 Synthesis

Materials were synthesised by solving different amounts of the surfactant OTAC or CTAC in a mixture of sodium hydroxide and water. Different ratios of the two precursors 1,4-bis(trimethoxysilyl)ethane (BTME) and *N,N*-bis[(trimethoxysilyl)propyl]amine (BTMPA) were mixed and stirred for 15 minutes before adding to the reaction solution. After adding the precursors the reaction mixture was stirred for additional 12 or 24 hours at different temperatures (room temperature (RT), 40 °C, 60 °C). A hydrothermal treatment followed for 24 hours at 95 °C. After thorough washing with water the precipitate was dried overnight in air to yield a fine white powder. Removal of the surfactant was accomplished by solvent

extraction (ethanol/HCl 100:3; v:v) in an Soxhlet apparatus for 6 hours. The final molar composition of the samples is listed in Table 3.1.

**Table 3.1:** Molar ratios of the ethane- and amine-bridged samples.

BTME	BTMPA	OTAC/CTAC	NaOH	H <sub>2</sub> O
x	y	z	2.36	353

with  $z = 0.85, 0.57, 0.28$  and  $x + y = 1$ .

The molar ratios of the ethane- and amine-bridged samples synthesised with OTAC are listed in Appendix A.II.1 in Tables A.II.1 – A.II.5. For all surfactant concentrations the relation of the precursor mixture varies between 1 BTME, 0 BTMPA and 0.55 BTME, 0.45 BTMPA. The variation of the oven temperature was studied with samples containing 0.55 BTME and 0.45 BTMPA. The molar ratios of the samples synthesised with CTAC as SDA are listed in Appendix A.II.2 in Tables A.II.6 – A.II.10.

### 3.1.2 Results

First samples were synthesised with an OTAC concentration of 0.57 mol. The amount of BTMPA was varied between 0 mol (2d hexagonal ordered material already published by Sayari et al.<sup>[25]</sup>) and 0.45 mol. The evolution of the mesostructures with increasing amount of BTMPA in the reaction solution can be observed from the powder X-ray diffraction patterns in Figure 3.1.

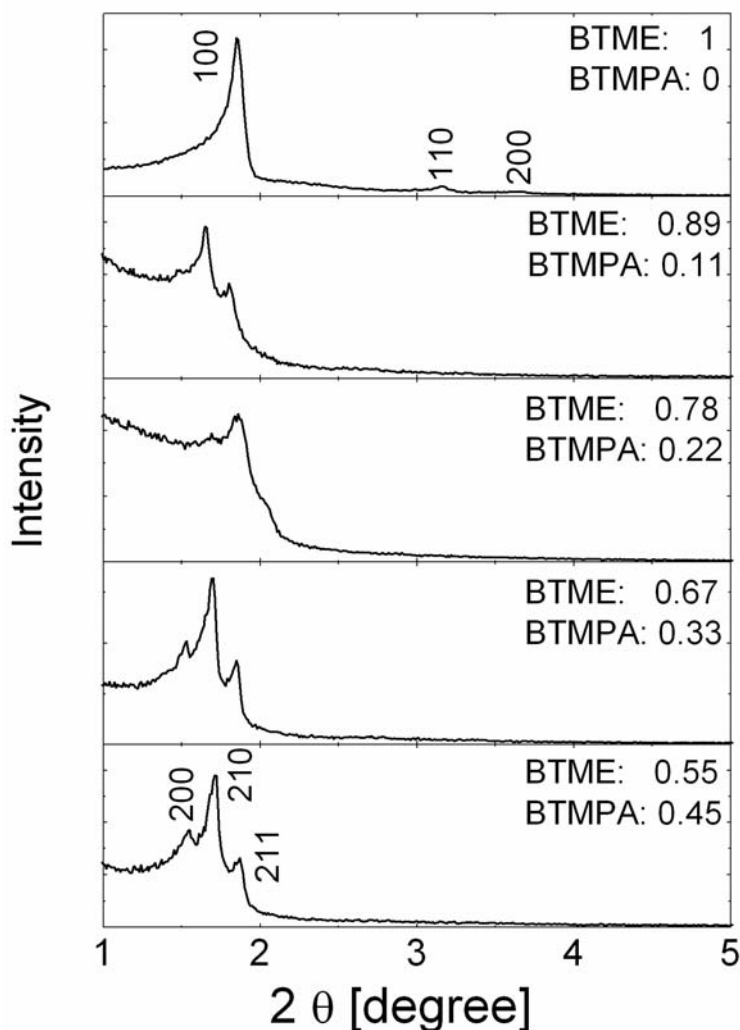


**Figure 3.1:** XRD patterns of the samples synthesised with a surfactant concentration of 0.57 mol and different ratios of BTME/BTMPA (molar ratios see Table 3.1).

The XRD pattern of the sample containing only BTME as organosilica precursor shows a 2d hexagonal mesophase (space group:  $p6mm$ ). The addition of BTMPA led to a phase transition from the 2d hexagonal to a cubic phase. The space group was indexed as  $Pm\bar{3}n$ . An improvement of the mesostructure with increasing amount of BTMPA up to 0.45 mol could be observed. Higher amounts of BTMPA did not lead to any ordered material.

The particle shape was proved by SEM because a phase transition from a 2d hexagonal to a cubic phase might also induce a change in the particle shape. The SEM images of the 2d hexagonal ordered sample (BTMPA: 0) and a cubic structured sample (BTMPA: 0.45) are depicted in Figure 3.2 a and b. The hexagonal ordered material exhibited a lot of hexagonal shaped particles in contrast to the cubic ordered material. Large spheres grown from smaller particles could be observed from the SEM image.

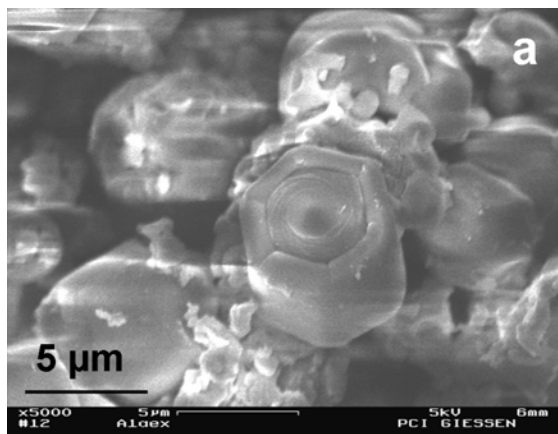


**Figure 3.2:** SEM image of the ethane-bridged sample (molar ratio: see Table 3.1;  $x = 1$ ;  $y = 0$ ,  $z = 0.57$ ).

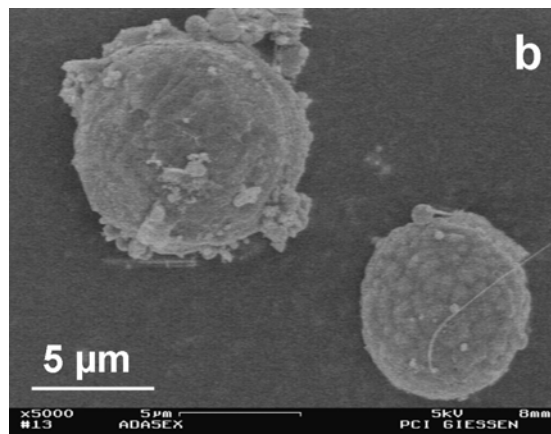


**Figure 3.2 b:** SEM image of an ethane- and amine-bridged sample (for molar ratio: see Table 3.1;  $x = 0.55$ ,  $y = 0.45$ ;  $z = 0.57$ ).

The nitrogen physisorption measurements showed type IV isotherms for all samples, which is typical for mesoporous materials.<sup>[132]</sup> The adsorbed volume decreased with increasing amount of BTMPA in the reaction solution and thus, the specific surface areas decreased from 1030 m<sup>2</sup>/g for the ethane-bridged sample to 370 m<sup>2</sup>/g for the sample synthesised with 0.45 mol BTMPA. The pore diameters were all in the range of 2.7 to 3.7 nm without showing a clear trend depending on the BTMPA concentration. A reason for this change of the adsorbed volumes and specific surface areas might be the flexibility of the alkyl chains of the amine-functionalised precursor. After the removal of the surfactant the organosilica network will be not as rigid as the network of pristine silica materials. The organic bridge might be able to change the conformation and is still flexible in the material. This is also a reason why a higher loading with amine functionalities will not be possible.

Two TEM images of the samples synthesised without BTMPA are shown in Figure 3.3 a and b. Figure 3.3 a shows the view perpendicular to the pores of the hexagonal pore system, Figure 3.3 b is a view parallel to the pores. Figure 3.3 c and d are images of a sample containing 0.33 mol BTMPA (c) and 0.45 mol BTMPA (d). No particles with parallel pores as shown in Figure 3.3 a could be seen in the samples containing different amounts of the amine bridge.

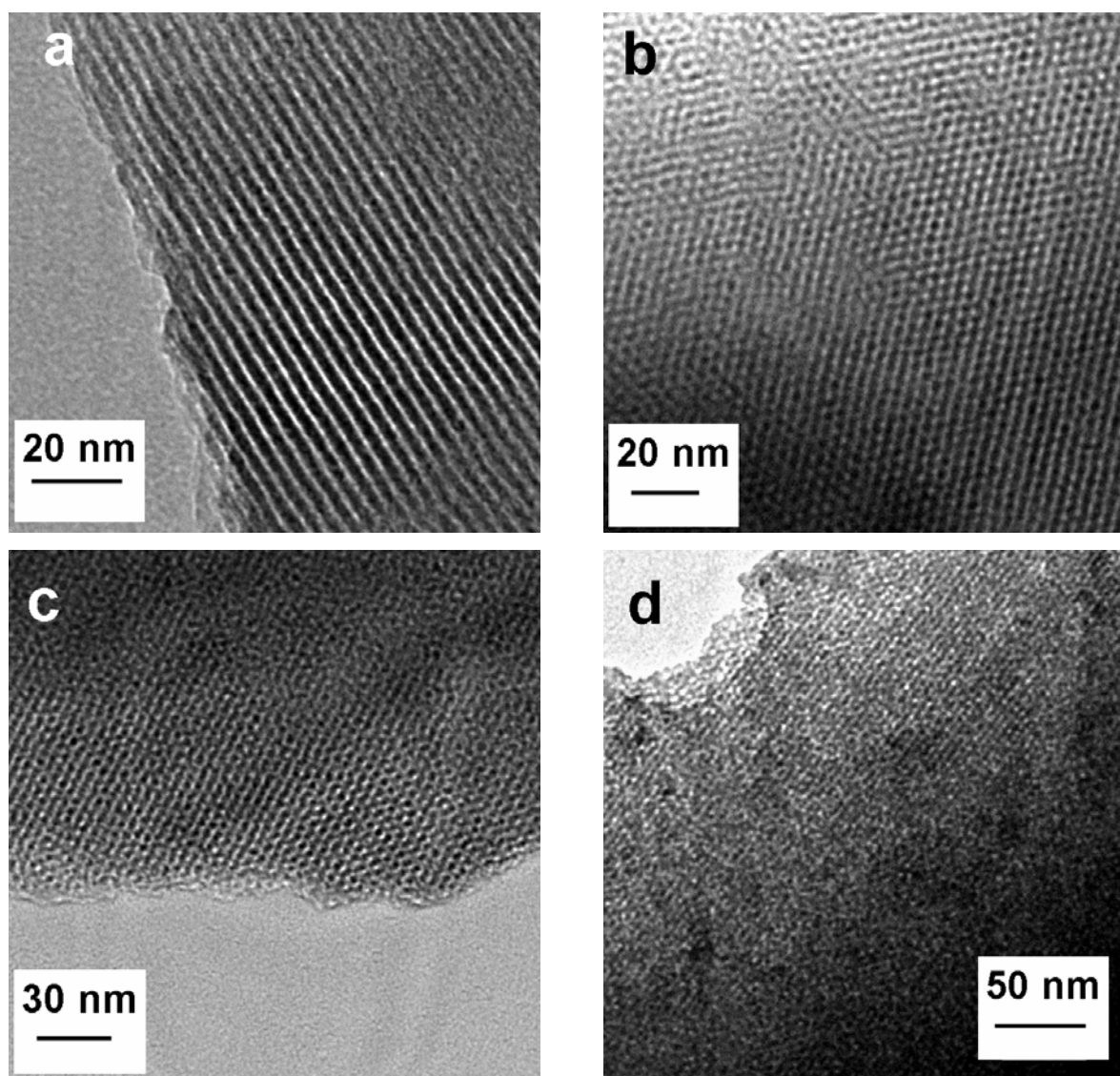


**Figure 3.3 a – d:** TEM images of the ethane-bridged and ethane- and amine-bridged samples (for molar ratios see Table 3.1).

(a + b):  $x = 1$ ;  $y = 0$ ; (c):  $x = 0.67$ ;  $y = 0.33$  and (d)  $x = 0.55$ ;  $y = 0.45$ .

For all samples large high ordered domains could be observed. In contrast to the 2d hexagonal structured sample a view along the pores could not be found anywhere in the sample. This corroborates the assumption that these samples show a cubic mesostructure. From the TEM measurements a relatively low thermal stability of the samples containing high amounts of the amine bridge could be concluded because the materials were destroyed within a few minutes while the ethane-bridged sample offered a significantly higher stability. Thus, thermogravimetric measurements combined with mass spectrometry (TG/MS) were carried out in order to obtain information about the decomposing behaviour of the samples at high temperatures. A TG/MS measurement of a sample containing 0.22 mol BTMPA is shown in Figure 3.4.

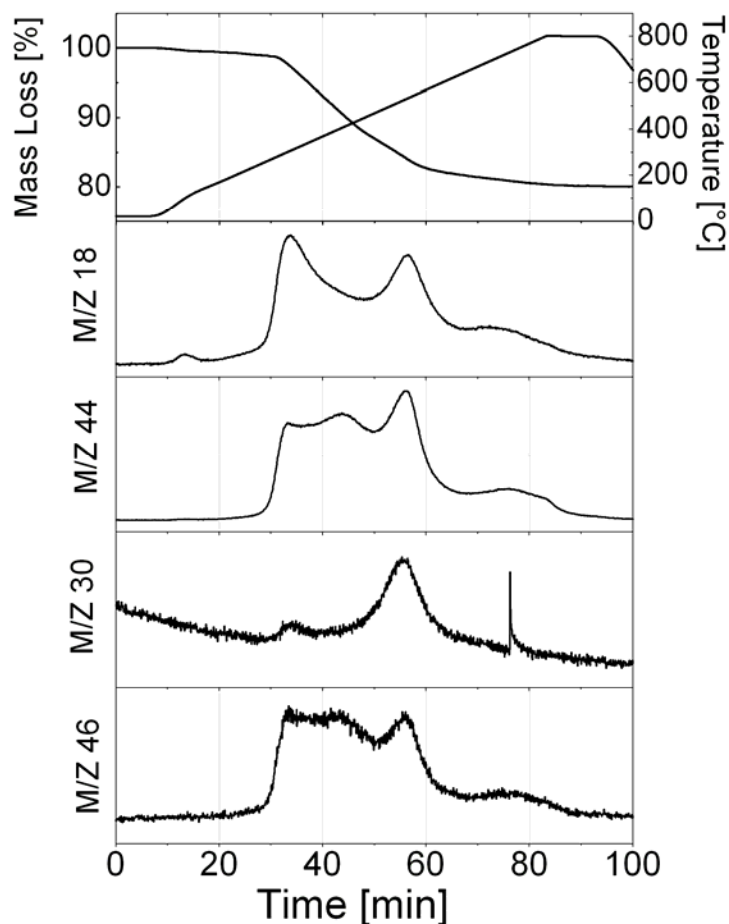


**Figure 3.4:** TG/MS of an ethane- and amine-bridged sample synthesised with a surfactant concentration of 0.57 mol (OTAC) and  $x = 0.78$  and  $y = 0.22$ .

In the temperature range of 100 – 150 °C a mass loss of 2 % was measured corresponding to a drying step. This was confirmed by mass spectrometry. The decomposition of the material started at 250 °C and ended at 500 °C. The masses of H<sub>2</sub>O, CO<sub>2</sub>, NO and NO<sub>2</sub> were detected, which results from the decomposition of the organic bridges in the material.

The degree of condensation and the stability of the Si-C bond in the materials were proved by Magic angle spinning nuclear magnetic resonance (<sup>29</sup>Si MAS NMR) measurements. A <sup>29</sup>Si MAS NMR spectrum of a sample containing 0.22 mol BTMPA is exemplarily shown in Figure 3.5. A high degree of condensation could be concluded from the <sup>29</sup>Si MAS NMR investigations. Only a T<sup>2</sup> signal (-57 ppm: SiC(OH)(OSi)<sub>2</sub>) and a T<sup>3</sup> signal (-66 ppm: SiC(OSi)<sub>3</sub>) were detected. The absence of any Q signals which correspond to a silicon surrounded by four oxygen atoms such as Si(OH)(OSi)<sub>3</sub> or Si(OSi)<sub>4</sub> which are usually observed between -90 ppm and -120 ppm proves that the carbon silicon bond of the original

organosilica precursors has not been cleaved during hydrolysis and condensation reactions. The ratio  $T^2/T^3$  was 31 /69 which confirmed the existence of a high condensed network.

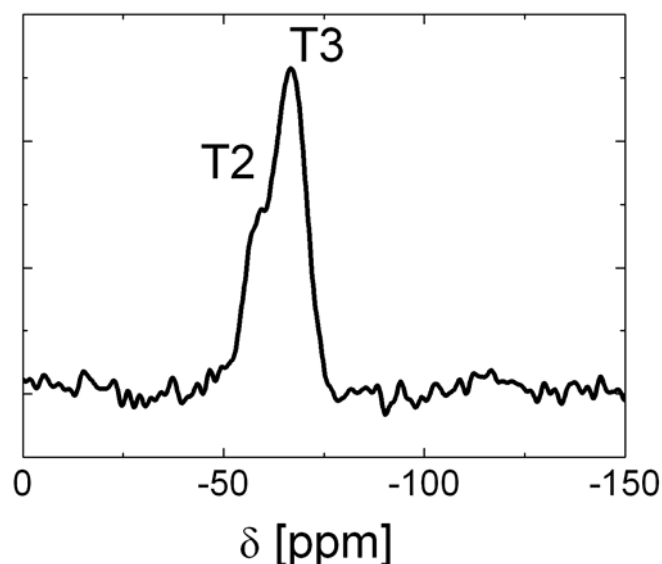


**Figure 3.5:**  $^{29}\text{Si}$  MAS NMR spectrum of an ethane- and amine-bridged sample synthesised with a surfactant concentration of 0.85 mol (OTAC) and  $x = 0.78$  and  $y = 0.22$ .

### 3.1.3 Influence of different synthesis parameters

As shown by the results of the first experiments the addition of the new organosilica precursor BTMPA combined with the reduction of the amount of BTME led to a transition from a high ordered hexagonal phase to a high ordered cubic phase. In order to obtain more information about the sensitivity of this system to changes in the synthesis conditions different synthesis parameters such as the aging time, the aging temperature, the temperature of the hydrothermal treatment and the surfactant concentration were varied. The influence of the alkyl chain length of the surfactant was investigated by changing the surfactant from OTAC to CTAC. For all test series samples were synthesised with five different organosilica precursor concentrations: BTMPA: 0, 0.11, 0.22, 0.33, 0.45 (BTME: 1, 0.89, 0.78, 0.67, 0.55).

#### *a) Surfactant concentration*

The surfactant concentration in the solution was varied in order to study the phase behaviour of the surfactant in dependence of the amine-bridged precursor concentration in the solution. As described above the addition of the amine-bridged organosilica precursor caused a phase

transition from a 2d hexagonal to a cubic phase. Similar experiments were carried out with different surfactant concentrations. Additional to the test series described above (surfactant concentration 0.57 mol) two further series the first with 0.28 mol OTAC and the second with 0.85 mol OTAC were synthesised. An overview is given in Table 3.2.

**Table 3.2:** Molar ratios of the test series synthesised with OTAC concentrations of 0.28 mol and 0.85 mol.

BTME [mol]	BTMPA [mol]	OTAC/CTAC [mol]	NaOH [mol]	H <sub>2</sub> O [mol]
1	0	0.28	2.36	353
0.89	0.11	0.28	2.36	353
0.78	0.22	0.28	2.36	353
0.67	0.33	0.28	2.36	353
0.55	0.45	0.28	2.36	353
1	0	0.85	2.36	353
0.89	0.11	0.85	2.36	353
0.78	0.22	0.85	2.36	353
0.67	0.33	0.85	2.36	353
0.55	0.45	0.85	2.36	353

From the test series with a surfactant concentration of 0.28 mol only the sample synthesised with 0.22 mol BTMPA exhibits a cubic structure (space group:  $Pm\bar{3}n$ ). All other samples show only a poor ordering even the sample synthesised without BTMPA. The resulting nitrogen physisorption isotherms are all of type IV but the adsorbed volumes differ to a high extent. The specific surface areas are all in the range of 200 – 350 m<sup>2</sup>/g, except the sample synthesised with 0.22 mol BTMPA. The specific surface area as well as the pore diameter was significantly higher than for all other samples.

The increase of the surfactant concentration to 0.85 mol influenced the formation of the mesostructure of the resulting materials as well. The sample synthesised without BTMPA shows two reflections in the XRD patterns which fit to the cubic space group  $Pm\bar{3}n$ . The intensities of these reflections were relatively low. With increasing amount of BTMPA in the reaction solution the quality of the mesostructure improved. A well ordered cubic material was obtained for the BTMPA concentration of 0.11 mol and 0.22 mol. Higher BTMPA concentration led to a degradation of the structure. Similar observations were made for the nitrogen physisorption measurements. The specific surface areas increase up to 750 m<sup>2</sup>/g for the sample synthesised with 0.11 mol BTMPA and decreased with degrading quality of the structure. The pore diameters decrease from 3.7 nm (pure ethane-bridged material) to 2.6 nm (0.45 mol BTMPA).

The complete nitrogen physisorption data of the samples synthesised with different surfactant concentrations are listed in Appendix A.II.3. An overview of the different structures dependent on the surfactant concentration and the BTMPA concentration in the reaction solution is depicted in Figure 3.6.

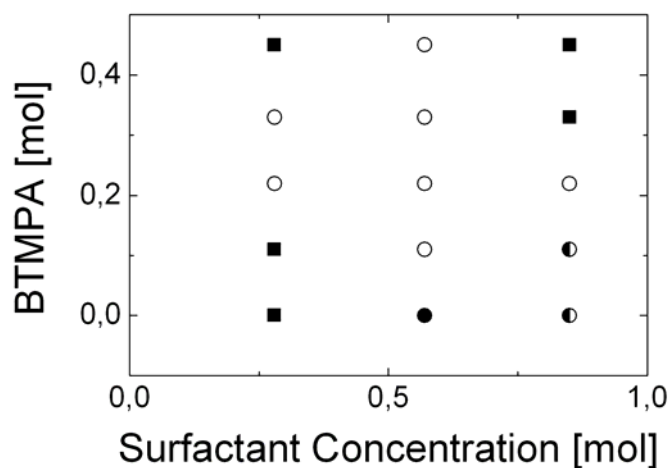


**Figure 3.6:** Different resulting mesostructures dependent on the surfactant and the BTMPA concentration: 2d hexagonal (space group:  $p6mm$ ) (●); cubic (space group:  $Pm\bar{3}n$ ) (○) and poor ordered (■).

As one can conclude from Figure 3.6 the preferred mesophase of the system consisting of both organosilica precursors is a cubic phase with the space group  $Pm\bar{3}n$ . A pure hexagonal phase was only obtained for the ethane-bridged material that was introduced by Sayari et al.<sup>[25]</sup>. An increase of the surfactant in the solution to 0.85 mol led to a mixture of the cubic and the hexagonal phase but evidence could not be given at this point. High BTMPA concentrations combined with high surfactant concentration led to samples that shown only one reflection in the XRD patterns. Thus, no mesostructure could be indexed for these samples. A similar problem occurred for samples synthesised with a surfactant concentration of 0.28 mol.

#### b) Temperature and time of the aging step

The temperature of the stirring step was varied between 23 and 60 °C. The stirring times were varied between 2 and 24 hours. For molar ratios of the samples see Table 3.1.

with  $x + y = 1$  ( $x = 0.89; 0.78, 0.67, 0.55$ ) and  $z = 0.57$

The variation of the synthesis temperature combined with the variation of the synthesis time led to interesting results concerning the structures of the synthesised materials. An increase of the temperature during the stirring step led to materials which show a poorer order in the XRD. In all cases only one broad reflection could be observed for these samples independent of the BTMPA concentration. But a reduction of the synthesis time led to hexagonal ordered materials. With increasing amount of BTMPA in the solution the stirring time had to be reduced in order to obtain a 2d hexagonal mesostructure. Samples synthesised with 0.33 mol BTMPA and a 12-hour stirring step at 60 °C led to 2d hexagonal structures as well as samples containing 0.45 mol BTMPA which was stirred only 2 hours at 60 °C. The XRD patterns of the samples synthesised with 0.33 mol BTMPA at different temperatures are depicted in Figure 3.7.

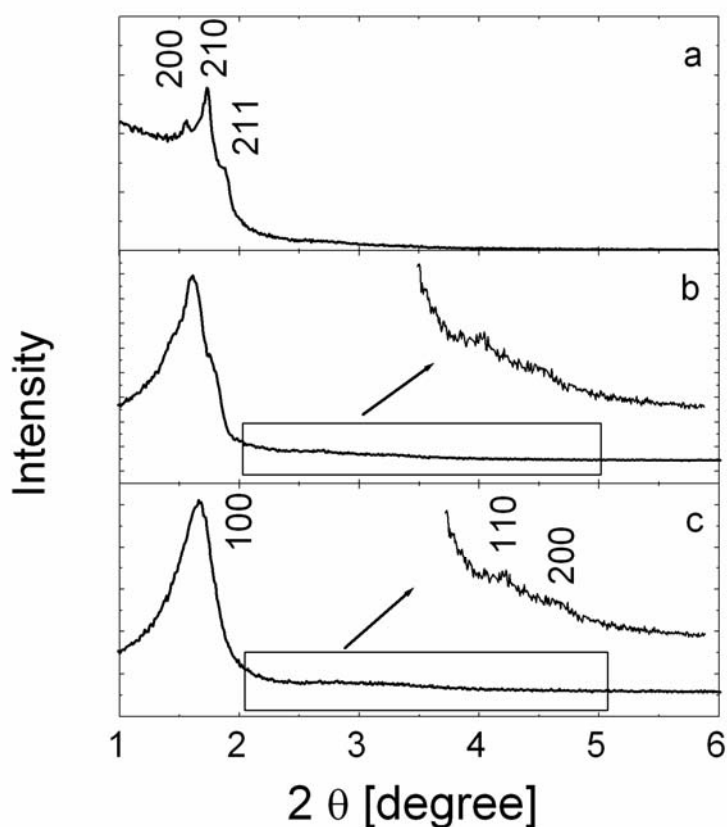


**Figure 3.7:** XRD patterns of the samples (molar ratio: see Table 3.1;  $x = 0.67$ ;  $y = 0.33$ ;  $z = 0.57$ ) synthesised with a 12-hour stirring step at 23 °C (a); 40 °C (b) and 60 °C (c).

The sample synthesised at a temperature of 23 °C is a cubic ordered material. An increase of the temperature up to 40 °C led to a sample exhibiting a mixture of a 2d hexagonal and a cubic phase (b). The first reflection is significantly broader than the 210 reflection of the cubic phase shown in the layer above (a) but two slight shoulders in this reflection can still be

seen. The sample synthesised at 60 °C exhibited a 2d hexagonal mesostructure. TEM investigations were carried out in order to prove the results obtained from the XRD measurements. The TEM images of the sample synthesised at 23 °C and 60 °C are shown in Figure 3.8 a, b and c.

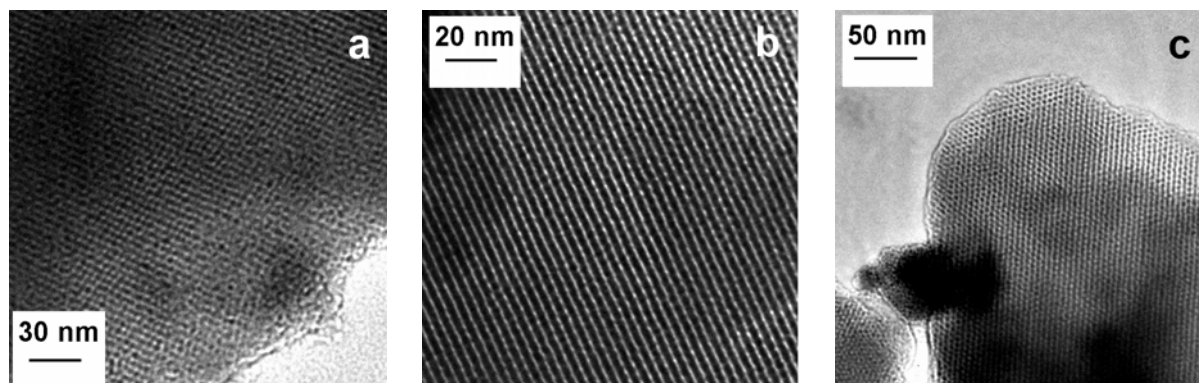


**Figure 3.8 a – c:** TEM images of the cubic structured sample synthesised at 23 °C (a) and the 2d hexagonal structured sample synthesised at 60 °C (b + c).

As one can see from the TEM images as well as from the XRD pattern shown above the stirring temperature mostly influenced the arrangement, the size and the shape of the micelles. At high temperatures rodlike micelles are formed in the solution in contrast to the formation of spherical micelles at temperatures below 40 °C. The specific surface area, the pore diameter and the wall thickness decrease during the transition from the cubic to the 2d hexagonal mesophase with increasing temperature.

Phase transitions caused by high reaction temperatures have often been observed and reported but in this case the temperature of the hydrothermal treatment is 95 °C for all samples. A possible reason for the formation of the hexagonal structure is the increase of the packing parameter which might be caused by the increasing temperature that might lead to a coiling of the hydrocarbon chain of the surfactant with preferred gauche conformations in the alkyl chains. The packing parameter  $g$  ( $g = V/a_0 \cdot l$ ) increased because the parameter  $l$  representing the kinetic surfactant tail length decreases while the volume ( $V$ ) and the  $a_0$  (the effective headgroup area at the micelle surface) does not change significantly. An increase of the packing parameter  $g$  means a change in the curvature of the micelles from a high curved to a lower curved surface. Thus, the curvature of the micelle surface decreased. This assumption could also be proven by TEM investigations which show a view perpendicular to the pores (Figure 3.8 b). The complete XRD and nitrogen physisorption data of the samples synthesised with different stirring times at different temperatures are listed in Appendix A.II.4. All

obtained mesostructures dependent on the aging time and aging temperatures are summarised in Figure 3.9.

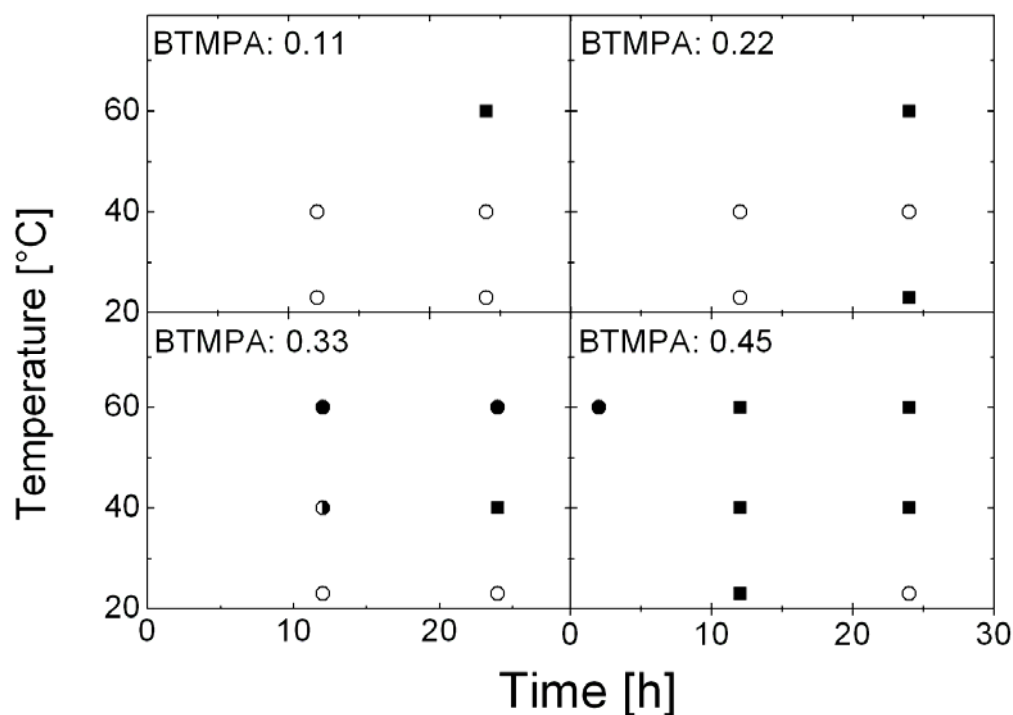


**Figure 3.9:** Overview of the obtained mesostructures dependent on the aging time and temperature: 2d hexagonal structured ( $p6mm$ ); (●); cubic structure ( $Pm\bar{3}n$ ) (○) and poor ordered (one reflection) (■).

### c) Temperature of the hydrothermal treatment

Samples with the molar ratio 0.55 BTME: 0.45 BTMPA: 0.57 OTAC: 2.36 NaOH: 353 H<sub>2</sub>O were synthesised applying four different temperatures (60 °C, 95 °C, 120 °C and 150 °C) for the hydrothermal treatment. From the XRD measurements one can conclude that the formation of the mesostructure is extremely sensitive concerning the temperature. The sample synthesised at 95 °C exhibited a cubic structure while the other samples did not show any ordering of the mesopores. The sample synthesised at 150 °C was completely non-porous as observed from the XRD pattern and the nitrogen physisorption measurement. The pore diameters of the other three samples increase from a narrow pore size distribution with a maximum of 2.2 nm (60 °C) up to a broad pore size distribution with its maximum at 3.7 nm (120 °C) (For the complete data see Appendix A.II.5).

*d) Application of a surfactant with shorter alkyl chain length*

The application of CTAC for the synthesis of a pure ethane-bridged material was already published by Sayari et al.<sup>[25,26]</sup> In contrast to the synthesis with OTAC as SDA a cubic structured material (space group:  $Pm\bar{3}n$ ) was obtained by applying the same molar ratios for the synthesis solution as chosen for samples synthesised with OTAC. The influence of the amine-bridged organosilica precursor on the mesostructure was studied by experiments with different CTAC concentrations (0.28 mol, 0.57 mol and 0.85 mol as described above) in combination with different BTME/BTMPA ratios ( $x = 1; 0.89; 0.78; 0.67; 0.55$ ).

In all cases either poor ordered or cubic structured materials were obtained. Best results of the test series with 0.28 mol CTAC were obtained for the sample synthesised with 0.11 mol BTMPA. This was proven by XRD as well as by nitrogen physisorption measurements. With increasing BTMPA concentration the structure degraded and the specific surface area decreased as well. Similar results were obtained for the experiments with 0.57 mol OTAC concerning the dependence between the mesostructure and the amine concentration in the reaction solution. The test series carried out with 0.85 mol CTAC led to well ordered materials with a cubic symmetry up to 0.33 mol BTMPA although the intensities of the reflections vary with the BTMPA concentration in the reaction solution. (Figure 3.10).

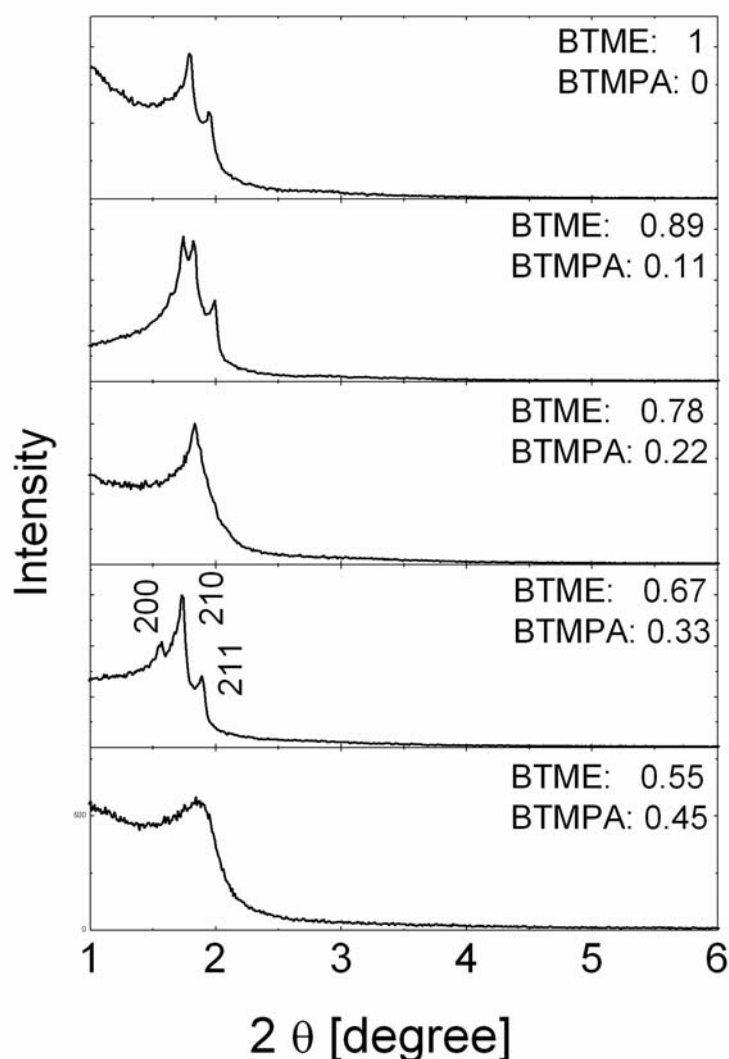


**Figure 3.10:** XRD patterns of the samples synthesised with 0.85 mol CTAC and different BTME/BTMPA ratios.

The specific surface areas calculated from the nitrogen physisorption isotherms led to values between 580 and 660 m<sup>2</sup>/g without following a certain trend. The pore diameters decreased with increasing amount of BTMPA in the reaction solution (for complete nitrogen physisorption data see Appendix A.II.6).

#### 3.1.4 Discussion and conclusion

As one can conclude from the results described above the addition of another organosilica precursor to a typical reaction mixture changes this system significantly. The addition of several amounts of BTMPA to a reaction mixture that was used by Sayari et al.<sup>[25]</sup> in order to obtain an ethane-bridged 2d hexagonal structured PMO material led to a phase transition from 2d hexagonal to cubic which implied an increase of the micelle curvature due to the change

from rodshaped to spherical micelles in the liquid crystalline phase. The variation of different synthesis parameters showed that the structure of the resulting materials depend on the amine concentration, the aging time and the aging temperature to a high extent. An increase of the BTMPA concentration up to 0.45 mol led to a highly ordered cubic mesostructure while the pure ethane-bridged material exhibited a 2d hexagonal structure. But another phase transition occurred with increasing aging temperature combined with decreasing aging time. High temperatures and short aging times led to a transition from the cubic to a 2d hexagonal mesophase at high BTMPA concentrations. In contrast to these results the variation of the temperature of the hydrothermal treatment led to poor ordered materials in all cases. The application of CTAC as SDA instead of OTAC led for all precursor mixtures in all cases either to a poor ordered or to a cubic structured material (space group:  $Pm\bar{3}n$ ). A cubic structure was also obtained for the samples synthesised with pure BTME. No 2d hexagonal structured materials could be obtained with this surfactant independent of the BTMPA concentration. Higher BTMPA concentrations than 0.45 mol led to a collapse of the structure independent of the other synthesis parameters.

The formation of the cubic structure with pure OTAC as SDA and any organosilica precursor or organosilica precursor mixture under alkaline conditions has not been reported up to now. In 2000, Sayari et al. first published a PMO synthesis with CTAC as surfactant and BTME as organosilica precursor under alkaline conditions which led to a cubic structured material (space group:  $Pm\bar{3}n$ ).<sup>[25]</sup> Investigations concerning the structure and the porosity depending on the alkyl chain length of the surfactant were carried out by the same authors.<sup>[26]</sup> Surfactants with alkyl chains from C<sub>8</sub> up to C<sub>18</sub> were applied. The sample synthesised with OTAC showed a well-defined 2d hexagonal mesostructure in the XRD pattern. The sample synthesised with CTAC exhibited a cubic structure. All samples synthesised with surfactants with shorter alkyl chains showed one broad reflection in the XRD patterns, which were indexed as 100 reflections of the 2d hexagonal phase by the authors. No evidence for this statement such as TEM or electron diffraction was given.

In case of the syntheses with the organosilica precursor mixtures described in this work most of the materials exhibited a cubic mesostructure. A possible description of the transition from the 2d hexagonal to the cubic phase is given as follows:

The surfactant concentration in the reaction solutions is below the second critical micelle concentration which implies the formation of the lyotropic crystalline phase at the time when the organosilica precursor is added. The addition of pure BTME led to the formation of another lyotropic crystalline phase than the addition of a mixture of BTME/BTMPA. In this

case, the packing parameter ( $g$ ) of the micelles seemed to be influenced by the addition of the second organosilica precursor. The cubic structure with the space group  $Pm\bar{3}n$  which is a cubic primitive lattice exhibits a  $g$  value of about  $\frac{1}{3}$ .<sup>[9]</sup> This structure is normally formed in acidic media with surfactants containing a relatively large headgroup which stabilise the spherical micelles. In the first case the ternary mixture (OTAC/H<sub>2</sub>O/BTME) led to a 2d hexagonal phase ( $g \approx \frac{1}{2}$ ). This implies that the curvature of the micelles increases at the time BTMPA was added to the reaction solution. The increasing curvature of the micelles can be explained by the different charge densities of hydrolysed and partly condensed BTME species and hydrolysed and partly condensed BTMPA species. The alkyl chain in the amine-bridged precursor is relatively long compared to the ethane bridge in the BTME molecule. Thus, the charge density during the condensation in the mixture BTME/BTMPA is definitely lower than in pure BTME. The micelles with the lowest charge density on the water/headgroup interface are spherical shaped. If the charge density of the organosilica species is as low as in this case the packing of the surfactant micelles had to change in order to maintain charge matching with the framework. A cubic phase is formed after the addition of different BTME/BTMPA mixtures. A quite good schematic illustration of this phase transition was given by Kamija et al. and is shown in Figure 3.11.<sup>[133]</sup> The micellar rods of the 2d hexagonal mesophase form interconnected spherical micelles during this phase transition. From these interconnected spherical micelles the typical cubic lattice is formed.

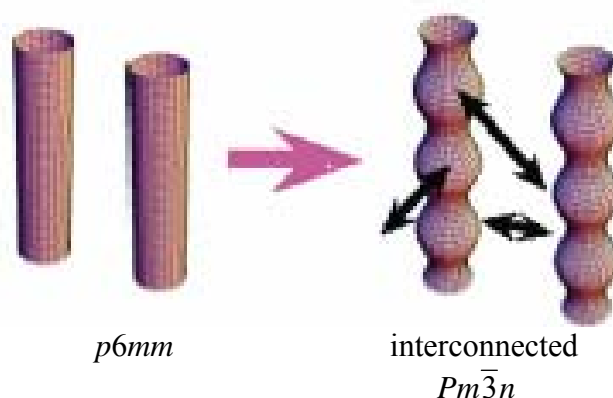


**Figure 3.11:** Scheme of the structural change from a 2d hexagonal ( $p6mm$ ) to a cubic phase ( $Pm\bar{3}n$ ).<sup>[133]</sup>

With increasing amount of BTMPA in the reaction mixture the quality of the cubic structure increased for a certain surfactant concentration. BTMPA concentrations above 0.45 mol in the organosilica precursor solution led to a complete loss of order. This fact might have three possible reasons. First, the charge density is decreased to a level where no formation of

ordered aggregates of micelles can take place anymore. Micelle shapes with a higher curvature than it is obtained for spherical micelles do not exist. Thus, charge density matching cannot be maintained in the framework. A second possibility for the resulting non-porous materials is the flexibility of the alkyl chain in the amine-bridged precursor. After removal of the surfactant the alkyl chain is able to change its conformation and as a result the structure collapses. This fact could be observed from a material synthesised with 0.42 mol BTME and 0.58 mol BTMPA. From the powder X-ray diffraction data of the “as synthesised” product a structural order could be concluded (one reflection). After solvent extraction no reflections could be observed in the P-XRD. The extracted material was completely non-porous. A third reason can be interactions between the headgroup of the micelles and the amine functionality which might distort or disturb the liquid crystal.

The observations concerning the samples synthesised with CTAC as SDA differ from the samples synthesised with OTAC. As described by Sayari et al. the material synthesised with pure BTME and CTAC as SDA was cubic structured.<sup>[25,26]</sup> A reason for the formation of the cubic structure with this SDA might be the shorter alkyl chains of the surfactant molecules while the headgroup of CTAC is the same as of OTAC. Therefore the packing parameter  $g$  changed because the effective headgroup area  $a_0$  remained constant while the chain length  $l$  and the total volume of the surfactant chain decrease. The packing parameter  $g$  decrease as well. For samples synthesised with CTAC the packing parameter is shifted to smaller values ( $\approx$  of  $\frac{1}{3}$ ) due to the smaller values of  $V$  and  $l$ .

New samples were then synthesised with other surfactant concentrations (0.28 mol, 0.85 mol) in order to obtain information about the surfactant concentration range of these phase transitions but no further 2d hexagonal structured samples were obtained. For the formation of the 2d hexagonal phase with BTME as organosilica precursor a surfactant concentration of 0.28 mol might be too low. But condensed organosilica species (oligomers of BTME and BTMPA) with a low charge density were able to induce the formation of the cubic structure. An increase of the surfactant concentration (0.85 mol) led to completely different results concerning the formation of the mesostructures. The sample synthesised with pure BTME showed two reflections with similar intensities. The addition of low amounts of BTME led to an increase of both reflection intensities and the formation of a shoulder. A co-existence of a 2d hexagonal and a cubic structure can be assumed. Similar observations concerning the evolution of the reflections and their intensities were made by Kamija et al. during an *in situ* TEM study of the phase transition from the hexagonal SBA-3 to the cubic SBA-1 silica material.<sup>[133]</sup> A further increase of BTMPA in the solution led to the formation of the cubic

structure while the hexagonal phase disappeared. Concentrations above 0.22 mol led to only poor ordered materials.

As a result of these experiments one can conclude that the amine-functionalised precursor (without the addition of a precursor containing a shorter or no organic bridge) is too large to form a hexagonal liquid crystalline phase in the typical self-assembly process because of its low charge density during the reaction. The single hydrolysed organosilica precursor molecules possess a quite low charge density which decreases with increasing degree of condensation. Thus, the charge density on the micelle surface has to decrease as well which leads to an increase of the curvature. The micelles with the highest curvature and the lowest charge density a spherical shaped. Thus, the organosilica precursor oligomers force the system to change the micelle aggregation. If the charge density on the organosilica oligomers is too low before first condensation around the micelles had taken place the liquid crystalline phase might be destroyed before an ordered material could be formed. The amine-bridged precursor without the addition of BTME is not able to initialise a structure which is as low curved as the 2d hexagonal mesostructure ( $g \approx \frac{1}{2}$ ). The preferred structure is the cubic structure with the space group  $Pm\bar{3}n$  with a curvature described by  $g = \frac{1}{3}$  which is of high quality for such high loadings of the amine function of 45 %.

Focus should also be set on the mixture of the two organosilica precursors. As described in chapter 1.2.2 the synthesis of materials with more than one organic functionality homogeneously distributed in the pore wall network is hardly possible. Different reaction rates caused by different organic functionalities often lead to homocondensation and domains with different concentrations of the organic moieties were obtained.

In case of BTME/BTMPA mixtures this problem might also occur. Some observations of the synthesis give some hints concerning the reaction speeds of both organosilica precursors. No precipitation could be observed during the stirring step of the synthesis of all described samples. Samples synthesised with 1 mol BTME or 1 mol BTMPA showed the same results. The high pH value of the reaction solution (above 12) slows down the condensation speed. This is the reason why even after 24 hours stirring at room temperature only negligible amounts of the hydrolysed organosilica species are condensed. Condensation reactions and precipitation of these systems only take place at higher temperatures. Both organosilica precursors have methoxy groups to hydrolyse and contain a saturated hydrocarbon unit. This led to the assumption that hydrolysis and condensation speed might be similar. The synthesis carried out with 1 mol BTME resulted in a 2d hexagonal structure (as described above), the synthesis conducted with 1 mol BTMPA led to a non-ordered and non-porous material (no

reflections in the XRD). The addition of the mixture of both precursors resulted in products exhibiting in most cases well ordered cubic mesostructures. These structures cannot be formed by the precursors reacting independently as shown in the experiments. A clear statement concerning the statistical distribution of the two precursors cannot be made but the thermal instability and the collapsing structure at BTMPA concentrations higher than 0.45 mol gives evidence for the incorporation of the amine function into the pore wall framework.

Experiments with mixtures of BTME and BTMPA have already been published by Wahab et al. but even the addition of low amounts of BTMPA to their reaction solution led to poor ordered materials.<sup>[134,135]</sup> For every synthesised sample only one broad reflection was observed in the XRD pattern although the amounts of added BTMPA were significantly lower than in the studies described in this work. No comment was given concerning the co-condensation of the different organosilica precursors. From these experiments one can conclude that the investigated system is quite sensitive to a variation of the reaction conditions. The usage of ammonia which was applied by Wahab et al. instead of sodium hydroxide did influence the pH value of the solution in that case that no ordered material could be obtained anymore.

### 3.2 Spherical ethane-bridged particles with an average particle diameter of 500 nm

#### 3.2.1 Synthesis

In a typical synthesis the surfactant (CTAC, OTAC, C<sub>20</sub>DEMAB) was dissolved in a mixture of distilled water, ethanol and ammonia (32 wt %). This solution was stirred for several minutes until the organosilica precursor BTME was added. The solution was kept under vigorous stirring for additional 30 to 120 minutes and was then filtered off, washed with water and dried in air to yield a fine white powder. A hydrothermal treatment was not necessary in this case. In order to remove the surfactant the samples were solvent extracted as described above in chapter 3.1.1. In order to obtain information about synthesis parameters that influence the particle morphology the ethanol concentration and the ammonia concentration were varied. The molar ratios of the samples are listed in Appendix A.III.1 in Tables A.III.1 and A.III.2.

#### 3.2.2 Results

##### 3.2.2.1 Comparison of the materials synthesised with different surfactants

For comparison of the three surfactants the samples of the highest quality concluded from the P-XRD, the nitrogen physisorption measurements and the SEM images were chosen. The molar ratios are listed in Table 3.3.

**Table 3.3:** Molar ratios of the ethane-bridged spheres of highest quality synthesised with different SDAs.

BTME	Surfactant	NH <sub>3</sub>	Ethanol	H <sub>2</sub> O
0.5	0.34 (CTAC)	9.38	40.51	148.35
0.5	0.30 (OTAC)	10.42	44.30	141.11
0.5	0.22 (C <sub>20</sub> DEMAB)	27.66	36.00	198.01

Figure 3.12 shows the powder X-ray diffraction patterns of the solvent-extracted porous products. The samples synthesised with CTAC (c) and OTAC (b) exhibit one strong but relatively broad reflection which corresponds to d-spacings in the 3-4 nm range (C<sub>16</sub>TAC: 3.38 nm, C<sub>18</sub>TAC: 3.58 nm). The product synthesised with C<sub>20</sub>DEMAB (a) shows at least two reflections. The corresponding d-spacings are d<sub>1</sub>: 3.77 nm and d<sub>2</sub>: 2.25 nm. An indexing of a special mesophase was not possible. The second broad reflection might be the

110 reflection of the hexagonal phase but it is more supposable that the broad reflection consists of the 110 and the 200 reflection and the resulting material exhibited a poor ordering as shown in the TEM below.

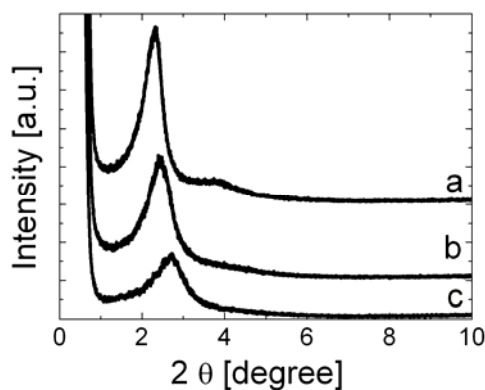


**Figure 3.12:** P-XRD patterns of the samples synthesised with C<sub>20</sub>DEMAB (a), OTAC (b) and CTAC (c).

The structural order is dependent on the ethanol concentration to a certain degree. The addition of ethanol to the synthesis solution leads to a change in the surfactant packing parameter  $g$  (see chapter 1.1). Accordingly, upon addition of low amounts of ethanol, the ethanol molecules penetrate into the micelles, which lead to a kind of swelling. The  $g$  value increases because of the increasing total volume of the surfactant chain  $V$ . In this case the ethanol has a co-surfactant function, although higher concentrations may cause a phase transition. Utilisation of ethanol as a co-surfactant in the synthesis of mesoporous materials may not be regarded as being responsible for the formation of spherical particles under basic synthesis conditions.<sup>[136]</sup> At higher concentrations ethanol acts as a co-solvent rather than co-surfactant. This can be explained as follows: At high alcohol concentration more and more alcohol molecules reside on the outer boundaries of the micelles. Thus, the ratio of alcohol in the aqueous solution to that placed in the micelles increases and the function of the alcohol changes from co-surfactant to co-solvent. The packing of the micelles will be not as dense as for materials synthesised without a co-surfactant due to the lower polarity of the solvent. The expected structure of the respective product would be hexagonal because the solution of lower polarity with a lower pH value due to the use of ammonia instead of sodium hydroxide enhances the repulsive forces between the headgroups of the surfactant molecules which lead to a higher effective area of the headgroup at the organic/inorganic interface  $a_0$  and therefore to a high curvature.<sup>[136]</sup> This result is similar to the hexagonal structured pure silica particles

published by Lind et al.<sup>[110]</sup> Apart from that the use of ethanol as a co-solvent leads to a lower structural order which can be explained by weaker cohesive forces of the solvent and, correspondingly, weaker forces controlling the surfactant aggregation which may also be the reason for the background noise in the XRD patterns.

As expected, the d-spacing increases with longer alkyl chains in the SDA. The same effect can be observed in pristine silica materials, such as high-quality MCM-41 silica or MCM-48 silica. In contrast to the aforementioned materials, the spherical organosilica particles do not exhibit a regular packing of pores and the d-spacing is smaller for the respective surfactant. Both effects may be attributed to modified interactions between the organosilica precursor and the SDA at the organic-inorganic interface during the synthesis as well as to the co-solvent function of the added ethanol.

A comparison of the TEM images approved the poor ordering of the mesopores. A wormlike pore structure could be observed for all samples. The TEM images of the samples synthesised with CTAC, OTAC and C<sub>20</sub>DEMAB are depicted in Figure 3.13 a – c.

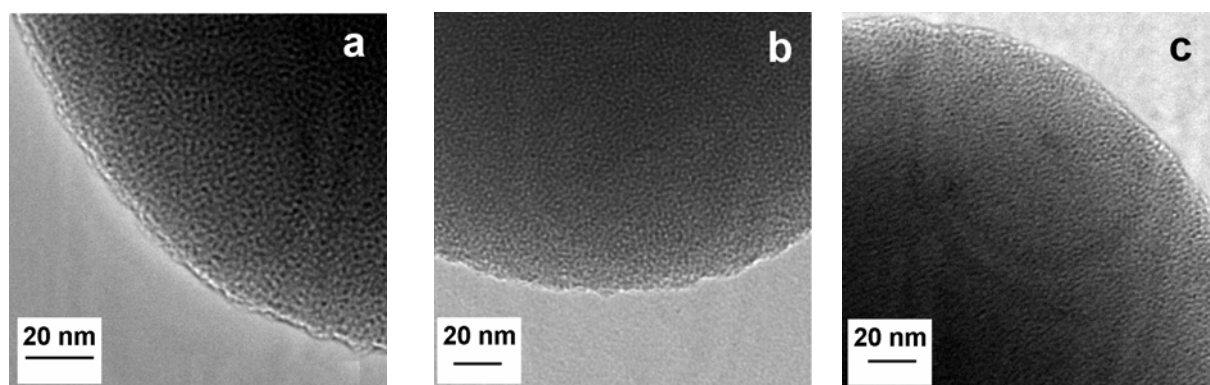


**Figure 3.13 a – c:** TEM images of the samples synthesised with C<sub>20</sub>DEMAB (a), OTAC (b) and CTAC (c).

Nitrogen physisorption measurements for the sample synthesised with C<sub>20</sub>DEMAB shows a typical type IV isotherm which is characteristic for mesoporous materials (Figure 3.14 a).<sup>[132]</sup> The adsorption branch shows capillary condensation at low relative pressures  $p/p_0$ . The resulting pore size distribution (calculated by NLDFT because of the small pore diameters) has its maximum at 3.3 nm (Figure 3.14 b).

In contrast, the isotherms obtained for the samples c and b, synthesised with CTAC and OTAC as SDAs, are not clearly of type IV or type I (see chapter 2.2). Both isotherms show a slight step in the adsorption and desorption branches which can be denoted as pronounced uptake due to the filling of the mesopores. The maximum pore diameters calculated from

NLDFT are 3.0 nm for sample b (OTAC) and 2.6 nm for sample c (CTAC). Both calculated average pore diameters are still within the range of mesopores. Only a very low degree of microporosity (between 1.4 and 2 nm) is observed for sample c. The absence of hysteresis is consistent with the small pore diameter and corresponds to a shift of the phase diagram of nitrogen due to confinement.<sup>[137]</sup>

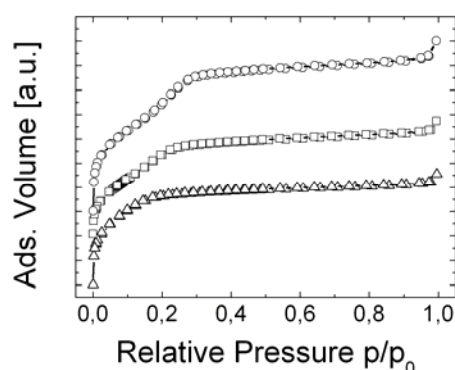


**Figure 3.14 a:** Nitrogen physisorption isotherms of the samples synthesised with CTAC ( $\Delta$ ); OTAC ( $\square$ ) and C<sub>20</sub>DEMAB ( $\circ$ ).

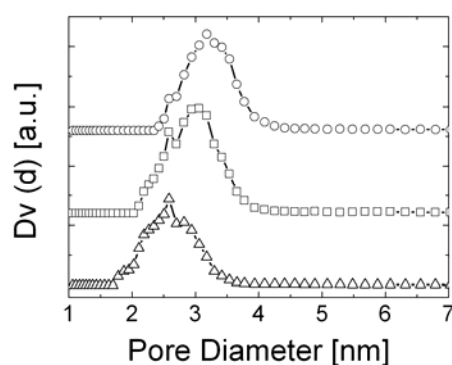


**Figure 3.14 b:** Pore size distributions of the samples synthesised with CTAC ( $\Delta$ ); OTAC ( $\square$ ) and C<sub>20</sub>DEMAB ( $\circ$ ).

All samples show high specific BET surface areas (C<sub>16</sub>TAC: 1435 m<sup>2</sup>/g, C<sub>18</sub>TAC: 1306 m<sup>2</sup>/g, C<sub>20</sub>DEMAB: 1310 m<sup>2</sup>/g), as is expected for pore diameters in this range. The pore diameters are lower than those in mesoporous M41S silica materials synthesised with surfactants of comparable chain length, which, as described above, is due to the addition of the co-solvent. In this comparison one can see that the increase of the alkyl chain length leads in this case to an increase of the pore diameters of the materials as expected. Of course, it would be possible to change the SDA to molecules with longer alkyl chains in order to obtain larger pore diameters. But as described by Köhn the increase of the pore diameter does not follow a linear correlation. With increasing alkyl chain length the magnification factor is reduced.<sup>[138]</sup> This effect can be explained by overlapping of the surfactant chains or different configurations (*cis/trans*) in the hydrocarbon chain. Furthermore, for surfactants with alkyl chains longer than C<sub>22</sub> the total volume of the hydrocarbon chain does not change significantly due to the coiling of the hydrocarbon chain.<sup>[9,138]</sup> This is the reason why most studies dealing with this topic describe only surfactant applications from C<sub>8</sub> to C<sub>22</sub>. This is the reason why no further experiments concerning the attempts to increase the pore size were carried out.

In order to obtain information about the thermal stability of these materials thermogravimetric analysis combined with mass spectrometry (TG/MS) was carried out. A TG curve with the respective detected masses is shown in Figure 3.15.

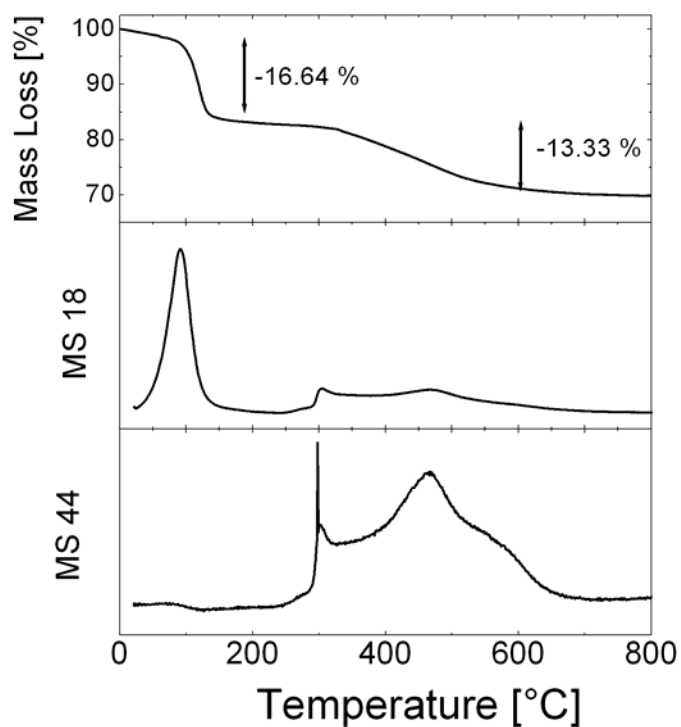


**Figure 3.15:** TG/MS measurement of an ethane-bridged spherical material.

The thermal stability of the organosilica materials depends on the organic bridge which is incorporated in the pore wall framework and is reduced compared to the thermal stability of pure silica materials which could be heated up to 500 °C without a damage of the structure. Thermogravimetric analysis showed that the material started to decompose at a temperature of 300 °C. During a continuous heating process (5 K/min) all samples show a drying step (40-150 °C, weight loss: 16.64 %) followed by the oxidation of the organic bridging groups (300-800 °C, weight loss: 13.33 %).

The scanning electron microscopic images of the three best samples are depicted in Figure 3.16 a – c.

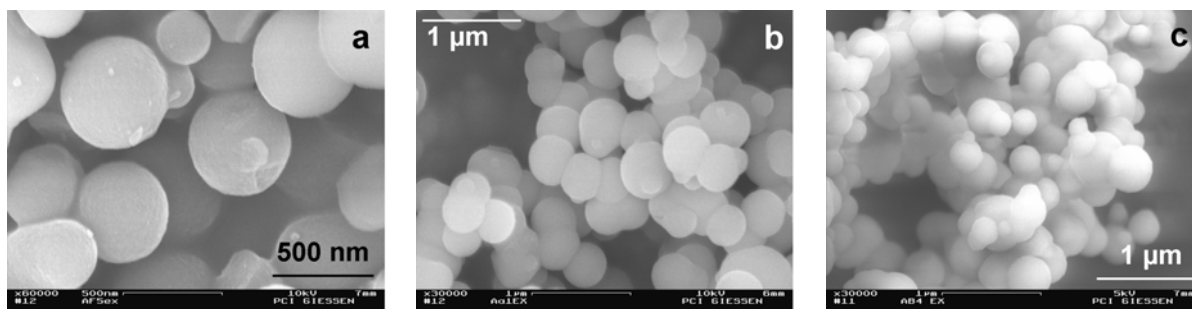


**Figure 3.16 a – c:** SEM images of spherical ethane bridged PMO particles synthesised with C<sub>20</sub>DEMAB (a); OTAC (b) and CTAC (c).

The resulting particle size distributions acquired from the SEM measurements are shown in Figure 3.17 a – c.

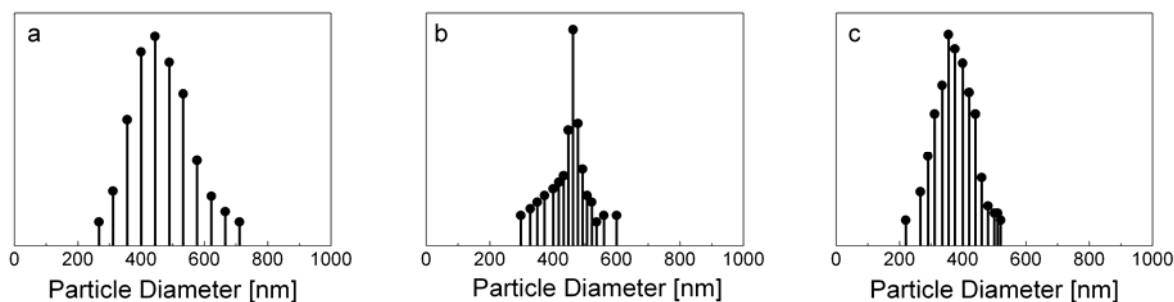


**Figure 3.17 a - c:** Particle size distributions of spherical ethane-bridged PMO particles synthesised with C<sub>20</sub>DEMAB (a); OTAC (b) and CTAC (c).

The diagrams were fitted using a Gauss profile. For the samples synthesised with CTAC and C<sub>20</sub>DEMAB a good correlation is obtained. For the sample synthesised with OTAC the size distribution is slightly asymmetric, but with a clear maximum. The calculation of the particle size distributions from the SEM images will be imprecise to some extent due to the calculation from the SEM images. But the mean particle diameter is around 400 nm for each sample. The size ratios between the largest and smallest particle are approximately 2 for samples c (CTAC) and b (OTAC), and 2.8 for sample a (C<sub>20</sub>DEMAB). For application in separation methods (chromatography) a value of 2 is acceptable.

In some cases the particles have aggregated or are grown together. This is most likely due to the drying step, since a dispersion of Stöber silica particles in highly concentrated solutions of ammonia is usually quite stable with respect to monodispersity. However, drying is necessary in order to obtain information on structure, specific surface area, and pore diameter of the particles. Similar results in particle aggregation behaviour and size distribution were reported

by Bossière et al.<sup>[95,96]</sup> and by Ma et al.<sup>[108]</sup>, both of whom synthesised spherical mesoporous silica particles and performed tests for HPLC application. Lind et al.<sup>[110]</sup> prepared larger particles with bimodal pore size distributions by a spray drying method. In all three cases the main focus was set on high specific surface areas, narrow pore size distributions, well ordered pore arrangement, particle shape, and particle size. The separation behaviour of the products was found to be promising despite particle aggregation and size distribution, which is not as narrow as for non-porous Stöber particles. For an overview all results are summarised in Table 3.4.

**Table 3.4:** Characteristics of the ethane-bridged Stöber particles synthesised with surfactants containing different alkyl chain lengths.

Surfactant	BET [m <sup>2</sup> /g]	Pore diameter [nm]	d <sub>p</sub> * [nm]	Particle ratio smallest/largest	Thermal stability	Structure
CTAC	1435	2.6	430	2	Decomposition start: at 300 °C	Poor ordered (1 reflection)
OTAC	1306	3.0	460	2		Poor ordered (1 reflection)
C <sub>20</sub> DEMAB	1310	3.3	400	2.8		Poor ordered/ 2d hexagonal

### 3.2.2.2 Influence of different synthesis parameters

The influence of the different synthesis parameters on the particle morphology as well as on the mesostructure and the pore diameter were investigated for samples synthesised with CTAC, OTAC and C<sub>20</sub>DEMAB. Due to the similarity of the results the experiments carried out with C<sub>20</sub>DEMAB as SDA are exemplarily shown in the following part. The influence of the ethanol concentration and the ammonia concentration was studied during several experiments.

The correlation between the addition of ethanol and the particle shape has often been discussed in literature. Many groups have shown different synthesis procedures, which involve the addition of alcohol to the reaction solution which lead to spherical particles.<sup>[88,90,91,107,108,136]</sup> Different theories exist concerning the formation of spheres

depending on the reaction conditions. A first theory was published by Bogush et al. who supposed a self-sharpening growth of the particles which means that small particles grow faster than larger particles.<sup>[139]</sup> They postulated that particle growth occurs primarily through the aggregation mechanism where monodispersity is achieved as a result of size dependence, that is, the probability of the aggregation between two particles of the same size decreases as the particles grow up. Many groups have then set focus on the particle growth. A satisfactory result concerning the nucleation and growing mechanism was found out by SAXS investigations.<sup>[140-142]</sup> As a result a mechanism was published that suggests that the first particles to appear have a diameter between 10 and 20 nm which subsequently aggregate and grow to form larger particles. This mechanism was also supported by NMR data.<sup>[143,144]</sup> The addition of a surfactant to the solution might influence the growing process to some extent but due to a similar pH value and ethanol concentration in the solution the mechanism might be nearly the same.

#### *a) Ethanol concentration*

The ethanol concentration in the reaction solution was varied combined with the water content. That means a higher concentration of ethanol results in a lower concentration of water. The XRD patterns of samples synthesised with different concentrations of ethanol and water show a shift of the d-spacings in dependence of the concentrations. An increase of the ethanol concentration led to a decrease in the d-spacings but also to a poorer ordered material. The sample synthesised without ethanol showed a broad reflection as well.

The nitrogen physisorption measurements show all type IV isotherms. The specific surface areas decrease with decreasing ethanol concentration. The mean pore diameter is 2.6 nm for all samples but the size distribution differs dependent on the ethanol concentration. High concentrations (concentrations above 60 mol) of ethanol led to broad pore size distributions. A narrow pore size distribution was obtained for the sample synthesised with 59.21 mol ethanol (see Figure 3.18).

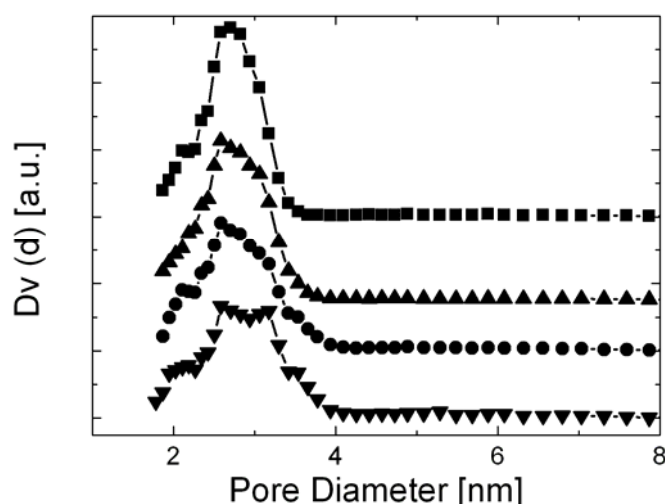


**Figure 3.18:** Pore size distributions of the samples containing different concentrations of ethanol: 59.21 mol (■); 28.86 mol (▲); 5.49 mol (●) and 0 mol (▼).

With decreasing ethanol concentrations the pore size distribution became slightly broader. The sample synthesised without ethanol exhibited a bimodal distribution with a maximum at 2.6 nm and one at 3.4 nm. Nitrogen physisorption data of the samples synthesised with different ethanol concentrations are listed in Appendix A.III.2.

A significant change in the morphology with increasing ethanol concentration in the solution could be observed from the SEM images (Figure 3.19 a – d). Nearly monodisperse spheres resulted from the synthesis with ethanol concentrations in the range of 26 to 48 mol. A decrease of the ethanol concentration and an increase in the water concentration led to larger particles up to a particle diameter of 2  $\mu\text{m}$  but also to an unacceptable broadening of the particle size distribution. The sample synthesised without ethanol led to irregular shaped particles and a very broad particle size distribution. Ethanol concentrations above 59.21 mol did not result in spherical particles. Large indefinite shaped particles were obtained in this concentration range. From these experiments one can conclude that the ethanol concentration in the reaction solution plays an important role for the formation of spheres. The function of ethanol changes with varying concentration. Ethanol in this case acted as co-solvent. Too low amounts of water in the reaction solution slow down the reaction speed significantly due to the slower hydrolysis in alcoholic reaction medium. As a result larger particles were formed. Thus, the addition of ethanol to the reaction solution should be in a narrow concentration range for obtaining spherical particles of the Stöber type.

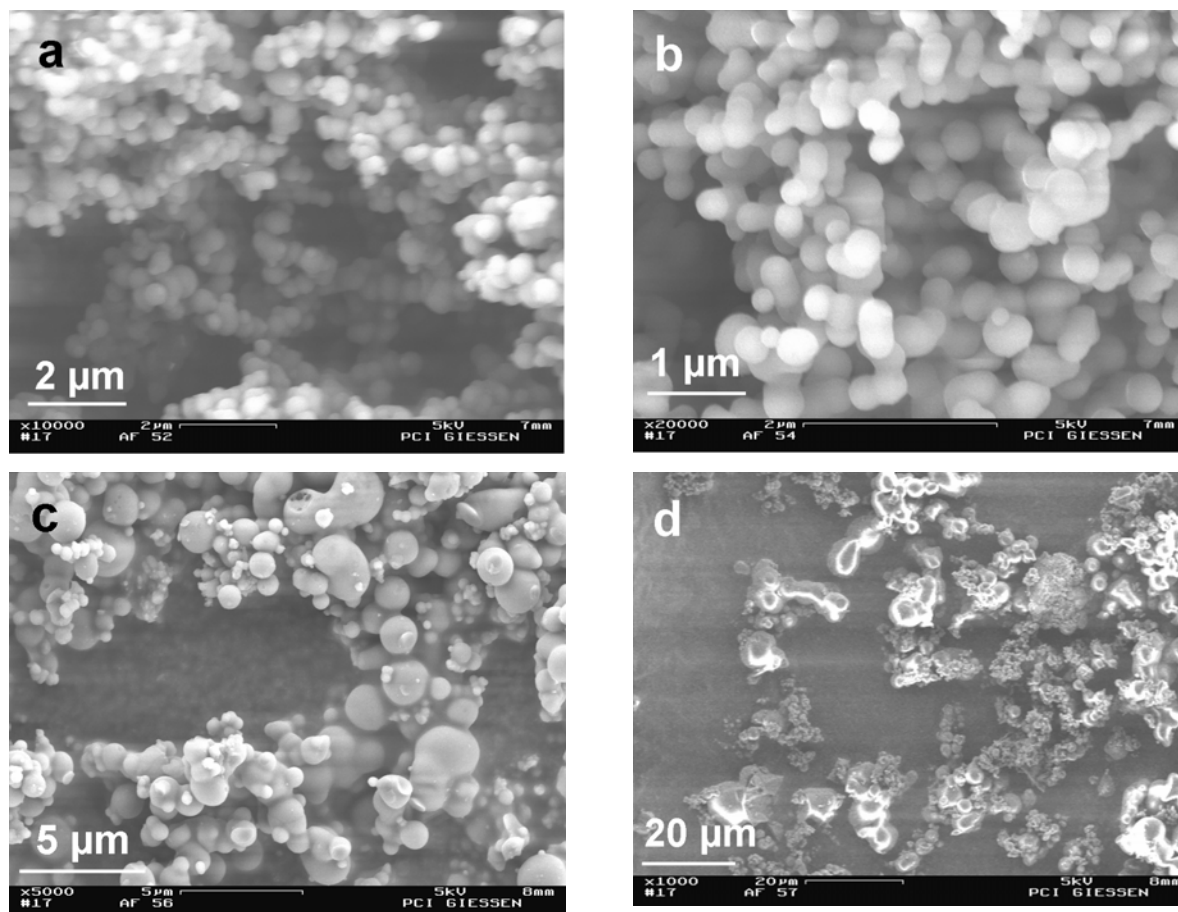


**Figure 3.19 a - d:** SEM images of the samples (molar ratios: 0.5 BTME: 0.22 C<sub>20</sub>DEMAB: 27.66 NH<sub>3</sub>) synthesised with different ethanol concentrations: 48.83 mol (H<sub>2</sub>O: 174.22) (a); 26.86 mol (H<sub>2</sub>O: 253.33) (b); 5.49 mol (H<sub>2</sub>O: 332.44) (c) and without ethanol (d) (H<sub>2</sub>O: 352.21).

#### *b) Ammonia concentration*

As described by Stöber et al. the particle diameter can be influenced by variation of the ammonia concentration.<sup>[81]</sup> Similar experiments were carried out with BTME as organosilica precursor and with the addition of a SDA. The mesostructure of the spherical ethane-bridged PMO material was not influenced by the different ammonia concentrations. The XRD patterns of all synthesised samples show one broad reflection with a d-spacing of 3.38 nm for all samples.

The nitrogen physisorption isotherms and the pore diameters show only slight differences. All pore size distributions exhibited broad maxima. The specific surface areas ( $\approx 900 \text{ m}^2/\text{g}$ ) and the pore size distributions did not vary significantly in dependence of the ammonia concentration in the solution. The SEM images are shown in Figure 3.20 a - d.

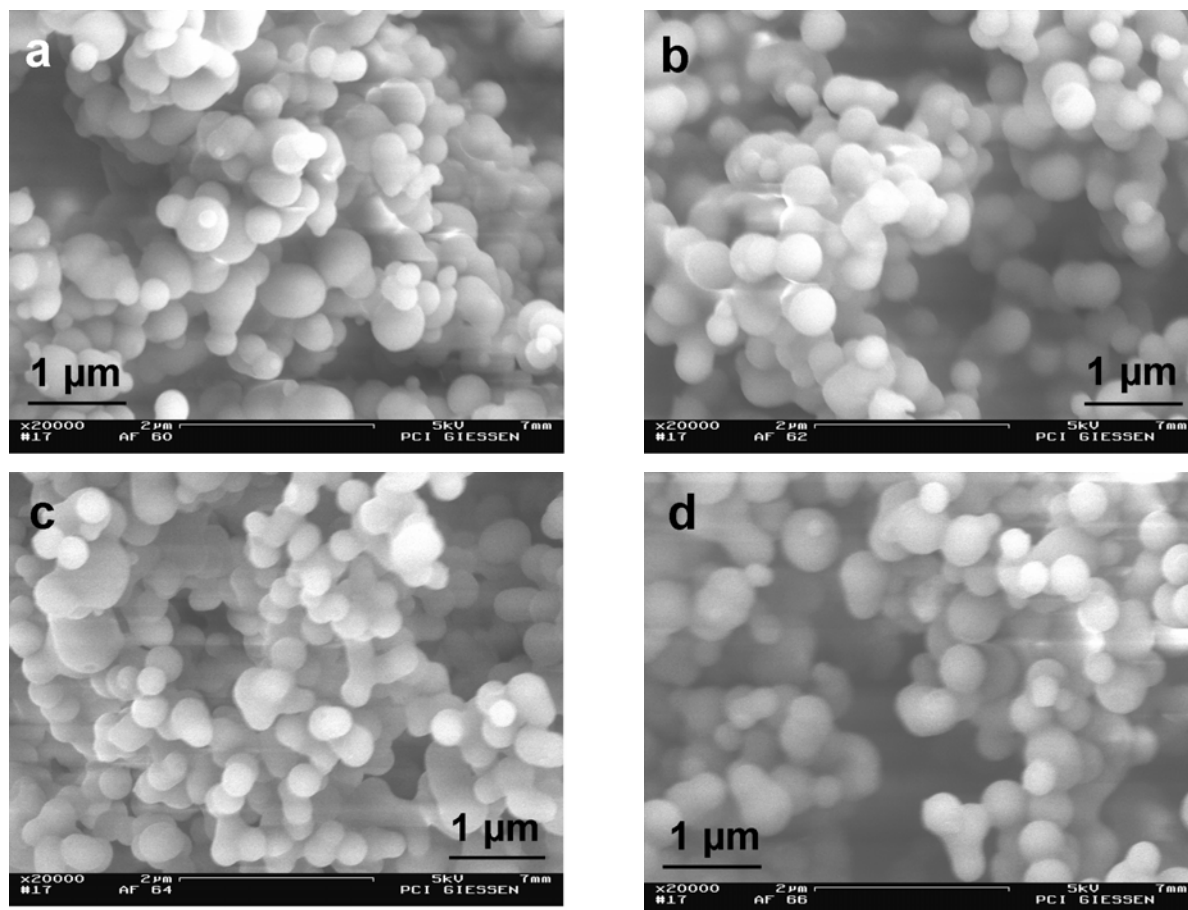


**Figure 3.20 a – d:** SEM images of the samples (molar ratio: 0.5 BTME: 0.22 C<sub>20</sub>DEMAB: 36.0 ethanol) synthesised with different ammonia concentrations: 17.72 mol (H<sub>2</sub>O: 178.02 mol) (a); 29.43 mol (H<sub>2</sub>O: 201.56 mol) (b); 47.10 mol (H<sub>2</sub>O: 237.06 mol) (c) and 70.63 mol (H<sub>2</sub>O: 284.40 mol) (d).

The particle diameter could not be expanded up to 3 μm, which is the optimal size for application in HPLC. In contrast to the observation Stöber et al. made during their experiments with high ammonia concentration no swelling or reducing of the particle size could be obtained in the PMO synthesis.<sup>[81]</sup>

According to the results of the ethane-bridged PMO particles the reason for the formation of spherical particles could be concluded. The concentration of ethanol and the addition of ammonia to the reaction solution are the main synthesis parameters that influence the morphology. As described by Liu et al.<sup>[136]</sup> the morphology of a growing particle depends on the balance between the rate of polymerisation of the positive charged micelle surface covered with the negative charge silica species and the rate of mesostructure formation. In case of slow polymerising silica seeds at high alcohol concentrations (as in the Stöber synthesis) the growth is driven by global surface tension forces to minimise its surface free energy by forming the shape of spheres. At lower amounts of alcohol in the solution the alcohol acts as a

co-surfactant and the polymerisation will be relatively faster because the ethanol molecules are located within the micelles and do not decrease the polarity of the reaction medium significantly. The morphology will be controlled by the deposition of silicate-micellar species onto specific regions of the growing seeds resulting in non-uniform agglomerates. It is quite important that this consideration does only work for identical pH values in the solution. The second reason for the formation of spheres under these typical synthesis conditions is the mild basic conditions in the solution caused by the addition of ammonia which favours a faster condensation of the hydrolysed silica or organosilica species compared to solutions with pH values above 12.

### 3.2.3 Conclusion

In summary, spherical PMO particles could be obtained by the modified Stöber reaction. The application of an organosilica precursor instead of a pure silica precursor led to well-defined spheres with an acceptable ordering of mesopores, high specific surface areas and narrow pore size distributions. The mean particle diameter was around 450 nm. Pore sizes could be varied by increasing the hydrocarbon chain length of the alkyltrialkylammonium surfactant from C<sub>16</sub> to C<sub>20</sub>. Surfactants with longer tail lengths were not investigated because a further increase of the alkyl chain does not lead to significantly larger pore diameters because the coiling of the hydrocarbon chain of the surfactant increases with increasing hydrocarbon chain length. For the synthesis of spherical PMOs in the size range of 0.5 – 1 µm the variation of the ammonia concentration in the applied concentration range did not lead to a significant change in the ordering of the mesopores, the specific surface areas and the pore diameters. Even the particle diameters did not change significantly. In contrast to these observations the particle diameter of the original Stöber particles can be influenced by the variation of the ammonia concentration. An increase of the particle diameter up to 2 µm could be obtained by an increase of the ammonia concentration<sup>[81]</sup> which can be explained by the decreasing condensation rate with increasing pH value in basic medium for pure silica precursors. Thus, the organic moiety of the organosilica precursor influences the way of reaction but no clear statement concerning the influence of ammonia on the reactivity of the organosilica precursors could be given without further experiments. Different results were obtained for the variation of the ethanol concentration. High and low ethanol concentrations led to broad pore size distributions and lower specific surface areas. Best results concerning the morphology were obtained between a H<sub>2</sub>O/ethanol ratio of 3.5 and 9.3. Ratios above and below this value

did not lead to perfectly shaped spheres. An increase of the particle size could be observed with decreasing ethanol concentration but the particle size distribution became significantly broader. As described by Lin et al. for pure silica materials an increase of the ethanol concentration leads to a decrease of the solvent polarity and thus, a lower nucleation and growth of the particles because of the slower hydrolysis and mesostructure assembly but also to the formation of shorter micelles.<sup>[145]</sup> Thus, the monodispersity of the particles could be achieved by a careful choice of the ethanol concentration in the reaction solution. As one can conclude from the data described for the ethane-bridged samples synthesised via the modified Stöber synthesis the main synthesis parameter that influences the formation of monodisperse highly ordered mesoporous particles is the ethanol concentration in the reaction solution. Compared to the pure mesoporous silica spheres synthesised via the modified Stöber reaction monodisperse mesoporous ethane-bridged PMO spheres could only be achieved in a size range of about 500 nm. In contrast, the non-porous pure silica particles as well as the mesoporous pure silica particles were obtained in a size range of 50 – 2000 nm.<sup>[81,88,90,91]</sup> One important fact should be also mentioned in this context. The addition of ammonia to the reaction solution in order to control the pH value of the reaction was held to be responsible for the spherical morphology by Stöber et al. as well as by the Unger group.<sup>[81,88,90,91]</sup> But Yano et al. were able to synthesise monodisperse spherical particles from a solution containing alkyltrialkylammonium surfactants, methanol and tetramethyl orthosilicate under alkaline conditions.<sup>[109]</sup> In their case sodium hydroxide was used to adjust the pH value of the solution. The particle size was varied by changing the concentration of the co-solvent methanol. From these results one can conclude that the pH value of the reaction combined with the co-solvent concentration is responsible for the spherical morphology of the resulting particles. Possible reasons for this fact can be the higher reactivity of central silicon atoms in the network compared to terminal silicon atoms which favours the formation of spherical particles. Although the organic moiety influences the reaction velocity a similar behaviour was observed for the ethane-bridged samples. The reaction velocity is slowed down due to the higher electron density at the silicon atoms caused by the +I effect of the ethane bridge but as shown in this chapter spherical particles could be obtained under similar reaction conditions. As one can conclude from the results shown above the synthesis of monodisperse spherical particles in basic reaction medium needs a careful adjustment of all synthesis parameters, especially the pH value and the co-solvent concentration. Particle diameters above 2  $\mu\text{m}$  could not be obtained under the described synthesis conditions.

### 3.3 Spherical ethane- and phenylene-bridged particles in the size range of 10 – 300 $\mu\text{m}$

#### 3.3.1 Synthesis of spherical ethane-bridged PMOs in the size range of 25-300 $\mu\text{m}$

For the synthesis of spherical ethane-bridged PMOs in a size range of 25-300  $\mu\text{m}$  dodecylamine (DA) was applied as SDA as described for the synthesis of pristine silica particles by Kosuge et al.<sup>[107]</sup> DA was dissolved in a mixture of the organosilica precursor 1,2-bis(triethoxysilyl)ethane (BTEE) and ethanol under vigorous stirring. After the complete dissolution of DA the hydrochloric acid and water were added and the solution was stirred (or mixed by shaking or ultrasonic treatment) for additional several minutes. The resulting white solid was filtered off, washed with ethanol and dried in air to yield fine white particles. Removal of the surfactant was accomplished as described in chapter 3.1.1. Different test series were carried out in order to study the influence of several synthesis parameters like stirring speed, the way of mixing, the pH value, co-solvent concentration and the addition of a co-surfactant. The molar ratios of the synthesised samples are listed in Appendix A.IV.1 in Tables A.IV.1 – A.IV.6.

#### 3.3.2 Synthesis of spherical phenylene-bridged PMOs in the size range of 10-300 $\mu\text{m}$

The typical synthesis of phenylene-bridged spherical PMOs in the size range of 10-300  $\mu\text{m}$  is similar to the synthesis procedure described for the ethane-bridged samples. DA was dissolved in a mixture of ethanol and the organosilica precursor BTEB. The mixture was stirred several minutes; the white solid was filtered off, washed with ethanol and dried in air. Removal of the surfactant was performed as described in chapter 3.1.1. Different test series with varying pH values and different mixing procedures were carried out. The complete data is listed in Appendix A.IV.2 in Tables A.IV.7 and A.IV.8.

#### 3.3.3 Results and discussion

##### 3.3.3.1 Characterisation of ethane-bridged and phenylene-bridged PMO spheres

Best results were obtained for the ethane-bridged PMO spheres as well as for the phenylene-bridged spheres with a mean diameter of  $\approx 80 \mu\text{m}$ . The molar ratios of the samples are listed in Table 3.5 and 3.6.

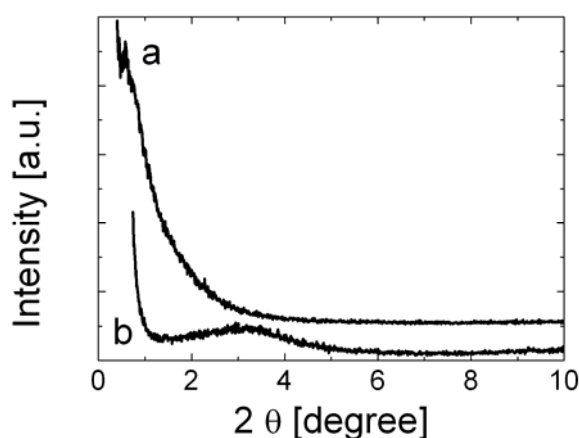
**Table 3.5:** Molar ratio of the ethane-bridged spheres with a particle diameter of 80  $\mu\text{m}$ .

BTEE	Ethanol	DA	HCl	H <sub>2</sub> O
0.5	2.43	0.32	0.0087	47.59

**Table 3.6:** Molar ratio of the phenylene-bridged spheres with a particle diameter of 80  $\mu\text{m}$ .

BTEB	Ethanol	DA	TMB	HCl	H <sub>2</sub> O
0.5	4.89	0.41	0.137	0.0068	73.68

The powder X-ray diffraction measurements show the poor ordering of pores in both materials (Figure 3.21).

**Figure 3.21:** XRD patterns of the ethane-bridged and the phenylene-bridged samples (for molar ratios see Table 3.5 and 3.6).

The phenylene-bridged material exhibited one small broad reflection with a d-spacing of 2.77 nm. The d-spacing of the reflection observed for the ethane-bridged material was 14.3 nm. The difference between both values indicates a difference in pore diameters as well. The poor ordering is due to the non-ionic SDA. Tanev and Pinnavaia first described the synthesis of mesoporous silica materials with long chain amines as SDAs.<sup>[15]</sup> The basis of the formation mechanism is hydrogen bonding and self-assembly between neutral primary amine micelles ( $S^0$ ) and neutral precursor molecules ( $I^0$ ), which was a pure inorganic precursor in the work of Tanev and Pinnavaia and which was an organosilica precursor in this case. For these materials in the XRD patterns only small scattering domains could be detected because of the missing long range electrostatic interactions which usually control the packing of the micellar rods. Typical for these materials are thicker pore walls compared to higher ordered silica materials such as the M41S materials. Thicker pore walls might be an advantage for the

application of the synthesised spheres because thicker walls increase the mechanical and thermal stability of the materials.

Optical microscopic images of the ethane-bridged and the phenylene-bridged sample are depicted in Figure 3.22 a and b. The particle size is comparable but the surface character is slightly different. The phenylene-bridged PMOs exhibit a smooth surface while the ethane-bridged PMOs are a bit rougher textured.

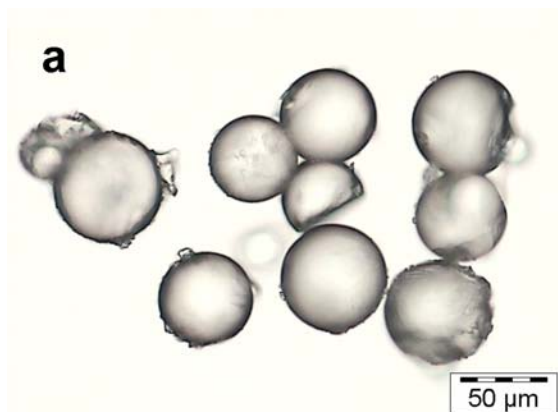


**Figure 3.22 a:** Optical microscopic image of ethane-bridged PMO spheres (molar ratio: see Table 3.5).

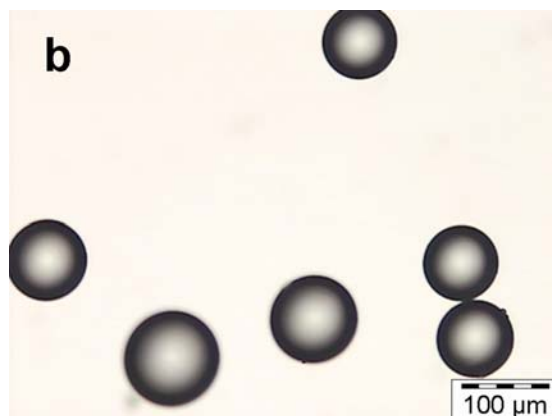


**Figure 3.22 b:** Optical microscopic image of phenylene-bridged PMO spheres (molar ratio: see Table 3.6).

The corresponding TEM images are shown in Figure 3.23 a and b. The large particle diameter necessitates a destruction of the particles. Thus, both materials were milled in a mortar before investigation. The TEM images show the different pore diameters and the non-uniform pore sizes of both materials.

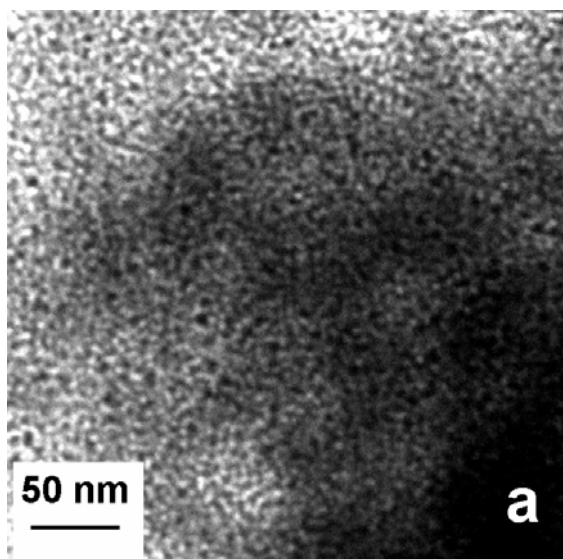


**Figure 3.23 a:** TEM image of a part of an ethane-bridged PMO sphere (molar ratio: see Table 3.5).

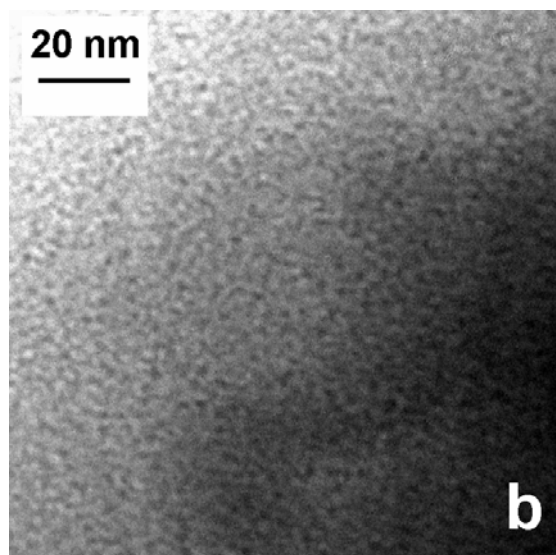


**Figure 3.23 b:** TEM image of a part of a phenylene-bridged PMO sphere (molar ratio: see Table 3.6).

The surface of the particles was investigated by atomic force microscopy (AFM). AFM images of both materials are depicted in Figure 3.24 a and b.

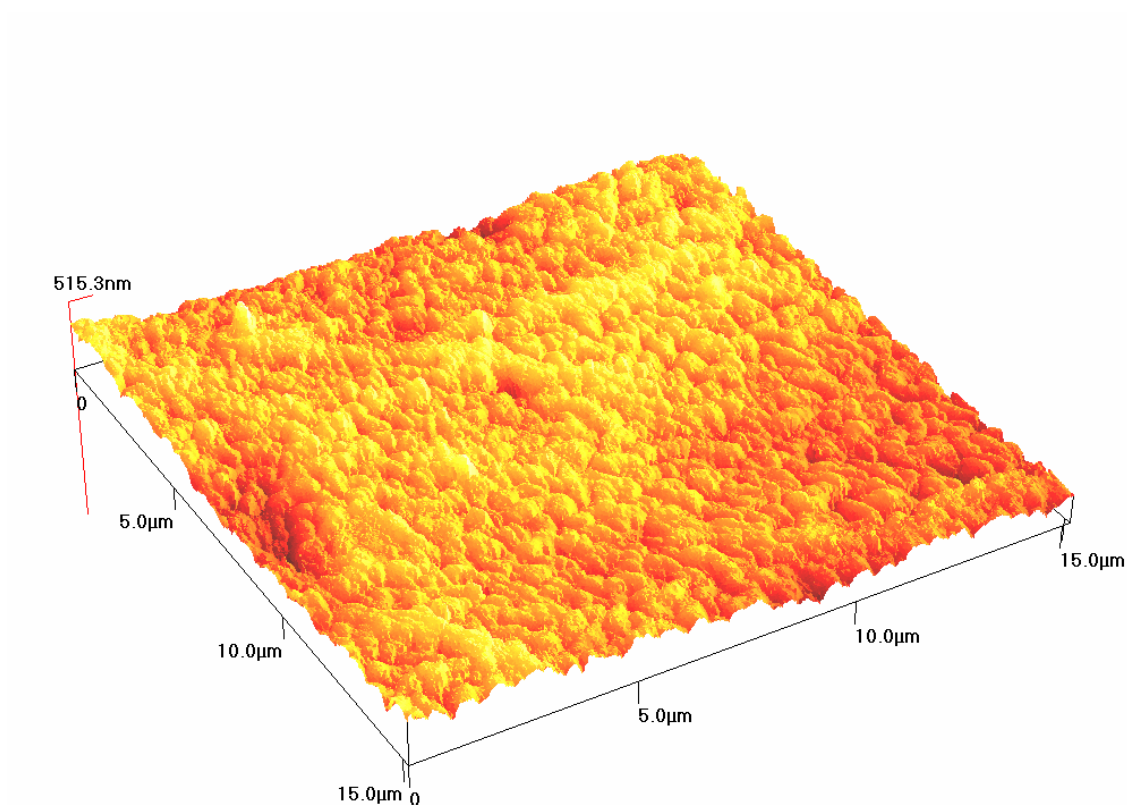


**Figure 3.24 a:** AFM image of the surface of an ethane-bridged microsphere (80 μm).

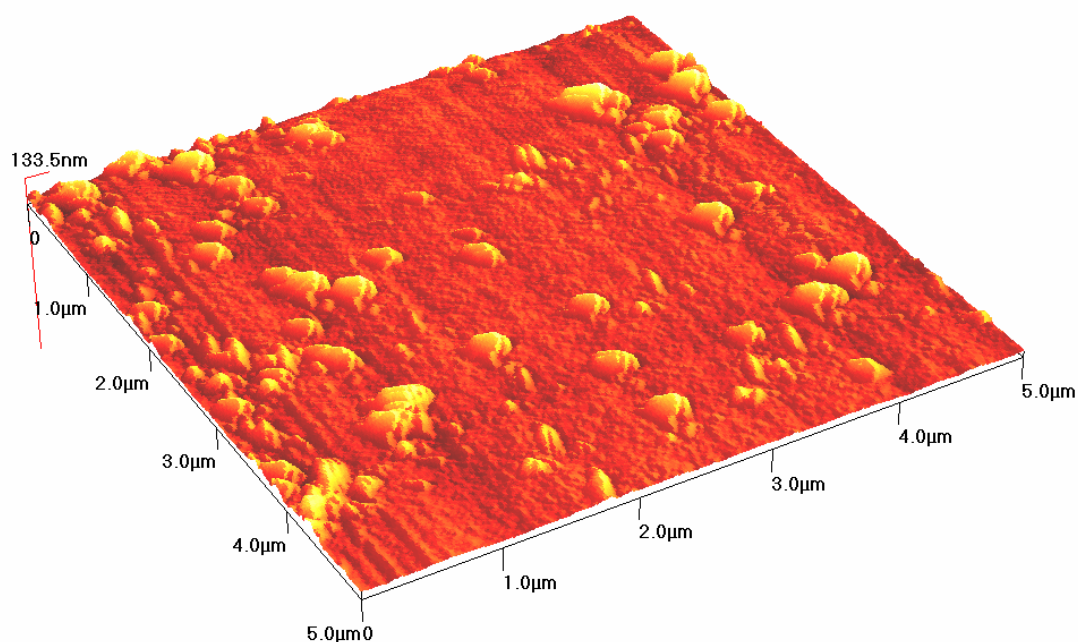


**Figure 3.24 b:** AFM image of the surface of a phenylene-bridged microsphere (80 μm).

From the AFM images of both samples significant differences in the surface structure could be observed. The surface of the phenylene-bridged spheres is smoother than the surface of the ethane-bridged spheres as it could also be seen from the optical microscopic images.

In order to compare the mean pore diameter and the pore size distribution nitrogen physisorption investigations were carried out. The nitrogen physisorption isotherms of both materials are shown in Figure 3.25 a, the pore size distributions are depicted in Figure 3.25 b.

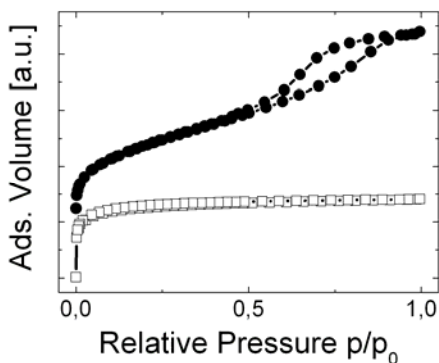


**Figure 3.25 a:** Nitrogen physisorption isotherms of the ethane- (●) and phenylene-bridged PMO spheres (□) (molar ratios: see Table 3.5 + 3.6).

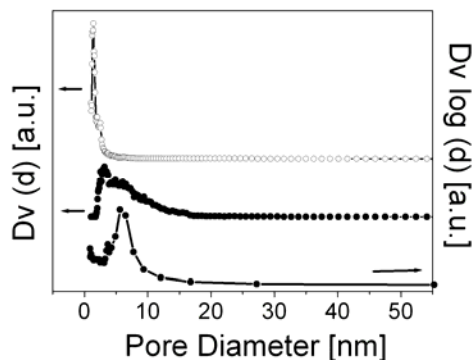


**Figure 3.25 b:** Pore size distributions of the ethane- (●) and phenylene-bridged PMO spheres (□) calculated by the NLDFT (left) and BJH (right) method (molar ratios: see Table 3.5+3.6).

The isotherm obtained for the ethane-bridged material is a type IV isotherm.<sup>[132]</sup> The shape of the isotherm is consistent with the results of the corresponding XRD measurement. The pore size distribution was calculated by NLDFT and by BJH. Both distributions are shown in Figure 3.24 b. The pores of the ethane-bridged sample are fairly disordered as expected from the TEM to some extent and the resulting pore diameter is rather broad independent of the calculation method. The pore diameter calculated by the BJH theory is slightly larger than calculated by NLDFT. The specific surface area is 1000 m<sup>2</sup>/g.

The isotherm of the phenylene-bridged material is a typical type I isotherm indicating that the pore diameter is around 2 nm or below. The pore size distribution is much sharper with a distinct maximum of 1.5 nm (NLDFT). No pores larger than 3 nm could be detected in the phenylene-bridged PMO material. A determination of the pore size distribution by BJH did not make sense due to the small diameter in the micropore range. The calculated BET surface is 600 m<sup>2</sup>/g. The differences in the pore diameters, the specific surface areas and the shape of the isotherms might be caused by the different influences of the organosilica precursors on the formation of the liquid crystalline phase due to their different terms of flexibility and the reaction rates.

The stability of the Si-C bond was proved by <sup>29</sup>Si MAS NMR investigations (see Figure 3.26 a and b). Differences in the condensation degrees of both samples can be concluded from the <sup>29</sup>Si MAS NMR measurements. For both samples no Q signals were obtained which proved the preservation of all Si-C bonds in the samples but the ratio T<sup>1</sup>/T<sup>2</sup>/T<sup>3</sup> is completely different depending on the applied organosilica precursor. An overview is given in Table 3.7.

**Table 3.7:**  $^{29}\text{Si}$  MAS NMR data of the ethane- and the phenylene-bridged sample.

	$\delta T^1$ [ppm]	$\delta T^2$ [ppm]	$\delta T^3$ [ppm]	$T^1$ [%]	$T^2$ [%]	$T^3$ [%]
Ethane-bridged spheres	-47.0	-57.5	-65.0	1.68	50.23	48.09
Phenylene-bridged spheres	-61.43	-70.81	-79.70	8.89	53.86	37.25

\*  $T^1$ :  $(\text{C}(\text{OH})_2\text{Si}(\text{OSi}))$ ;  $T^2$ :  $(\text{C}(\text{OH})\text{Si}(\text{OSi})_2)$ ;  $T^3$ :  $(\text{CSi}(\text{OSi})_3)$

The significant difference especially in the amount of the  $T^3$  signal can be explained by the different size of the organic moieties. Thus, the complete condensation of the phenylene-bridged organosilica precursor could not be obtained. The differences between the chemical shift of the ethane-bridged and the phenylene-bridged spheres of nearly 15 ppm can be explained by the significantly higher screening of the Si nucleus caused by the +M effect of the aromatic bridge.<sup>[146]</sup> The signal width correlates with the angle at the Si-O-Si unit and due to the higher flexibility of the organic bridge the signals measured for the ethane-bridged samples are broader.

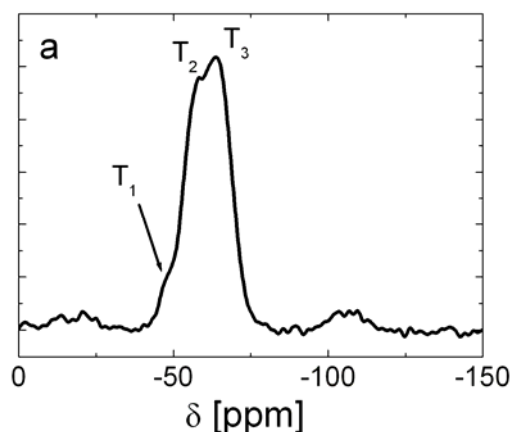


**Figure 3.26 a:**  $^{29}\text{Si}$  MAS NMR spectrum of an ethane-bridged sample (molar ratio: see Table 3.5).

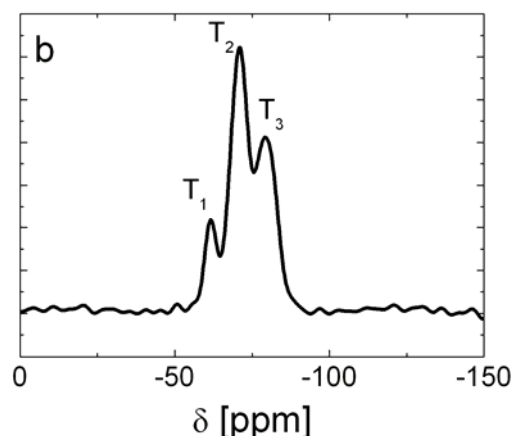


**Figure 3.26 b:**  $^{29}\text{Si}$  MAS NMR spectrum of the phenylene-bridged material (molar ratio: see Table 3.6).

### 3.3.3.2 Influence of different synthesis parameters

The system containing a neutral surfactant as SDA and TEOS as silica source has been investigated by several groups. The addition of a co-solvent as well as the influence of the pH value of the solution on the resulting material was studied intensively. First investigations were carried out by Tanev and Pinnavaia.<sup>[15]</sup> First experiments with different amounts of ethanol as a co-solvent were published by Zhang et al. in 1997.<sup>[147]</sup> They showed that the addition of small amounts of ethanol led to a material consisting of very small particles producing a high textural porosity additional to the mesopore porosity. The addition of high amounts of ethanol to the synthesis mixture led to larger particles without textural porosity. First ideas concerning the formation mechanism were given by the authors. The different morphologies were ascribed to the differences in solvent polarities and thus, to the relative rates of hydrolysis of the neutral inorganic species and the supramolecular assembly in the reaction medium. Higher solvent polarities (high amounts of water) lead to a rapid nucleation of the mesostructure resulting in a solid product formed within minutes of mixing the reactants at ambient temperatures. These particles aggregate into agglomerates. The same reaction carried out in a solvent of lower polarity (high ethanol amount) takes several hours because the hydrolysis of the inorganic species  $I^0$  and the mesostructure assembly are slowed down. The resulting materials consist of spherical particles with a mean particle diameter of more than 100 nm. This synthesis of mesoporous spherical silica particles was modified by Kosuge et al.<sup>[99,107]</sup> who added low amounts of hydrochloric acid to the reaction mixture. As a result large mesoporous spherical silica particles were obtained. The long chain alkylamine was mixed with TEOS and ethanol. A neutral assembly ( $S^0I^0$ ) was initially formed. By the addition of HCl intermediate nucleation assembly of  $S^+X^-I^+$  was performed with a Coulombic interaction between the protonated amine ( $S^+$ ), the coordinating anions ( $Cl^-$ ) and the positive charged silica oligomer ( $I^+$ ). The development of  $S^+X^-I^+$  assembly proceeds in the formation of primary particles which grow up and lead to spherical particles in the micrometer or submicrometer range. Different research groups carried out experiments concerning the formation of monodisperse spheres and the differences in the nucleation and the growth rates are considered to be the dependent factors for monodisperse particle formation, indicating that the higher degree of separation between nucleation and the growth process leads to more monodisperse particles.<sup>[147-150]</sup> The discrimination of the assembly from the hydrolysis step can be achieved by the addition of ethanol which slows down the reaction. Another effect of the co-solvent is a decrease of the micelle length and thus, a lower ordering of the materials

which is often observed for spherical particles.<sup>[145]</sup> Thus, the result of the synthesis depends on the pH value of the solution, the ethanol concentration and, as described by Kosuge et al., on the stirring speed.<sup>[107]</sup> In order to obtain information whether the organosilica materials show similar evolutions with varying synthesis parameters, the stirring speed, the ethanol concentration and the pH value were varied and the samples were investigated by P-XRD, nitrogen physisorption and SEM. The addition of a neutral co-surfactant was tested in order to expand the pore diameters of the materials.

#### 3.3.3.2.1 Ethane-bridged PMO spheres

##### *a) Stirring speed*

As described by Kosuge et al.<sup>[107]</sup> the stirring speed influences the particle size to a high extent.<sup>[104]</sup> A decrease of the stirring rate led to an increase of the particle size but also to broadening of the particle size distribution. Thus, different stirring speeds (300, 400, 500, 600, 700, 800 and 900 rpm) were tested and the resulting products were first investigated by optical microscopy. With increasing stirring speed the particle diameter decreases to a diameter of about 20  $\mu\text{m}$ . With decreasing particle size the particles agglomerate (optical microscopic images are shown in Appendix A.IV.3). This effect was mentioned already by Kosuge et al. Thus, all further investigations were carried out with a stirring speed of 300 or 400 rpm. Other ways of mixing the reaction solution such as shaking with different speeds or ultrasonic treatment did not lead to perfectly shaped particles anyway. An interesting fact was the well-defined spherical morphology of particles synthesised without any mixing of the solution. The pore diameter as well as the specific surface area is not influenced except the data of the sample synthesised without mixing the solution. The pore diameter was much broader than it was observed for all stirred samples (for nitrogen physisorption data see Appendix A.IV.3).

##### *b) Influence of the ethanol concentration*

As a result from the Stöber experiments as well as a result from the experiments carried out under acidic synthesis conditions by Kosuge et al.<sup>[99,107]</sup> and Zhang et al.<sup>[147]</sup> the ethanol concentration in the solution might be important for the spherical morphology. Thus, two test series were carried out with different organosilica precursor concentrations (0.14 mol, 0.5 mol). Interesting results were obtained for both test series. The samples synthesised without ethanol did not contain any spherical particles. These results were expected because

the addition of a co-solvent like alcohols or THF is often hold responsible for the spherical shape by several research groups.<sup>[88,90,91,106,107,136,147]</sup> Just one of the tested concentration of ethanol (2.4 mol) led to nearly perfect shaped particles, which was used for all further experiments concerning the study of the influence of the different synthesis parameters.

*c) Influence of the pH value of the solution*

The variation of the pH value led to an interesting correlation. Particles synthesised at different pH values are depicted in Figure 3.27. With increasing pH value the particles grew up to a particle diameter of 2 mm. Low pH values (HCl concentrations above 0.026 mol) led to irregular particle shapes with rough textured surfaces. The observation of the synthesis procedure led to the conclusion that low pH values lead to small particles. At high concentrations of hydrochloric acid the precipitation occurred almost immediately. With increasing pH value of the reaction solution the span of time between the addition of HCl and the precipitation of the solid extended. A low pH value causes a high speed of hydrolysis reactions. The condensation rate increases as well with decreasing pH value. Most of the organosilica precursor molecules are hydrolysed and condensed within the first minutes. If the reaction is too fast no formation of spherical particles could be observed anymore. High pH values (between 8 and 10) led to a slow formation of particles due to an extremely low hydrolysis speed in this pH range, which is the limitation step in the formation of spheres. The growth of large spheres is the consequence because condensation reactions preferred at central silicon atoms take place as soon as organosilica species are hydrolysed which is quite slow. If the particles have enough time and silica source to grow a particle size of almost 2 mm could be achieved. The specific surface areas did not show significant differences (between 900 and 1100 m<sup>2</sup>/g). The pore size distribution became sharper with increasing pH value (For complete nitrogen physisorption data see Appendix A.IV.4).

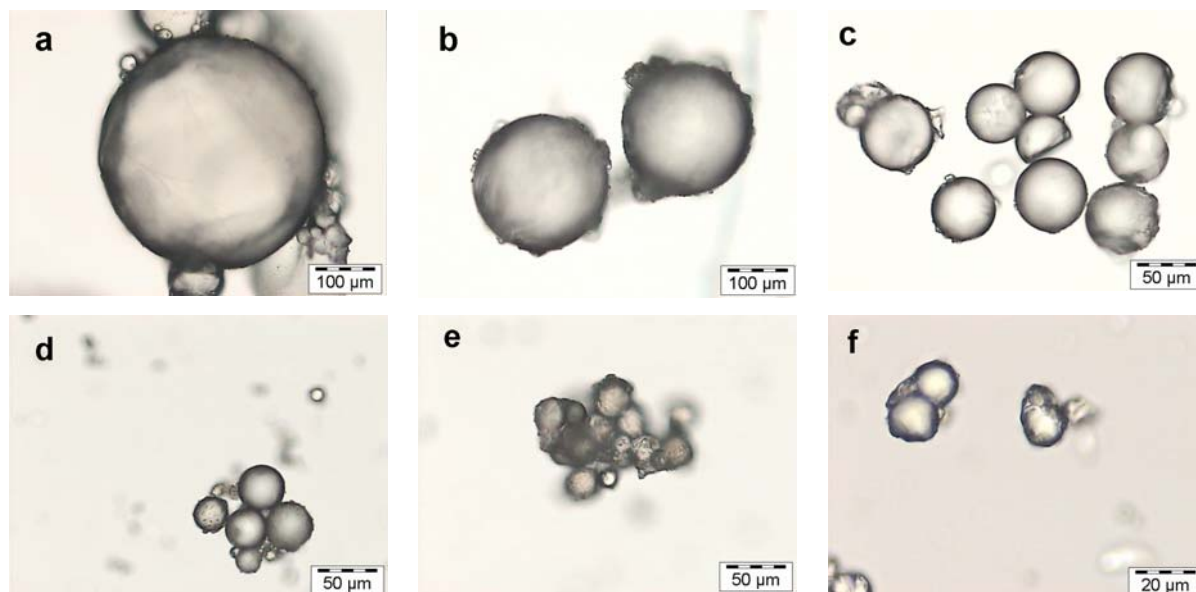


**Figure 3.27** a – f: Ethane-bridged spherical particles (molar ratios except HCl: see Table 3.5) synthesised with different HCl concentrations: 0.0017 mol (a); 0.0043 mol (b); 0.0087 mol (c); 0.013 mol (d); 0.017 mol (e) and 0.026 mol (f).

#### *d) Influence of co-surfactants*

In some cases the particle or the pore diameter could be influenced by the addition of small amounts of other SDAs.<sup>[89,108]</sup> A variation of the pore diameter might open up a wide range of applications of these materials. Experiments carried out with the addition of an alkyltrialkylammonium surfactant like OTAC did not lead to spherical particles. In contrast to the addition of OTAC the addition of non-polar SDAs like Pluronic<sup>®</sup> P123 or Pluronic<sup>®</sup> F127 led to spherical shaped particles. Spheres synthesised with the addition of F127 are shown in Figure 3.28 a – d. The mean particle diameter of this sample is 25 µm. The surface properties of the materials stay the same but the spheres synthesised with a triblock copolymer as co-surfactant are hollow in contrast to the original materials. From all data described above, especially the AFM image and the optical microscopic investigation, one can conclude that the difference between the two synthesis procedures, the first one without any co-surfactants and the second with the addition of a triblock copolymer, lead to similar materials except the hole in the particles. Thus, the holes in the particles must be caused by the triblock copolymers. This leads to the assumption that different amounts of the triblock copolymer are surrounded by dodecylamine micelles and the condensation of the organosilica species took place around the dodecylamine micelles but not around the triblock copolymer. Thus, the dodecylamine must screen the triblock copolymer in the particles. Due to the hole inside the

particles the mechanical stability decreased and lots of particles broke during the milling process before extraction.

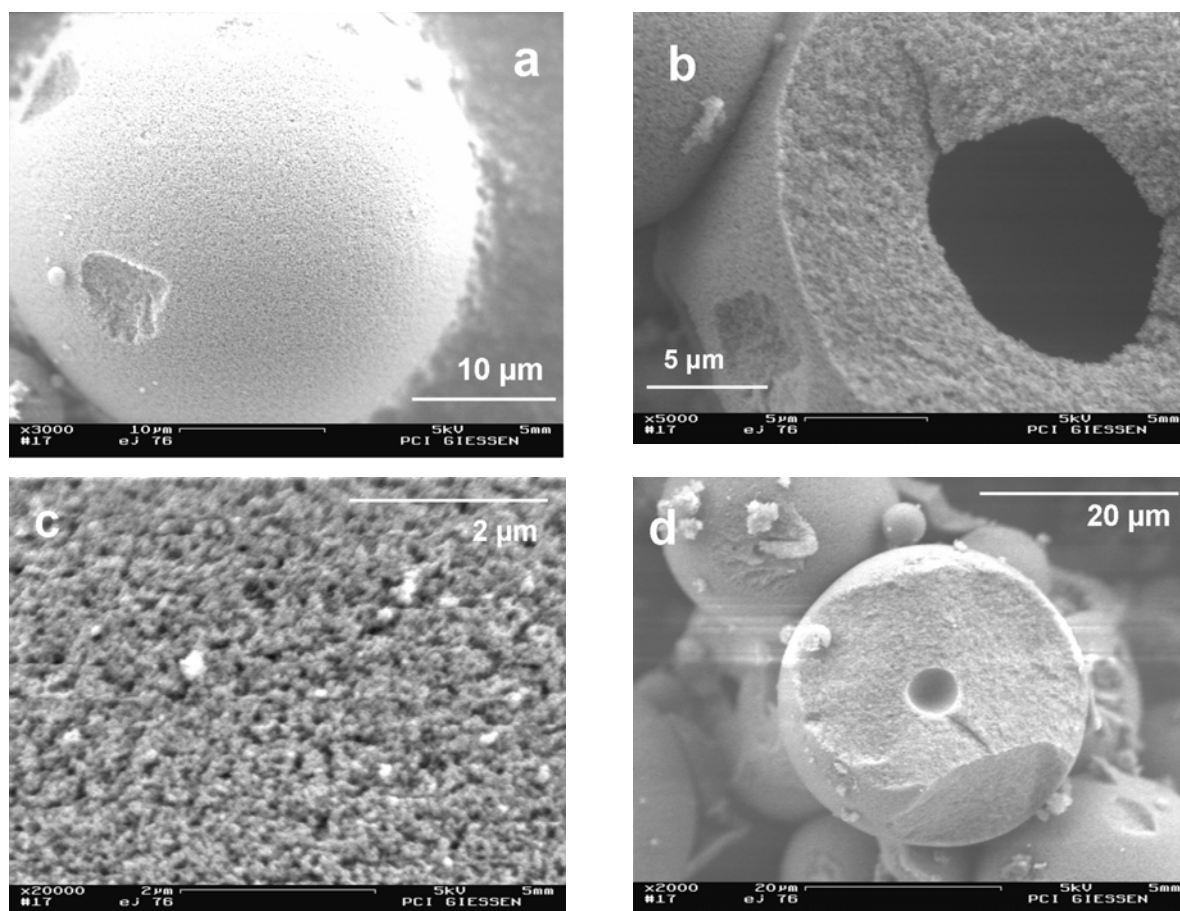


**Figure 3.28 a – d:** SEM images of spheres synthesised with F127 as “co-surfactant” (molar ratio: 0.86 BTEE: 2.72 ethanol: 0.46 DA:  $7.9 \cdot 10^{-6}$  F127: 0.0075 HCl: 41.13 H<sub>2</sub>O).

The relatively low concentration of F127 or P123 did not facilitate a high ordering of mesopores and resulted in such foam-structure. The nitrogen physisorption isotherms and the resulting pore size distributions (calculated via NLDFT) are shown in Figure 3.29 a and b. The pore size distribution is broad for both samples. The sample synthesised with F127 as SDA shows a maximum at 5 nm but pores with diameters up to 50 nm were detected. Similar results were obtained for the sample synthesised with P123 as SDA. Specific surface areas above 1000 m<sup>2</sup>/g were obtained for both samples (optical microscopic images and nitrogen physisorption data: see Appendix A.IV.5).

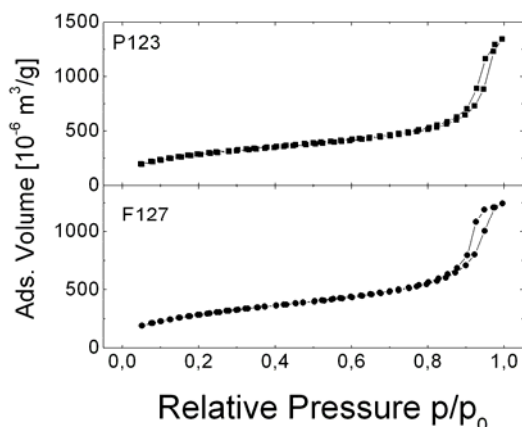


**Figure 3.29 a:** Nitrogen physisorption isotherms of the samples synthesised with the addition of P123 (■) and F127 (●).

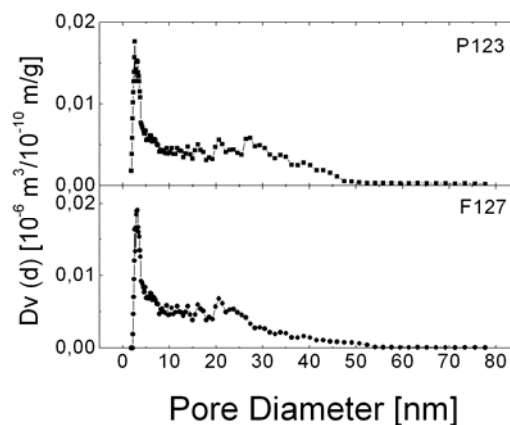


**Figure 3.29 b:** Pore size distributions of the samples synthesised with the addition of P123 (■) and F127 (●).

### 3.3.3.2.2 Phenylene-bridged PMO spheres

Similar to the experiments with the ethane-bridged PMO precursor different synthesis parameters were studied during the synthesis of the phenylene-bridged material. The pH value of the solution was first varied because similarities to the ethane-bridged materials are assumed. Again the influence of the stirring step was investigated in order to confirm or to disprove the correlation between the particle size and the stirring speed made by Kosuge et al.<sup>[107]</sup>

#### *a) Influence of the pH value*

The most interesting synthesis parameter was the pH value of the reaction solution because the particle shape and particle size depend on this parameter to a high extent. Thus, phenylene-bridged particles were first synthesised with different pH values in the reaction solution.

From the microscopic images in Figure 3.30 a – h the dependence between the particle size and the pH value is obvious. The explanation was already given for the ethane-bridged samples. With increasing pH value of the solution the morphology became more uniform. Well-defined and monodisperse spheres could be obtained with BTEB as organosilica precursor. All samples exhibit either no or only a poor ordering of the mesopores. The nitrogen physisorption measurements show that the large particles were completely non-porous. Particles with HCl concentrations below 0.021 mol exhibited a well-defined

morphology but no pores anymore. The samples synthesised with higher HCl concentrations all show typical type I isotherms and the resulting pore diameters prove the microporous character of the materials (pore diameters between 1.2 and 1.4 nm). The missing porosity of the samples synthesised with low HCl concentrations might be due to the pH value that is estimated to be around six and prevents the formation of the liquid crystalline phase. Thus, the DA molecules are suspended in the solution. The organosilica precursor hydrolysed and condensed without a liquid crystalline phase as “template” and compact large and transparent spheres were observed. The microscopic images and atomic force microscopic measurements prove the smooth surface of the large particles (complete nitrogen physisorption data are listed in Appendix A.IV.6).

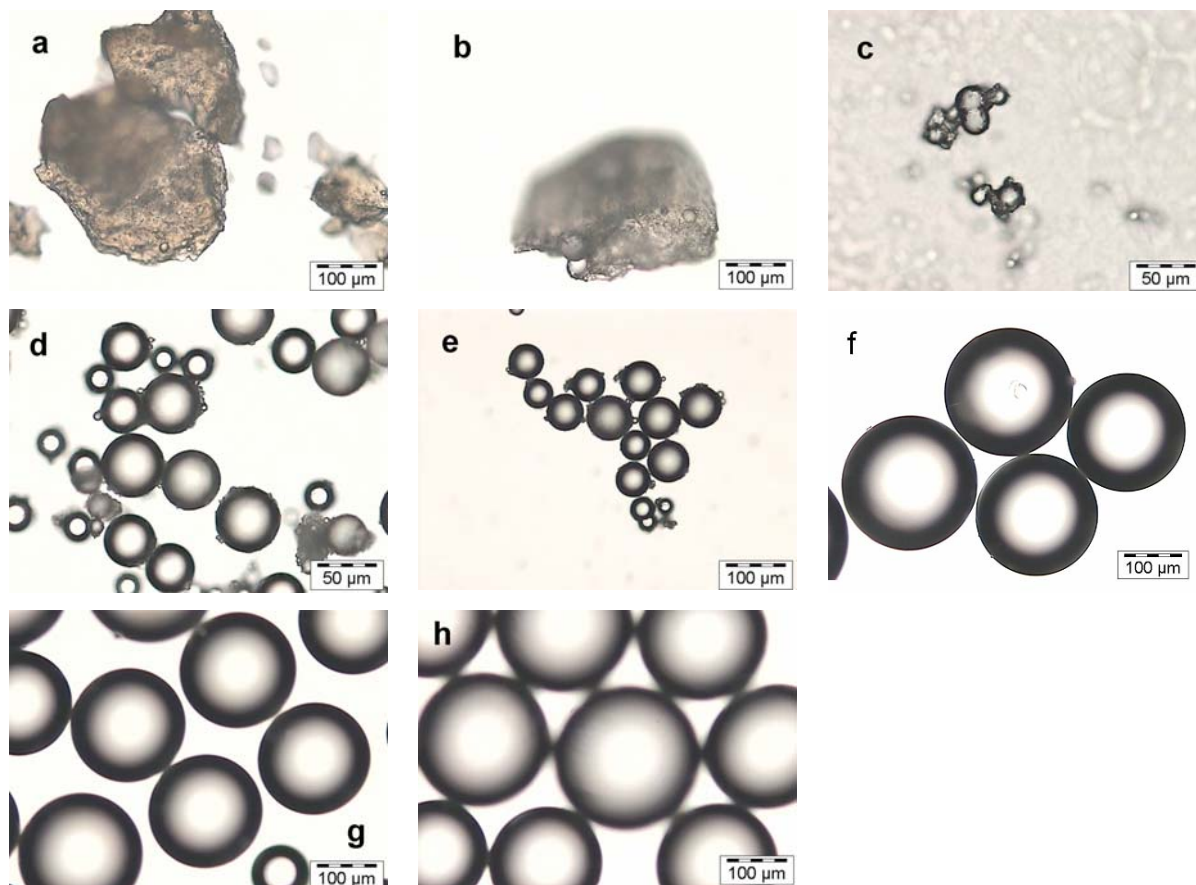


**Figure 3.30 a – h:** Optical microscopic images of the samples (molar ratios except HCl: see Table 3.6) synthesised with different HCl concentrations: 0.28 mol (a); 0.21 mol (b); 0.14 mol (c); 0.021 mol (d); 0.014 mol (e); 0.0095 mol (f); 0.0068 mol (g); 0.0027 mol (h).

#### *b) Influence of the mixing procedure*

The statements made by Kosuge et al. concerning stirring speed being the parameter which influences the particle diameter could not be proved by the results for the ethane-bridged

samples shown above.<sup>[107]</sup> A faster but more uniform mixing of the reaction mixture could be accomplished by shaking. The aim of the test series was to obtain a particle diameter around 10  $\mu\text{m}$ . Thus, relatively high concentrations of HCl were chosen. In all cases spherical particles were obtained. Even particle sizes between 4 and 10  $\mu\text{m}$  were obtained by shaking the reaction solution with 1400 shakes/min (see Figure 3.31 a – e).

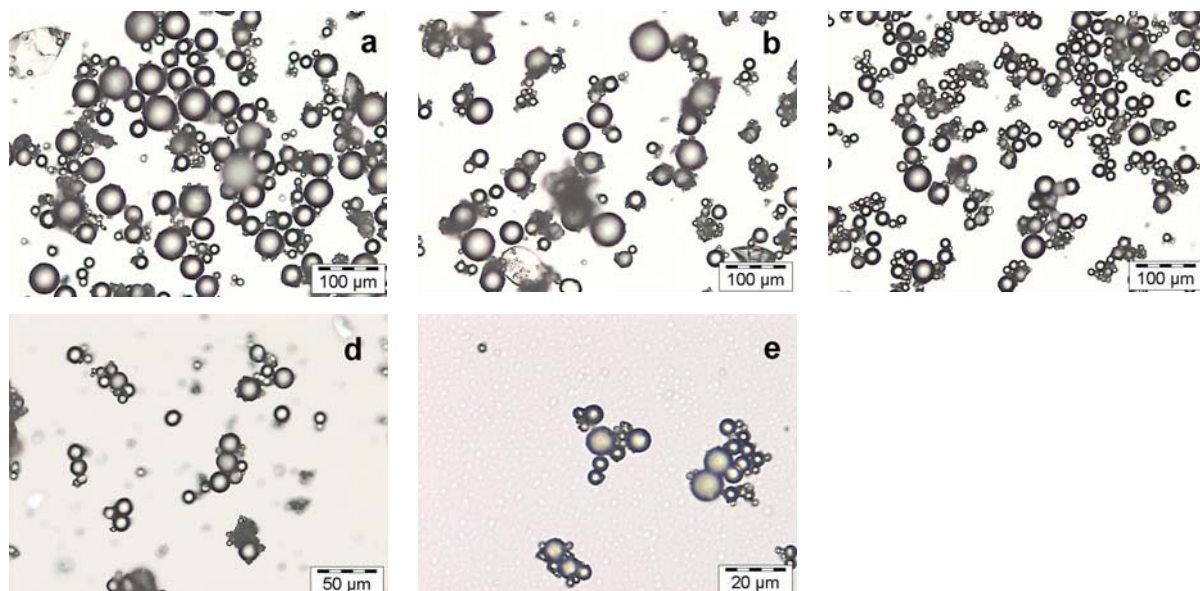


**Figure 3.31 a – e:** Phenylene-bridged spheres (molar ratios except HCl: see Table 3.6) synthesised with different HCl concentrations at different shaking intensities: 0.28 mol/600 spm (a); 0.42 mol/600 spm (b); 0.21 mol/1000 spm (c), 0.21 mol/1400 spm (d), 0.42 mol/1400 spm (e).

Nitrogen physisorption data of all samples showed typical type I isotherms<sup>[132]</sup> and pore diameters in the micropore range. The specific surface areas decreased with increasing shaking intensity (complete data are listed in Appendix A.IV.7).

### 3.3.4 Conclusion

In summary, ethane-bridged spheres synthesised under acidic conditions with dodecylamine as SDA could be obtained up to a size of 300  $\mu\text{m}$ . The particle size could be influenced by the pH value of the reaction solution. An increase of the pH value led to an increase of the particle size. Although this synthesis procedure was similar to the procedure Kosuge et al.<sup>[107]</sup> applied for their synthesis of mesoporous silica particles the size could only partly be influenced by the stirring speed of the solution. Agglomeration occurred at about 500 rpm

while Kosuge et al. obtained first agglomerated particles at a stirring speed of 1200 rpm. The surface structure of these particles depends on the organosilica precursor concentration. Thus, the system is quite sensitive to changes in the organosilica precursor concentration. A change in the ethanol concentration led to a complete loss of the spherical morphology. The addition of a triblock copolymer acting as co-surfactant led to a similar morphology but the addition of the triblock copolymer caused the formation of hollow spheres.

In contrast to our expectations for the materials synthesised with BTEE as organosilica precursor, different results were obtained for the synthesis of phenylene-bridged spheres in the size range of 10-300  $\mu\text{m}$ . The particle size could be influenced by the pH value of the solution as well but the pore sizes were all in the range of micropores. Large spheres did not show any porosity. An increase of the pore diameters could not be achieved by swelling agents or co-surfactants. The surfaces of the phenylene-bridged particles are smoother than the surfaces of the ethane-bridged samples.

From these results concerning the synthesis of ethane- and phenylene-bridged spheres a significant difference between the formation mechanisms could be concluded. From the AFM image of the ethane-bridged material (Figure 3.24 a) one can assume that the formation of the spheres occurred by aggregation of small particles with a mean diameter of about 100 nm. The smooth surface of the phenylene-bridged particles (see AFM image in Figure 3.24 b) led to the assumption that the formation of the large particles occurred by a different procedure. Two possibilities should be discussed. The first idea is the formation of the spheres by mergence of significantly smaller seeds compared to the ethane-bridged samples. Thus, the size of the primary particles might depend on the structure and the reactivity of the organosilica precursor. The second possibility is a growing process occurring by condensation of single hydrolysed organosilica species or very small oligomers without mergence of particles. A clear explanation for the formation cannot be given at the moment. Further investigations like *in situ* TEM or *in situ*  $^{29}\text{Si}$  MAS NMR has to be carried out.

The size of the phenylene-bridged samples could be reduced to a diameter of 10  $\mu\text{m}$  which was not possible for the ethane-bridged spheres. The ethane-bridged samples show agglomeration of the particles at higher stirring rates which might be caused by the lower reactivity of BTEE in contrast to BTEB under acidic conditions.

Besides this, the pore sizes of the phenylene-bridged materials could not be influenced by the variation of different synthesis parameters such as surfactant concentration, addition of a co-surfactant, ethanol concentration or pH value. A possible explanation might be the distortion of the liquid crystalline phase by addition of the aromatic organosilica precursor BTEB.

Further experiments are necessary in order to obtain information about the formation of the liquid crystalline phase and the behaviour of the liquid crystal during and after the addition of the organosilica precursor. *In situ* SAXS experiments might be an interesting opportunity.

### 3.4 Spherical phenylene-bridged PMOs in the size range of 5 – 10 $\mu\text{m}$

The spherical particles in the size range of 5 – 10  $\mu\text{m}$  should be used for high performance liquid chromatography. In order to estimate the properties of the synthesised phenylene-bridged spheres a commercial material for HPLC application was chosen as a reference material. Nucleosil 50-10 was purchased from Machery-Nagel. This material was sold with the following characteristics: a mean particle diameter of 10  $\mu\text{m}$ , a specific surface area of 350  $\text{m}^2/\text{g}$  and a pore diameter of 5 nm. All measurements, of the reference material as well as of the phenylene-bridged spheres, were carried out parallel in order to find similarities or differences between both materials. If the phenylene-bridged spheres show nearly the same properties concerning the particle size distribution both materials should be filled in a column and tested in a HPLC instrument. A pure silica material was chosen as a reference because the remaining silanol functions on the surface of the PMO materials offer similar separation properties to the silica gel.

#### 3.4.1 Synthesis

The synthesis of phenylene-bridged spherical particles in the size range of 5 to 10  $\mu\text{m}$  is based on a synthesis procedure for spherical SBA-15 silica particles already published by Ma et al.<sup>[107]</sup> In a typical synthesis deionised water, ethanol and hydrochloric acid were mixed. The SDAs Pluronic<sup>®</sup> P123 and CTAB were added under vigorous stirring. Shortly after the complete dissolving of P123 and CTAB the organosilica precursor BTEB was added. The solution was stirred for additional 30 minutes with 500 rpm and was then transferred into a teflon lined steel autoclave. A hydrothermal treatment at 80 °C for 5 hours and then at 130 °C for 12 hours followed. The resulting white solid was filtered off and washed with ethanol. Removal of the SDAs was accomplished as described in chapter 3.1.1. In order to obtain an acid-free material the powder was washed again with ethanol and then dried in air. Different test series were carried out. First experiments were carried out in order to check if the two-step hydrothermal treatment is necessary. In a second series the influence of the pH value was investigated. Additional, the influence of the ethanol concentration was studied. The function of the SDA and the co-surfactant was checked by four different experiments: the first without the addition of any SDA, the second with P123, the third with CTAB and the fourth with the addition of both SDAs. The molar ratios of the described samples are listed in Appendix A.V.1.

### 3.4.2 Results

#### 3.4.2.1 Comparison of the phenylene-bridged spheres and Nucleosil 50-10

In order to obtain information about the purchased material from the Company Machery-Nagel (particle diameter: 10  $\mu\text{m}$ , pore diameter: 5 nm) powder X-ray diffraction investigations and nitrogen physisorption measurements were carried out as well as scanning electron microscopic and transmission electron microscopic investigations. The results were compared to the results of the characterisation of the phenylene-bridged PMO material (molar ratio: 0.5 BTEB : 0.017 P123 : 0.044 CTAB : 14.14 ethanol : 1.95 HCl 163  $\text{H}_2\text{O}$ ) because both materials should be used for HPLC experiments.

As one can see from the powder X-ray diffraction patterns in Figure 3.32 there is no ordering of pores in the Nucleosil 50-10 in contrast to the phenylene-bridged particles, which exhibit one reflection and a slight shoulder. The synthesised phenylene-bridged particles show a periodic but relatively poor ordering of the mesopores while no periodicity in the pore arrangement can be observed in the pattern of Nucleosil 50-10. The poor ordering of the mesopores of the phenylene-bridged material might be caused by the formation of shorter micelles due to the addition of ethanol to the reaction solution and thus, the long range hexagonal order cannot be obtained.<sup>[145]</sup> Thus, a high hexagonal or cubic symmetry in a spherical particle with a diameter of at least 10  $\mu\text{m}$  seems to be hardly achievable.

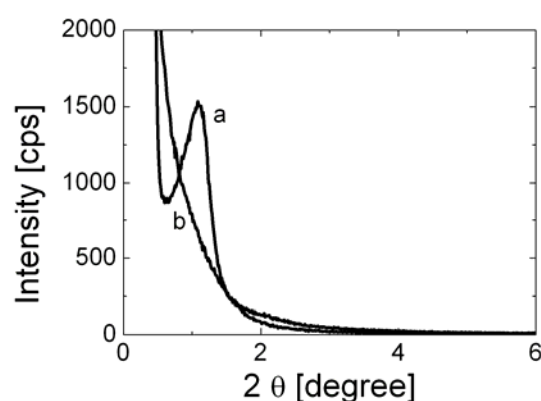


**Figure 3.32:** XRD patterns of the phenylene-bridged PMO material (a) and Nucleosil 50-10 (b).

For both materials the nitrogen physisorption investigations show type IV isotherms, which is typical for mesoporous materials (Figure 3.33 a).<sup>[132]</sup> The isotherm of the phenylene-bridged

spheres exhibits a type H2 (for explanation see chapter 2.2) hysteresis with a clear capillary condensation step that is caused by a broader pore size distribution and not well-defined cylindrical pores. This effect is also caused by the formation of shorter micelles due to the addition of the co-solvent and the resulting spherical morphology. The isotherm of Nucleosil 50-10 shows the capillary condensation and the pore evaporation over a wide relative pressure range and a type HI hysteresis loop. This isotherm form is typical for materials synthesised via the sol-gel process, which is assumed for Nucleosil 50-10. The calculated specific surface areas using the BET theory are 350 m<sup>2</sup>/g for Nucleosil 50-10 and 1100 m<sup>2</sup>/g for the phenylene-bridged spherical PMO material. Both pore size distributions were calculated using the NLDFT method. The resulting pore diameter of the spherical PMO material shows a relatively narrow pore size distribution between 4.5 and 6.5 nm with its maximum at 5.7 nm. Nucleosil 50-10 exhibits a pore size distribution reaching from 4 to 30 nm with its maximum at 8.1 nm (Figure 3.33 b). Thus, the average pore diameter of 5 nm given by the manufacturer could not be confirmed.

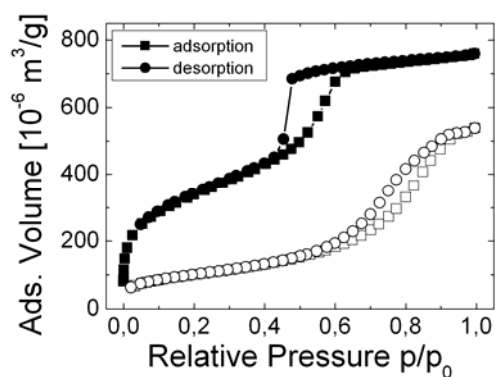


**Figure 3.33 a:** Nitrogen physisorption isotherms of the phenylene bridged PMO material (■/●) and Nucleosil 50-10 (□/○)

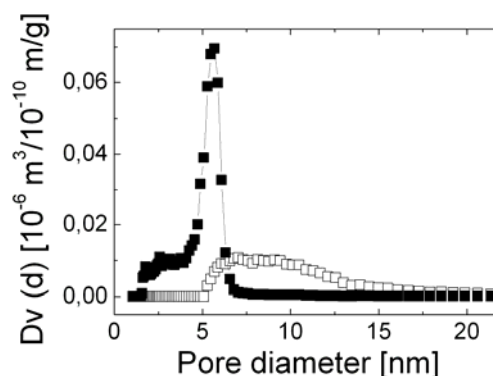


**Figure 3.33 b:** Pore size distribution of the PMO material (■) and Nucleosil 50-10 (□) (calculated by the NLDFT).

The nitrogen-physisorption data of both samples are summarised in Table 3.8.

**Table 3.8:** Nitrogen physisorption data of the phenylene-bridged PMO material and Nucleosil 50-10.

	BET surface [m <sup>2</sup> /g]	Pore diameter [nm]	Micropore volume [ccm/g]	Pore volume [ccm/g]
Nucleosil 50-10	356	8.1	0.00	0.80
PMO	1180	5.7	0.03	1.12

The particle size distributions of the phenylene-bridged PMO spheres and Nucleosil 50-10 were measured with laser diffraction and are shown in Figure 3.34. Both samples contain small amounts of particles smaller than 3  $\mu\text{m}$ . The first maximum in both distributions is ascribed to the impreciseness occurring during the diameter calculation because the requirement for the calculation was the spherical shape of all particles which, in reality, is not the case. The maximum of the distribution for the PMO spheres is 10.3  $\mu\text{m}$ , for Nucleosil 9.9  $\mu\text{m}$ .

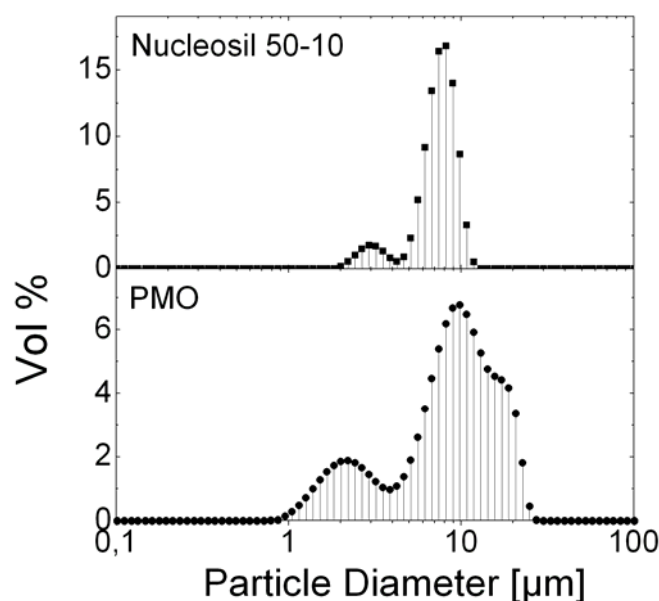


**Figure 3.34:** Particle size distribution of Nucleosil 50-10 (upper layer ■) and the spherical PMO material (lower layer ●) measured with laser diffraction.

For a better comparison SEM images of both samples were recorded. The PMO spheres are depicted in Figure 3.35 a, Nucleosil 50-10 spheres are shown in Figure 3.34 b. Both materials show well-defined spheres.

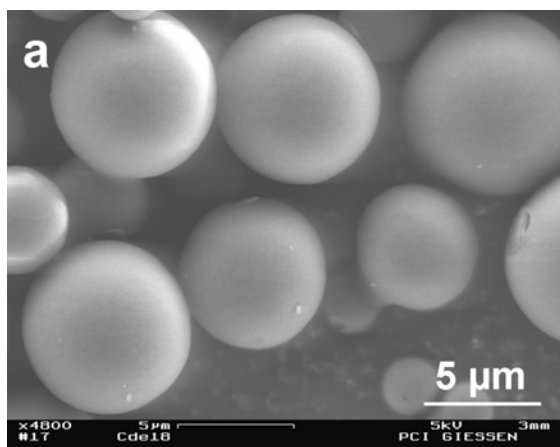


**Figure 3.35 a:** SEM image of the spherical phenylene-bridged PMO material.

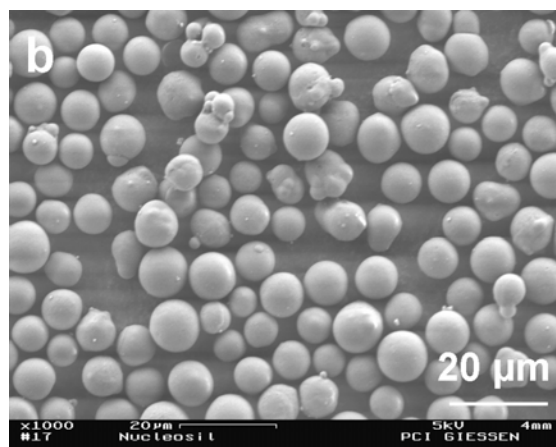


**Figure 3.35 b:** SEM image of Nucleosil 50-10.

The TEM images of both materials are shown in Figure 3.36 a and b. Due to the large particle diameter only parts of particles could be shown in the images. Pores can be seen only at the surface of the particles. The surfaces of the Nucleosil 50-10 particles are not as smooth as the surfaces of the phenylene-bridged spheres.

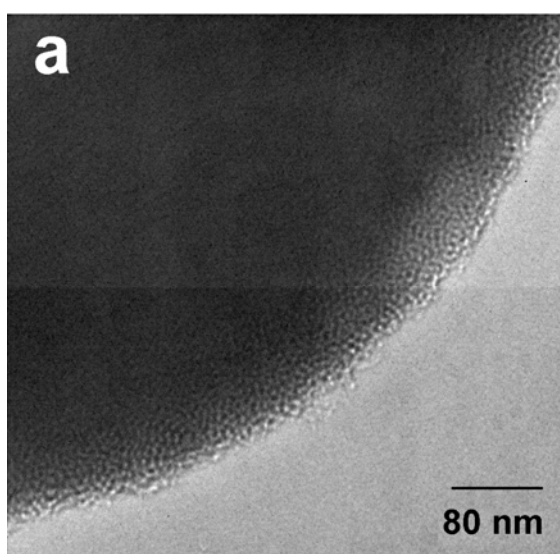


**Figure 3.36 a:** TEM image of the spherical phenylene-bridged PMO material.

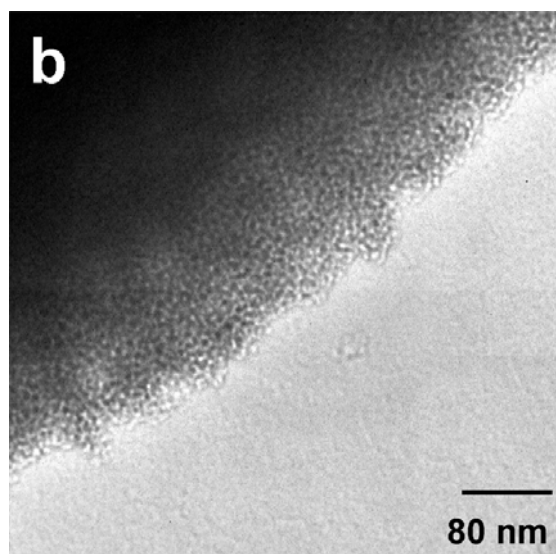


**Figure 3.36 b:** TEM image of the Nucleosil 50-10.

In case of the phenylene-bridged material an AFM investigations were carried out in order to obtain information about the surface structure of the material. An AFM image of some particles is shown in Figure 3.37 a, The AFM image of the particle's surface is depicted in Figure 3.37 b. From the image of the particle's surface one can see that the surface is rough in the nanometer region.

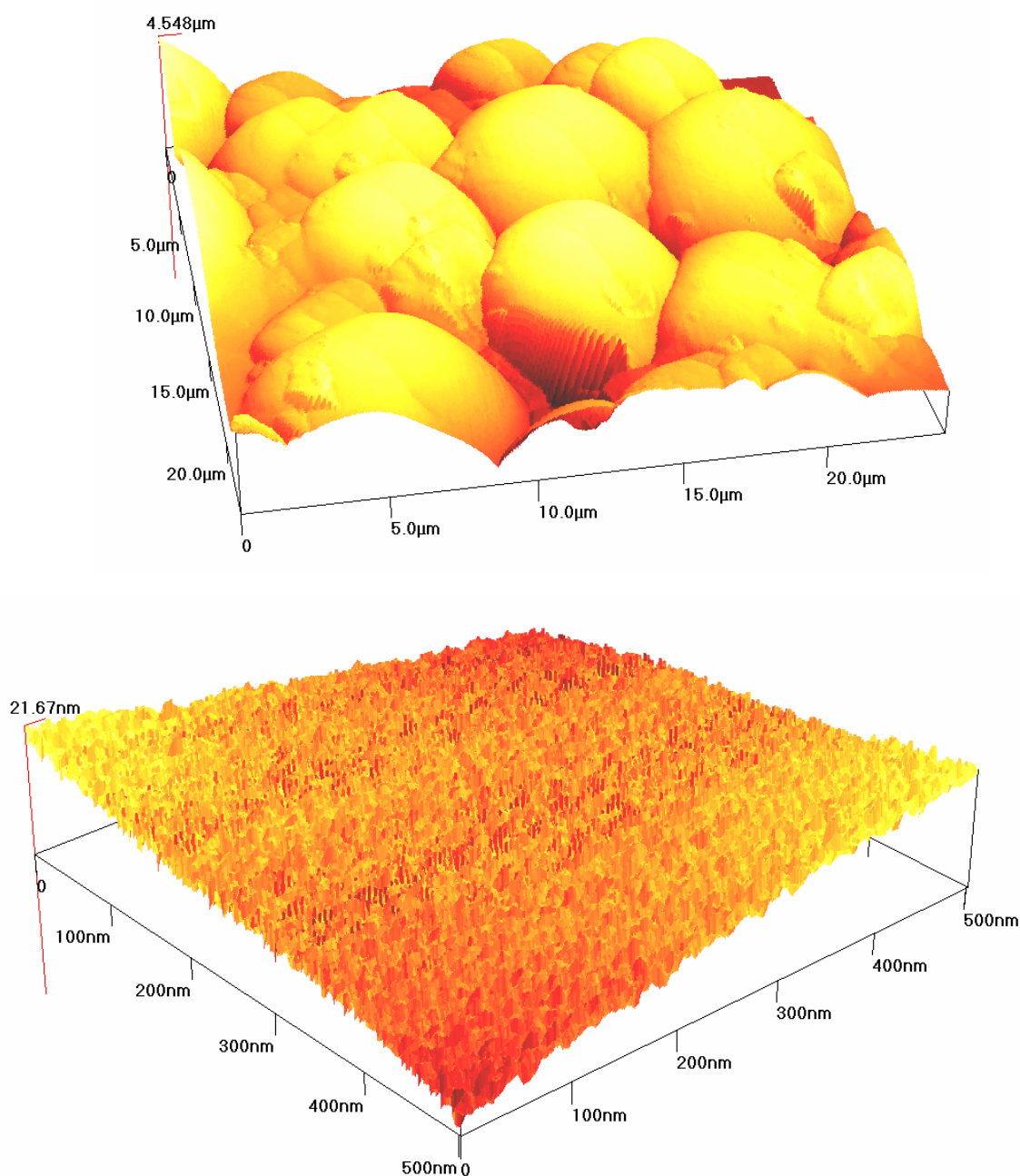


**Figure 3.37 a and b:** AFM image of some phenylene-bridged spherical particles (a) and of a particle's surface (b).

In case of Nucleosil 50-10 the silanol functions are the only functions on the surface while on the phenylene-bridged PMO material the silanol functions remaining on the surface as well as the phenylene bridges in the pore wall network play important roles for the adsorption properties. This is the reason why the determination of the silanol functions on the surfaces of both materials is essential for a comparison and an estimation concerning the separation quality. The number of silanol functions of Nucleosil 50-10 was given by Macherey-Nagel.

The determination of the surface silanol functions of the PMO material was accomplished by exchanging the protons of the silanol functions by deuterons. The phenylene-bridged PMO material was investigated by  $^2\text{H}$  solid state NMR. Via a deuterium standard (sodium-trimethylsilylpropionate-2,2,3,3- $d_4$ ) and normalisation of the signals the number of deuterium atoms per  $\text{nm}^2$  could be specified. The  $^2\text{H}$  NMR of the standard and of the phenylene-bridged material are shown in Figure 3.38 a and b.

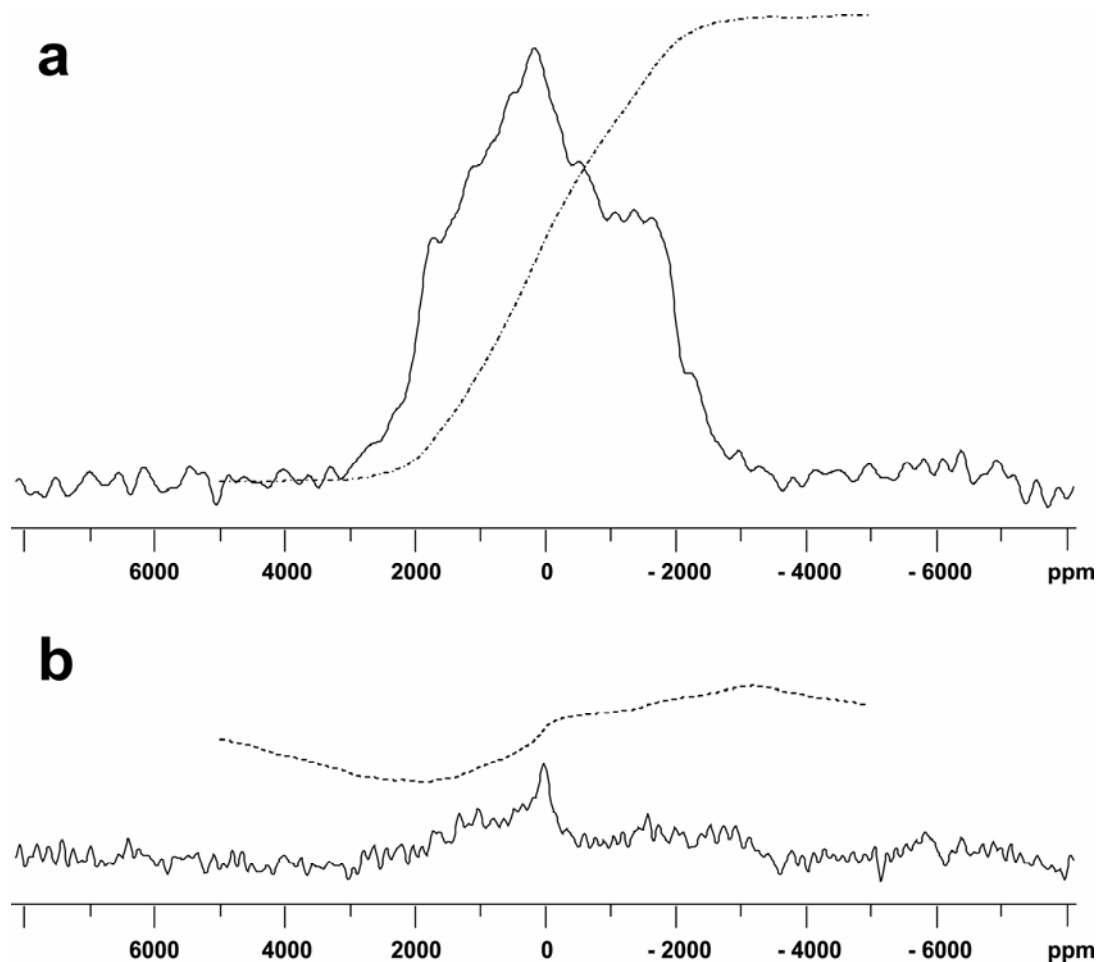


**Figure 3.38:**  $^2\text{H}$  solid state NMR investigations: sodium-trimethylsilylpropionate-2,2,3,3- $d_4$  (a), phenylene-bridged PMO material (molar ratios: see Table A.V.2: Cde18) (b).

The resulting data are listed in Table 3.9. A difference in the number of silanol functionalities was expected and thus, the phenylene-bridged spheres should have different separation properties.

**Table 3.9:** Numbers of silanol functionalities on the surface of Nucleosil 50-10 and the phenylene-bridged PMO material.

	Mass [mg]	Intensity [a.u.]	Concentration Si-OH [ $\mu\text{mol}/\text{m}^2$ ]	Number Si-OH [number/ $\text{nm}^2$ ]
Standard	81.5	1 (normalised)	-	-
PMO	46.8	0.03	0.26 <sup>+</sup>	0.16
Nucleosil 50-10	-	-	8.00 <sup>*</sup>	4.82

<sup>+</sup>The number of silanol functions on the surface of the spherical phenylene-bridged material was calculated by comparison of the intensities of the  $^2\text{H}$  signal of the standard sodium-trimethylsilylpropionate-2,2,3,3-*d*4 (normalised) and the phenylene-bridged PMO material.

<sup>\*</sup>Information given by Macherey-Nagel

The thermal stability of the phenylene-bridged PMO material was investigated by thermogravimetric measurements coupled with mass spectrometry (see Figure 3.39).

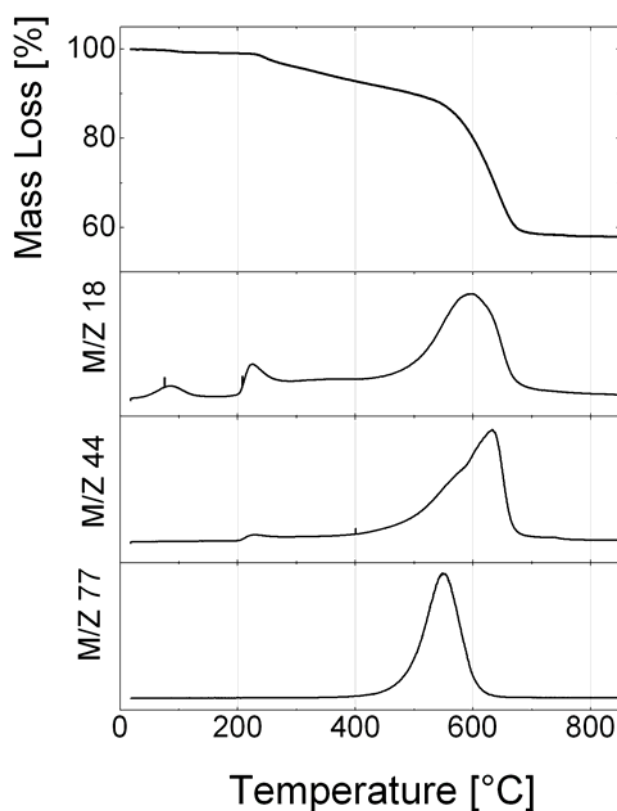


**Figure 3.39:** TG/MS measurement of a phenylene-bridged spherical material (for molar ratios see Table A.V.2: Cde18).

The total mass loss is 40 %. The TG curve can be divided in three steps. The first step from 20-200 °C is a drying step. The mass loss is one percent. In the mass spectrum only the mass of water can be detected. Between 200 and 450 °C a mass loss of 9 % occurs. The detected masses in the spectrum are water and CO<sub>2</sub>. The phenylene bridge is still stable at these temperatures. So the mass loss can be attributed to molecules of the SDAs which remained in the sample after the extraction procedure. At a temperature of 450 °C the organic bridge started to decompose. The detected mass in the spectrum is 77 for the phenyl fragment and water and CO<sub>2</sub>. The decomposition is completed at a temperature of 650 °C. The high thermal stability of the PMO material can be attributed to the aromatic system in the organosilica precursor.

<sup>29</sup>Si MAS NMR investigations proved that the Si-C bond was not cleaved during the reaction and extraction procedure. The <sup>29</sup>Si MAS NMR spectrum is shown in Figure 3.40. The ratio of the signals is depicted in the Figure as well.

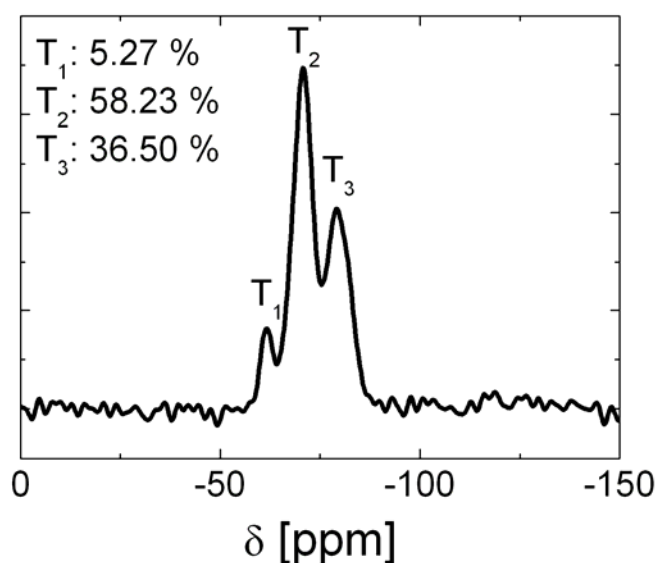


**Figure 3.40:** <sup>29</sup>Si MAS NMR spectrum of a phenylene-bridged spherical material (for molar ratios see Table A.V.2: Cde18).

#### 3.4.2.2 Influence of different synthesis parameters

In contrast to the syntheses of the modified Stöber PMO particles (chapter 3.2) and the large spheres synthesised under mild acidic conditions (chapter 3.3), the applied synthesis for phenylene-bridged spheres in the size range of 5 to 10  $\mu$ m under acidic conditions is more

complex due to the application of a co-solvent, a co-surfactant and a two-step hydrothermal treatment. Thus, a determination of the reaction parameters that influence the most important characteristics of the materials might be more complicated. The synthesis of a SBA-15 silica material with the addition of a co-surfactant has only been reported twice.<sup>[108,151]</sup> Zhao et al. synthesised a SBA-15 silica material with nearly spherical shaped particles of 1  $\mu\text{m}$  in diameter.<sup>[151]</sup> But the morphology was not perfectly spherical. A synthesis performed without the co-surfactant led to ropelike particles. Thus, the addition of the co-surfactant should be one important parameter that controls the morphology. The synthesis of the spherical SBA-15 silica material was modified by Ma et al. in 2003.<sup>[108]</sup> The addition of a co-solvent to the reaction solution combined with the co-surfactant and a two-step hydrothermal treatment led to perfectly shaped spheres in the diameter range of 3 to 6  $\mu\text{m}$ . The two-step hydrothermal treatment was found out to be necessary by the authors. During the first step at 80 °C spherical particles were formed. Heating up the solution to 130 °C in the first step led to irregular shaped particles. Thus, the temperature of 130 °C is too high for the formation of spherical particles. As already mentioned, the ethanol concentration was held to be responsible for the formation of spherical particles and thus, the authors carried out an experiment without the addition of ethanol. Irregular shaped particles mixed with spherical particles were the result. But a detailed description of synthesis parameters that can influence the particle diameter was not given by Ma et al.<sup>[108]</sup> From these experiments one can conclude that the co-solvent, the co-surfactant and the hydrothermal treatment should be investigated in detail. According to the results described for the modified PMO Stöber particles (chapter 3.2) and the large spheres (chapter 3.3) experiments with different pH values of the solution were carried out in order to obtain information about the dependence between the pH value and the particle diameter.

Thus, detailed investigations concerning the influence of the pH value, the ethanol concentration, the necessity of the co-surfactant and the hydrothermal treatment were carried out.

#### *a) Influence of the hydrothermal treatment procedure*

The necessity of applying a two-step hydrothermal treatment was investigated by synthesising samples without a hydrothermal treatment step, with one hydrothermal treatment step at 80 °C for 5 hours, at 130 °C for 12 hours and the two-step hydrothermal treatment at 80 °C for 5 hours and 130 °C for 12 hours. These experiments show that the condensation degree is significantly influenced by the temperature of the hydrothermal treatment. The condensation

degree of the sample synthesised without a hydrothermal treatment is so low that the reaction solution did not contain any precipitation. Low temperatures (in this case 80 °C) lead to poorer ordering of the mesopores and to small pore diameters. A spherical morphology was obtained for all three remaining samples but the sample heated up to 130 °C without the heating step of 80 °C showed also large irregular shapes particles (Optical microscopic images and nitrogen physisorption data are shown in Appendix A.V.2).

*b) Influence of the variation of the pH value*

The amount of hydrochloric acid was varied by keeping all other synthesis parameters constant. The variation of the pH value of the reaction solutions led to an interesting result. The resulting mesostructures did not show significant changes with increasing pH values of the reaction solution in the range between -0.05 and 0.8. Specific surface areas between 900 and 1200 m<sup>2</sup>/g were obtained. A slight increase of the pore diameters could be observed with increasing pH value of the reaction solution (for complete nitrogen physisorption data see Appendix A.V.3).

A well-defined spherical morphology for all samples was obtained in the pH value range of -0.05 and 0.8. The particle size depended on the pH value of the solution in this range. The increasing pH value resulted in larger particles but also in broader particle size distributions. An overview is given in Figure 3.41 a – f. This dependence between the pH value of the solution and the resulting particle diameters can be explained by the different reaction velocities at different pH values. In acidic medium the reaction rate which implies hydrolysis and condensation increased with decreasing pH value of the solution. Under acidic conditions the hydrolysis is faster than the condensation. Thus, after a short reaction time the organosilica source is completely hydrolysed and condensed. With increasing pH value of the solution the ratio between hydrolysis and condensation increases and the reaction is slowed down (up to a pH value of about five). The growth of the particles is slowed down as well and larger particles were obtained due to the increased reaction time. As shown in Figure 3.41 f a pH value of 0.8 leads to particles with more than 20 µm in diameter but also to a broad particle size distribution. This is a result of the slow nucleation process. Even during the on-going reaction new seeds are formed, which do not have time to grow in this advanced stadium of the reaction.

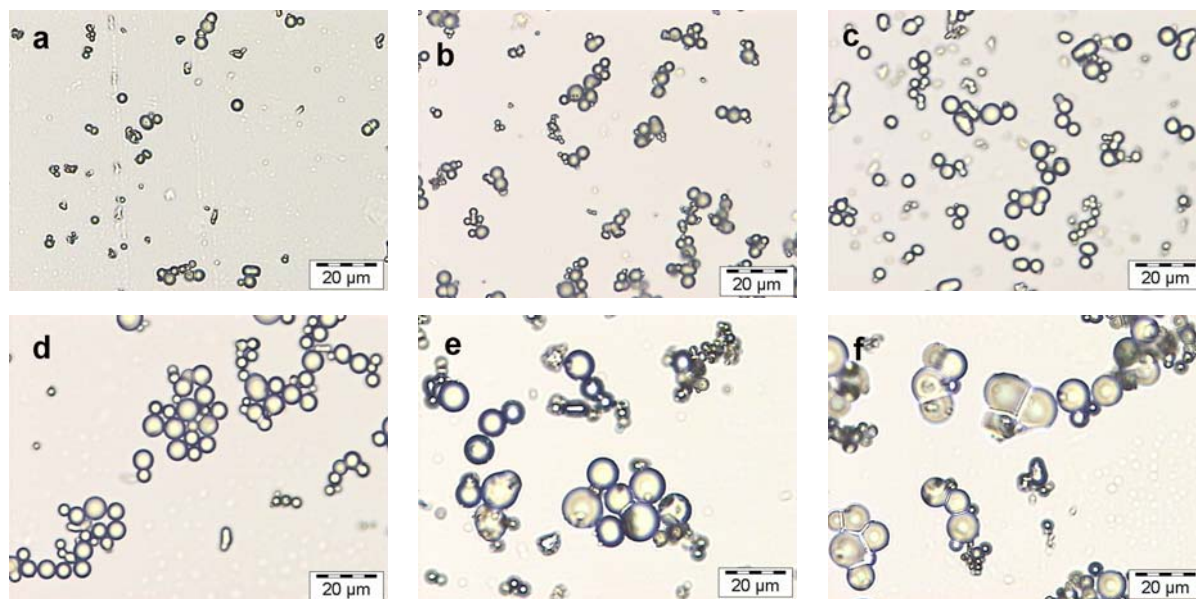


**Figure 3.41 a – f:** Optical micrographs of samples synthesised at different pH values: pH -0.02 (a); pH 0.1 (b); pH 0.2 (c); pH 0.3 (d); pH 0.5 (e); pH 0.8 (f). The molar ratios were: 0.5 BTEB : 0.017 P123 : 0.044 CTAB : 14.14 ethanol : 163 H<sub>2</sub>O and 3.90 HCl (a); 3.25 HCl (b), 2.60 HCl (c); 1.95 HCl (d); 1.30 HCl (e); 0.65 HCl (f).

*c) Influence of the variation of the ethanol concentration*

As often pronounced in the literature the addition of alcohols as co-solvents to a reaction solution might be responsible for the spherical morphology of the resulting materials. [88,90,91,107,108] Thus, samples were synthesised with different amounts of ethanol. The sample synthesised without the addition of ethanol exhibited a 2d hexagonal mesostructure. With increasing amount of ethanol in the solution the long-range order decreased and the d-spacings are shifted to higher values. This fact can be explained by the weaker cohesive forces of the solvent and the consequential weaker forces controlling the surfactant aggregation. This leads to a packing of micelles which is not as dense as it is for samples synthesised without a co-solvent and normally results in thicker pore walls. This could be proved by nitrogen physisorption measurements. The nitrogen physisorption isotherms showed only slight differences in the adsorbed volumes and the isotherm shape. The form of the hysteresis and the capillary condensation step remained unchanged. An increase of the specific surface areas was observed which can be explained by the increasing amount of micropores in the materials synthesised with higher ethanol concentrations. The mesopore diameters were nearly the same for all samples. According to the shift in the d-spacings the pore wall thickness increased with higher ethanol concentration in the reaction solution. With

increasing pore wall thickness the micropore area increased as well which explains the increase of the specific surface area. The particle morphology is dependent on the amount of ethanol in the reaction solution to a high extent. The sample synthesised without ethanol showed many different shaped particles. An increase of the ethanol concentration up to 35.35 mol led to mostly spherical but also oval shaped particles. Thus, the co-solvent concentration plays a significant role for the formation of spherical particles (Optical microscopic images and nitrogen physisorption data are shown in Appendix A.V.4).

#### *d) Influence of both SDAs*

The necessity of applying two different SDAs in order to obtain the desired mesostructure, the pore diameter and the particle morphology was investigated by experiments with different combinations of the SDAs. The sample synthesised via the sol-gel procedure without the addition of any SDA and the sample synthesised with CTAB exhibited only a poor ordering of pores as one could observe in the XRD patterns. Samples synthesised via the sol-gel reaction usually show a poor or even no ordering of the pores. The missing structure of the material synthesised with CTAB can be explained by the low CTAB concentration which normally acts as a co-surfactant in this synthesis. The sample synthesised without CTAB but with P123 as SDA exhibited a well-defined 2d hexagonal mesostructure ( $p6mm$ ) in contrast to the sample synthesised with both SDAs. The nitrogen physisorption measurements confirmed the structural differences. The sample synthesised without SDAs and the sample with CTAB showed isotherms typical for samples synthesised via the sol-gel procedure. The resulting pore size distributions were very broad. The sample synthesised with P123 as SDA shows a typical type IV isotherms and a H1 hysteresis loop which proved the cylindrical pore geometry. The resulting pore diameter was 6.8 nm which is more than 1 nm wider than the pore diameter of the sample synthesised with both SDAs. This effect was noticed by other groups before.<sup>[151-154]</sup> For nitrogen physisorption data see Appendix A.V.5.

The morphology of the samples depends on the addition of the co-surfactant to a high extent. Only the sample synthesised with both SDAs showed the required spherical morphology (see Figure 3.42 a – d). No clear explanation for the correlation between the spherical morphology and the co-surfactant has been given up to now but similar results were observed by other groups as well.<sup>[89,108]</sup>

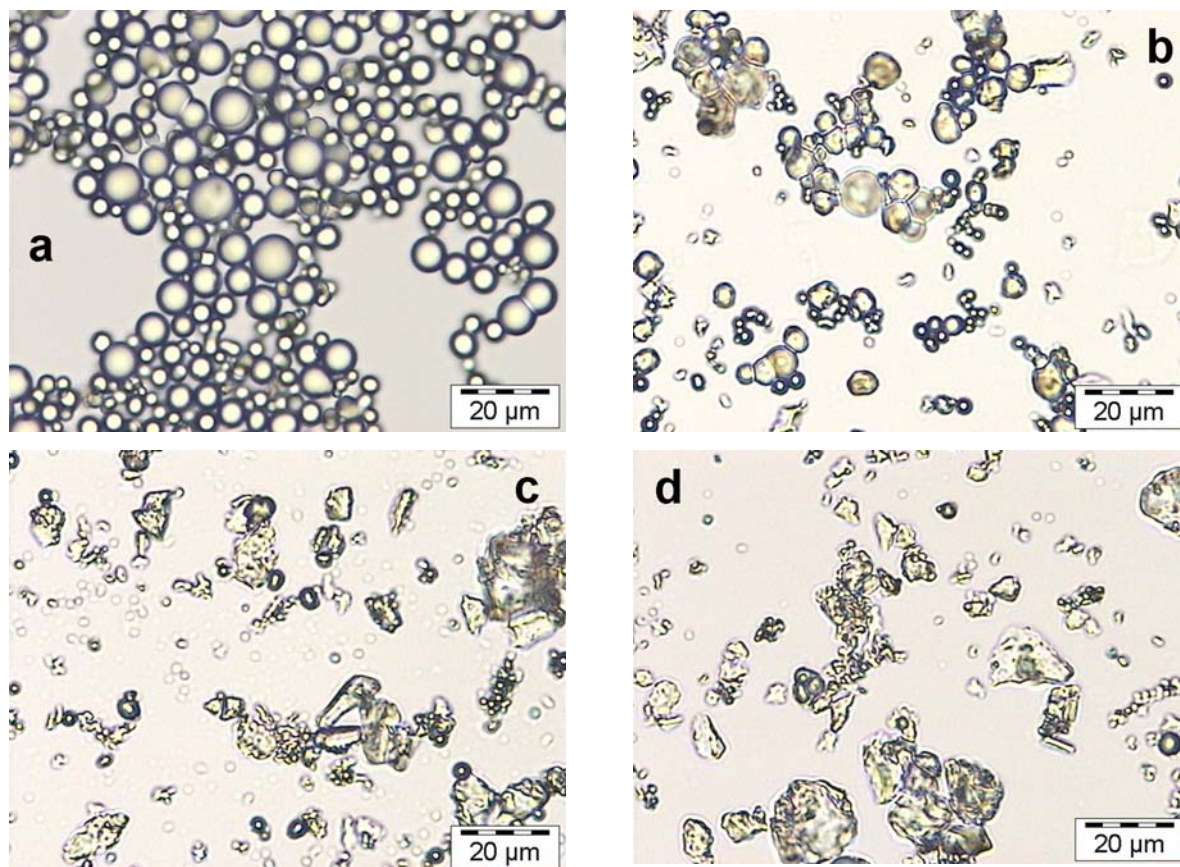


**Figure 3.42 a – d:** Optical microscopic images of the phenylene-bridged samples synthesised with different SDA contents (molar ratios: see Table A.V.5): P123 + CTAB (a); P123 (b); CTAB (c) and without SDAs (d).

### 3.4.3 Conclusion

In summary, phenylene-bridged PMO spheres in the size range between 5 and 10  $\mu\text{m}$  were obtained by applying a modified method first introduced by Ma et al.<sup>[108]</sup> for the synthesis of spherical SBA-15 silica particles. This synthesis includes the addition of a co-solvent (in this case ethanol) and a co-surfactant (CTAB) additional to the triblock copolymer that was used as SDA. As described by Ma et al. the morphology is influenced by the co-surfactant concentration, the co-solvent concentration and the two-step hydrothermal treatment. Similar observations were made for the synthesis of phenylene-bridged PMO particles in the size range of 5 to 10  $\mu\text{m}$ . The investigations concerning the hydrothermal treatment showed that a heating of the solution is necessary. Otherwise no solid occurred during the experiment. Spherical particles were obtained after heating the solution up to 80  $^{\circ}\text{C}$ . But the degree of condensation in this material is quite low which can be proved by nitrogen physisorption. The

specific surface area ( $813 \text{ m}^2/\text{g}$ ) and the pore diameter (3 nm) are significantly lower compared to the sample heated up to  $130^\circ\text{C}$  after the first heating step. A direct increase of the temperature to  $130^\circ\text{C}$  led to many irregular shaped particles additional to the spheres.

The particle size could be influenced by the variation of the pH value of the solution. An increase of the pH value led also to an increase of the particle diameter as already observed for the synthesis of large spheres described in chapter 3.3. As described above, this can be explained by the reduced reaction velocity with increasing pH value in the range between zero and six.

The variation of the ethanol concentration led to similar results compared to the studies of Ma et al.<sup>[108]</sup> The morphology is influenced by the addition of ethanol to a high extent. Perfectly shaped spheres were obtained in a relatively broad range of concentration but samples synthesised without ethanol showed lots of irregular shaped particles. The function of the co-solvent has been discussed in chapter 3.3.

The last quite interesting synthesis parameter was the mixture of two SDAs. In this case P123 acted as SDA and CTAB was added as a co-surfactant. As one can conclude from the results shown above the addition of CTAB is necessary for the formation of spherical particles. No explanation for this effect is given anywhere in the literature. This is the reason why only an assumption concerning the function of the co-surfactant could be made. As described by Lin et al. the addition of a co-solvent to the reaction solution leads to shorter self-assembled micelles and thus, to a decrease of long-range order in the mesoporous material.<sup>[145]</sup> The sample synthesised without CTAB but with ethanol as a co-solvent revealed a well ordered 2d hexagonal mesostructure (space group:  $p6mm$ ). The addition of ethanol did not lead to the missing long-range order that was expected. The long-range order decreased with the addition of CTAB to the solution. Thus, the formation of the micelles is influenced so that no long rodshaped micelles occur. But as shown by the experiments the formation of monodisperse mesoporous phenylene-bridged spheres is a complex mechanism in which the co-surfactant, the co-solvent, the synthesis temperature and the pH value of the solution are involved. Thus, a detailed description concerning this mechanism is not possible at the moment.

From the syntheses described in chapter 3.2 – 3.4 one can see that there are many different possibilities to synthesise spherical particles. Different pH values were chosen and spherical particles were obtained under mild basic conditions (modified Stöber PMO synthesis), under mild acidic conditions (modified Kosuge PMO synthesis) and under heavy acidic conditions at pH values around zero (modified Ma PMO synthesis). Thus, the formation of spheres is not

limited to the basic pH value region as one would expect from the reactivity of the single silicon atoms during the condensation reactions. In all three cases a co-solvent was added to the reaction solution which was in all cases necessary to obtain spherical particles. Syntheses without the addition of ethanol led to irregular shaped particles in all applied synthesis procedures. Therefore, one could assume that the addition of an alcohol as a co-solvent plays an important role for the formation of spherical particles. But one interesting publication showed that the synthesis of spherical PMO particles is also possible without the addition of any co-solvent. This reaction takes place under basic conditions obtained by the addition of NaOH with CTAB as surfactant and BTME as organosilica precursor. The hydrothermal treatment via microwave heating was hold to be responsible for the spherical shape by the authors.<sup>[118]</sup>

In all three described syntheses pathways the careful adjustment of the pH value seems to be important for the successful synthesis of spherical particles.

The necessity of a hydrothermal treatment procedure depends on the pH value of the reaction solution. In pH value region where the condensation reactions are quite fast a hydrothermal treatment is not necessary while under extreme acidic or basic conditions (around zero and above twelve) higher temperatures are needed to obtain any solid. As shown by Kim et al. as well as in chapter 3.4 the temperature of this hydrothermal treatment step influences the particle morphology as well. Temperatures above 130 °C favour the formation of irregular shaped particles.

As shown in by the syntheses procedures described in chapter 3.2 – 3.4 different structure-directing agents could be applied for the synthesis of spherical particles. Alkyltrialkylammonium surfactants as well as long chain amines or non-ionic block copolymers were chosen to obtain porous materials.

From all these experiments concerning the synthesis of spherical shaped particles one can conclude that independent of the pH value and the structure-directing agent the synthesis parameters have to be adjusted carefully because, as shown above, spherical particles are obtained in a small range of synthesis conditions. In most cases variation of synthesis parameters led to materials containing lots of irregular shaped particles.

## 4 Formation mechanism studies

### 4.1 *In situ* small angle X-ray scattering (SAXS) experiments

Since the introduction of the highly ordered mesoporous silica materials in 1992 much effort was spent in data acquisition during the synthesis procedure of the different structured materials additional to the characterisation of the resulting solids. As described above the formation process of these mesoporous materials is based on a cooperative mechanism which is mostly determined by interactions between the headgroup of the surfactant and the respective silica species of different degrees of polymerisation at the surfactant/silica interface. Monnier et al. suggested that the key factors for the formation of the mesophase are multidentate binding of silicate oligomers to the cationic surfactant headgroup, preferred polymerisation of silica at the silica/surfactant interface, and charge density matching between the surfactant and the silica.<sup>[11]</sup> That means the charge density of the silica walls guides the size of the headgroup area  $a_0$ . At early stages of the synthesis, the presence of small highly charged silica oligomers favours a small value of  $a_0$ . This can be achieved by a lamellar packing of the micelles. With proceeding rearrangement and polymerisation of the silica species the density of anionic silanol groups diminishes and the headgroup area increases while the number of compensating cations decreases, which can lead to a phase transition from a low to a higher curved surface. Thus, the evolution of the mesostructure during the synthesis that implies stirring of the reaction solution containing the SDA and a silica source in aqueous solution in basic or acidic medium and a hydrothermal treatment, were of great interest. *In situ* X-ray diffraction offers the possibility of observing the evolution of the single reflections during the complete formation process. In most cases synchrotron radiation was used because of the low scattering rates of the reactions solutions and the higher energy of the synchrotron radiation which offers significantly shorter measuring times.

Various *in situ* small angle X-ray scattering (SAXS) investigations have been carried on the system consisting of alkyltrialkylammonium surfactants and a silica source (mostly TEOS) under basic conditions. First data of *in situ* experiments were published by Regev.<sup>[155]</sup> The MCM-41 silica material was synthesised in an open vessel. Three different samples were taken from the vessel: the first before the addition of the silica source, the second after 3 minutes and the last after 15 minutes. X-ray diffraction patterns of these three samples as well as of the calcined solid were measured in a glass capillary. The sample without TEOS showed a broad reflection while the addition of TEOS led to the growth of the 2d hexagonal

mesophase. Similar observations were made by Lindén et al. by using a tubular reactor setup for their experiments.<sup>[156]</sup> Further investigations with the addition of hexanol or butanol as co-surfactants were also carried out.<sup>[157]</sup> The addition of hexanol led to the coexistence of different mesophases. Dependent on the amount of co-surfactant a 2d hexagonal and a swollen 2d hexagonal (space group:  $p6mm$ ) or a swollen 2d hexagonal (space group:  $p6mm$ ; with higher d-spacings compared to the original 2d hexagonal structure) and a lamellar phase ( $p2$ ) could be observed. An extensive study concerning the influence of the surfactant chain length and the surfactant concentration was conducted by O'Brien et al.<sup>[158]</sup> A phase transition from a 2d hexagonal to a lamellar phase could be shown by decreasing the surfactant concentration and heating up the reaction solution. The influence of the addition of *n*-hexane and toluene to a solution containing CTAB as SDA and TEOS as organosilica source was studied by Lindén et al.<sup>[159]</sup> The addition of different amounts of *n*-hexane to the typical MCM-41 synthesis route led to a 2d hexagonal and a swollen 2d hexagonal structure. With increasing *n*-hexane concentration the intensities of the 2d hexagonal structure decreased while the intensities of the swollen structure increased. In contrast, the addition of toluene led only to one hexagonal phase which showed also a kind of swelling but without the evolution of another phase. Further investigations about the influence of co-surfactants were carried out by the addition of short chain amines like *n*-butylamine and *n*-octylamine.<sup>[160]</sup> The addition of *n*-butylamine led to a contraction of the structure while the addition of *n*-octylamine showed a swelling. Gross et al. presented an extensive study concerning the influence of the pH value (9 – 11) in the reaction solution and the condensation degree on the transition from a 2d hexagonal to a lamellar phase.<sup>[161-163]</sup> A lower pH value of the solution favoured silica condensation and inhibited the transition from a 2d hexagonal to a lamellar phase while a pH value around 11 led to a transition from the 2d hexagonal to the lamellar phase during the heating step. *In situ* SAXS investigations of the formation of the bicontinuous cubic phase were first carried out by Penvzner and Regev.<sup>[164]</sup> The first observation at the real beginning was a phase transition from 2d hexagonal ( $p6mm$ ) to lamellar ( $p2$ ). With increasing temperature a retransformation from lamellar to hexagonal occurred. With further increase of the temperature the bicontinuous cubic phase appeared (space group:  $la\bar{3}d$ ). The phase transition from 2d hexagonal ( $p6mm$ ) to cubic ( $la\bar{3}d$ ) without the appearance of a lamellar phase was observed by Landry et al.<sup>[165]</sup> The experiments were carried out under basic conditions at temperatures above 100 °C and with the addition of different fluorides as catalysts. In 2002, Lind et al. conducted SAXS experiments with fatty acids (hexanoic, octanoic, decanoic, dodecanoic and tetradecanoic acid) as co-surfactants under basic synthesis

conditions.<sup>[166]</sup> An increase of the co-surfactant concentration caused a transition from a 2d hexagonal ( $p6mm$ ) to a lamellar ( $p2$ ) phase. First experiments under acidic conditions were carried out by Tiemann et al.<sup>[167]</sup> The influence of benzene as swelling agent on mesostructure formation from the reaction solution containing CTAB and TEOS under basic conditions was studied. The authors could show that an increasing amount of benzene in the reaction solution initiated a formation of a lamellar phase additional to the original 2d hexagonal phase of the MCM-41.

Only few but very detailed results have been published concerning the formation mechanism of mesoporous silica materials with triblock copolymers as SDAs with the formula  $\text{PEO}_x\text{PPO}_y\text{PEO}_x$  (e.g. Pluronic<sup>®</sup> P123:  $\text{PEO}_{20}\text{PPO}_{70}\text{PEO}_{20}$ ). The PEO and the PPO units are coiled and the PEO units form the hydrophilic shell of the micelle while the PPO units represent the hydrophobic core as illustrated in Figure 4.1.

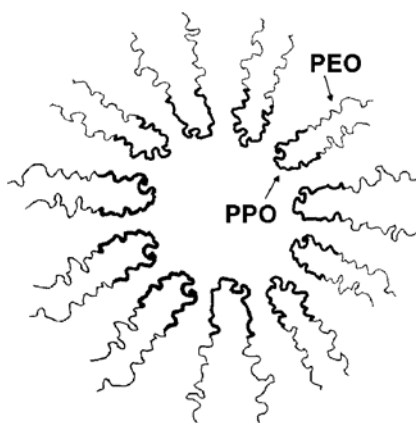


**Figure 4.1:** Schematic illustration of a triblock copolymer (consisting of  $\text{PEO}_x\text{PPO}_y\text{PEO}_x$ ) micelle.

The silica condenses around the micelles and parts of the PEO chains are protruding into the silica network. This is the reason for the different silica densities of these materials. Impérator-Clerc et al. first published SAXS investigations of the mesoporous SBA-15 silica.<sup>[168]</sup> As a result from the analysis of the intensities of the single reflections different structural models of the hexagonal unit cell were introduced. The form factor, which is the Fourier transform of the electron density distribution in the unit cell, was calculated with different models of the unit cell. The best agreement of the experiments and the calculations were obtained for the model of the calcined sample with empty pores. A linear increase of the electron density from the microporous region to the region of the dense silica matrix was assumed. The micropores

are a result of PEO chains from the shell of the micelles embedded into the silica matrix. Based on these results Flodström et al. calculated electron density maps for the SBA-15 silica at different stages of the reaction measured with *in situ* SAXS in a flow-through capillary.<sup>[121]</sup> Similar results were also obtained by Khodakov et al.<sup>[169]</sup> The influence of the PEO chain length on the resulting structure of the mesoporous material was investigated by Kipkemboi et al.<sup>[170]</sup> Different PEO chain lengths were tested (4, 17, 27, 37 and 132 PEO units while the number of PPO units was kept constant at 57). The solubility of these triblock copolymers depends on the one hand on the PEO/PPO ratio due to the hydrophilic character of the PEO units and the hydrophobic character of the PPO units. Thus, triblock copolymers containing short PEO chains are hardly soluble in water. On the other hand, the solubility in water is determined by the temperature dependence of the hydrophilicity of the PEO blocks in the triblock copolymer. The conformation of an EO group which is gauche around the C-C bond and anti around the C-O bond (a-g-a) has the lowest energy of all conformers and a large dipole moment and is dominant at low temperatures. With increasing temperature other conformations with lower or no dipole moment more like the anti-anti-anti (a-a-a) conformation become more dominant (see Figure 4.2). Thus, the solubility of the PEO chains decreases and the hydrophobic core increases.

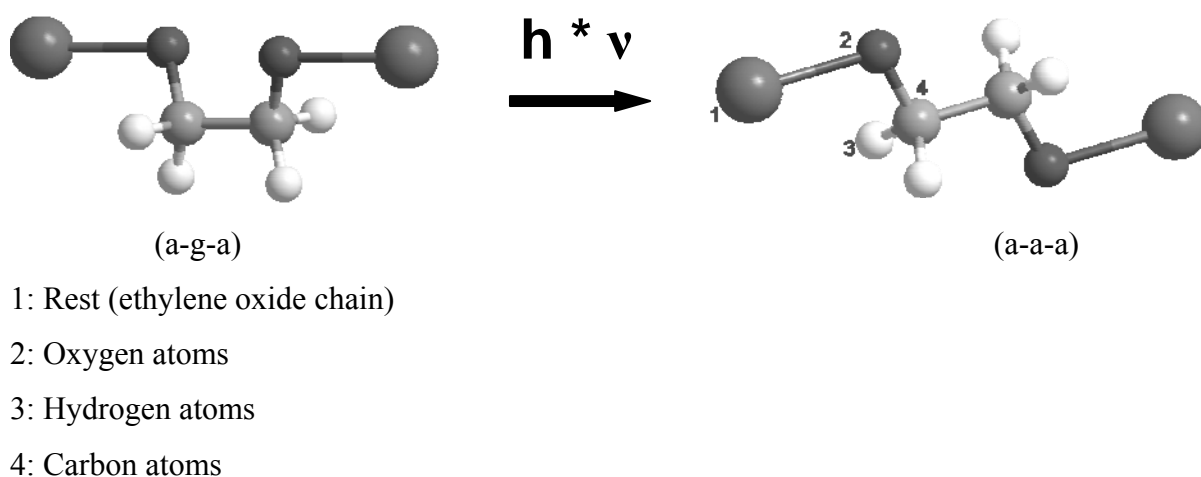


**Figure 4.2:** Change of the conformation in the PEO chain from gauche (mostly present at low temperatures) to anti (dominating at high temperatures).<sup>[171]</sup>

Because of the low solubility in water the temperature of the reaction mixture containing PEO<sub>4</sub>PPO<sub>57</sub>PEO<sub>4</sub> had to be kept below 10 °C. The resulting mesostructure was lamellar. An increase of PEO units to 17 showed the evolution of a 2d hexagonal phase. With increasing temperature a second phase occurred consisting of multi lamellar vesicles due to the more

hydrophobic character of the SDA at higher temperatures. The application of PEO chain lengths of 27 and 37 units led to high ordered 2d hexagonal phases; an increase of the temperature did not influence the formation of the structure in both cases. The 132-unit PEO block led to the formation of a cubic phase (space group:  $Im\bar{3}m$ ) due to the large parts of hydrophilic chains in the SDA. The formation of a cubic structure ( $Im\bar{3}m$ ) was also described by Flodström et al.<sup>[172]</sup> This group was also able to obtain a bicontinuous cubic phase (space group:  $Ia\bar{3}d$ ) by the application of Pluronic<sup>®</sup> P103 (PEO<sub>17</sub>PPO<sub>59</sub>PEO<sub>17</sub>) as SDA with sodium iodide as a catalyst. Although many *in situ* SAXS investigations were carried out on the mesoporous systems of acidic and basic synthesis pathways no data concerning the evolution of different mesophases for the synthesis of periodic mesoporous organosilicas have been carried out up to now. One publication about periodic mesoporous organosilicas dealing with studies of the evolution of the mesophase reflection and the evolution of the reflections caused by the periodicity of the organic moiety on molecular scale was published up to now.<sup>[37]</sup>

## 4.2 Experimental

### 4.2.1 Synthesis of 2d hexagonal ordered phenylene-bridged PMOs

#### 4.2.1.1 Structure-directing agent: Pluronic<sup>®</sup> P123<sup>[53]</sup>

Samples measured at the beamline were prepared by dissolving P123 in 0.1 m hydrochloric acid. After complete solution of the SDA the temperature was increased to 40 °C and the solution was transferred into the four neck vessel which was the reaction vessel for the SAXS experiments. Then the organosilica precursor 1,4-bis(triethoxysilyl)benzene (BTEB) was added to the solution under vigorous stirring and the complete solution was pumped through tubings and the capillary which was placed in the synchrotron beam (for experimental setup see chapter 2.12). The data acquisition started two minutes after the addition of the organosilica precursor. The molar concentrations are listed in Table 4.1.

**Table 4.1:** Molar ratios of the phenylene-bridged PMOs synthesised with P123 as SDA.<sup>[53]</sup>

BTEB [mol]	Pluronic <sup>®</sup> P123 [mol]	HCl [mol]	H <sub>2</sub> O [mol]
0.5	0.035	0.071	395.6

Eight samples were synthesised in the laboratory in order to investigate the final products. The first four samples were stirred for different times (90, 180, 360 and 540 min), filtered off and dried in vacuum. The other four samples were stirred for 2 hours (2 samples) and for 24 hours (2 samples). Two of these samples (2 and 24-hour stirring step) were filtered off and dried in vacuum; the other two samples were treated at 105 °C under autogeneous pressure for 24 hours. Removal of the surfactant was accomplished as described in chapter 3.1.1. The molar ratios and the treatment of the samples are listed in Appendix A.VI.1. XRD patterns were recorded of these materials in order to compare the samples synthesised at the beamline and in the laboratory.

#### 4.2.1.2 Structure-directing agent: Brij<sup>®</sup> 76<sup>[61]</sup>

For the synthesis of hexagonal ordered phenylene-bridged PMOs with small pore diameters Brij<sup>®</sup> 76 was dissolved in 0.1 m HCl at a temperature of 50 °C. After a clear solution was obtained the reaction solution was transferred into the four neck vessel. The organosilica precursor BTEB was added under vigorous stirring and the data acquisition started two minutes after the addition of BTEB. The molar ratios are listed in Table 4.2.

**Table 4.2:** Molar ratios of the phenylene-bridged PMOs synthesised with Brij<sup>®</sup> 76 as SDA.<sup>[61]</sup>

BTEB [mol]	Brij <sup>®</sup> 76 [mol]	HCl [mol]	H <sub>2</sub> O [mol]
0.5	0.082	0.33	184.84

Similar as described above, eight further samples were prepared in the laboratory. The first four samples were synthesised with different stirring times (120, 240, 455 and 550 min) before filtering off and drying in vacuum. The other four samples were stirred for 2 hours (2 samples) and 24 hours (2 samples). The further treatment was the same as described above (chapter 4.2.1.1). The complete data is listed in Appendix A.VI.2.

### 4.3 Results and discussion

#### 4.3.1 Phenylene-bridged PMOs with Pluronic® P123 as SDA

The powder X-ray diffraction patterns of the samples synthesised in the laboratory with different stirring times without hydrothermal treatment all show a shoulder in the primary beam (see Figure 4.3 a). These results confirm the formation process of the mesophase to be started during the aging procedure. High d-spacings due to the low degree of condensation of the organosilica species were observed. Only the samples treated at 105 °C for 24 hours reveal a well ordered hexagonal arrangement of pores as it can be seen from Figure 4.3 b. The three reflections can be indexed to the 100, 110 and 200 reflection of the 2d hexagonal mesostructure (space group:  $p6mm$ ).

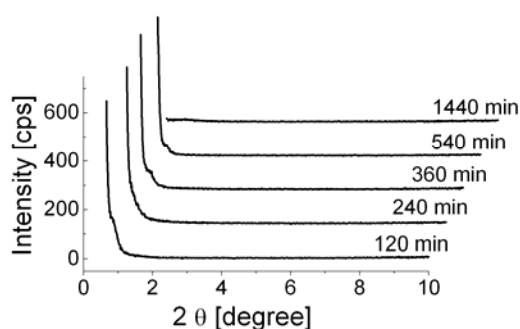


**Figure 4.3 a:** P-XRD investigations of samples stirred for different periods of time.

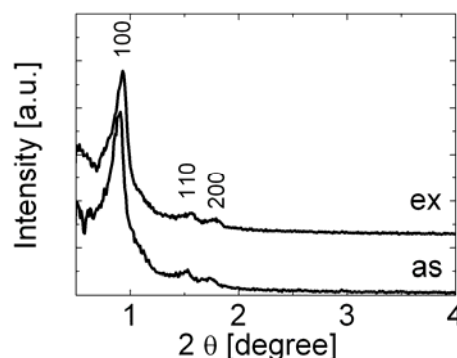


**Figure 4.3 b:** P-XRD patterns of the sample stirred for 2 hours at RT and treated for 24 hours at 105 °C: as synthesised (as) and extracted (ex).

After about 20 minutes stirring at RT the solution turned slightly turbid and after about 30 minutes solid particles could be observed in the solution. Thus, this reaction offers the opportunity of being investigated by *in situ* SAXS experiments. The only difference to the synthesis in the laboratory was the pumping of the solution through a capillary which was placed in the synchrotron beam. The first sample was stirred at a constant temperature of 40 °C. Each measurement took three minutes. A break of one second between each measurement was inserted. The measurement started almost two minutes after the addition of BTEB. The evolution of the SAXS patterns measured at a constant temperature are shown in Figure 4.4 a and b.

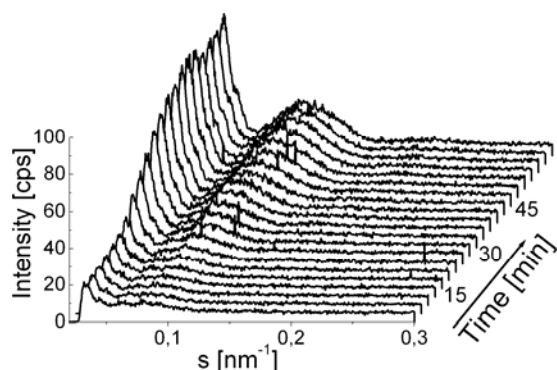


**Figure 4.4 a:** Evolution of the SAXS patterns of the sample containing P123 as SDA at 40 °C (0-60 min).

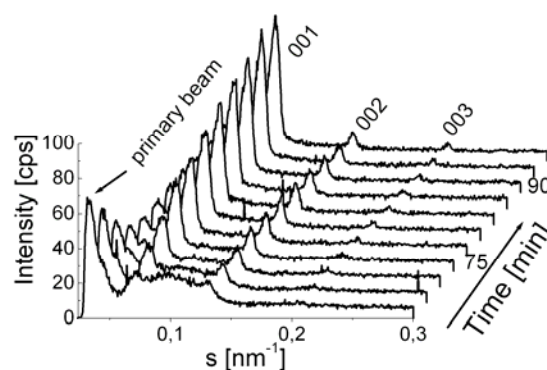


**Figure 4.4 b:** Evolution of the SAXS patterns (63-93 min).

The relatively high background noise can be explained by the low scattering rate of the solution. With increasing amount of precipitation the scattering rate was increasing as well. During the first 45 minutes of the measurement one broad reflection peak arose with a d-spacing of 15.3 nm ( $s = 0.095 \text{ nm}^{-1}$ ) and the intensity was increasing with on-going reaction. The increase of the first broad reflection could be attributed to an increase of the electron density contrast caused by the adsorption of silicate species to the protonated PEO groups of the triblock copolymer and the increasing particle sizes as it is described by Flodström et al.<sup>[121]</sup> After 60 minutes reaction time two reflections arose from the broad one (d-spacings: 13.16 nm and 7.25 nm) combined with the growth of a third reflection with a d-spacing of 4.6 nm. These three reflections could be indexed to the 001, 002 and 003 reflection of a lamellar mesophase (space group:  $p2$ ). The reaction was interrupted after 90 minutes reaction time.

The SAXS patterns of the samples synthesised with the same concentrations but with increasing temperature during the SAXS experiment are depicted in Figure 4.5. The first patterns up to 24 minutes showed the same broad reflection as described above for the samples synthesised at a constant temperature of 40 °C. In this case the broad hump is ascribed to single micelles as well. The heated sample showed precipitation almost after 6 minutes due to the high temperature and the resulting higher reaction speed. After 24 minutes a 2d hexagonal mesophase developed. The d-spacings of the hexagonal phase are  $d_{100} = 14.08 \text{ nm}$ ,  $d_{110} = 8.12 \text{ nm}$  and  $d_{200} = 7.04 \text{ nm}$ . The decreasing intensities of all reflections after 33 minutes were caused by the irregular flow which was a result of the faster growing particles at higher temperatures.

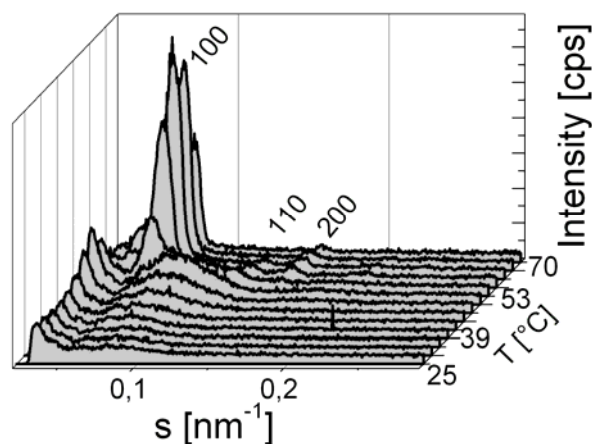


**Figure 4.5:** Evolution of the SAXS patterns of the sample containing P123 as SDA measured at increasing temperature up to 70 °C (Measurement time: about 40 minutes).

A possible explanation for the different evolution of the SAXS patterns of the phenylene-bridged PMO sample depending on the temperature is given in the following part.

Regarding the evolution of the first patterns in both, the temperature- and the time-dependent measurement one can observe similarities during the initiation of the mesophase. Both patterns show one broad reflection with three reflections arising from the broad one. The differences of the intensities are due to the lower scattering of the heated sample caused by a lower condensation degree after 6 minutes reaction time.

In Figure 4.6 the diffraction patterns with the best structure concerning each measurement are depicted. The pattern of the sample measured at the constant temperature was obtained after 90 minutes (a). Three clear reflection peaks could be observed. The d-spacings are 13.16 nm, 7.25 nm and 4.61 nm. The three d-spacings do not fit perfectly to a lamellar phase. The diffraction pattern b in Figure 4.8 shows the sample synthesised at increasing temperature after a reaction time of 30 minutes. In this pattern three resolved reflection peaks could be observed. The d-spacings 14.08 nm, 7.87 nm and 6.49 nm can be indexed to the 100, 110 and 200 reflection of the 2d hexagonal mesophase.

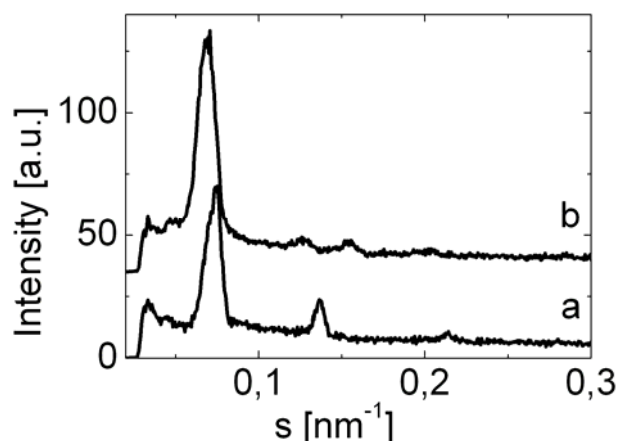


**Figure 4.6:** Diffraction patterns of the sample at a constant temperature of 40 °C after 90 minutes (a) and of the sample measured with increasing temperature after 30 minutes (b).

The evolution of the d-spacings during both measurements is depicted in Figure 4.7 a and b.

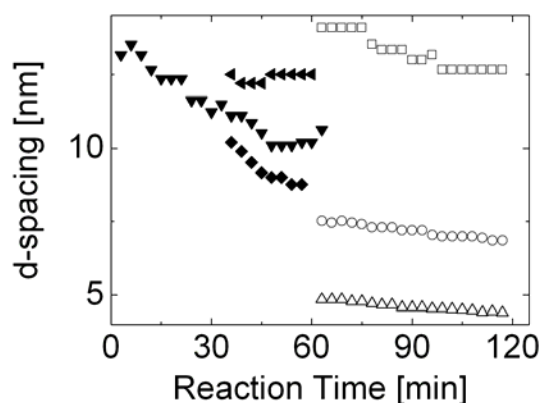


**Figure 4.7 a:** Evolution of the d-spacings of the reflections of the sample synthesised at a constant temperature of 40 °C during a continuous running experiment.

(■: first reflection from the broad one, ●: second reflection from the broad one, ▲: third reflection from the broad one, ▼: 001, ◆: 002, ◄: 003)

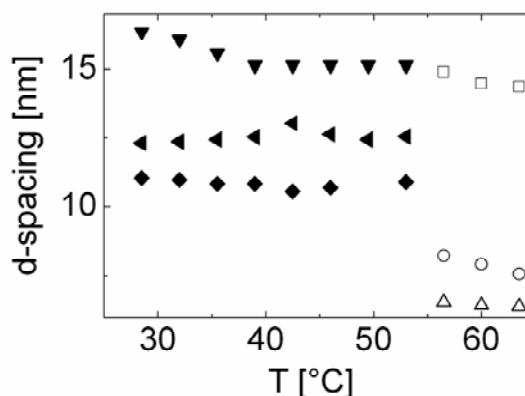


**Figure 4.7 b:** Evolution of the d-spacings of the reflections of the samples synthesised at increasing temperature during a continuous running experiment.

(■: first reflection from the broad one, ●: second reflection from the broad one, ▲: third reflection from the broad one, ▼: 100, ◆: 110, ◄: 200)

An interesting observation which could be made from Figure 4.7 a and b is the similarity of the evolution of the d-spacings during the first part of the reaction. The evolution of the first three reflections (◆, ▼ and ◄ three small reflection arising from the broad one right at the

beginning of the experiment) was nearly the same. From that point where the first three reflections disappeared the formation of the structure differs dependent on the synthesis temperature. From Figure 4.7 a and b it could be concluded that both experiments were not over at the time they were interrupted. The values of the d-spacings of the respective reflections ( $\circ$ ,  $\square$  and  $\Delta$ ) did not remain constant at the end of the experiment. The lamellar phase is a transition state in the synthesis of the 2d hexagonal phenylene-bridged PMO material synthesised with P123 as SDA. The lamellar transition state during the formation of the 2d hexagonal mesophase is a logical possibility for the micellar evolution. Due to the charge density matching theory the surface with the highest charge density reveals a low surface curvature, which means a lamellar arrangement of the liquid crystalline phase in this case (packing parameter  $g \approx 1$ ). With increasing condensation of the organosilica species the charge density is reduced and thus, the curvature of the micelles increased due to an increase of the effective headgroup area  $a_0$  (see chapter 4.1). A transition from a lamellar to a 2d hexagonal phase (packing parameter  $g \approx \frac{1}{2}$ ) occurred as it was already published by Monnier et al.<sup>[11]</sup> for the synthesis of the mesoporous silica materials.

For a comparison between the sample measured at the beamline and the samples synthesised in the laboratory the mixture investigated during the SAXS experiment with the constant temperature was filtered off and washed with water. A powder X-ray diffraction was measured in the laboratory as well as from the extracted product. This data was compared to the samples synthesised in the laboratory.

All XRD patterns of the samples synthesised in the laboratory and the samples measured at the beamline showed only one reflection. No lamellar structure could be observed as it was expected from the SAXS measurements. The reason for the low order of the dry materials is the incomplete condensation of the samples after such short reaction times. During the SAXS investigations the scattering of the liquid crystals formed by the triblock copolymer as well as the partly condensed silica species was measured because the complete solution was pumped through the capillary. After filtering off the solution at the initial state of the formation only a very low amount of solid was in the mixture. The SDA was partly removed by the washing procedure. The structure collapsed because of the low degree of condensation in this reaction stadium. Thus, no definite mesostructure could be seen in the XRD patterns of the dry materials.

The optimal synthesis conditions of the phenylene-bridged PMO material were a stirring time of at least 2 hours at 40 °C and a 24-hour hydrothermal treatment at 95 °C in order to obtain a material with a 2d hexagonal pore arrangement. But from the SAXS experiments shown

above the occurring of a lamellar transition state during the formation of the 2d hexagonal structure could be evidenced. Thus, the formation follows the pathway that was already shown by Monnier et al.<sup>[11]</sup>

As described in chapter 4.1 similar experiments were carried out by Flodstöm et al. concerning the synthesis of the SBA-15 silica.<sup>[121]</sup> The temperature was set to 35 °C and the evolution of the SAXS patterns showed a 2d hexagonal mesophase after a certain period of time. Similar to the results described for the phenylene-bridged material a broad reflection could be observed at the beginning of the experiment which was attributed to appearance of single micelles by the authors. The first sharp reflection they observed was the 110 followed by the 100 and the 210. The 200 reflection evolved later. The evolution of the reflections in the experiments described above was completely different and showed the typical reflections for a lamellar phase. Thus, the influence of the organic moiety in the organosilica precursor is of great importance for the formation of the mesophase and its transition states.

#### 4.3.2 Phenylene-bridged PMOs with Brij<sup>®</sup> 76 as SDA

The powder X-ray diffraction patterns of the samples synthesised with different stirring times but without subsequent hydrothermal treatment are depicted in Figure 4.8 a. All samples were washed with water. An additional 24-hour hydrothermal treatment at 105 °C led to a highly ordered 2d hexagonal material as it can be seen from Figure 4.8 b. All samples synthesised without a hydrothermal treatment show one reflection in the XRD pattern with a d-spacing of 5.5 nm. The d-spacing of the 100 reflection of the hydrothermal treated sample shows a slightly smaller value (5.2 nm). The contraction of the mesostructure caused by the hydrothermal treatment is quite low in this case.

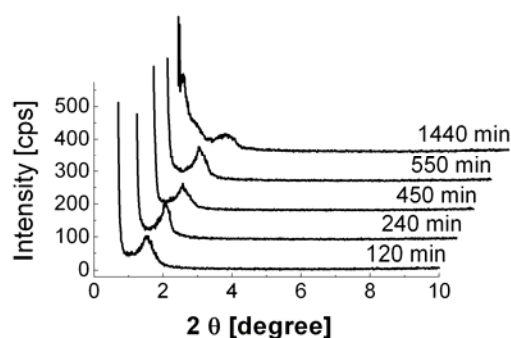


**Figure 4.8 a:** P-XRD patterns of samples synthesised with different stirring times at a constant temperature of 50 °C.

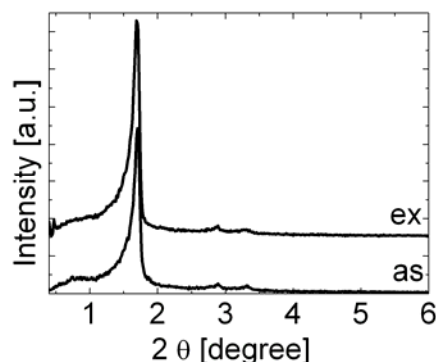


**Figure 4.8 b:** P-XRD patterns of a sample synthesised with 120 minutes stirring time and a 24 hour hydrothermal treatment at 105 °C.

In order to obtain more information about the evolution of the reflections during the synthesis procedure this reaction solution was investigated by SAXS experiments at the beamline A2 (HASYLAB@Desy, Hamburg, Germany). The evolution of the SAXS patterns of the sample containing Brij<sup>®</sup> 76 as SDA and BTEB as organosilica precursor measured at a constant temperature of 50 °C is depicted in Figure 4.9 a the last three diffraction patterns are shown in Figure 4.9 b. An increase of the temperature up to 105 °C was not possible due to the fast reaction and the large particles occurring in the solution within the first minutes.

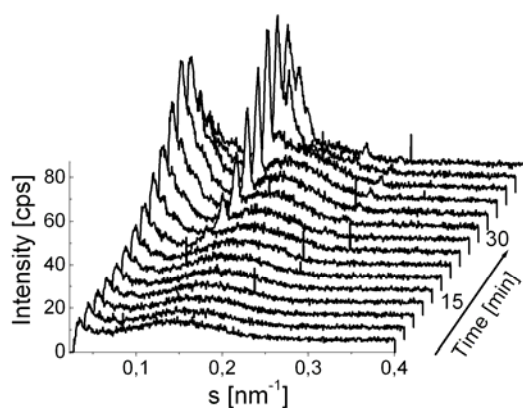


**Figure 4.9 a:** Evolution of the SAXS patterns of a sample containing Brij<sup>®</sup> 76 as SDA measured at 50 °C.

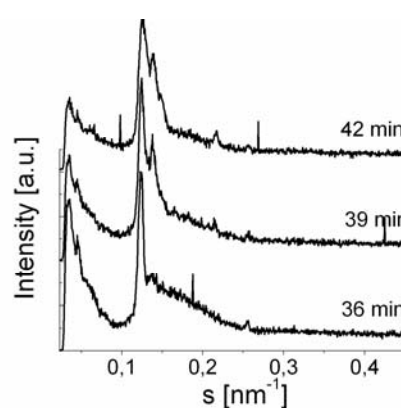


**Figure 4.9 b:** SAXS patterns measured after 36, 39 and 42 minutes.

Brij<sup>®</sup> 76 consists of an octadecyl chain and 10 ethylene oxide units. The EO units that are a little more hydrophilic than the alkyl chain form the headgroup of the surfactant. The chain of

EO units is coiled as it is described for the triblock copolymer P123. The octadecyl chain is the hydrophobic part and therefore the tail of the surfactant. D-spacings below the values measured with P123 as SDA were expected due to the smaller SDA molecules. The temperature of 50 °C was necessary due to the low solubility of the surfactant in hydrochloric acid of the applied concentration.

During the first 7 measurements only a broad hump was detected in the patterns. The intensity was increasing until one sharp reflection evolved from the broad hump after 21 minutes. The d-spacing was 7.88 nm. With proceeding time the intensity of this reflection increased. After 39 minutes another reflection with a d-spacing of 7.25 nm evolved from the hump. The last pattern showed five reflections with the following d-spacings: 1.) 7.8 nm, 2.) 7.2 nm, 3.) 6.8 nm, 4.) 4.57 nm, 5.) 3.89 nm.

In this case it is a lot more complicated to give clear information about the transition states of this material. The d-spacings 1, 4 and 5 can be indexed to a 2d hexagonal mesophase which was expected from the laboratory synthesis. Thus, a mixture of two or more different mesostructures occurred during this experiment. A second possibility is the co-existence of a 3d hexagonal phase (space group:  $P6_3/mmc$ ) and a 2d hexagonal mesophase (space group:  $p6mm$ ). The unit cell parameters were  $a = 9.00$  nm and  $c$  (for the 3d hexagonal structure) = 14.47. The resulting ratio  $c/a$  is 1.61. The ideal  $c/a$  ratio for a typical hexagonal close packed phase (hcp) is 1.633. In this case the reflections can be indexed as listed in Table 4.3.

**Table 4.3:** d-spacings of the single reflections indexed for the 2d hexagonal and the 3d hexagonal mesostructure.

	$d_{100}$	$d_{002}$	$d_{101}$	$d_{110}$	$d_{200}$	$a^*$	$c^*$
	[nm]	[nm]	[nm]	[nm]	[nm]	[nm]	[nm]
2d hexagonal ( $p6mm$ )	7.8	-	-	4.57	3.89	9.00	0
3d hexagonal ( $P6_3/mmc$ )	7.8	7.2	6.8	4.57	-	9.00	14.47

$$* a = \frac{2}{3} * \sqrt{3} * d_{100}, c \text{ can be calculated from: } \sin^2 \theta = \frac{\lambda^2}{4a^2} \left[ \frac{4}{3} (h^2 + k^2 + hk) + \left( \frac{a}{c} \right)^2 l^2 \right]^{[173]}$$

The reflections observed in the last three patterns led to the assumption that both hexagonal mesophases coexist. It is not possible to give further evidence for this thesis because the

transition state appears only during the aging step and an isolation of the material was not possible because of the low degree of condensation of the organosilica oligomers. Most of the precipitation was dissolved after filtering off and washing with water. Thus, electron diffraction which would be necessary to prove the appearance of the 3d hexagonal structure of the product could not be carried out. But the possibility of a 3d hexagonal transition state during the formation of the 2d hexagonal mesophase is probable due to the applied surfactant. The synthesis of the 3d hexagonal ordered SBA-12 was carried out with Brij<sup>®</sup> 76 as SDA as well.<sup>[174]</sup> The formation of the 3d hexagonal structure was also observed for the SBA-2 which is synthesised with gemini surfactants of the formula  $C_{n-s-1}$ .<sup>[175]</sup> The formation of the globular aggregate structure is ascribed to the large effective headgroup areas and the high charge density of the surfactants. The EO units of the non-ionic surfactant Brij<sup>®</sup> 76 appears to behave analogous to the large headgroups of the cationic surfactant species.<sup>[175-177]</sup> An interesting fact that should be mentioned is the phase transition from the 3d to the 2d hexagonal mesophase which was observed by Zhao et al. during an additional hydrothermal treatment of the SBA-12 silica.<sup>[174]</sup>

In case of the investigated PMO material the 3d hexagonal structure is also a transition state which appears between the formation of single micelles in the solution and the formation of the final mesostructure of the product. In this experiment the phase transition from a high to a lower curved mesostructure was observed. The large headgroup of the surfactant is the reason for the formation of such high curved surface. With increasing degree of condensation the curvature of the structure increased. This fact is the opposite from the evolution that was expected taking into consideration that the change from a lower to a higher curved surface is initiated by charge density matching. The reason was, as already mentioned by Zhao et al.,<sup>[174]</sup> the high reaction temperature during the hydrothermal treatment. But a clear explanation for this effect was not given by the authors. Thus, only assumptions can be made concerning the phase behaviour of this system.

During the aging step of the described experiment which takes place at 50 °C both hexagonal phases were formed parallel due to the surfactant concentration in the solution which might be at the point where both phases can be formed dependent on the other synthesis parameters such as temperature, pH value or organosilica precursor concentration. One possible explanation might be the decrease of the effective headgroup area  $a_0$  which might be caused by the change in the conformation of the EO units. The change from anti-gauche-anti to anti-anti-anti leads to a decrease in hydrophilicity and thus, to a decrease of  $a_0$ . The other possibility to increase the value  $g$  is a decrease in the surfactant tail length. The application of

a Brij surfactant with a hydrocarbon chain containing only 16 carbon atoms instead of 18 (as in Brij<sup>®</sup> 76) led to the formation of 2d hexagonal mesostructures in all experiments.<sup>[174]</sup> From this information one can conclude that the surfactant tail length plays an important role for the formation of the structure. An increase of the temperature might lead to a coiling of the hydrocarbon chain and thus, to a shorter effective surfactant tail length.

#### 4.4 Conclusion

Two different systems of PMO synthesis mixtures have been investigated by SAXS measurements. In both cases a 2d hexagonal structured material was the result of the complete synthesis procedure consisting of an aging step and a hydrothermal treatment step. The aging steps of both syntheses were studied by *in situ* SAXS and for both materials a transition state during the aging step of the synthesis was observed. Samples synthesised with P123 as SDA show a lamellar transition state which can be explained by charge density matching during the condensation of the organosilica round the liquid crystal template as described by Monnier et al.<sup>[11]</sup> The synthesis carried out with Brij<sup>®</sup> 76 showed a 3d hexagonal transition state which is transferred into the 2d hexagonal mesostructure at high temperatures during the hydrothermal treatment. Similar observations were made by Zhao et al. for the SBA-12 silica.<sup>[174]</sup> The reason for this phase transition cannot be given by applying the charge density matching theory. In this case the packing parameter  $g$  is increased, which can only be achieved by a reduction of the surfactant tail length or the effective headgroup area.

## 5 Copper adsorption experiments

### 5.1 Adsorption of heavy metal ions on organic-inorganic hybrid silica materials

The adsorption of heavy metal ions on functionalised mesoporous silica materials could be one possible solution for cleaning contaminated soils. The heavy metal pollution in soils affects the growing process of plants and the activity of soil organisms<sup>[178-180]</sup> but also contributes to high heavy metal concentrations in the ground water or in food.<sup>[181]</sup> Three different possibilities of eliminating the contamination from the soils have been described in the literature up to now. First the electrokinetic remediation,<sup>[182,183]</sup> second the bioremediation<sup>[184,185]</sup> and third the chemoremediation. The method of electrokinetic remediation combines the technique of electrodialysis and electromigration of heavy metal ions in the polluted soils. The success of this method depends on the pH value, the lime content and, to a high extent, on the heavy metal itself.<sup>[186]</sup> Phytoremediation and microorganism remediation reveal ecological advantages compared to the environmental destructive physical remediation methods. But in most cases these methods are time-consuming and not effective for soils with high contaminations of many different heavy metal ions. For chemoremediation inorganic or organic adsorber such as hydroxyapatite,<sup>[187]</sup> lime,<sup>[188]</sup> beringite,<sup>[189]</sup> birnessite,<sup>[190]</sup> zeolites,<sup>[191]</sup> and bauxite residue<sup>[180]</sup> were added in order to reduce the mobility and availability of heavy metal ions.

From this point of view mesoporous materials and especially functionalised ones are promising materials for heavy metal adsorption. Many heavy metal adsorption experiments were carried out applying functionalised mesoporous silica materials as adsorber materials.<sup>[192-197]</sup> In most cases the surfaces of these materials were grafted with mercaptoalkyl- or aminoalkylsilanes. The post synthetic treatment of the pure mesoporous silica materials with this relatively long alkyl chains containing mercapto- or amino-functionalities led in all cases to a significant reduction of the specific surface areas and the pore diameters, which influences the adsorption capacity of the resulting functionalised materials to a high extent. Because of the mercury affinity of sulphur molecules  $\text{Hg}^{2+}$  ions were mostly chosen for adsorption experiments but experiments concerning the adsorption of  $\text{Cu}^{2+}$ ,  $\text{Zn}^{2+}$ ,  $\text{Cr}^{3+}$ ,  $\text{Ni}^{2+}$ ,  $\text{Co}^{2+}$  and  $\text{Cd}^{2+}$  were carried out as well. First experiments were presented by Mercier and Pinnavaia.<sup>[192,193]</sup> Mercaptopropyl functions were grafted onto the surfaces of their hexagonal ordered mesoporous silica (HMS) materials HMS C12 and HMS C8 (C12: synthesised with dodecylamine as SDA; C8: synthesised with octylamine as SDA)

just differing in the pore sizes and onto the surface of a MCM-41 silica material (MP-HMS C12, MP-HMS C8, MP-MCM-41). Then  $\text{Hg}^{2+}$  adsorption experiments were carried out. The authors could show a dependency between the pore diameter and the adsorption capacity. Pore diameters above 2 nm led to a  $\text{Hg}^{2+}/\text{S}$  ratio of 1. The adsorption capacities were 0.6 mmol  $\text{Hg}^{2+}/\text{g}$  MP-MCM-41; 1.5 mmol  $\text{Hg}^{2+}/\text{g}$  MP-HMS C12 (pore diameter: 2 nm) and 0.6 mmol  $\text{Hg}^{2+}/\text{g}$  MP-HMS-C8 (pore diameter: 1.5 nm). Brown et al. synthesised mercaptopropyl-functionalised MSU silica materials via co-condensation of TEOS and mercaptopropyltrimethoxysilane (MPTS).<sup>[194]</sup>  $\text{Hg}^{2+}$  adsorption capacities between 1 mmol  $\text{Hg}^{2+}/\text{g}$  material (MSU with 2 % MPTS loading) and 2.2 mmol  $\text{Hg}^{2+}/\text{g}$  material (MSU with 5 % MPTS loading) could be obtained. Studies of  $\text{Hg}^{2+}$  adsorption experiments were also presented by Nooney et al.<sup>[195]</sup> The investigated materials were, on the one hand, co-condensation products of tetrabutyl orthosilicate (TBOS) and MPTS, and, on the other hand, mercaptopropyl-functionalised materials (HMS materials and amorphous silica) synthesised via grafting. The highest MPTS content in the co-condensation reaction was 20 mol % (7.36 wt % sulphur) and 0.78 wt % for the amorphous silica. Data concerning the loading of the grafted HMS materials was not given. With increasing amount of MPTS in the material synthesised via co-condensation an increase of the adsorbed  $\text{Hg}^{2+}$  amount was observed up to a value of 1.26 mmol/g. The adsorption capacities of the materials synthesised via grafting was significantly lower: 1.04 mmol  $\text{Hg}^{2+}/\text{g}$  MP-HMS and 0.28 mmol  $\text{Hg}^{2+}/\text{g}$  amorphous silica.

Two further interesting studies concerning the adsorption of several heavy metal ions have been published. In 2000, Liu et al. presented an adsorption study on functionalised mesoporous SBA-15 silica.<sup>[196]</sup> Three different materials were applied for waste water purification (metal contents: 0.05 mmol  $\text{Hg}^{2+}$ , 0.082 mmol  $\text{Cu}^{2+}$ , 0.154 mmol  $\text{Zn}^{2+}$ , 0.1 mmol  $\text{Cr}^{3+}$  and 0.174 mmol  $\text{Ni}^{2+}/\text{L}$  solution): first, a pure SBA-15 silica phase, second, a 3-mercaptopropyl-functionalised SBA-15 silica and third, a 3-aminopropyl-functionalised SBA-15 silica. Only very low amounts of  $\text{Cu}^{2+}$  (0.0001 mmol/g) and  $\text{Cr}^{3+}$  (0.0001 mmol/g) were adsorbed by the pristine SBA-15 silica. The 3-mercaptopropyl-functionalised material showed an excellent affinity towards  $\text{Hg}^{2+}$  ions. No  $\text{Hg}^{2+}$  could be detected in the solution after treatment with the 3-mercapto-functionalised SBA-15 silica (0.005 mmol/g). The adsorption properties concerning the other metal ions were significantly lower ( $\text{Cu}^{2+}$ : 0.0032 mmol/g,  $\text{Zn}^{2+}$ : 0.0003 mmol/g,  $\text{Cr}^{3+}$ : 0.001 mmol/g and  $\text{Ni}^{2+}$ : 0.0087 mmol/g). The 3-aminopropyl-functionalised SBA-15 exhibited completely different adsorption

properties. The affinity towards  $\text{Hg}^{2+}$  ions was lower (0.004 mol/g) while the other metal ions were completely removed from the solution.

Other interesting experiments concerning the adsorption behaviour of different amine-functionalised materials were presented by Bois et al.<sup>[197]</sup> Materials were synthesised via the co-condensation pathway using TEOS and different terminal organosilica precursors such as aminopropyl- (N), [amino-ethylamino]propyl- (N-N), (2-amino-ethylamino)-ethylamino]propyl- (N-N-N) and mercaptopropyltriethoxysilane (S). All amine-functionalised materials exhibited high affinities towards  $\text{Cu}^{2+}$ -,  $\text{Ni}^{2+}$ -,  $\text{Co}^{2+}$  and  $\text{CrO}_4^{2-}$ . The highest adsorption capacity of  $\text{Cu}^{2+}$ -,  $\text{Ni}^{2+}$ -,  $\text{Co}^{2+}$  and  $\text{CrO}_4^{2-}$  was measured for the sample with the highest nitrogen content (0.6 mmol/g  $\text{Cu}^{2+}$ , 0.2 mmol/g  $\text{Ni}^{2+}$ , 0.2 mmol/g  $\text{Co}^{2+}$  and 0.25 mmol/g  $\text{CrO}_4^{2-}$ ), while the mercaptopropyl-functionalised materials showed the highest adsorption of  $\text{Cd}^{2+}$  ions (0.25 mmol/g).

Only few studies of heavy metal adsorption experiments on periodic mesoporous organosilica materials have been published yet although these materials have a lot of advantages compared to the functionalised mesoporous materials. With the direct incorporation of the organic function into the pore wall network pore blocking and reduced pore diameters could be avoided. These materials offer excellent properties for application in heavy metal adsorption, effluent treatment or soil remediation, respectively. The adsorption capacity depends on the organic function itself as well as on the number of organic functions incorporated in the framework.

Yang et al. published a synthesis of a 3-mercaptopropyl-functionalised PMO material by a co-condensation of BTME and 3-mercaptopropyltrimethoxysilane (MPTS).<sup>[198]</sup> In this case the 3-mercaptopropyl functions protrude into the pores but the space that is needed for these organic functions is lower compared to a material functionalised via the grafting procedure. The application of P123 as SDA implemented pore diameters up to 6.5 nm. The adsorption capacity of these material concerning  $\text{Hg}^{2+}$ ,  $\text{Cd}^{2+}$ ,  $\text{Zn}^{2+}$ ,  $\text{Cu}^{2+}$  and  $\text{Cr}^{3+}$  was studied. The experiments concerning the adsorption of  $\text{Hg}^{2+}$ ,  $\text{Cd}^{2+}$  and  $\text{Cr}^{3+}$  showed that relatively high amounts of these three metal ions were removed from the solution ( $\text{Hg}^{2+}$ : 0.75 mmol/g;  $\text{Cd}^{2+}$ : 1.65 mmol/g;  $\text{Cr}^{3+}$ : 3.26 mmol/g). The affinity to  $\text{Zn}^{2+}$  and  $\text{Cu}^{2+}$  was lower resulting in lower adsorption capacities ( $\text{Zn}^{2+}$ : 0.36 mmol/g;  $\text{Cu}^{2+}$ : 1.29 mmol/g).

Zhang et al. presented a material synthesised via co-condensation (see chapter 1.2.2).<sup>[199]</sup> The combination of TEOS and  $(\text{EtO})_3\text{Si}(\text{CH}_2)_3\text{S-S-S}(\text{CH}_2)_3\text{Si}(\text{OEt})_3$  leads to a material with an extremely high affinity towards  $\text{Hg}^{2+}$  ions. Studies with different aqueous solutions of  $\text{Pb}^{2+}$ ,  $\text{Cd}^{2+}$ ,  $\text{Zn}^{2+}$ ,  $\text{Cu}^{2+}$  and  $\text{Hg}^{2+}$  show the high selectivity towards  $\text{Hg}^{2+}$  ions. The material

containing 2 % of the tetrasulfide adsorbed 3 mmol  $\text{Hg}^{2+}$ /g PMO, the adsorption capacity of a material containing 15 % tetrasulfide was 13.5 mmol/g PMO material.

The synthesis of an organic-inorganic hybrid mesoporous anion exchange resin was published by Lee et al.<sup>[200]</sup> *N*-((trimethoxysilyl)propyl)-*N,N,N*-trimethylammonium chloride or alternatively *N*-((trimethoxysilyl)propyl)-*N,N,N*-tri-*n*-butylammonium chloride was integrated into a PMO network containing ethane or phenylene bridges. The adsorption behaviour of these materials concerning perrhenate anions ( $\text{ReO}_4^-$ ) was investigated. An important point was the dependence of the adsorption capacity of the material on the pH value of the solution. Highest perrhenate amounts were adsorbed from neutral solutions. From an aqueous solution containing  $10^{-4}$  mol/L  $\text{NaReO}_4$  99.9 %  $\text{ReO}_4^-$  were removed by adsorption. 1.86 mg  $\text{ReO}_4^-$  /g PMO resin could be adsorbed at a pH of 7. The adsorption from an acidic solution was lower (1.26 mg  $\text{ReO}_4^-$ /g PMO resin at a pH of 1), which corresponds to a ratio of 67.5 %. The adsorption of  $\text{Re}^{+\text{VII}}$  is only weakly influenced by the presence of sulphate ions in the solution, which allows the application for solutions containing other anions as well.

## 5.2 Experimental

For  $\text{Cu}^{2+}$  adsorption experiments three different samples were chosen. Sample PMO-11 and sample PMO-33 are PMO materials synthesised via co-condensation of 1,2-bis(trimethoxysilyl)ethane (BTME) and *N,N*-bis[(trimethoxysilyl)propyl]amine (BTMPA) in two different molar ratios with CTAC as SDA under basic conditions (for detailed description of these materials see chapter 3.1). The molar ratios of the samples PMO-11 and PMO-33 are listed in Table 5.1. The third sample was a pure SBA-15 silica phase. The molar ratio of components is listed in Table 5.2.

**Table 5.1:** Molar ratios of the ethane- and amine-bridged PMO samples chosen for  $\text{Cu}^{2+}$  adsorption experiments.

	BTME	BTMPA	CTAC	NaOH	$\text{H}_2\text{O}$
PMO-11*	0.89	0.11	0.85	2.36	353
PMO-33*	0.67	0.33	0.85	2.36	353

\* PMO-11: 11 % BTMPA, 89 % BTME (for BTME + BTMPA = 100 %)

\* PMO-33: 33 % BTMPA, 67 % BTME (for BTME + BTMPA = 100 %)

**Table 5.2:** Molar ratio of the pristine SBA-15 silica chosen for  $\text{Cu}^{2+}$  adsorption experiments.<sup>[12]</sup>

	TEOS	Pluronic <sup>®</sup> P123	HCl	H <sub>2</sub> O
SBA-15	1	$1.8 \cdot 10^{-4}$	3.27	187.5

For the concentration-dependent investigations solutions containing various concentrations (0.001, 0.005, 0.01, 0.05 and 0.1 mol/L) of  $\text{CuCl}_2$  were added to 200 mg of the PMO material or 50 mg SBA-15 silica and stirred for 2 hours. The solid was filtered off and the remaining solution was investigated by atomic absorption spectroscopy (AAS). From the remaining  $\text{Cu}^{2+}$  concentration in the solution the adsorbed  $\text{Cu}^{2+}$  amount can be calculated. For time-dependent adsorption investigations 200 mg of the PMO material and 50 mg SBA-15 silica were stirred in 5 mL of an aqueous  $\text{Cu}^{2+}$ -solution ( $c(\text{Cu}^{2+}) = 0.01$  mol/L) for different periods of time (10, 30, 60, 120 and 480 minutes). The solid was filtered off and the remaining solution was measured with AAS in order to obtain the time dependent  $\text{Cu}^{2+}$  adsorption. P-XRD measurements as well as nitrogen physisorption measurements were carried out for all samples before and after the adsorption experiments.

A 24-hour washing step (stirring with 500 rpm at room temperature in 5 mL demineralised water) followed for all samples in order to obtain information whether the  $\text{CuCl}_2$  remains inside the pore system of the materials or will be washed out by this procedure. The remaining solution was again investigated by AAS and the remaining  $\text{Cu}^{2+}$  in the pore network of the mesoporous materials was calculated. The complete treatment of the samples is listed in Appendix A.VII.1. All samples were investigated again by P-XRD and nitrogen physisorption after drying.

## 5.3 Results and discussion

### 5.3.1 Comparison of the adsorber materials

Only a short description of the adsorption measurements is given in this chapter because the experiments are still at the beginning. But in order to give first ideas if the chosen materials will be suitable for heavy metal adsorption first results are shown. As described in chapter 5.1 the heavy metal adsorption properties of mesoporous materials are already investigated to some extent. The presence of a secondary amine-function in a mesoporous material as

described in chapter 3.1 might offer the opportunity of heavy metal adsorption on these materials.

The X-ray diffraction patterns of the three investigated materials are shown in Figure 5.1. The comparison of these materials is difficult due to the different structures. The SBA-15 exhibited a 2d hexagonal pore system (space group:  $p6mm$ ) while the ethane- and amine-bridged samples showed a cubic symmetry (space group:  $Pm\bar{3}n$ ).

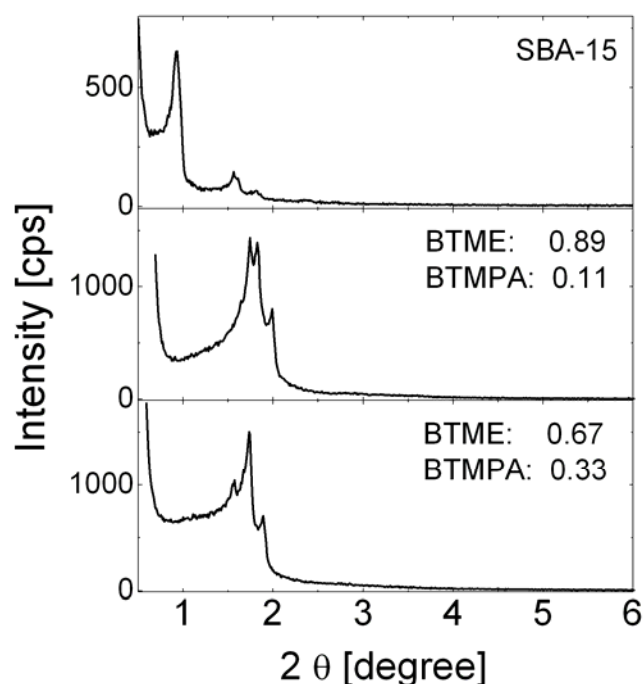
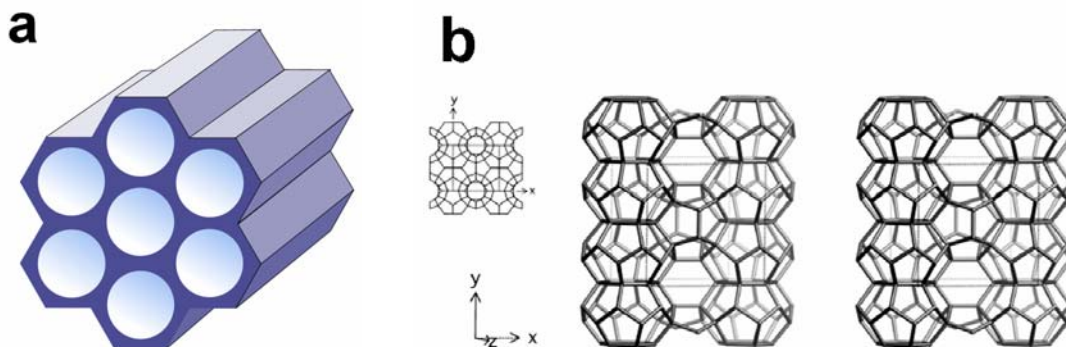


Figure 5.1: XRD patterns of the SBA-15 silica, the amine-functionalised material containing 11 % BTMPA and 33 % BTMPA (for molar ratios see Table 5.1 and 5.2).

The 2d hexagonal pore system of the SBA-15 silica offers a completely different mobility for the heavy metal ions because of the rodshaped pores (Figure 5.2 a). As one can see from Figure 5.2 b the pores of the cubic structured material are interconnected. The mobility of the heavy metal ions in the pore network might be much higher due to the cage like structure and the resulting three dimensional network in contrast to the one dimensional mobility in the hexagonal structure (a). A dependency between the adsorption capacity and the pore diameter is also important and is discussed later on.



**Figure 5.2 a and b:** Schematic illustration of the 2d hexagonal pore arrangement of the SBA-15 silica (space group:  $p6mm$ ) (a) and the cubic pore arrangement of the PMO materials (space group:  $Pm\bar{3}n$ ) (a) (left: projection down  $[001]$ , right: framework viewed along  $[001]$ <sup>[201]</sup> (b).

From the nitrogen physisorption measurements different results concerning the pore diameters were obtained. All isotherms are type IV isotherms<sup>[132]</sup> but the capillary condensation step in the PMO materials occurs between 0.2 and 0.3  $p/p_0$  (see chapter 3.1) while the capillary condensation takes place at higher relative pressures (0.7  $p/p_0$ ) for the SBA-15 silica. Thus, the resulting pore diameters differ between 2.8 nm (PMOs) and 7.5 nm (SBA-15). Higher pore diameters might be advantageous for adsorption experiments because the pore blocking by cluster formation of heavy metal ions at the pore mouths will be lower compared to materials with small pore diameters. The amount of micropores (the specific pore volume) in the SBA-15 silica materials differs between 10 and 30 % strongly dependent on the determination method.<sup>[202-204]</sup> The complete nitrogen physisorption data of the three samples is listed in Table 5.3.

**Table 5.3:** Nitrogen physisorption data of the SBA-15 and the ethane- and amine-bridged PMOs.

	BET surface [m <sup>2</sup> /g]	Pore diameter [nm]
SBA-15	515	7.5
PMO-11	610	2.8
PMO-33	570	2.8

Regarding the differences in the structure both materials should exhibit good adsorption properties; the SBA-15 material due to the high pore diameter and the amine-bridged samples due to the cubic structure and the secondary amine function in the pore wall network.

### 5.3.2 Adsorption experiments

#### 5.3.2.1 Concentration-dependent $\text{Cu}^{2+}$ adsorption

Figure 5.3 shows the correlation between the adsorbed  $\text{Cu}^{2+}$  and the concentration of the original  $\text{Cu}^{2+}$ -solution. Figure 5.3 shows a linear increase of the adsorbed  $\text{Cu}^{2+}$  ions with increasing  $\text{Cu}^{2+}$  concentration in the solution for the ethane- and amine-bridged samples. Both samples independent from the amine concentration adsorbed more than 99 %  $\text{Cu}^{2+}$  from the solutions. These data show that the adsorption capacity of the amine-bridged materials is higher than it could be tested with the applied concentrations. Further experiments are necessary in order to obtain the adsorption limit of the ethane- and amine-bridged materials. In contrast to these results, the adsorption capacity of the SBA-15 in dependence of the  $\text{Cu}^{2+}$  concentration could be figured out. A linear increase of adsorbed  $\text{Cu}^{2+}$  amounts was observed up to a concentration of 0.05 mol. A further increase of the  $\text{Cu}^{2+}$  concentration in the solution did not lead to a higher loading with the metal ions. The maximum amount of  $\text{Cu}^{2+}$  was 1.2 mmol/g SBA-15 silica (the complete results of the concentration-dependent adsorption are listed in Appendix A.VII.2).

The specific surface areas of all materials as well as the pore diameter were not influenced to a high extent. The pore diameters remain unchanged and the specific surface areas decreased slightly (between 5 and 10 %).

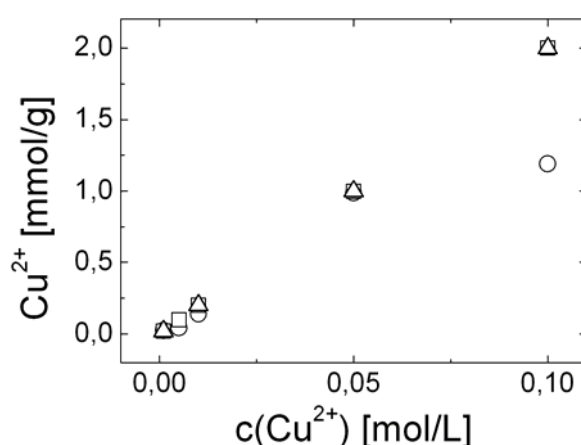


**Figure 5.3:** Illustration of the correlation between the  $\text{Cu}^{2+}$  content of the SBA-15 silica (○), PMO-11 (□) and PMO-33 (Δ) and the  $\text{Cu}^{2+}$ -concentrations of the applied solutions.

There are two possible explanations for the different results concerning the adsorption capacity of the ethane- and amine-bridged samples and the pure SBA-15 silica. As described in literature the adsorption capacity for  $\text{Cu}^{2+}$  ions depends on the number of amine-functions in the adsorption material to a high extent.<sup>[196,197]</sup> Amine-functionalised materials synthesised via grafting or co-condensation exhibited loadings of maximal 15 % of the silica source due to the reaction procedure (as described in chapter 1.2.1 and 1.2.2). The ethane- and amine-bridged PMOs exhibit 11 % and 33 % amine-functions incorporated in the framework. In contrast to the materials described by Liu et al.<sup>[196]</sup> and Bois et al.<sup>[197]</sup> no pore blocking or reduction of the specific surface areas due to anchored amine containing alkyl chains occurred in the PMOs. The relatively high loading with amine functionalities combined with a pore diameter of 2.8 nm might be one reason for the high capacity for  $\text{Cu}^{2+}$  ions. Another possibility why the new PMO materials show such high adsorption capacities is the cage-like cubic structure. As one can see from Figure 5.2 b the pores in the network are interconnected in contrast to the rodshaped pores of the 2d hexagonal ordered SBA-15 silica. Thus, the diffusion of the  $\text{Cu}^{2+}$  ions into and within the pore network takes place in the whole particle while the diffusion into and inside the pores of the SBA-15 is limited due to the 2d hexagonal mesostructure. The relatively high adsorption capacity of the SBA-15 compared to pristine MCM-41 or HMS materials might be caused by the relatively large pore diameter of 7.5 nm as well as by the micropore interconnections of the mesopores which allow a certain mobility of the heavy metal ions in the hexagonal pore network.

The use in chemoremediation of contaminated soils or in waste water treatment requires the incorporation of the ions in the materials even during long periods of water treatment. These terms are simulated by washing all three samples with water over 24 hours under vigorous stirring. The following AAS investigations led to interesting results: The amount of adsorbed  $\text{Cu}^{2+}$  was nearly the same as before washing the samples with water. The results of the AAS measurements are listed in Appendix A.VII.3. An overview is given in Table 5.4.

**Table 5.4:** Amounts of  $\text{Cu}^{2+}$  adsorbed on the materials after 24-hour treatment with water.

Treated with $\text{Cu}^{2+}$ [mol/L]	Adsorption SBA-15 [%]	Adsorption PMO-11 [%]	Adsorption PMO-33 [%]
0.001 (a)	97.36	99.80	97.00
0.005 (b)	99.04	99.08	-*
0.01 (c)	99.90	99.60	99.58
0.05 (d)	99.97	99.73	99.20
0.1 (e)	99.94	99.50	97.00

\* sample was broken in the centrifuge

For all three samples no clear coherence between the amounts of adsorbed  $\text{Cu}^{2+}$  in the network before the water treatment and the adsorption (%) after water treatment could be figured out. But all samples still contain more than 97 % of the adsorbed  $\text{Cu}^{2+}$  after the 24-hour washing step.

### 5.3.2.2 Time-dependent $\text{Cu}^{2+}$ adsorption

In order to obtain information about the adsorption speed time-dependent experiments were carried out. The samples were stirred in a solution containing 0.01 mol/L  $\text{CuCl}_2$  for different periods of time (10, 30, 60, 120 and 480 min), were then filtered off and the  $\text{Cu}^{2+}$  concentrations in the solution after treatment were measured. The sample weights were the same as for the experiments described above. The complete data are listed in Appendix A.VII.2.

The time-dependent  $\text{Cu}^{2+}$  adsorption in the different materials is depicted in Figure 5.4. From Figure 5.4 one can conclude that the adsorption capacity of the ethane- and amine-bridged materials is significantly higher than the  $\text{Cu}^{2+}$  amount in the solution. In all cases over 99 % of the  $\text{Cu}^{2+}$  ions were adsorbed within the first 10 minutes. The SBA-15 silica material does not show a clear correlation between the  $\text{Cu}^{2+}$  adsorption and the treating time. The adsorption took more time than on the ethane- and amine-bridged samples. The adsorbed  $\text{Cu}^{2+}$  amount from the solution differed between 44.8 and 53.3 % due to the lower sample weight of the SBA-15 silica applied for these experiments. Similar to the results shown above the nitrogen physisorption data did not change significantly.

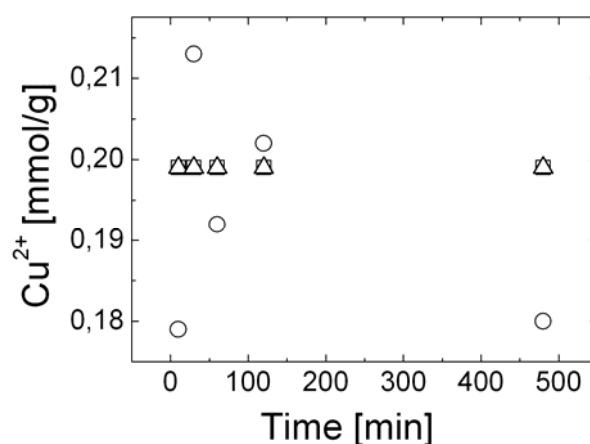


**Figure 5.4:** Time-dependence of the  $\text{Cu}^{2+}$  adsorption on SBA-15 silica ( $\circ$ ), PMO-11 ( $\square$ ) and PMO-33 ( $\Delta$ ) from solutions containing 0.01 mol/L  $\text{Cu}^{2+}$ .

Similar to the results described above the 24-hour washing step did not influence the amount of adsorbed  $\text{Cu}^{2+}$  significantly. In all cases more than 99 % of the adsorbed  $\text{Cu}^{2+}$  remained inside the pore systems of the materials. The results of the AAS investigations are summarised in Table 5.5.

**Table 5.5:** Amounts of  $\text{Cu}^{2+}$  adsorbed on all materials after the 24 hours washing with water compared to the  $\text{Cu}^{2+}$  amounts before the washing procedure.

Time of $\text{Cu}^{2+}$ treatment [0.01 mol/L] [min]	Adsorption SBA-15 [%]	Adsorption PMO-11 (11 % amine-bridges) [%]	Adsorption PMO-33 (33 % amine-bridges) [%]
10 (f)	99.97	99.74	99.51
30 (g)	99.78	99.59	99.90
60 (h)	99.52	99.57	99.69
120 (i)	99.72	99.33	99.58
480 (j)	99.69	99.43	99.98

From these experiments the  $\text{Cu}^{2+}$  adsorption properties of both, the silica and the PMO materials, are quite usable for chemoremediation of contaminated soils or waste water treatment but the PMO material is much more effective. The bonding of the  $\text{Cu}^{2+}$  ions in the material was not investigated yet but should be of great interest in order to obtain information about whether the particles are only incorporated in the network or the ions are adsorbed on special coordination sites in the pore walls.

## 5.4 Conclusion

The  $\text{Cu}^{2+}$  adsorption of PMO-11 and PMO-33 was quite successful. In both cases 2 mmol  $\text{Cu}^{2+}$ /g PMO material were adsorbed without reaching the saturation. The time-dependent experiments show that almost all  $\text{Cu}^{2+}$  was adsorbed from solution within the first ten minutes.

The results of the AAS investigations shown above lead to the assumption that the ethane- and amine-bridged PMOs are promising materials for  $\text{Cu}^{2+}$  adsorption. On the basis of these experiments studies concerning the decontamination of soils and waste water might be of great interest.

Compared to the adsorptive behaviour of the 3-mercaptopropyl-functionalised materials (synthesised via the grafting procedure; BET surface: 814  $\text{m}^2/\text{g}$ ; pore diameter: 7.6 nm)

introduced by Liu et al. the  $\text{Cu}^{2+}$  adsorption on the PMO materials PMO-11 and PMO-33 described above was significantly higher although the specific surface area and the pore diameter of the material introduced by Liu et al. are significantly larger.<sup>[196]</sup> The  $\text{Cu}^{2+}$  adsorption of the 3-aminopropyl-functionalised material (synthesised via the grafting procedure) was higher than of the 3-mercaptopropyl-functionalised silica material. But a comparison between the single  $\text{Cu}^{2+}$  adsorption capacities could not be made because Liu et al. used a mixture containing several heavy metals in contrast to the experiments shown above. The adsorption behaviour of the pristine SBA-15 which was also studied by Liu et al. differed from the results described above. The  $\text{Cu}^{2+}$  adsorption capacity of the SBA-15 silica was 1.2 mmol/g while the experiments carried out by Liu et al. showed only very low adsorption of different ions from the solution added to the SBA-15 silica.

As described in chapter 5.1  $\text{Cu}^{2+}$  adsorption experiments on mesoporous silica materials functionalised with alkyl chains containing different numbers of amino functions were carried out by Bois et al.<sup>[197]</sup> The ligand concentration on the pore surface decreased with increasing chain length of the organic moieties (690  $\text{m}^2/\text{g}$  without functionalization,  $\approx 64 \text{ m}^2/\text{g}$  (N),  $\approx 170 \text{ m}^2/\text{g}$  (N-N) and  $\approx 280 \text{ m}^2/\text{g}$  (N-N-N)). Thus, the sample with the longest amine-functionalised alkyl chains on the surface exhibited the highest specific surface area due to the lowest ligand concentration. The  $\text{Cu}^{2+}$  adsorption experiments were carried out mixing 0.1 g functionalised material with 10 mL of aqueous solutions containing different amounts of  $\text{Cu}^{2+}$  (between  $10^{-4}$  and  $10^{-3}$  mol/L). The highest  $\text{Cu}^{2+}$  adsorption was obtained for the materials functionalised with [amino-ethylamino]propyl groups (0.6 mmol/g) and [(2-aminoethylamino)ethylamino]propyl groups (0.6 mmol/g). From these data one can conclude that the adsorption of several heavy metal ions could be increased by an increase of amine functionalities on the pore surface.

One additional comparison should be given in order to show the excellent adsorption properties of the ethane- and amine-bridged materials. A commercial adsorber for soil remediation was investigated by Wang et al.<sup>[205]</sup> This material named Divergan (polyvinylpyrrolidone) was investigated in different experiments: First, heavy metal ion adsorption from aqueous solutions, second, from mixtures with heavy metal contaminated soils and third, of plants growing on a mixture of Divergan and contaminated soils. This material was found to have excellent adsorption properties towards  $\text{Cu}^{2+}$ ,  $\text{Cd}^{2+}$  and  $\text{Zn}^{2+}$ . 4 mmol  $\text{Cu}^{2+}/\text{g}$  Divergan could be adsorbed.

The complete data of the  $\text{Cu}^{2+}$  adsorption experiments already published is given in Table 5.6.

**Table 5.6:** Overview of the Cu<sup>2+</sup> adsorption experiments carried out on different adsorbers.

Authors	Material	Ads. Cu <sup>2+</sup> [mmol/g]	Comment
Liu et al. Ref. [196]	SBA-15	0.0001	Adsorption from a solution containing Hg <sup>2+</sup> , Cu <sup>2+</sup> , Zn <sup>2+</sup> , Cr <sup>3+</sup> , Ni <sup>2+</sup>
	3-mercaptopropyl-SBA-15 (grafting procedure)	0.0032	
	3-aminopropyl-SBA-15 (grafting procedure)	0.008	
Bois et al. Ref. [197]	Aminopropyltriethoxysilane / TEOS (co-condensation)		<ul style="list-style-type: none"> <li>• decreasing ligand concentration with increasing chain length</li> <li>• increasing specific surface areas with increasing chain length</li> </ul>
	[amino-ethylamino]propyltriethoxysilane / TEOS (co-condensation)	0.6	
	2-[amino-(ethylamino)ethylamino]propyltriethoxysilane / TEOS (co-condensation)	0.6	
	3-mercaptopropyltriethoxysilane / TEOS (co-condensation)		
Yang et al. Ref. [198]	3-mercaptopropyltrimethoxysilane / BTME (co-condensation)	1.29	
Wang et al. Ref. [205]	Divergan (polyvinylpyrrolidone)	4	
Rebbin et al.	SBA-15	1.2	2 mmol/g is not the adsorption limit of the PMO materials. Higher concentrations were not tested.
	PMO-11 (BTMPA 11 / BTME 89) (co-condensation)	2	
	PMO-33 (BTMPA 33 / BTME 67) (co-condensation)	2	

One thing which should be mentioned at this point is a probable dependency between the adsorption behaviour and the specific surface areas and the pore diameters of the materials. In case of the ethane- and amine-bridged materials a comparison of materials was carried out

without referring to the differences in both characteristics. The specific surface areas do not differ to a high extent but the influence of the pore diameters should be investigated in further experiments as well as the influence of the different mesostructures. Thus, a reference material consisting of pristine  $\text{SiO}_2$  with the cubic structure ( $Pm\bar{3}n$ ) will be interesting. Otherwise, the synthesis of an amine- and ethane bridged 2d hexagonal ordered material could give interesting correlations between the adsorption capacity and the mesostructure of the materials.

The limit of adsorption capacity of the PMO materials was not reached in these experiments. Thus, further investigations with higher heavy metal concentrations have to be carried out. In all publications described above no clear data is given concerning the bonding properties of the heavy metal ions on the surface. Therefore, investigations concerning bonding properties of the heavy metal ions on the surface of the adsorption materials are a field of research that has to be studied as well.

The 24-hour washing step with water showed that in most cases nearly the complete amount of adsorbed  $\text{Cu}^{2+}$  remained inside the pore system of the applied materials. This is of essential importance of the application of these materials as adsorber substances for waste water treatment or soil remediation. Removal of the heavy metal ions can be accomplished by a hot-water treatment because of the higher mobility of the metal particles at higher temperatures. Unfortunately, no comments are given concerning the release of the heavy metal ions in the literature. This is a field which has to be further investigated as well, due to the possible recycling of the materials and a possible reuse.

## 6 Solvent vapour adsorption

### 6.1 Solvent sorption experiments

The adsorption of organic vapours on porous materials had attracted a lot of interest over the past decades. In a variety of different publications the adsorption of different organic molecules on zeolites is described. A short description of the existing patents is given in the following part. The first system was invented in order to remove low amounts of organic solvent from air, which might be important for companies producing air contaminated with low concentrations of organic solvent gas which is usually produced in large quantities in coating installations for various machines and tools and in printing factories. Zeolites with a pore diameter between 0.5 and 1 nm were used in order to remove xylene and 2-butanone from air. A honeycomb structure made of ceramic fibres was coated with the zeolites of different types dependent on the organic solvent which should be adsorbed. The carrier is a single-sided corrugated board composed of a high-void corrugated sheet and a flat sheet both made of ceramic fibre, which is rolled up into a cylinder to form tubular passageways through which air to be treated is made to flow.<sup>[206]</sup>

The second patent is dealing with the removal of hydrocarbons like *n*-pentane, *n*-hexane, benzene, toluene etc., originating from gasoline and fuel oil vapours. Activated carbon was used in a system called evaporative loss control device canister.<sup>[207]</sup>

Another promising class of adsorptive materials are the metal organic frameworks (MOFs). These MOFs are investigated concerning their gas storage properties by many research groups at the moment because materials for effective hydrogen or methane storage are of great interest for new ways of energy recovery. A comprehensive overview is given by Kitagawa et al.<sup>[208]</sup> Different types of MOFs have already shown the possibility of selective solvent sorption.<sup>[209]</sup>

But the solvent vapour adsorption on mesoporous molecular sieves was improved in the last years as well. Different adsorption experiments have been carried out applying the mesoporous MCM-41 silica material. Experiments concerning the adsorption of different aliphatic hydrocarbons (methane, ethane, *neo*-pentane, *n*-hexane)<sup>[210-219]</sup> but also aromatics<sup>[2, 212-214, 217-220]</sup> and alcohols have been presented.<sup>[212-214, 216, 220]</sup> Different experimental setups have been used for these experiments. In most cases isotherms were measured by applying microcalorimetry or temperature-programmed desorption. Another method in order to study the adsorptive behaviour of these solids was gaschromatography. In

all cases the isotherms were determined in dependence of the relative pressure  $p/p_0$ . Similar experiments investigating the adsorptive behaviour of periodic mesoporous organosilicas in dependence on their incorporated organic moieties have not been carried out up to now.

Another possibility to analyse the adsorption of different solvent vapours on different types of materials can be carried out in miniaturised systems. For a variety of applications in chemical analysis as well as in synthesis, miniaturised systems are preferable for a number of reasons, such as enhanced flexibility, speed or yield, reduced consumption of reactants and safety.<sup>[221,222]</sup> These systems contain small channels that can be coated or filled with adsorptive materials. Due to the limited size only small amounts of vapour can be adsorbed and thus, the adsorption of extremely toxic gases might be investigated with a relatively low risk.

## 6.2 Characteristics of the applied PMO spheres

For the solvent vapour experiments phenylene-bridged particles (p-PMOs) as well as ethane-bridged particles (e-PMOs) were applied. The synthesis and characterisation is described in chapter 3.3. The data of both samples is summarised in Table 6.1 in order to give an overview of the chosen materials.

**Table 6.1:** Characteristics of the phenylene-bridged and the ethane-bridged samples.

	BET surface [m <sup>2</sup> /g]	Pore diameter [nm]	Diameter [nm]	range	Particle diameter [μm]
p-PMOs	600	1.5	1 – 4		≈ 80
e-PMOs	1000	3	2 – 18		≈ 80

## 6.3 Results and discussion

The Stokes-Raman spectra of liquid benzene, liquid ethanol and of PMO spheres with ethane bridge and phenylene bridge incorporated in the network are shown in Figure 6.1. All four Raman spectra exhibit characteristic features (peaks labelled as a, b, c, d, e and f) which allow to distinguish between the four substances. In particular, it enabled one to identify individual PMO spheres in the mixture inside the reactor channel as well as the detection of the solvent

vapour adsorbed by the single PMO sphere. The empty reactor was measured as well during the continuous solvent vapour flow but no free solvent could be detected by the Raman microscope. Thus, the changes of the spectra of the pristine PMO spheres measured during the solvent vapour flow were caused by the adsorption of solvent molecules on the surface of the PMO materials.

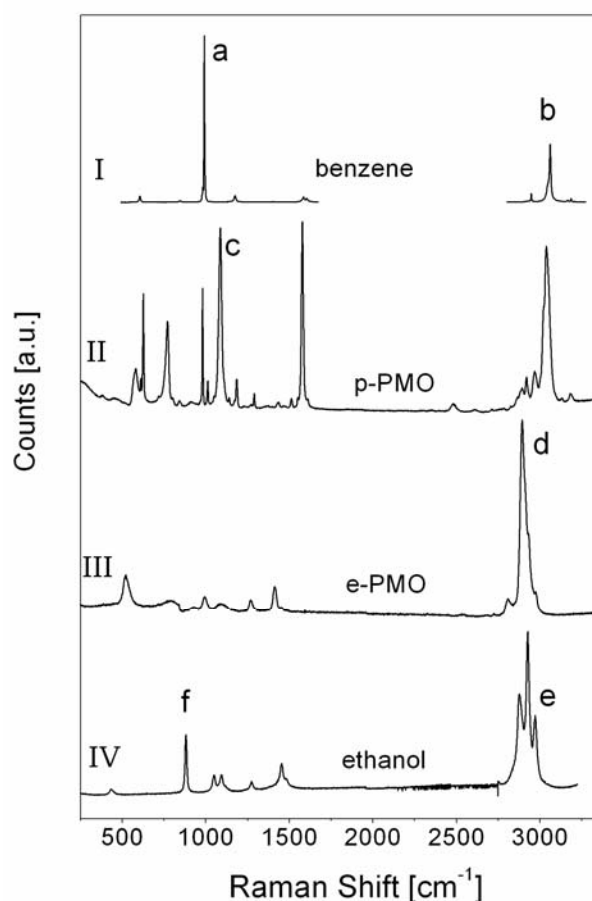


**Figure 6.1:** Raman spectra of liquid benzene (I); a phenylene-bridged PMO microsphere (II), an ethane-bridged PMO microsphere (III) and liquid ethanol (IV). All spectra were recorded at room temperature.

A careful analysis of the latter could be employed for extracting the temperature characteristics of solvent adsorption by a PMO material from a series of Raman spectra taken of an individual PMO sphere inside the microreactor at different temperatures.

Information about the temperature-dependent behaviour of the amount of solvent (in this case benzene and ethanol) adsorbed by a PMO material (in our case ethane- and phenylene-bridged) could be obtained because the Raman spectrum of the solvent adsorbed by the PMO microspheres is not significantly altered compared to that of the liquid solvent as the

adsorption and desorption processes are of physical origin, which means that no chemical transformation of the adsorbent took place. Furthermore, the Stokes Raman spectra, which involve the creation of vibrational quanta are to a first approximation independent of temperature. Therefore, the intensity ratio of a characteristic solvent peak and a characteristic PMO peak in the spectrum of a PMO microsphere inside the reactor is a measure for the amount of benzene or ethanol adsorbed in the steady state.

The following peak ratios were chosen in the four cases:

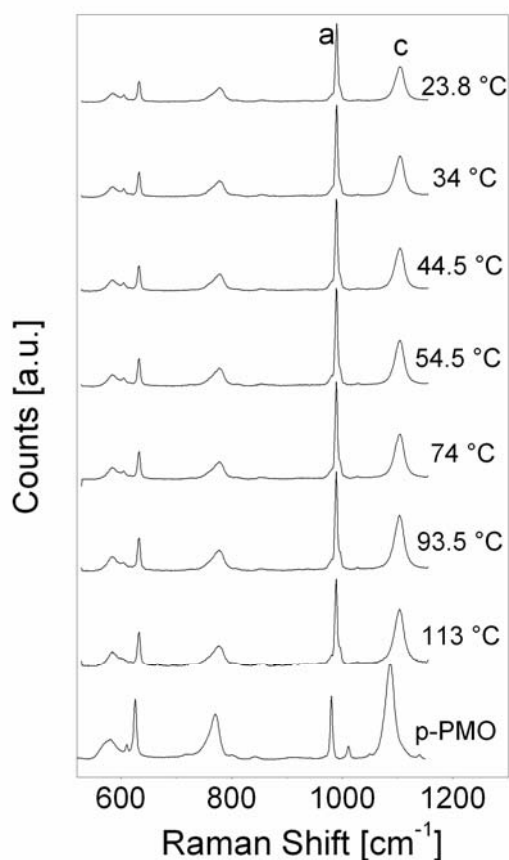
**Table 6.2:** Peak ratios of the characteristic PMO and solvent peaks

Number	Material	Solvent	Ratio
1	p-PMO	benzene	a : c
2	p-PMO	ethanol	f : c
3	e-PMO	benzene	b : d
4	e-PMO	ethanol	e : d
5	empty reactor	benzene	no bands
6	empty reactor	ethanol	no bands

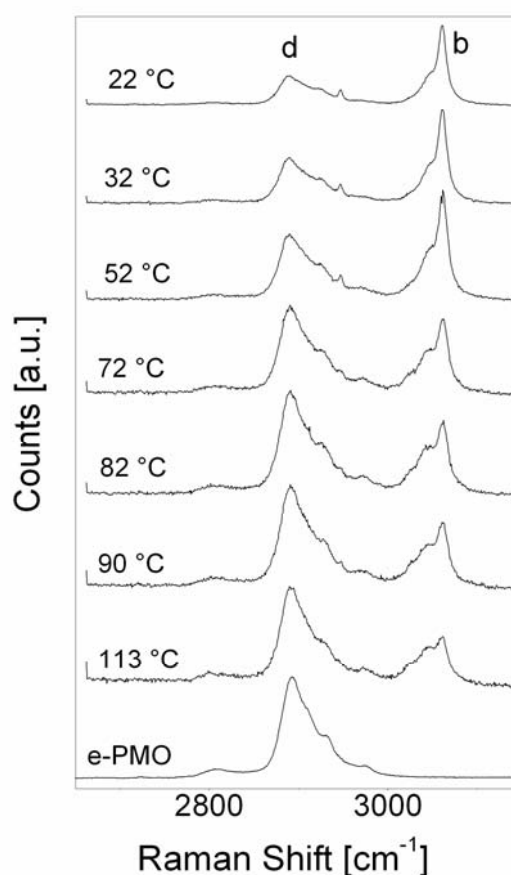
For the comparison of two bands it is important that both bands are closed to each other so that both bands can be measured in the same spectrum. In the first three cases the evaluation is straight forward as the corresponding peaks in the spectra are spectrally separated (Figure 6.1). Therefore, and because the line width of the Raman signals did not change with temperature, it is sufficient to analyse the ratio of the peak intensities for determining the characteristic adsorption curve of the solvent. In the fourth case the analysis is more complicated because the Raman signals (group of three peaks e and peak d in Figure 6.3) overlap. For extracting the peak ratio a fit of the spectra taken inside the microreactor at different temperatures by a linear combination of spectra (III) and (IV) in Figure 6.1 using a least-squares routine was accomplished.

Figure 6.2 (p-PMO) and 6.3 (e-PMO) depict series of Raman spectra taken of PMO microspheres in benzene environment at different temperatures. Spectra taken with the laser spot focussed on the vapour flow alone did not yield to any benzene signals. Therefore the benzene signals a and b in the spectra acquired when focussing on individual ethane- or phenylene-bridged PMO spheres, respectively are indicative for the amount of benzene adsorbed by the microsphere. The Raman intensity of the peak a of the adsorbed benzene overlay the band that could be observed in the spectrum of the p-PMO material. This bond

exhibit a quite low intensity and can be seen as slight shoulder of the peak a in the test series. This fact was considered during the calculation.



**Figure 6.2:** Series of Raman spectra of a phenylene-bridged PMO microsphere with adsorbed benzene vapour taken inside the microreactor at different temperatures in the range from 23.8 °C to 113 °C. The bottom spectrum is that of the pristine PMO microsphere.



**Figure 6.3:** Series of Raman spectra of an ethane-bridged PMO microsphere with adsorbed benzene vapour taken inside the microreactor at different temperatures in the range from 22 °C to 113 °C. The bottom spectrum is that of the pristine PMO microsphere.

One can see from Figure 6.2 that the amount of benzene adsorbed by the PMO microsphere decreased, though weakly, with increasing reactor temperature. A considerable amount of benzene is still adsorbed even at the highest reactor temperature of 113 °C as is clearly visible when comparing the corresponding Raman spectrum with that of the pristine phenylene-bridged PMO microsphere (spectrum at the bottom of the Figure).

The adsorption behaviour of benzene on the ethane-bridged PMO microspheres is quite different as illustrated by the relative intensity changes of peak b and d in Figure 6.3. The

intensity of the benzene peak b changes by almost a factor of 4 compared to the reference peak d of the ethane-bridged PMO whereas the benzene peak only changed by a factor of about 2 in the same temperature range with respect to the reference peak c of the benzene bridged PMO. This effect might be caused by the significant differences in the specific surface areas and the pore diameters of both materials. Again by comparing the lowest spectra in Figure 6.3 one find that even at a reactor temperature of 113 °C some benzene remained adsorbed on the ethane-bridged PMO material.

Series of Raman spectra taken from phenylene-bridged PMO and ethane-bridged PMO microspheres in an ethanol vapour environment are shown in Figures 6.4 and 6.5. Similar to the results described for the adsorption of benzene no signals could be detected with ethanol streaming through the empty microreactor. The signals belonging to pure ethanol, which could clearly be observed in the spectra are due to the adsorbed vapour on the microspheres. The amount of ethanol adsorbed by the phenylene-bridged PMO microspheres decreased with increasing reactor temperature but even at 117 °C small amounts of ethanol remained on the inner surface of the material.

The adsorption of ethanol is a lot higher on the ethane-bridged PMO microsphere at low temperatures. With increasing temperatures the amount of adsorbed ethanol decreases similar to the observations made for the phenylene-bridged material. At 119.5 °C some ethanol molecules are still adsorbed on the surface.

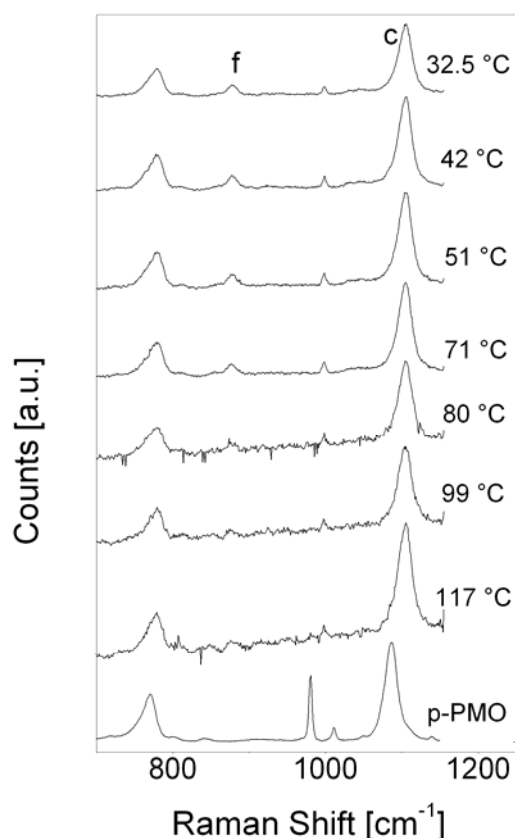


**Figure 6.4:** Series of Raman spectra of a phenylene-bridged PMO microsphere with adsorbed ethanol vapour taken inside the microreactor at different temperatures in the range from 32.5 °C to 117 °C. The bottom spectrum is that of the pure PMO microsphere.

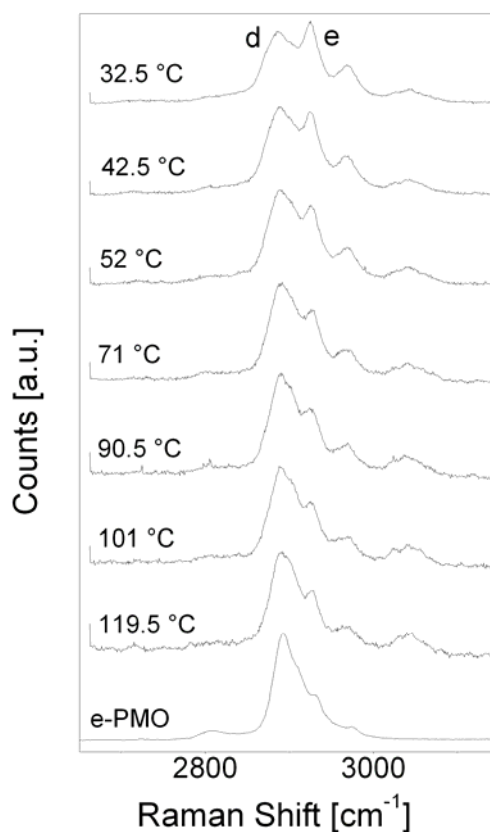


**Figure 6.5:** Series of Raman spectra of an ethane-bridged PMO microsphere with adsorbed ethanol vapour taken inside the microreactor at different temperatures in the range from 32.5 °C to 119.5 °C. The bottom spectrum is that of the pure PMO microsphere.

The absolute intensities of the benzene vapour peaks a and b detected on the phenylene-bridged PMO and the ethane-bridged PMO, respectively allows the comparison of the absolute capabilities of the two types of PMO spheres. In a similar fashion, the absolute adsorption capability of ethanol by the two types of PMO spheres could be determined. All values were normalised to the active inner surface.

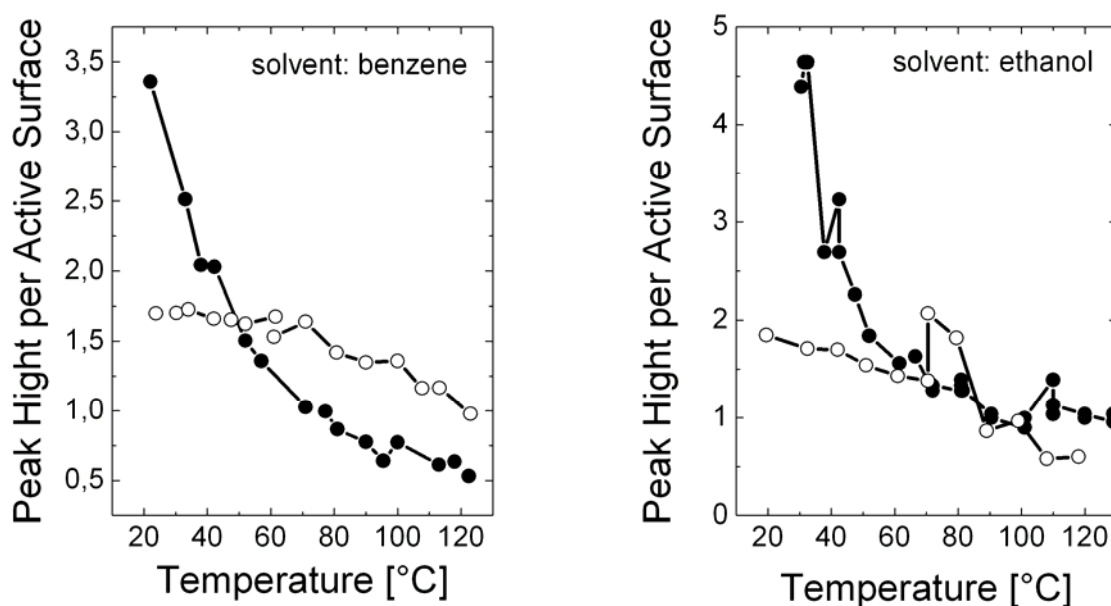


**Figure 6.6 a and b:** Temperature-dependence of the solvent vapour adsorption capabilities of e-PMO (●) and p-PMO microspheres (○), respectively. Letters a to f refer to the peak labels in Figure 6.1. Left: adsorption of benzene; right: adsorption of ethanol.

Figure 6.6 depicts the temperature-dependent adsorption of benzene (a) and of ethanol (b) by the two types of PMO microspheres. The adsorption behaviour of both solvents varied with the type of organic functionality inside the pore wall network. For the adsorption on the ethane-bridged PMO microspheres a positive curvature of the temperature dependence was observed and the amount of adsorbed benzene dropped by a factor of 3 between 20 °C and 120 °C while the amount of adsorbed ethanol dropped by the factor of 5 between 30 °C and 130 °C.

In contrast, the curvature of the temperature-dependent adsorption that is observed for both solvents in case of the phenylene-bridged PMO material looks completely different. The curvature might be negative but a clear statement cannot be given because of the outlier in the ethanol adsorption. The amount of adsorbed benzene only dropped by a factor of 1.8 between 20 °C and 100 °C and is almost constant up to 70 °C. The amount of adsorbed ethanol changed by a factor of 4 between 20 °C and 100 °C. It is worth noting that for both solvents the absolute amount adsorbed at 20 °C by the ethane-bridged PMOs is twice as large as that adsorbed by the phenylene-bridged PMOs, even after correction for the active surface. For each solvent the adsorption characteristics of the two types of PMO microspheres could be directly compared as the curves were obtained at the same solvent partial pressure in the reactor. Therefore, the observed differences must be due to the differences in pore

morphology and chemical interactions. A possible explanation of these effects is given in the following part.

The materials' properties differ to a high extent (see Table 6.1) and thus, a comparison does not really make sense. If one considers a benzene molecule, which has a (kinetic) diameter of about 0.46 nm inside a 2 nm pore of a phenylene-bridged PMO material what means that the pore walls are covered with incorporated benzene to a very high extent, at most 4 molecules have space in a typical cross section of the pore. Thus, the diffusion of the molecules in and out of the completely filled pore system will be inhibited. The pore system of the ethane-bridged PMO with nearly 6 nm in diameter but a broad pore diameter distribution could not be blocked as easily as the small pores of the phenylene-bridged PMOs. This explains why the amount of benzene adsorbed at 20 °C by the phenylene-bridged PMOs is smaller than for the ethane-bridged PMOs despite the  $\pi$ - $\pi$  interaction of the benzene molecules with the pore walls of the phenylene bridged PMOs. The weaker temperature dependence of the adsorption compared to the ethane-bridged PMOs is also partly due to the pore size effect. In addition, there is a contribution due to the differences in the chemical interaction between benzene and the pore walls. It is dominated by the  $\pi$ - $\pi$  interactions in the phenylene-bridged PMOs whereas in the ethane-bridged PMOs the much weaker interactions between the aromatic benzene and the silanol groups are dominant.

The same arguments in terms of pore morphology hold for adsorption of ethanol molecules by the two types of PMO materials. This is the cause for the strong similarities between Figure 6.6 a and b. In contrast to benzene, the dominant chemical interactions between ethanol and both PMOs is hydrogen bonding with the silanol groups. This difference in chemical interactions as well as the solvent partial pressure will explain to a large extent the remaining differences between the two graphs of Figure 6.6, e.g. why the adsorption rate of ethanol from the phenylene-bridged PMOs is twice as large as the corresponding one of benzene.

## 6.4 Conclusion

In summary, the ethane-bridged as well as the phenylene-bridged microspheres exhibit adsorption properties to solvents like benzene or ethanol. For both materials the adsorption capacity decreased with increasing temperature but low amounts of the solvent were still adsorbed even at temperatures above 100 °C. Different adsorption mechanisms are assumed

for the different materials. The active sites of the ethane-bridged samples are mainly the silanol functionalities while the phenylene-bridged spheres possess two different types of active sites: the silanol functionalities and the phenylene groups. Thus, the adsorption of benzene and ethanol might follow different mechanisms on the different materials. For the phenylene-bridged material the  $\pi$ - $\pi$  interactions as well as hydrogen bondings influence the adsorption process while the adsorption process on the ethane-bridged samples is guided only by hydrogen bondings. Despite the similar particle diameter of both materials a comparison is still difficult due to the different pore diameters and specific surface areas.

For low amounts of solvent vapour e.g. adsorption of toxic vapours from compartment air this method might be interesting. But a lot of research and work has to be done in order to optimise the materials concerning specific surface areas and pore size distributions.

A new versatile approach of integrating periodic mesoporous organosilica spheres in a macroporous device was developed by using microstructured components. The incorporation of the spheres into the reactor leads to an effective enhancement of the active reactor surface, which might be interesting for catalytic applications. But a change of the morphology from large spherical particles to thin films would be more promising for catalytic application. The incorporation of new functionalities onto the reactor surface leads to new active sites. Up to now about 22 organic bridges could be incorporated in the pore wall network of periodic mesoporous organosilicas or organic-inorganic hybrid materials synthesised via a sol-gel mechanism or co-condensation products of TEOS and an organosilica precursor. This establishes a wide choice of functionalities or mixtures of different functionalities as described for the mixture of ethane-bridged and phenylene-bridged organosilica spheres in this study. These possibilities suggest that there is great potential for implementation of a wide range of physico-chemical operations beyond the selective separation of solvent vapours and nitrogen gas as demonstrated here. The functionalities inside the pores influence the adsorption behaviour of the solvent vapour. But the pore geometry and the size do also play an important role. The pore diameter as well as the structure of the PMO material could be varied by changing the SDA, the pH of the synthesis solution or the hydrothermal treatment procedure. These variations in the synthesis conditions lead to a wide field of optional applications. The strong temperature-dependence, which was observed during the experiments offers the prospect of temperature modulated adsorption-desorption based devices, which will be able to work at short cycle times due to the low thermal mass of the microreactor employed.

## 7 Chromatography on spherical phenylene-bridged PMOs

### 7.1 Chromatography on (functionalised) spherical mesoporous silica particles

For HPLC normal phases (NP) (pristine silica gels or aluminium oxide) or reversed phases (RP) (different organic moieties grafted on the surface silanol functions) are used. The quality of separation on NP columns is dependent on the pH value. These materials exhibit a low stability at pH values below two and above eight. A separation with an elution solvent with a pH value below two or above eight destroys the silica network. Thus, most separations are carried out on RP columns because of the higher stability at extreme pH values because the coverage with organic functions prevents the contact of the solvent with the siloxane bondings to a high extent.

As described above most separations are carried out on reversed phase columns. These organic-inorganic hybrid materials are synthesised in two steps: Spherical silica gels are synthesised by complete hydrolysis of sodium silicate or by polycondensation of emulsified polyethoxysiloxane with following dehydration. In a post synthetic treatment the organic groups are grafted onto the surface as described in chapter 1.2.1. The most employed materials for HPLC are the so-called RP18 materials, which exhibit an octadecyl chain grafted onto the surface of the silica matrix. Remaining silanol functions are “endcapped” in an additional reaction, in which remaining free silanol groups react with trimethylchlorosilane in order to avoid free polar silanol functions on the surface.

The quality of separation can be influenced by different characteristics of the stationary phase. Spherical shaped monodisperse but also irregular shaped packing materials are available as stationary phases. Columns packed with spherical particles offer a more homogeneous packing and thus, higher separation qualities in contrast to columns filled with irregular shaped particles. The particle diameters of the materials should be in the range of 3 to 10  $\mu\text{m}$ . Lower particle diameters could lead to an increase of the back pressure in the column, larger particle diameters cause peak broadening due to increasing Eddy-diffusion. Larger particles also exhibit a deeper pore network and thus, the mass transfer during the separation is slowed down, which also leads to peak broadening. The ratio largest particle/smallest particle should be around 1.5 in the optimal case and the most applied pore diameters of the stationary phases are in the range of 10 to 30 nm. Materials with a pore diameter smaller than 10 nm are available but these stationary phases are not often applied for separation.

The combination of the spherical morphology of the pure silica materials described in chapter 1.3 combined with the organic functionalisation via a typical PMO synthesis (chapter 1.4) should offer a wide field of new separation materials.

The highly ordered mesoporous materials offer a significant higher stability at extreme pH values because of their formation under extreme pH conditions (in basic medium: 12 – 14, under acidic conditions: 0 – 1). Spherical mesoporous silica particles (as described in chapter 1.3) might be a good alternative to the commercial silica gels. The mesoporous materials provide excellent properties for application in separation techniques such as high specific surface areas, narrow pore size distributions, and the chance of creating a bimodal or even a trimodal pore size distribution as well as the high thermal stability and the stability at high pH values. Some chromatographic experiments with modified and unmodified mesoporous silica particles have been published up to now.

First chromatographic experiments were performed by the Unger group in 1997.<sup>[223]</sup> The particles obtained via the modified Stöber reaction (pore diameter: 4 nm, particle diameter 0.5  $\mu\text{m}$ ) were functionalised with octyldimethylchlorosilane and packed in a column (inner diameter: 100  $\mu\text{m}$ , length: 380 mm). Due to the particle size HPLC experiments were not possible. In that case capillary electrochromatographic tests were carried out with an electroosmotic flow of 3 mm/s generated at a voltage of 30 kV. A successful separation of thiourea, benzene, ethylbenzene, propylbenzene, *n*-butylbenzene and *n*-pentylbenzene was accomplished with acetonitrile/25 mM Tris-HCl (80:20; v:v) in a quite short analysis time of 1 min. An extremely high efficiency of the column could also be measured ( $N$  (plate number) = 288800 for *n*-alkylbenzenes).

The first application of spherical mesoporous particles in HPLC was presented by Gallis et al. in 1999.<sup>[224]</sup> Acid prepared mesoporous silica particles (APMS) (particle diameter: 4  $\mu\text{m}$ , pore diameter 2.4 nm) were functionalised with octyl chains and compared with a commercial  $\text{C}_8$  reversed phase (Hypersil MOS-2.5  $\mu\text{m}$ , pore diameter 12 nm). The separation of uracil, benzene, naphthalene and biphenyl was successful on both materials but the retention times on the APMS phase were significantly higher, the peaks broader, and an increasing peak tailing was observed with higher retention times. But the resolution was comparable on both materials.

In 2000, again two studies concerning chromatographic application of particles smaller than 3  $\mu\text{m}$  were published.<sup>[225,226]</sup> The application of these materials in HPLC is quite complicated because of the high pressure in the column. The best applications for these materials are miniaturised high resolution chromatography or capillary electrochromatography.

Interesting separation experiments were accomplished by Thoelen et al. in 2000.<sup>[227]</sup> Spherical MCM-41 silica particles (synthesised via the modified Stöber reaction) with a diameter of 1  $\mu\text{m}$  were functionalised with (*R*)- $\alpha$ -(1-naphthyl)ethylamine after being silylated with  $\gamma$ -aminopropyltriethoxysilane. The coverage of the surface with the chiral selector was 0.31 mmol/g. After packing this material into a 100 mm column, racemic mixtures of dinitrobenzoyl derivatives of naphthylethylamine and phenylethylamine were separated on this column as well as on a column filled with chiral functionalised MCM-41 silica synthesised via the classical method without the addition of ammonia and ethanol. The resulting particles were agglomerates of hexagonal rods in the size range of 5 – 15  $\mu\text{m}$ . The separation quality of the spherical material was higher compared to the functionalised MCM-41 material with hexagonal rodshape morphology. Lower retention times, a higher resolution of the single peaks and a better peak shape concerning the peak widths and the peak symmetries were obtained. No statement is given concerning the inner diameter of the column or the back pressure during the measurement which is of great interest because of the low particle diameter.

Bossière et al. used spherical MSU-1 mesoporous particles for normal and reversed phase HPLC.<sup>[7]</sup> A comparison of the materials' characteristics between the MSU-1 material and a commercial material, a Nucleosil 50-7 phase, was accomplished before first chromatographic investigations were carried out. Before application of the MSU-1 material, particles smaller than 3  $\mu\text{m}$  were removed by several sedimentation steps. The mean particle diameter after sedimentation was 9  $\mu\text{m}$ , the particle size of Nucleosil 50-7 was 7  $\mu\text{m}$ . A mixture of benzene, naphthalene, biphenyl and phenanthrene was chosen and injected on both columns. In both cases a baseline separation of these four substances could not be achieved. On Nucleosil 50-7 naphthalene, biphenyl and phenanthrene could not be resolved, on MSU-1 only biphenyl and phenanthrene did not show a clear baseline separation. The retention times on MSU-1 were significantly higher, which could be explained by the higher specific surface area of the material (MSU-1: 890  $\text{m}^2/\text{g}$ , Nucleosil: 360  $\text{m}^2/\text{g}$ ) and the difference in the pore diameters (MSU-1: 2.5 nm; Nucleosil: 11 nm). Nevertheless, the MSU-1 material is suitable for chromatographic application as shown in those experiments.

Because of the high importance of the surface silanol functions for the separation properties of the stationary phase Grossmann et al. performed extensive studies concerning the influence of the calcination and rehydroxylation of the material on the density of silanol functions on the material's surface.<sup>[228]</sup> The number of silanol functions per  $\text{nm}^2$  is important for NP as well as for RP materials. In the NP material the silanol functions are the active sites for

adsorption, in the RP materials the silanol functions are functionalised with organic moieties. Chromatographic tests were accomplished with materials synthesised with different calcination temperatures, rehydroxylation times and endcapping procedures. The different amounts of octadecyl chains per nm<sup>2</sup> influence the separation of the substances in the test mixture to a high extent but in all cases the peaks exhibited acceptable shapes.

Different biomolecules were separated on a spherical SBA-15 silica material with octadecyl chains grafted on the surface by Zhao et al.<sup>[229]</sup> Cysteine, glutathione, 6-thiopurine and dopamine could be separated with a 0.1 M phosphate buffer. The separation on a commercial reversed phase showed broader peaks and a lower resolution of the single peaks.

Size exclusion chromatographic tests on mesoporous MCM-41 silica particles, on acid prepared mesoporous silica spheres and on Nucleosil were performed by Nassivera et al.<sup>[230]</sup> by injecting different polystyrene molecules onto all three columns. Due to the smaller pore diameters of the MCM-41 particles and the acid prepared spherical particles the molecular weight cut-offs are significantly smaller than the respective weight cut-off of Nucleosil. Thus, size exclusion chromatography on the spherical MCM-41 particles and the acid prepared silica particles can only be performed for small molecules with a low molecular weight.

Chromatographic applications of different reversed phases were presented by Salesch et al.<sup>[231]</sup> Spherical particles were synthesised in a co-condensation reaction of R-Si(OR')<sub>3</sub> and TEOS (R = C<sub>8</sub>H<sub>17</sub>; C<sub>12</sub>H<sub>25</sub>; C<sub>18</sub>H<sub>37</sub> and R': methyl, ethyl) by using long chain *n*-alkylamines as SDA and ethanol as a co-solvent. For the first time a co-condensation was carried out in order to obtain a new reversed phase for HPLC. A grafting procedure was not necessary anymore. The disadvantage of the co-condensation procedure is, as described already in chapter 1.2.3, the relatively low coverage of the material's surface with alkyl chains (ratio TEOS/R-Si(OR')<sub>3</sub> = 19:1 or 15:1). A separation of 16 different polycyclic aromatic hydrocarbons was accomplished but none of the experiments was completely successful because co-elution of different substances took place dependent on the number of organic moieties/nm<sup>2</sup>.

Good results concerning the separation of different aromatic substances (phenol, benzene, naphthalene, toluene, anthracene and benzopyrene) on spherical SBA-15 particles functionalised with octyldimethylchlorosilane and additional endcapping were obtained by Mesa et al.<sup>[232]</sup> Information about the separation of these substances on a commercial material was not given in this work.

Spherical SBA-15 silica particles were used for HPLC by Ma et al.<sup>[108]</sup> The original spherical SBA-15 phase as well as the spherical SBA-15 material functionalised with octadecyl chains

were tested. The separation of naphthalene, biphenyl and phenanthrene was accomplished on both materials but only the separation on the reversed phase was successful. The co-elution of the three substances on the pristine silica material was caused by the choice of the elution solvent, which was typical for RP chromatography (ethanol/water). A mixture containing human serum albumin, lysozyme and bovine serum albumin was successfully separated on the RP column. A comparison to a separation on a commercial material was not given.

Detailed investigations concerning the separation properties of spherical MCM-41 silica particles synthesised via the pseudomorphic procedure<sup>[104]</sup> were carried out by Martin et al.<sup>[233]</sup> Three different silica materials, Nucleosil 100-5 (particle diameter: 5  $\mu\text{m}$ , pore diameter: 10 nm), Nucleosil 120-5 (particle diameter: 5  $\mu\text{m}$ , pore diameter: 120 nm), and Lichrospher 100 (particle diameter: 15  $\mu\text{m}$ ) were used as preformed silica materials. The resulting three different mesoporous MCM-41 silica spheres were functionalised with octyl chains and their separation properties were compared to the functionalised original materials concerning plate height (H), linear velocity (u), and the measured particle diameter (with SEM). The separation of seven different alkyl benzenes was successful on their synthesised materials.

## 7.2 Chromatography on spherical periodic mesoporous organosilicas

Only few results concerning chromatographic application of PMOs have been published up to now. In 2003, the group of Cheong presented first chromatographic tests using an ethane-bridged PMO material.<sup>[118,234]</sup> In both cases octadecyl chains were grafted onto the surface. Remaining free surface silanol groups were endcapped in an additional reaction. Because of the small particle diameter ( $\approx 1 \mu\text{m}$ ) short columns and low flow rates were chosen in order to prevent high back pressures in the column. A mixture consisting of 4-methoxyphenol, acetophenone, ethylbenzoate, ethylbenzene, acenaphthylene, acenaphthene, phenanthrene and anthracene was separated and the results were compared to experiments carried out with the same mixture of substances but on a commercial silica material functionalised in the same way. The commercial material offered a slightly better baseline separation. An increase of the separation quality was accomplished by an improvement of the particle shape. Well-defined monodisperse spheres were obtained by microwave heating and then used as stationary phase for the further experiments.<sup>[118]</sup>

A study dealing with chromatographic application of phenyl-functionalised PMOs was recently published by Zhu et al.<sup>[120]</sup> Spheres were synthesised via co-condensation of BTME and phenyltrimethoxysilane (PTMS) in presence of P123 as SDA and CTAB as a co-surfactant under acidic conditions with the addition of ethanol as a co-solvent. The remaining surface silanol functionalities were endcapped in a post synthetic treatment. Benzene, naphthalene, biphenyl, phenanthrene and pyrene were successfully separated using this material. In order to obtain information about the separation quality the same experiments were carried out using a commercial phenyl stationary phase. A successful separation on the commercial material was conducted with a slightly better peak shape. Thus, the new material did not offer advantages for such experiments. But an interesting test concerning the stability of the stationary phases under basic condition was carried out and showed a high resistance of the new material to basic separation conditions while the commercial material showed a significant loss of efficiency after 3 hours treatment with triethylamine solution (50 mmol triethylamine in water).

### 7.3 Experimental

#### 7.3.1 Sieving procedure

In order to remove particles with particle diameters below 3  $\mu\text{m}$  the phenylene-bridged spheres were suspended in bidistilled water and transferred into a sieve tower consisting of three sieves with different meshes: 200  $\mu\text{m}$ , 63  $\mu\text{m}$  and 20  $\mu\text{m}$ . The complete suspension was sieved by a continuous addition of water under continuous mechanical extrusion. The last fraction consisting of all particles below 20  $\mu\text{m}$  in diameter was transferred into another sieve tower consisting of three further sieves with different meshes: 100  $\mu\text{m}$ , 20  $\mu\text{m}$  and 5  $\mu\text{m}$ . These sieves consisting of a nickel foil are depicted in Figure 7.1 a and b.



**Figure 7.1 a:** Sieves consisting of perforated nickel foil and the rubber gasket.



**Figure 7.1 b:** Enlargement of the foil.

In this case the powder is suspended in distilled water. A sample weight of about 3 g could be sieved per circle. Particles smaller than 5  $\mu\text{m}$  could not be collected completely. This sieve tower was immersed in a water-filled ultrasonic bath. Under continuous addition of water and ultrasonic treatment the suspension was again fractionated. The sieving time was 6 hours. In this time 15 L of distilled water flew through the sieving tower. Ultrasonic treatment was used to support the procedure. The cycle consists of 15 min with ultrasonic treatment and 15 minutes without ultrasonic treatment. The fractions were dried in vacuum at 120 °C for 24 hours. A photograph of the second sieve tower is shown in Figure 7.2.

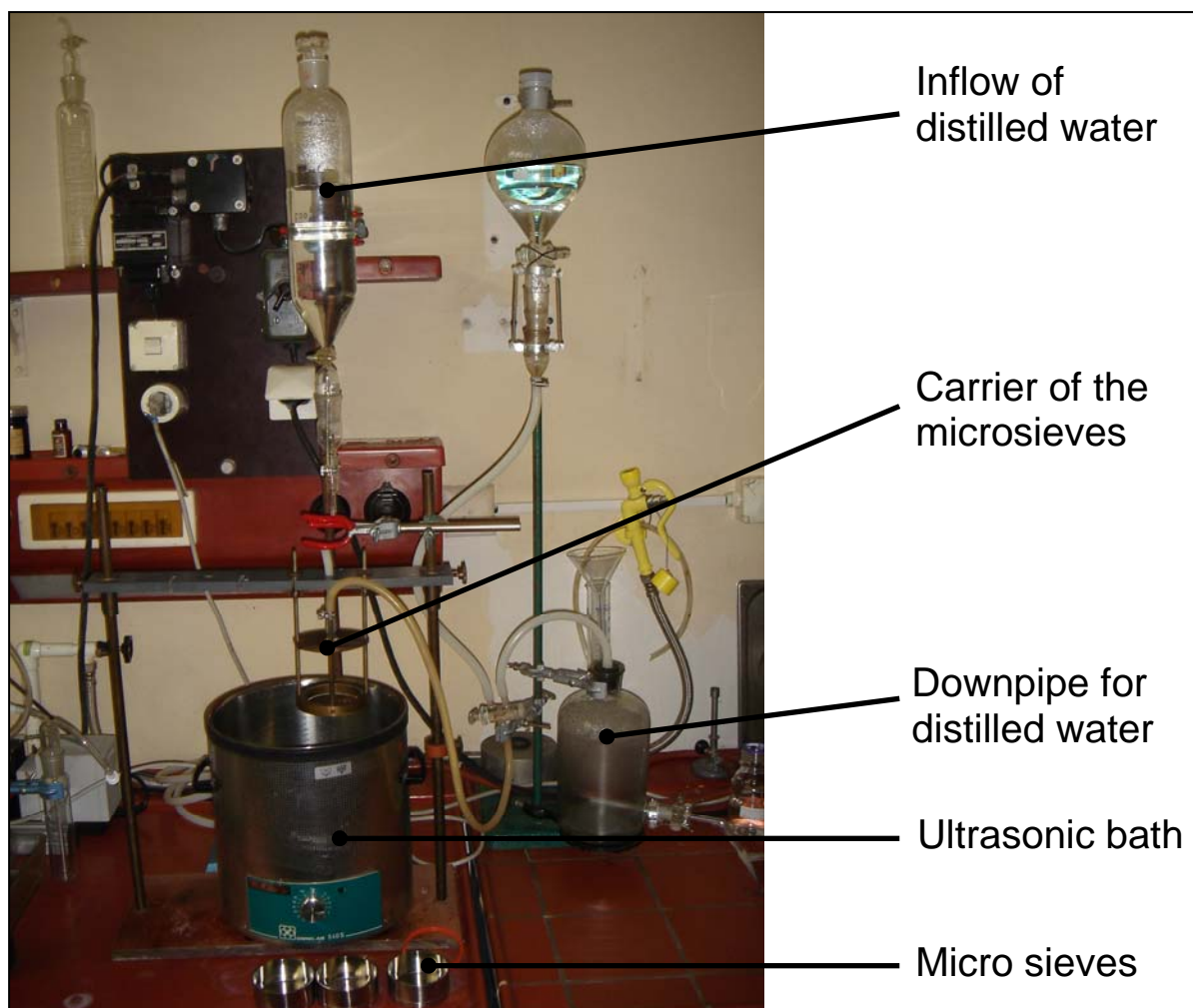


**Figure 7.2:** Sieving setup.

### 7.3.2 Characteristics of the applied materials

Both materials were characterised by different methods as described in chapter 3.4. All results are summarised in Table 7.1 in order to give an overview for the following experiments.

**Table 7.1:** Characteristics of Nucleosil 50-10 and the PMO material which are relevant for chromatographic application (see chapter 3.4).

	BET surface [m <sup>2</sup> /g]	Pore diameter [nm]	Micropore volume [ccm/g]	Pore volume [ccm/g]	n(OH)* [1/nm <sup>2</sup> ]	c(OH) <sup>+</sup> [μmol/m <sup>2</sup> ]
Nucleosil 50-10	356	8.1	0.00	0.80	4.82	8.00
PMO	1180	5.7	0.03	1.12	0.16	0.26

\* Number of accessible silanol functions on the surface

<sup>+</sup> Concentration of accessible silanol functions on the surface

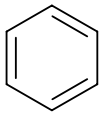
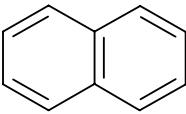
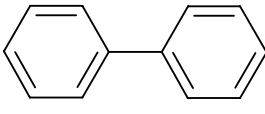
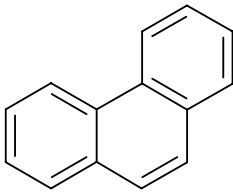
## 7.4 Chromatographic experiments

### 7.4.1 Separation of benzene, naphthalene, biphenyl and phenanthrene

For first chromatographic experiments a mixture of benzene, naphthalene, biphenyl and phenanthrene was chosen to be separated. Several reasons led to the use of this composition of aromatic molecules. First, the same mixture of substances was chosen by Bossière et al.<sup>[7]</sup> in order to prove the separation quality of their spherical MSU-1 material. Ma et al.<sup>[108]</sup> used a mixture of naphthalene, biphenyl and phenanthrene for first tests on their spherical SBA-15 silica material. Thus, a comparison between their results and results obtained during the experiments on the phenylene-bridged PMO materials might be interesting and perhaps gives information about the differences between the pure silica materials and the phenylene-bridged PMO material. The second reason is the UV activity of all aromatic substances.

The structures and the log K<sub>OW</sub> values of benzene, naphthalene, biphenyl and phenanthrene are listed in Table 7.2.

**Table 7.2:** Structures and log  $K_{ow}$  values of benzene, biphenyl, naphthalene and phenanthrene.

	Benzene (1)	Naphthalene (2)	Biphenyl (3)	Phenanthrene (4)
Structure				
log $K_{ow}$ (calculated)*	1.99	3.17	3.76	4.35

\* calculated with Syracuse Research Corporation's LogKow (KowWin) Online Version

The hydrophobicity increases from benzene to phenanthrene. The differences between the single values showed that the separation should be possible. The high polarity of Nucleosil 50-10 requires a solvent with low polarity. The detection wavelength was set to 254 nm after measuring the UV/Vis spectra (see Appendix A.VIII.1).

Separation tests were always carried out first on the Nucleosil 50-10 column and afterwards on the column filled with the phenylene-bridged PMO spheres. In case of Nucleosil 50-10 a successful baseline separation of benzene, naphthalene, biphenyl and phenanthrene was accomplished with pure *n*-hexane as elution solvent and a flow of 1 mL/min (see Figure 7.6). Elution solvents of higher polarity as well as higher solvent flow rates lead to co-elution of the substances. The identification of the single fractions was accomplished by injecting the single substances onto the column. The same separation experiment carried out with the PMO material showed a slightly different result (Figure 7.3). Best separation was accomplished with *n*-hexane as elution solvent and a flow of 2 mL/min.

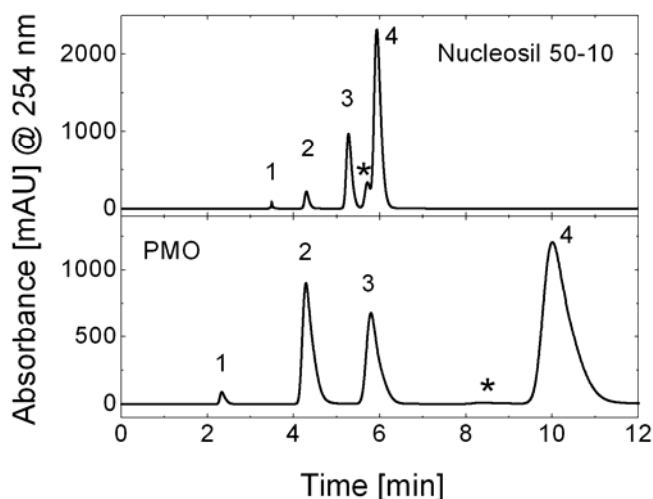


**Figure 7.3:** Chromatograms (HPLC) of benzene (1), naphthalene (2), biphenyl (3) and phenanthrene (4) on Nucleosil 50-10 (solvent flow: 1 mL/min) and on the phenylene-bridged PMO material (solvent flow: 2 mL/min) (\*: caused by the impurity of phenanthrene).

The sequence of the peaks remained the same but the retention times were significantly higher although the solvent flow was 1 mL/min on the Nucleosil 50-10 phase and 2 mL/min on the PMO phase. This effect is due to the higher specific surface area but also due to the differences in pore diameter as described by Bossière et al.<sup>[7]</sup> for corresponding pure mesoporous silica materials. In addition, the elution strength of *n*-hexane is lower in case of the PMO material because of the high amount of phenylene bridges in the material. This leads to peak broadening as well. Sharper and more symmetric peaks were obtained in experiments carried out with an elution solvent containing small amounts of *tert*.-butylmethylether (TBME) (0.5 – 1 %). Differences in the evolution of the peak tailings of the single substances on both columns were observed. The peak symmetry was measured by determination the segments A and B to the left and to the right of the peak maximum at 10 % peak height (see Figure 2.13). A value of one is a totally symmetric peak (see chapter 2.13.1). The resulting values are listed in Table 7.3.

**Table 7.3:** Peak symmetries of benzene, naphthalene, biphenyl and phenanthrene on Nucleosil 50-10 and the PMO material.

	B/A (benzene)	B/A (naphthalene)	B/A (biphenyl)	B/A (phenanthrene)
Nucleosil 50-10	2.03	1.75	1.70	1.43
PMO	1.22	1.38	1.96	2.09

As observed from the chromatograms all peaks in this experiment show a slight peak tailing. In most cases no totally symmetric peaks can be obtained and a slight peak tailing is usual. But the evolution of the peak symmetries from benzene to phenanthrene is different dependent on the stationary phase. The pure silica material led to an increase of the peak tailing with decreasing hydrophobicity while the organically modified silica surface of the PMO material showed the opposite behaviour. This effect observed for the Nucleosil 50-10 phase can be explained by weaker retention with lower polarity of the substances. The interactions of the molecules with the surface of the stationary phase are the weaker on a normal phase column the higher the hydrophobicity is.

The increasing peak tailing of the aromatic molecules on the PMO material might have several reasons. With increasing retention times the peak tailing is normally increasing, which can be explained by increasing diffusion of the analytes in the stationary phase. Another reason for the increasing peak tailing is the polarity of the surface of the PMO material that is reduced due to the high amount of aromatic functionalities in the pore walls. The number of silanol functions is lower by a factor of about 30. The retention of the substances on the PMO material depends on the number of silanol functions as well as on the number of phenylene bridges. Interactions between the  $\pi$ -systems of the pore walls and the  $\pi$ -systems of the molecules occur as well as interactions between the silanol functions and the aromatic molecules similar to the interactions on Nucleosil 50-10. The result is a mixed retention mechanism which often leads to peak tailing. A second reason is the particle size distribution and thus, the packing of the column. As described in chapter 3.4 the particle size distribution of the PMO material is broader than the particle size distribution of Nucleosil 50-10. Bossière et al.<sup>[7]</sup> conducted an experiment on materials differing only in the particle size distribution. They observed definitely better peak shapes for the material with the narrow particle size distribution. These investigations confirm an improvement of the separation quality with decreasing width of the particle size distribution.

The plate height of the column filled with the phenylene-bridged PMO material was 1.2 times lower than that of the column filled with Nucleosil 50-10, which proved the better separation efficiency. So far, similar experiments were carried out on spherical pure mesoporous silica particles. A separation of benzene, naphthalene, biphenyl and phenanthrene could be achieved by Bossière et al. on their spherical MSU-1 particles (specific surface area: 890 m<sup>2</sup>/g) as well as on Nucleosil 50-7 (specific surface area: 360 m<sup>2</sup>/g, particle diameter: 7  $\mu$ m, pore diameter: 5 nm) as stationary phases.<sup>[7]</sup> The separation was successful on both columns but biphenyl and phenanthrene were not baseline separated. The retention times of the four substances

were significantly higher on the MSU-1 column due to the differences of the specific surface areas and pore diameters but the resolution of biphenyl and phenanthrene was the same on both columns.

Ma et al.<sup>[108]</sup> conducted a similar experiment with their spherical SBA-15 silica particles. They injected naphthalene, biphenyl and phenanthrene on the column but chose an elution solvent which was normally used for reversed phase chromatography and thus, were not successful.

Further investigations were carried out concerning the stability of the retention times. This is necessary because of the sensitivity of the normal phases compared to the reversed phases. The equilibrium is usually accomplished faster on reversed phases. In order to obtain information about the stability of the retention times on our material and on Nucleosil 50-10 benzene was injected 14 times on both columns and the evolution of the retention times was analysed. A similar experiment was carried out with biphenyl. The chromatograms of seven injections of biphenyl on Nucleosil 50-10 and seven injections of biphenyl on PMO 50-10 are shown in Figure 7.4 a and b.

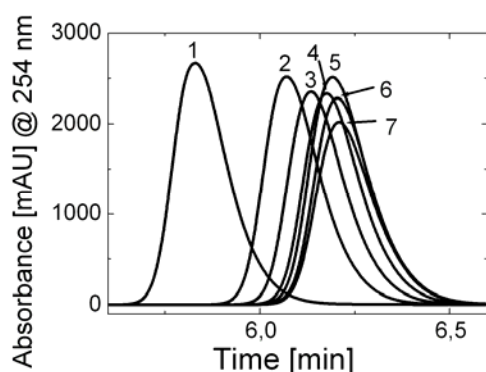


**Figure 7.4 a:** Chromatograms of the injection series of biphenyl on Nucleosil 50-10 as a function of the number of injections.

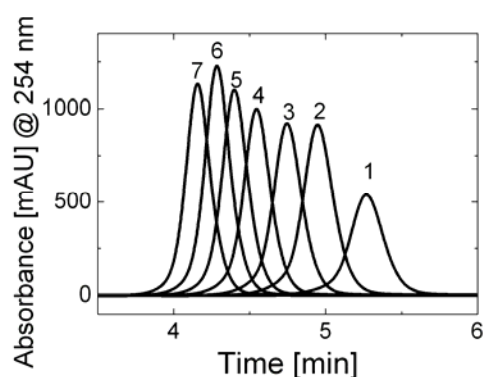


**Figure 7.4 b:** Chromatograms of the injection series of biphenyl on the PMO material as a function of the number of injections.

The peak widths and the peak heights as well as the peak areas of biphenyl on Nucleosil 50-10 are nearly constant. Small errors may be caused by the injection volume of 1  $\mu$ L that is difficult to measure exactly. The PMO column showed a completely different behaviour. A clear evolution of the peak shape from broad to narrow could be observed with proceeding injection number. The evolution of the retention times of benzene and biphenyl are shown in Figure 7.5.

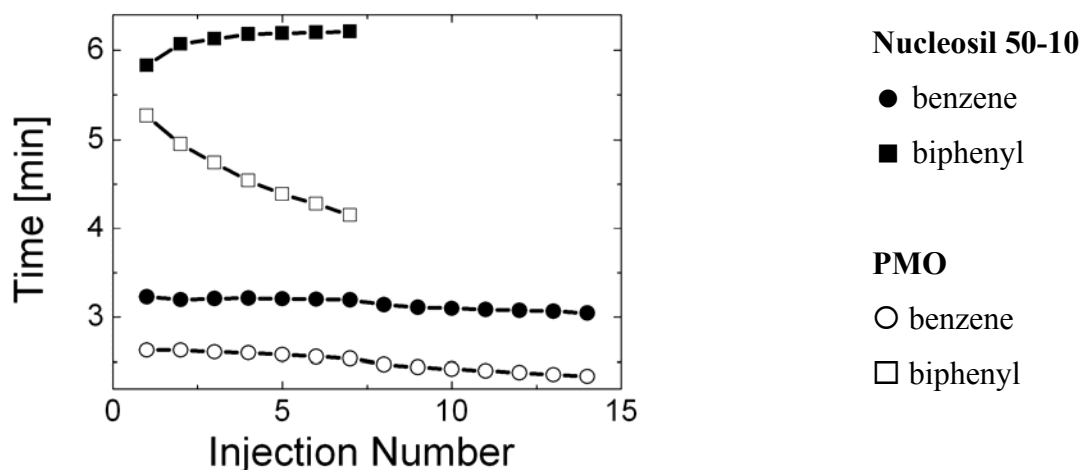


**Figure 7.5:** Evolution of the retention times of benzene and biphenyl on Nucleosil 50-10 and the PMO material with proceeding injection number. The elution solvent was *n*-hexane in both cases. The solvent flow was 1 mL/min on the Nucleosil 50-10 phase and 2 mL/min on the PMO phase. Benzene and biphenyl were injected apart from each other.

The retention times of benzene on both columns did not change significantly with the injection number. Only a slight decrease could be observed for both materials. This effect is stronger for the PMO material. The evolution of the retention times of biphenyl showed a completely different behaviour. On Nucleosil 50-10 the retention time is increasing until it remained constant after four injections. No clear explanation can be given for this behaviour at the moment. On the PMO material the retention time of biphenyl decreased. The curvature leads to the assumption that the retention time approaches a constant value but this is of course not acceptable for a stationary phase in chromatography. In this experiment the adjustment of the equilibrium takes too much time. Another reason for the low stability of retention times might be a possible blocking of the active sites on the PMO material. The aromatic molecules can adsorb on aromatic molecules in the stationary phase; *n*-hexane is too weak to elute them completely. As a result the number of active sites decreased and the separation is guided only by the silanol groups. At this point the retention times will remain constant. But this is only an assumption, further experiments concerning the stability of the retention times and the separation of polycyclic hydrocarbons will be an interesting research topic for the future. The elution with pure TBME led to a complete elution of all substances; a new start of identical experiments showed the reproducibility of these results described above.

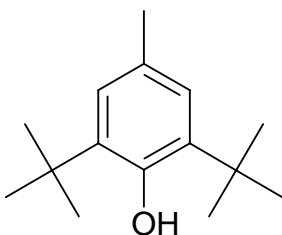
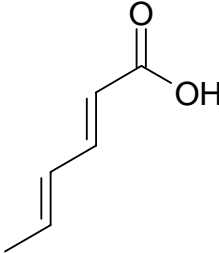
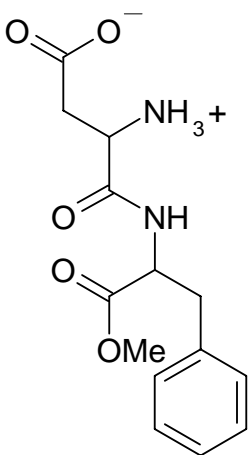
It should be mentioned that the separation of polycyclic hydrocarbons is usually performed on RP18 phases. On these columns it is possible to separate more than four different molecules.

In contrast to our experiments the surface of the stationary phase is almost completely non-polar and the elution is accomplished with polar solvents like methanol and water.

#### 7.4.2 Separation of aspartam, BHT and sorbic acid

The second mixture of substances to be separated was chosen in order to find the limits of the phenylene-bridged PMO material. Ionic substances are usually separated on reversed phases with elution solvents containing high amounts of water or buffer. The behaviour of the ionic substance aspartam (L-aspartyl-L-phenylalanine methyl ester) on the Nucleosil 50-10 phase and the phenylene-bridged material should give information about advantages or disadvantages of the phenylene bridges in the pore walls. The influence of the acidic character of sorbic acid on the separation quality should be tested and a comparison between both stationary phases should help to find out properties of the new stationary phase. BHT (butylhydroxytoluene, 2,6-di-*tert*-butyl-4-methylphenol) was added to the mixture in order to span a wide range of different log  $K_{OW}$  values in one mixture. The structures of the molecules and the calculated log  $K_{OW}$  values are listed in Table 7.4.

**Table 7.4:** Structures and log  $K_{OW}$  values of BHT, aspartam and sorbic acid.

	BHT (1)	Sorbic acid (2)	Aspartam (3)
Structure			
log $K_{OW}$ (calculated)*	5.03	1.62	0.07

\* calculated with Syracuse Research Corporation's LogKow (KowWin) Online Version

The separation of these three substances was complicated because of the high differences between their log  $K_{OW}$  values. BHT is hydrophobic, while aspartam is extremely hydrophilic.

The choice of the elution solvent was difficult. A relatively high polarity was necessary to elute aspartam from both columns while BHT and sorbic acid could be separated with a solvent of lower polarity. Co-elution of BHT and sorbic acid should be avoided. The detection wavelength was set to 210 nm because aspartam shows only one absorption maximum around 210 nm. Although sorbic acid does not show a maximum in this region the detection was possible. The UV/Vis spectra of aspartam, sorbic acid and BHT are depicted in Appendix A.VIII.1.

BHT, sorbic acid and aspartame were dissolved in methanol(MeOH)/TBME (50:50, v:v) and injected on both columns (Figure 7.6). Again, identification was achieved by injecting every single substance on the column. The separation of the three substances on the Nucleosil 50-10 was more complicated because of their different polarities. Best separation results were obtained with a mixture of MeOH/TBME 50:50 (v:v), but a baseline separation of BHT and sorbic acid could not be achieved on this column. The same mixture was injected onto the PMO column. The elution mixture was optimized and best results were obtained for the same mixture of MeOH/TBME 50:50 (v:v). The resolution of BHT and sorbic acid was much better on the PMO column than on Nucleosil.

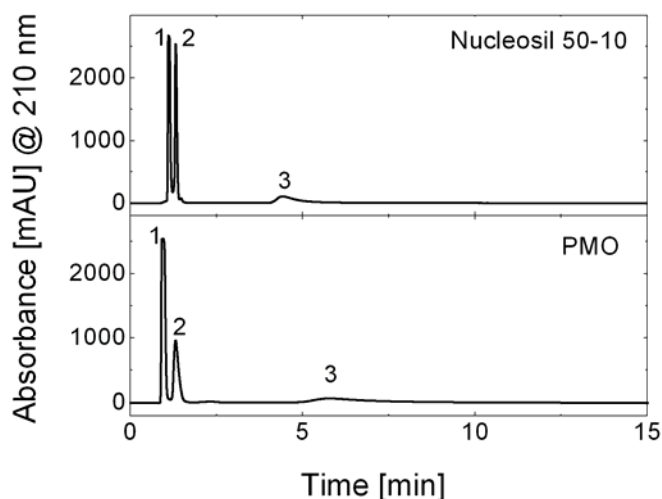


**Figure 7.6:** Chromatograms of BHT (1), sorbic acid (2) and aspartam (3) separated on Nucleosil 50-10 and on the phenylene-bridged PMO material. The elution solvent was MeOH/TBME 50:50 (v:v) in both cases and the solvent flow was set to 2 mL/min.

The elution strength of MeOH/TBME mixtures is quite high for NP chromatography (for more information: see the elutropic series of the solvents depicted in Appendix A.VIII.2).

This is the reason why the differences between the retention times on the different materials differ hardly. The slight differences can be attributed to the higher specific surface area of the PMO material as described above.

As one can see from Figure 7.6 all peaks show a tailing. Peak symmetries (see chapter 7.1) were calculated from the chromatograms and the values are listed in Table 7.5.

**Table 7.5:** Peak symmetries of BHT, sorbic acid and aspartam on Nucleosil 50-10 and the PMO material.

	B/A (BHT)	B/A (sorbic acid)	B/A (aspartam)
Nucleosil 50-10	1.76	1.36	4.21
PMO	1.62	2.03	3.80

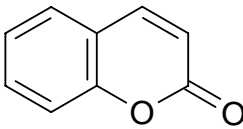
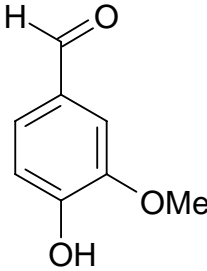
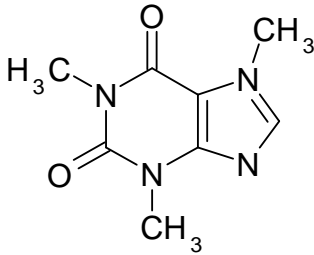
The strong peak tailing of aspartam on both columns is due to the ionic character of the molecule and the strong interactions with the silanol groups on the surface of both materials. The lower number of silanol functionalities on the PMO material reveals a slightly lower peak tailing. For a better peak shape a solvent of higher polarity should be applied but this prevents the separation of BHT and sorbic acid on both columns. In contrast to the peak symmetries of BHT and aspartam which are lower on the PMO material a stronger tailing could be observed for sorbic acid. In this case the interaction with the stationary phase might be different and thus, the phenylene bridges in the pore walls seem to influence the retention of sorbic acid more than the retention of the other substances. The difference in the asymmetry of the BHT peak is quite low. But the worse resolution of BHT and sorbic acid on Nucleosil 50-10 led to difficulties in determining the values A and B and thus, the symmetries might be not completely correct. The separation quality corresponds to the assumption made from the log  $K_{OW}$  values. A gradient elution will solve the problem in this case but a gradient elution on normal phases is difficult because of the slow adjustment of the equilibrium during the separation. From the data shown above and from the chromatograms of aspartam, BHT and sorbic acid one can conclude that this mixture of substances should not be separated on a normal phase.

The stability of the retention times was no problem during these experiments.

## 7.4.3 Separation of caffeine, coumarin and vanillin

The mixture 3 contained caffeine, coumarin and vanillin. The chromatographic experiments should be the most interesting ones due to the different organic functionalities of each substance. Caffeine was chosen to obtain information about the behaviour of basic substances on both columns. The intermolecular ester functionality of coumarin and the hydroxyl, aldehyd and the ether functionality of vanillin might be interesting concerning different kinds of interactions with the phenylene-bridged PMO material. The log  $K_{OW}$  values show that all substances are relatively hydrophilic. The structures and the log  $K_{OW}$  data of caffeine, coumarin and vanillin are listed in Table 7.6.

**Table 7.6:** Structures and log  $K_{OW}$  values of caffeine, coumarin and vanillin.

	Coumarin (1)	Vanillin (2)	Caffeine (3)
Structure			
Log $K_{OW}$ (calculated)	1.51	1.05	0.16

\* calculated with Syracuse Research Corporation's LogKow (KowWin) Online Version

From the log  $K_{OW}$  data one can see that the separation could be successful because the values show small differences but all three values are still in the range between zero and two. The separation of coumarin and vanillin will be interesting due to the slight difference between both log  $K_{OW}$  values. As described above the detection wavelength was acquired by measuring the UV/Vis spectra (see Appendix A.VIII.1) and thus, the absorption maxima of each substance. As a result the detection wavelength for the mixture of caffeine, coumarin and vanillin was set to 272 nm.

First chromatographic tests on Nucleosil 50-10 were carried out with an a mixture of  $\text{CH}_2\text{Cl}_2/\text{MeOH}$  90:10 (v:v) as elution solvent. A baseline separation of these three substances could not be obtained with this solvent (Figure 7.7 upper layer). In contrast, the separation of coumarin, vanillin and caffeine was successful on the PMO column by applying the same elution solvent (Figure 7.7 bottom layer).

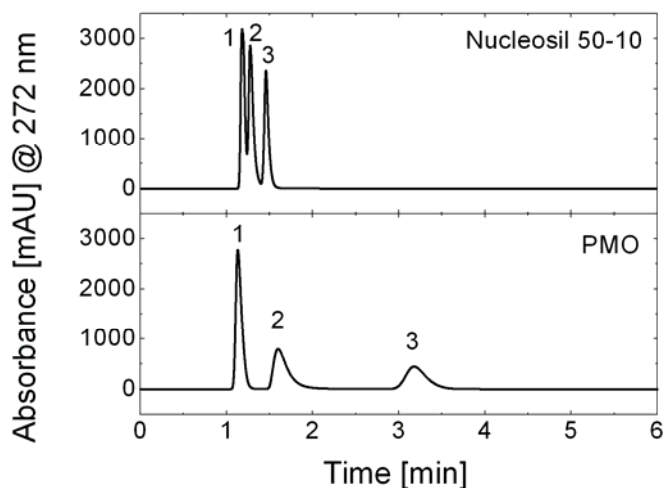


**Figure 7.7:** Chromatograms of coumarin (1), vanillin (2) and caffeine (3) recorded on Nucleosil 50-10 and on the phenylene-bridged PMO material with a mixture of  $\text{CH}_2\text{Cl}_2/\text{MeOH}$  90:10 (v:v) as elution solvent and a solvent flow of 2 mL/min.

The successful separation of coumarin, vanillin and caffeine on Nucleosil 50-10 was accomplished with a mixture of  $\text{CH}_2\text{Cl}_2/\text{MeOH}$  98:2; (v:v) and a solvent flow of 2 mL/min (Figure 7.8 upper layer). The same elution solvent led to very high retention times (caffeine elutes after about 60 minutes) of all substances as well as peak broadening on the PMO column which is the reason why the data is not shown in Figure 7.8. The polarity of the elution solvent had to be increased up to 10 % methanol in  $\text{CH}_2\text{Cl}_2$  again in order to achieve comparable retention times. This effect might be due to the aromatic molecules in the pore wall framework. The hydrophobic phenylene bridges decrease the polarity of the surface. Therefore an increase of the polarity of the elution solvent is necessary in order to obtain acceptable retention times and peak shapes.

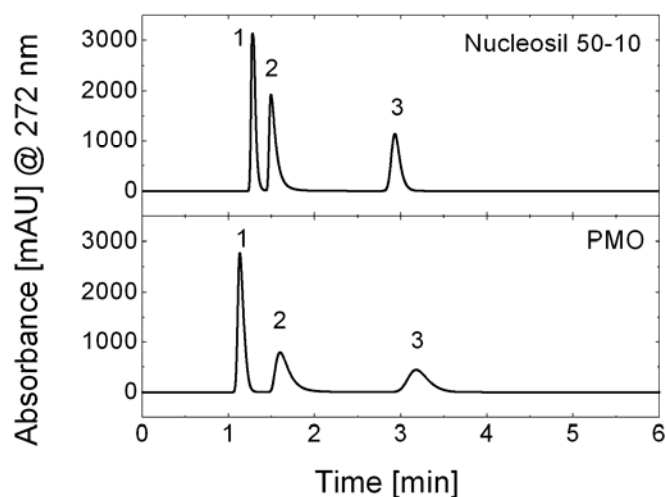


**Figure 7.8:** Chromatograms of coumarin (1), vanillin (2) and caffeine (3) separated on Nucleosil 50-10 and on the new phenylene-bridged material under the following conditions:  
 Nucleosil 50-10: Elution solvent:  $\text{CH}_2\text{Cl}_2/\text{MeOH}$  98:2 (v:v); solvent flow: 2 mL/min  
 PMO material: Elution solvent:  $\text{CH}_2\text{Cl}_2/\text{MeOH}$  90:10 (v:v); solvent flow: 2 mL/min.

Further investigations concerning the peak symmetry were carried out by determining the values A and B as described above (see chapter 2.13.1 and Figure 2.13). But a comparison of the peak symmetries is difficult in this case because of the application of different elution solvents. But similarities concerning the peak symmetries of coumarin, vanillin and caffeine on both materials separated with different elution solvents could be observed. The peak symmetries are listed in Table 7.7.

**Table 7.7:** Peak symmetries of coumarin, vanillin and caffeine extracted from chromatograms recorded during separation on Nucleosil 50-10 and on the PMO material.

	B/A (coumarin)	B/A (vanillin)	B/A (caffeine)
Nucleosil 50-10			
95 $\text{CH}_2\text{Cl}_2$ / 5 MeOH	1.81	2.78	1.71
98 $\text{CH}_2\text{Cl}_2$ / 2 MeOH	2.06	3.73	1.59
PMO 50-10			
80 $\text{CH}_2\text{Cl}_2$ / 20 MeOH	2.04	2.43	1.7
90 $\text{CH}_2\text{Cl}_2$ / 10 MeOH	2.24	3.00	1.65

The evolution of the peak tailings is the same on both columns. Vanillin shows the strongest tailing, caffeine the lowest. This fact is interesting because the different surface properties of

the materials do not seem to influence the peak tailing of the single substances. A decreasing concentration of MeOH in the elution solvent led to a decreasing peak tailing of caffeine on both materials and to increasing peak tailings of coumarin and vanillin. One reason for the decreasing peak tailing of caffeine with decreasing concentration of MeOH is the solubility of caffeine. The solubility of caffeine is significantly higher in DCM than in MeOH. Thus, an increasing amount of  $\text{CH}_2\text{Cl}_2$  leads to a better solubility of caffeine in the mobile phase and lower peak tailing. The values around 1.5 are nearly perfectly shaped peaks in chromatography. The peak tailing of vanillin and coumarin is stronger which can be ascribed to the strong interactions with the silanol functions of the stationary phase. The strong tailing of vanillin on Nucleosil 50-10 compared to the tailing on the PMO material can be explained by the high number of functional groups of the vanillin molecules interacting with the silanol functionalities, which number is significantly higher on Nucleosil 50-10 than on the PMO material. The lower elution strength of the solvent used for the separation on the Nucleosil 50-10 column increased the retention of the substances with the silanol groups of the stationary phase and thus, the peak tailing increased. An interesting effect was found out by changing the solvent from  $\text{CH}_2\text{Cl}_2$  to TBME. Figure 7.9 shows chromatograms of coumarin, vanillin and caffeine separated on the PMO material with different elution solvents.

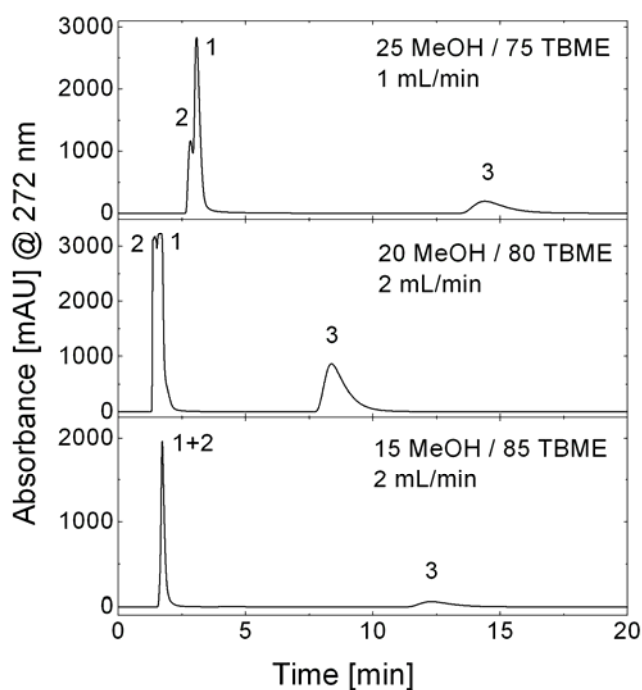


**Figure 7.9:** Chromatograms of coumarin (1), vanillin (2) and caffeine (3) on the PMO column using different mixtures of elution solvents.

As one can observe from Figure 7.9 a separation of coumarin and vanillin was not possible. Coumarin and vanillin elute in reverse order when eluting with a mixture of MeOH/TBME 25/75 (v:v) but without baseline separation. An increase of the methanol concentration in order to avoid the co-elution of coumarin and vanillin led to a significant increase of the retention time and the peak tailing of caffeine and thus, was not successful. A decrease of the methanol concentration led to the elution of both substances in one peak as shown in Figure 7.9 in the bottom layer. The application of high amounts of TBME in the solvent mixture led to seriously stronger tailing behaviour of all substances compared to the separation with the solvent mixture  $\text{CH}_2\text{Cl}_2/\text{MeOH}$ . As an example the chromatograms of coumarin and vanillin as well as the chromatograms of caffeine are shown in Figure 7.10 a and b.

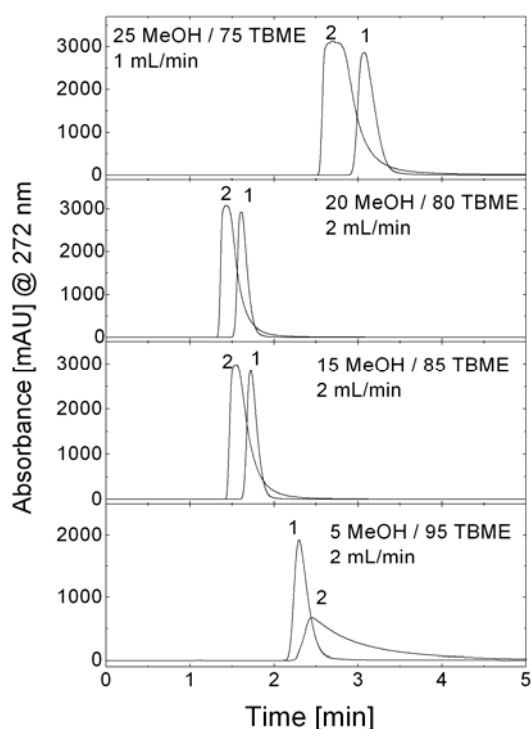


**Figure 7.10 a:** Chromatograms of coumarin (1) and vanillin (2) on the PMO material separated with different MeOH/TBME mixtures. (The vanillin peak is broad due to a slight overload of the column. But this is of low importance for the separation sequence).

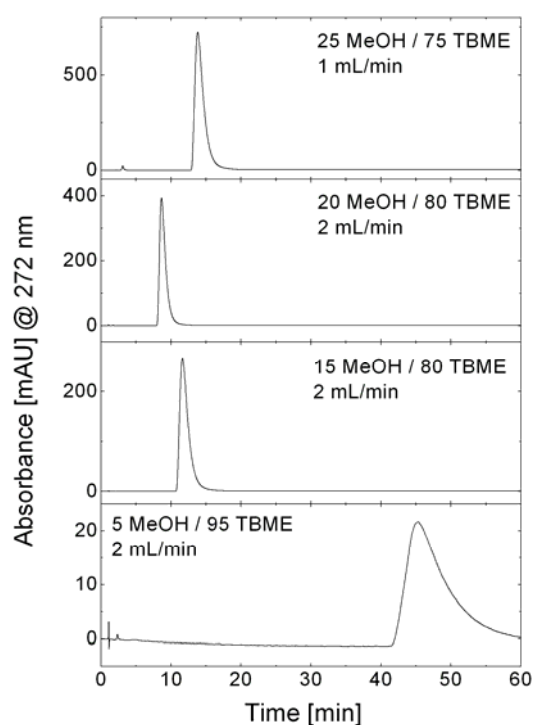


**Figure 7.10 b:** Chromatograms of aspartam on the PMO material separated with different MeOH/TBME mixtures.

This is due to the different selectivity of these solvents. TBME exhibits a relatively strong basicity and is also a locating solvent while  $\text{CH}_2\text{Cl}_2$  reveals neither basicity nor locality. Thus, the exchange of TBME by  $\text{CH}_2\text{Cl}_2$  offered a strong difference in the selectivity of the elution solvent. (Localisation is a measure of the ability of certain solvents to interact with the surface of the stationary phase. Ethers, esters, alcohols, nitriles and amines are localising solvents. These solvents are preferably located at certain positions concerning the silanol groups. The surface of the stationary phase is covered with an accurately defined layer of solvent molecules. In contrast to these solvents the interactions of non-locating solvents with the surface are much weaker and the surface coverage is coincidental. Further information about the characteristics of the single solvents are illustrated Appendix A.VIII.2).<sup>[130]</sup>

No irregularities concerning the stability of the retention times occurred during this series of experiments.

### 7.5 Conclusion of the separation experiments

In summary, the separation of all three test mixtures was successful on both columns. But differences between both materials occurred in all experiments. The aromatic molecules of mixture 1 were separated with *n*-hexane on both columns but with different flow velocities. Higher retention times and an increasing peak tailings with increasing molecule size were observed for the PMO material. BHT, sorbic acid and aspartam were separated on both columns under the same conditions. The resolution of BHT and aspartam was higher on the PMO column. The third test mixture was the most interesting one because in this case different elution solvents had to be chosen in order to obtain successful separations on both columns. This experiment showed the significantly lower polarity of the PMO surface.

The results of the HPLC separation experiments show the possible application of the spherical phenylene-bridged PMO particles in HPLC. The particle size as well as the pore diameter and the specific surface area are in a typical range for application in HPLC. A decrease of the particle diameter to 5 or even 3  $\mu\text{m}$  might be an interesting aim for further investigations because the peak shape and the peak width are influenced by the particle diameter to a high extent. The Eddy-diffusion, which increases with increasing particle diameter, will be reduced as well and the peak widths will decrease. The peak shapes as well as the peak widths show that the packing of the column is of high quality. The similarities as well as the differences between the PMO material and a commercial normal phase could be figured out in several experiments.

The most interesting result of these experiments is the possible interactions of the aromatic molecules in the pore walls with different aromatic substances, which were chosen for separation. This assumption has to be evidenced in further investigations. Aromatic molecules might interact with the phenylene bridge in the pore wall as described above and perhaps open up new separation properties. Substances that can only be separated by these special interactions have to be found. Regarding the results from the separation of the aromatic molecules biphenyl and biphenyl derivatives such as polychlorinated biphenyls (PCBs) might be interesting substances. The analysis of PCBs is of great importance in environmental science at the moment.

Only two research groups have published results dealing with the chromatographic applications of PMO materials up to now. The first tests were accomplished by Kim et al.<sup>[118]</sup> This group synthesised very small ethane-bridged PMO particles via microwave heating. The heating procedure seems to be a possibility of influencing the particle shape without the addition of a co-solvent or a co-surfactant to the reaction solution. The resulting particle diameter of the spheres was between 1 and 3  $\mu\text{m}$  and the pore diameter between 2.8 and 3 nm, which are not in the typical range for separation materials. From these particles a reversed phase was created by grafting octadecyl chains onto the surface of the material. The surface coverage with octadecyl chains prevented the contact of substances with the organic functionalities in the PMO material and thus, is not necessary. Pure silica materials functionalised with octadecyl chains could be taken as well for such experiments. Besides this, the ethane bridge does not offer special properties. The separation of different aromatic molecules (4-methoxyphenol, acetophenone, ethylbenzoate, ethylbenzene, acenaphthylene, acenaphthene, phenanthrene, anthracene) could be achieved under the same separation conditions on a commercial NP material as well.

The chromatographic tests carried out by Zhu et al.<sup>[120]</sup> are a lot more interesting. Phenyl-functionalised PMOs were synthesised via co-condensation of PTMS and BTME with P123 as SDA, CTAB as a co-surfactant and ethanol as a co-solvent. Except the disadvantages of the co-condensation procedure which is described in detail in chapter 1.2.2, the resulting experiments are interesting because these were the first tests on a PMO material. Particle sizes between 2 and 8  $\mu\text{m}$  were obtained but a particle size investigation was not carried out. The pore diameters were between 2.9 and 3.9 nm but also the presence of micropores was detected during the nitrogen physisorption measurement which was not figured out by the authors. The remaining silanol groups on the surface were endcapped which leads to a reversed phase but without grafting large molecules onto the material's surface. A successful separation of

benzene, naphthalene, biphenyl, phenanthrene and pyrene was shown and compared to separation data of a commercial phenyl stationary phase. The separation was nearly of the same quality on both materials. An additional test concerning the stability of the material was carried out, which is of essential importance for all separating materials. The stability was proved by exposing both columns to a triethylamine solution (50 mM, pH: 10, 1.5 mL/min). The commercial column showed significant degradation even after 5 hours while the PMO material was hardly influenced by this procedure. The authors ascribed this stability to the ethane-bridged matrix.<sup>[235-237]</sup> From that point of view the PMO materials offer new applications due to the high stability of the materials towards extreme pH values and this could be of great importance for the future of HPLC.

In order to classify the phenylene-bridged PMO material many different tests should be carried out. The column efficiency and the shape selectivity should be determined. The storage stability and the hydrophobicity should be investigated in order to obtain detailed information about the material and the potentials of applications.

## 8 Summary

Over the last seven years the research field of ordered organic-inorganic hybrid materials, especially the research in developing new periodic mesoporous organosilicas, has attracted a lot of attention. From the discovery of these materials great attention arose for different fields of materials science e.g. catalysis, heavy metal adsorption or separation techniques. Fine tuning the chemical properties of these materials is possible just by variation of the organic bridge in the organosilica precursor while the pore sizes and the specific surface areas can be influenced by choosing different structure-directing agents similar to the synthesis of the pristine mesoporous silica materials.

The main aim of this work, the synthesis of spherical PMO particles in different sizes, was investigated in three different parts.

Spherical phenylene-bridged particles in the size range of 5 – 10  $\mu\text{m}$  for chromatographic application were synthesised by the addition of a co-solvent (ethanol) and a co-surfactant (CTAB) to a typical reaction solution consisting of water, HCl and a structure-directing agent (P123). Different parameters of the synthesis were studied in order to obtain information about the spherical shape and the particle size. The particle size could be varied by changing the pH value of the solution. The ethanol concentration and the organosilica precursor concentration influenced the particle shape to a high extent. Only in small concentration intervals nearly monodisperse spherical particles could be synthesised. Particles with a mean diameter of 10  $\mu\text{m}$ , a specific surface area of  $\approx 1200 \text{ m}^2/\text{g}$  and a pore diameter of 5.7 nm were chosen for separation experiments in HPLC. Particles below 3  $\mu\text{m}$  were removed by sieving first in a wet sieving procedure over three different sieves (200  $\mu\text{m}$ , 63  $\mu\text{m}$  and 20  $\mu\text{m}$  mesh) and additionally over three sieves via ultrasonic treatment (100  $\mu\text{m}$ , 20  $\mu\text{m}$  and 5  $\mu\text{m}$ ). The phenylene-bridged PMO spheres as well as a commercial silica material with comparable particle size and pore diameter was filled into a HPLC column in a wet filling procedure with 400 bar pressure.

By successful separation of three different test mixtures the differences between both stationary phases were investigated. The separation of benzene, naphthalene, biphenyl and phenanthrene could be achieved on both materials but under different conditions. The significantly higher specific surface area of the phenylene-bridged PMO spheres compared to Nucleosil 50-10 as well as the aromatic adsorption sites led to significantly higher retention

times in spite of a higher solvent flow rate. The usage of the same elution solvent (100 % *n*-hexane) showed the low relevance of the different surface polarities for this experiment. The separation of aspartam, BHT and sorbic acid was performed with MeOH/TBME 50:50 (v:v) and a solvent flow of 2 mL/min on both columns. A better separation was obtained on the PMO material because the resolution of the single peaks was much higher. The broader peaks, especially in case of aspartam, and the resulting higher retention time were in that case a disadvantage compared to the separation on Nucleosil 50-10. Significant differences between both materials regarding the surface polarity could be figured out by the separation of caffeine, coumarin and vanillin. Completely different separation conditions had to be chosen in order to obtain acceptable results on both materials. As elution solvent for the separation of caffeine, coumarin and vanillin on the PMO column a mixture of dichloromethane and methanol 90:10 (v:v) and a flow rate of 2 mL/min was applied. In contrast to these results the baseline separation on Nucleosil 50-10 was achieved with dichloromethane/methanol 98:2 (v:v) and a solvent flow of 2 mL/min. These results show that the incorporation of an organic functionality into the commercial “normal phases” might open up a new pathway of synthesising new separation materials. By incorporating a chiral organic moiety into the PMO material and endcapping the free silanol functionalities new columns for the separation of stereoisomers e.g. enantiomers can be developed. Another possibility is the incorporation of different organic functionalities and thus, the chance of tuning the polarity of the materials’ surfaces.

Even larger spherical particles for solvent vapour adsorption were synthesised by a new synthesis procedure including long chain alkylamines as structure-directing agents combined with the addition of ethanol as a co-solvent under mild acidic conditions. 1,2-bis(triethoxysilyl)ethane as well as 1,4-bis(triethoxysilyl)benzene were used as organosilica precursors. In both cases well-defined spherical particles in the size range of 10 to 300  $\mu\text{m}$  were obtained. The particle size could be influenced by the pH value of the reaction solution. With increasing pH value of the solution the particle size could be expanded up to 2 mm but the specific surface areas decrease and the pore diameters span over a wide range. All synthesised samples reveal only a poor ordering of mesopores which was proved by P-XRD as well as by TEM. A wormlike pore structure and an irregular pore size could be observed for all samples. Pore sizes of the ethane-bridged materials as well as the specific surface areas were higher in all cases ( $\text{BET} \approx 1000 \text{ m}^2/\text{g}$ ; pore diameter  $\approx 3 \text{ nm}$ ). Phenylene-

bridged spheres could only be obtained with micropores in the range between 1.2 and 1.5 nm and a specific surface area of maximal 600 m<sup>2</sup>/g.

Ethane-bridged and phenylene-bridged spheres were then synthesised with a mean particle diameter of  $\approx 80$  nm and filled in the channels of a microreactor. Vapour adsorption experiments were carried out by pumping benzene vapour or ethanol vapour mixed with nitrogen through the reactor. The adsorption capacity of the materials was measured by Raman spectroscopy. The adsorption capacity of the ethane-bridged PMO spheres was higher in case of benzene as well as in case of ethanol. This can be explained by the higher specific surface area and the larger pore diameters. The adsorption capacity of benzene and ethanol on the phenylene-bridged PMO spheres was significantly lower. With increasing temperature the adsorption capacity of both materials decreased. At the moment no clear explanation for the isotherm forms can be given. Further experiments are necessary and in progress.

The synthesis of spherical ethane-bridged PMOs via the modified Stöber reaction which means under mild basic conditions (addition of ammonia to the reaction solution) was successful and led to particles in the size range of 400 to 600 nm in diameter. The pore sizes could be varied with one surfactant species of alkyltrialkylammonium halide type. The formation of larger mesopores was achieved by application of surfactants with different alkyl chain lengths and different headgroups. The pore diameter could be expanded from 2.6 nm to 3.3 nm with increasing alkyl chain length of the surfactant from C<sub>16</sub> to C<sub>20</sub>. The influence of different synthesis parameters such as ammonia concentration and ethanol concentration were tested in order to expand the particle diameters. The variation of the ammonia concentration did not influence the particle size and the particle shape to a high extent but an increase of the ethanol concentration in the reaction solution led to larger particles but also to broader particle size distributions. All synthesised materials, independent of the applied surfactant, exhibited a wormlike pore structure which could be observed from several TEM images. The application of these materials in separation techniques such as chromatography is limited due to the small particle diameters. For capillary electrochromatography the particle size is suitable but separation tests were set aside because of the complexity of the chromatographic system that would be necessary.

Further experiments concerning the synthesis of PMO materials containing heteroatoms in the organic unit were carried out for this work.

Due to the possibility of incorporation of special coordination sites into the pore walls of the periodic mesoporous organosilicas these materials gained high relevance for application in the field of adsorption, especially for heavy metal ion adsorption. The synthesis of a new material containing secondary amine functionalities as well as ethane bridges by keeping the characteristics for mesoporous materials such a high ordering in pore arrangement, high specific surface areas and narrow pore size distributions was conducted and materials were stable up to an amine/ethane ratio of 0.45/0.55. Interesting observations concerning the phase behaviour of the resulting materials were made. Phase transitions from 2d hexagonal (space group  $p6mm$ ) to cubic (space group:  $Pm\bar{3}n$ ) were obtained with increasing amount of the amine-bridged organosilica precursor in the solution. Phase transitions from cubic ( $Pm\bar{3}n$ ) to 2d hexagonal ( $p6mm$ ) could be observed as well dependent on the synthesis temperature.

The particle morphology played an inferior role for application in heavy metal adsorption and thus, no focus was set on the synthesis of spherical particles. These materials as well as pristine SBA-15 silica were tested in  $\text{Cu}^{2+}$  adsorption experiments from aqueous solutions. For the concentration-dependent experiments two amine-bridged PMO materials (PMO-11 containing 11 % BTMPA, and PMO-33 containing 33 % BTMPA) and a SBA-15 silica material were chosen. The concentration-dependent adsorption showed the high capacity of the amine-bridged PMO material. Solutions with different  $\text{Cu}^{2+}$  concentrations were applied (0.001, 0.005, 0.01, 0.05, 0.1 mol) and in all cases nearly the complete  $\text{Cu}^{2+}$  was removed from the solutions. The measured region from the adsorption isotherm could be fitted linear with correlation coefficient of 0.999. No saturation with  $\text{Cu}^{2+}$  could be obtained during these experiments. In contrast, the adsorption on the SBA-15 showed a clear limit. The adsorption capacity is lower especially at high  $\text{Cu}^{2+}$  concentrations in the solutions. The maximum  $\text{Cu}^{2+}$  concentration was 1.2 mmol/g. For solutions with  $\text{Cu}^{2+}$  concentrations above 0.05 mol/L no further adsorption could be measured. Time-dependent adsorption investigations on the amine-bridged PMOs show that nearly the complete adsorption of the  $\text{Cu}^{2+}$  ions occurred within the first 10 minutes while the adsorption on the SBA-15 silica did not follow such a clear correlation. The washing step that followed in order to obtain information about the removal of the  $\text{Cu}^{2+}$  only by washing with water over a period of 24 hours proved the adsorption capacity of both materials. In most cases, for the PMO materials as well as for the SBA-15 silica, over 99 % of the adsorbed species remained inside the pore network of the mesoporous materials. In conclusion, both materials but especially the amine-bridged PMO material is suited for  $\text{Cu}^{2+}$  removal of polluted aqueous solutions.

Additional to the synthesis and application of (spherical) periodic mesoporous organosilica materials the formation mechanism of two well known materials was studied by *in situ* small angle X-ray scattering (SAXS).

The observation of the single reflections of mesoporous silica materials in the XRD patterns of highly ordered mesoporous materials has become a great field of interest because the data acquisition during the complete synthesis procedure facilitates drawing a conclusion about the different stages of the mesophase formation.

In order to obtain information about eventual occurring transition stages during the synthesis of 2d hexagonal ordered phenylene-bridged PMO materials *in situ* SAXS investigations of two different syntheses mixtures were recorded. Both synthesis pathways only differ from each other by the application of different structure-directing agents. The *in situ* SAXS investigations of the synthesis mixture containing the non-ionic triblock copolymer Pluronic® P123 as structure-directing agent confirmed that during the aging step a lamellar transition state is passed before forming the 2d hexagonal mesophase. Three well-defined reflections that could be indexed to a lamellar phase could be observed in the SAXS patterns of this synthesis mixture. The synthesis mixture containing the non-ionic surfactant Brij® 76 showed a completely different formation behaviour although the resulting material was 2d hexagonal structured as well. The reflections fit to a 3d hexagonal phase combined with the evolution of a 2d hexagonal phase with on-going reaction.

As a result of the complete work one can conclude that the research field of the periodic mesoporous organosilicas offers a wide domain of applications due to the incorporation of different organic moieties into the pore wall framework. Three of these possible applications were successfully investigated in this work. On this basis of research an improvement of the single methods can be carried out.

## 9 Zusammenfassung (German summary)

Innerhalb der letzten sieben Jahre wurde dem Forschungsgebiet der geordneten organisch-anorganischen Hybridmaterialien, besonders der Entwicklung neuer periodisch mesoporöser Organosilica-Materialien, viel Aufmerksamkeit gewidmet. Seit diese Materialien erstmals hergestellt wurden, wuchs das Interesse an der Anwendung auf vielen Gebieten der Materialwissenschaften wie zum Beispiel der Katalyse, der Schwermetall-Adsorption oder im Bereich der Stofftrennung ständig. Die chemischen Eigenschaften dieser Materialien können durch die Wahl der entsprechenden organischen Einheit des Organosilica-Präcursors gezielt gesteuert werden, während Porendurchmesser und die daraus resultierende spezifische innere Oberfläche ähnlich wie bei den reinen Silica-Materialien durch die Auswahl des strukturdirektierenden Agens beeinflusst werden können.

Das Hauptziel, die Synthese sphärischer PMO-Partikel in verschiedenen Größen, wurde in drei verschiedenen Teilen bearbeitet.

Sphärische phenylenverbrückte PMO-Partikel in einem Größenbereich von 5 bis 10  $\mu\text{m}$  für die Anwendung als Trennmaterial in der HPLC wurden in einer typischen Synthese, allerdings mit dem Zusatz eines Co-Solvens und eines Co-Tensids hergestellt. Verschiedene Syntheseparameter wurden untersucht, um Informationen über die Partikelform und die Partikelgröße zu erhalten. Auch hier konnte der Partikeldurchmesser durch Variation des pH-Wertes beeinflusst werden. Veränderungen in den Konzentrationen sowohl des Ethanol als auch des Präcursors zeigten signifikante Veränderungen der Partikelform. Nur in sehr geringen Konzentrationsintervallen konnten fast monodisperse Partikel erhalten werden. Für die chromatographischen Experimente wurden Partikel mit einem mittleren Durchmesser von 10  $\mu\text{m}$ , einer spezifischen Oberfläche von  $\approx 1200 \text{ m}^2/\text{g}$  und einem Porendurchmesser von 5.7 nm ausgewählt. Durch zwei verschiedene Siebprozeduren, einer Nasssiebung über drei verschiedene Siebe (200  $\mu\text{m}$ , 63  $\mu\text{m}$  und 20  $\mu\text{m}$  Maschenweite) sowie eine Nasssiebung mittels Ultraschall über drei weitere Siebe (100  $\mu\text{m}$ , 20  $\mu\text{m}$  und 5  $\mu\text{m}$  Maschenweite), konnten Partikel mit einem geringeren Durchmesser als 3  $\mu\text{m}$  fast vollständig entfernt werden. Es wurden HPLC-Säulen mit dem neu synthetisierten Material und mit einem kommerziellen reinen Silica-Material mit vergleichbaren Eigenschaften bezüglich der Partikelgröße und des Porendurchmessers nass und unter 400 bar Druck gepackt.

Durch die Trennung von drei verschiedenen Mischungen von Testsubstanzen konnten Unterschiede zwischen den beiden stationären Phasen herausgearbeitet werden. Eine erfolgreiche Trennung von Benzol, Naphthalin, Biphenyl und Phenanthren konnte auf beiden Materialien erzielt werden, allerdings unter verschiedenen Bedingungen. Die verglichen mit dem Nucleosil 50-10 deutlich höhere spezifische Oberfläche sowie die aromatischen Funktionen innerhalb der Porenwände des neuen Materials führten zu höheren Retentionszeiten trotz schon erhöhter Flussrate des Eluenten. Allerdings zeigte die Verwendung des gleichen Lösungsmittels (100 % *n*-Hexan) für die Trennung auf beiden Säulen, dass die unterschiedliche Polarität der Oberflächen für dieses Experiment nur von geringer Bedeutung war. Die Trennung von Aspartam, BHT und Sorbinsäure wurde auf beiden Säulen unter den gleichen Bedingungen bezüglich des Eluenten und der Fließgeschwindigkeit durchgeführt. Aufgrund der höheren Auflösung der einzelnen Peaks auf dem phenylenverbrückten PMO-Material war die Trennung dieser Substanzen qualitativ höherwertig als auf der Nucleosil-Säule, wobei die breiteren Peaks und die höheren Retentionszeiten des Aspartams auf der PMO-Säule einen Nachteil des neuen Materials darstellten. Dass signifikante Unterschiede in der Oberflächenpolarität beider Materialien bestehen, konnte schließlich bei der Trennung von Koffein, Cumarin und Vanillin gezeigt werden. Hier konnte die Mischung nicht mit dem gleichen Eluenten auf beiden Säulen getrennt werden. Die Trennung der drei Substanzen auf der PMO-Säule erfolgte mit einem Eluentengemisch bestehend aus Dichlormethan/Methanol 90:10 (v:v) und einem Eluentenfluss von 2 mL/min, während eine Grundlinientrennung der Stoffe auf der Nucleosil-Säule in akzeptabler Analysenzeit mit einem Eluentengemisch bestehend aus Dichlormethan/Methanol 98:2 (v:v) und einer Flussrate von 2 mL/min erfolgte. Diese Ergebnisse zeigen, dass das Einbringen einer organischen Einheit in das Netzwerk der Porenwand einer herkömmlichen „Normalphase“ neue Wege für die Synthese neuer Trennmaterialien darstellt. Die Einbindung einer chiralen Einheit in ein PMO-Material kombiniert mit anschließendem Endcapping der freien Silanolgruppen ermöglicht so, Säulen herzustellen, auf denen Stereoisomere wie z.B. Enantiomere getrennt werden können. Eine weitere Möglichkeit der Nutzung dieser Synthese ist die Einbindung verschiedener organischer Funktionen, was eine Einstellung der Oberflächenpolarität des Materials realisierbar macht.

Größere sphärische Partikel, die in der Lösungsmitteldampf-Adsorption eingesetzt werden sollten, wurden nach einer neuen Syntheseprozedur mittels eines langkettigen Amins als

Strukturdirektor und dem Zusatz von Ethanol zur Synthesemischung unter schwach sauren Bedingungen hergestellt. Sowohl 1,2-Bis-(triethoxysilyl)ethan (BTEE) als auch 1,4-Bis-(triethoxysilyl)benzol (BTEB) wurden als Präkursoren verwendet. Mit beiden Präkursoren konnten Partikel in der Größe zwischen 25 und 300 bzw. 10 und 300  $\mu\text{m}$  synthetisiert werden. In mehreren Experimenten wurde herausgearbeitet, dass die Partikelgröße abhängig vom pH-Wert der Lösung ist. Hohe pH-Werte lieferten bis zu 2 mm große Partikel, allerdings sank die spezifische Oberfläche und die Porenradienverteilungen wurden deutlich breiter. Alle Materialien wiesen nur eine geringe Ordnung der Poren auf, was mittels Röntgenbeugung belegt wurde. Die wurmartige Porenstruktur und die breite Verteilung der Porendurchmesser wurden anhand der TEM-Messungen verdeutlicht. Die Porendurchmesser der ethanverbrückten Materialien lagen unabhängig von der Variation der Syntheseparameter immer deutlich höher ( $\text{BET} \approx 1000 \text{ m}^2/\text{g}$ , Porendurchmesser  $\approx 3 \text{ nm}$ ). Die Porendurchmesser der phenylenverbrückten PMOs wiesen dagegen immer Poren im Mikroporenbereich zwischen 1.3 und 1.5 nm auf. Die maximal erzielten spezifischen Oberflächen betrugen  $600 \text{ m}^2/\text{g}$ .

Ethan- und phenylenverbrückte PMO-Partikel mit einem mittleren Partikeldurchmesser von 80  $\mu\text{m}$  wurden in die Kanäle eines Mikroreaktors gefüllt und die Adsorption von Benzol bzw. Ethanol untersucht, indem ein Gasgemisch aus Stickstoff und Lösungsmitteldampf durch den Reaktor gepumpt wurde. Die Adsorptionskapazität beider Materialien wurde dann mittels Raman-Spektroskopie bestimmt. Die Adsorptionskapazität der ethanverbrückten Partikel sowohl bezüglich Benzol als auch Ethanol war deutlich höher, was auf die höhere Oberfläche und die größeren Poren zurückgeführt werden kann. Die Adsorption von Benzol und Ethanol in den phenylenverbrückten Partikeln war dagegen deutlich geringer. Die Adsorption sank für beide Materialien mit steigender Reaktortemperatur. Eine Begründung für die Isothermenformen kann an dieser Stelle noch nicht gegeben werden, allerdings sind weitere notwendige Versuche in Arbeit.

Die erfolgreiche Darstellung sphärischer ethanverbrückter PMO-Partikel mittels der modifizierten Stöber-Reaktion unter schwach basischen Bedingungen (durch den Zusatz von Ammoniak) lieferte Partikel mit Durchmessern zwischen 400 und 600 nm. Die Porengrößen wurden mit nur einer Spezies vom Alkyltrialkylammoniumhalogenid-Typ durch Variation der Kopfgruppen oder der Alkylkettenlänge verändert. Auf diese Weise konnte der Porendurchmesser von 2.6 nm auf 3.3 nm erweitert werden. Der Einfluss verschiedener Syntheseparameter wie der Ethanol- und der Ammoniakkonzentration wurde dahingehend

untersucht, die Partikeldurchmesser zu vergrößern. Die Variation der Ammoniakkonzentration zeigte keinen nennbaren Effekt auf die Partikelgröße und Partikelform wohingegen höhere Ethanolkonzentrationen größere Partikel und breitere Partikelverteilungen zur Folge hatten. Die TEM Aufnahmen zeigten für alle untersuchten Partikel eine wurmartige Porenstruktur. Eine mögliche Anwendung dieser Materialien in der Chromatographie ist allerdings beschränkt auf Kapillarelektrochromatographie, da die Partikeldurchmesser für normale Hochleistungsflüssigkeitschromatographie zu gering sind.

In dieser Arbeit wurden außerdem weitere Experimente mit dem Ziel der Synthese eines PMO-Materials mit einem Heteroatom in der organischen Einheit durchgeführt.

Die Möglichkeit spezielle Koordinationszentren in die Porenwände der PMO-Materialien zu integrieren, ist von hoher Bedeutung für Anwendung auf dem Gebiet der Adsorption, speziell der Schwermetallionen-Adsorption. Die Synthese eines neuen Materials, welches sekundäre Aminfunktionen ebenso wie Ethanbrücken enthält und dabei die für die mesoporösen Materialien typischen Merkmale wie eine hohe Ordnung der Poren, hohe spezifische Oberflächen und schmale Porenradienverteilungen aufweist, wurde durchgeführt und Materialien bis zu einem Amin/Ethan-Verhältnis von 0.45/0.55 konnten synthetisiert werden. Diese Materialien lieferten interessante Ergebnisse bezüglich der erhaltenen Strukturen. Es trat ein Phasenübergang von zweidimensional hexagonal (Raumgruppe:  $p6mm$ ) zu einer kubischen Struktur mit der Raumgruppe  $Pm\bar{3}n$  mit steigender Konzentration des aminverbrückten Präcursors auf. Phasenübergänge von der kubischen Struktur ( $Pm\bar{3}n$ ) zu einer zweidimensionalen hexagonalen Struktur wurden mit steigender Synthesetemperatur und kürzeren Rührzeiten erhalten.

Da die Partikelmorphologie für diese Anwendung in der Schwermetallionen-Adsorption eher eine untergeordnete Rolle spielt, wurde der Schwerpunkt bei diesen Materialien nicht auf die Synthese sphärischer Partikel gelegt. Für die Kupfer-Adsorptionsexperimente aus wässriger Lösung wurden zwei der neuen Materialien mit unterschiedlicher Aminkonzentration (11 % Amin und 33 % Amin) sowie ein reines Silica-Material (SBA-15) gewählt. Die konzentrationsabhängigen Experimente bewiesen die hohe Adsorptionskapazität der neuen PMO-Materialien. Lösungen unterschiedlicher Kupferkonzentrationen (0.001, 0.005, 0.01, 0.05, 0.1 mol) wurden verwendet und in jedem Test wurde durch das PMO-Material mehr als 99 % des Kupfers aus der Lösung entfernt. Der gemessene Bereich der Adsorptionsisotherme wurde linear angefüttet und ergab eine Gerade mit einem Korrelationskoeffizienten von 0.999. Eine Sättigung mit  $\text{Cu}^{2+}$  konnte in diesem Konzentrationsbereich nicht erhalten werden. Im

Gegensatz zu diesen Ergebnissen war die Adsorptionskapazität des SBA-15 Silica-Materials für  $\text{Cu}^{2+}$  Ionen mit einem Grenzwert von 1.2 mmol  $\text{Cu}^{2+}$ /g SBA-15 deutlich geringer. Ab einer bestimmten  $\text{Cu}^{2+}$ -Konzentration in der Lösung (0.05 mol/L) wurde keine weitere Steigerung der Adsorption festgestellt. Die zeitabhängigen Adsorptionsexperimente zeigten, dass durch das PMO-Material über 97 % des Kupfers innerhalb von 10 Minuten aus der Lösung entfernt wurde, während hier die Ergebnisse der Adsorption am reinen Silica-Material keinen eindeutigen Zusammenhang zwischen Adsorptionsmenge und Einwirkzeit zeigten. Der sich an diese Experimente anschließende Waschschrift von 24 Stunden sollte über das Auswaschen des Kupfers aus dem jeweiligen Material Aufschluss geben. In fast allen Fällen, sowohl bei den PMO-Materialien als auch beim SBA-15 Silica, blieb über 99 % des adsorbierten Kupfers innerhalb der Poren. Aus diesen Experimenten kann man schließen, dass die Materialien, allerdings besonders die PMO-Materialien, für die Entfernung von Kupferionen aus wässrigen Lösungen sehr gut geeignet sind.

Zusätzlich zu den Synthesen und der Anwendung der (sphärischen) periodisch mesoporösen Organosilica-Materialien wurden im Rahmen dieser Arbeit auch Studien über den Bildungsmechanismus zweier bekannter PMO-Materialien mit Hilfe von *in situ* Kleinwinkelstreuung (SAXS) durchgeführt.

Die Betrachtung der Entwicklung der einzelnen Reflexe in den entsprechenden Röntgenbeugungsdiagrammen der mesoporösen Organosilica-Materialien entwickelte sich zu einem weiteren Gebiet von hohem Interesse, da die Datenaufzeichnung während der gesamten Synthesedauer Rückschlüsse auf eventuell auftretende andere Strukturierungen als Übergangszustände zulässt.

Um Informationen über die eventuelle Bildung von anderen Mesophasen während der Synthese von zweidimensional hexagonal geordneten phenylenverbrückten PMO-Materialien zu erhalten, wurde *in situ* Kleinwinkelstreuung an zwei verschiedenen Synthesemischungen gemessen. Der Unterschied der beiden Synthesen lag nur in der Verwendung verschiedener nichtionischer strukturdirigierender Agenzien. Die *in situ* SAXS Experimente der Synthesemischung mit Pluronic® P123 als strukturdirigierendem Agens zeigen, dass während der Rührphase der Synthese ein lamellarer Zwischenzustand durchlaufen wird, bevor es zur Bildung der zweidimensional hexagonalen Struktur kommt. Das Beugungsdiagramm eines Zwischenzustandes zeigte drei gut aufgelöste Reflexe, die als 001, 002 und 003 einer lamellaren Phase induziert werden konnten. Die Reaktionsmischung, die das Tensid Brij® 76 enthielt, zeigte ein anderes Verhalten während der Synthese, obwohl das resultierende

Material ebenfalls eine zweidimensional hexagonale Struktur aufweist. Die Reflexe konnten einer dreidimensional hexagonalen Phase zugeordnet werden, wobei eine fast zeitgleiche Entwicklung der zweidimensionalen hexagonalen Phase mit fortschreitender Reaktion beobachtet werden konnte.

Das Fazit dieser Arbeit ist, dass das Gebiet der periodisch mesoporösen Organosilica-Materialien durch die Einbindung organischer Funktionalitäten in die Netzstruktur der Porenwand eine weite Palette and Anwendungsmöglichkeiten bietet, von denen drei verschiedene Bereiche in dieser Arbeit erfolgreich untersucht wurden. Auf Basis dieser Grundlagenforschung ist es nun möglich die einzelnen Methoden zu verfeinern.

## 10 References

- [1] C. T. Kresge, M. E. Leonowicz, W. J. Roth, J. C. Vartuli, J. S. Beck, *Nature* **1992**, 359, 710.
- [2] J. S. Beck, J. C. Vartuli, W. J. Roth, M. E. Leonowicz, C. T. Kresge, K. D. Schmitt, C. T.-W. Chu, D. H. Olson, E. W. Sheppard, S. B. McCullen, J. B. Higgins, J. L. Schlenker, *J. Am. Chem. Soc.* **1992**, 114, 10834.
- [3] F. J. Brieler, P. Grundmann, M. Fröba, L. Chen, P. J. Klar, W. Heimbrod, H.-A. Krug von Nidda, T. Kurz, A. Loidl, *J. Am. Chem. Soc.* **2004**, 126, 797.
- [4] F. J. Brieler, P. Grundmann, M. Fröba, L. Chen, P. J. Klar, W. Heimbrod, H.-A. Krug von Nidda, T. Kurz, A. Loidl, *Eur. J. Inorg. Chem.* **2005**, 18, 3597.
- [5] T. Tsoncheva, D. Paneva, I. Mitov, H. Huwe, M. Fröba, M. Dimitrov, C. Minchev, *React. Kinet. Catal. Lett.* **2004**, 83, 299.
- [6] C. Michev, H. Huwe, T. Tsoncheva, D. Paneva, M. Dimitrov, I. Mitov, M. Fröba, *Microporous Mesoporous Mater.* **2005**, 8, 333.
- [7] C. Bossière, M. Kümmel, M. Persin, A. Larbot, E. Prouzet, *Adv. Funct. Mater.* **2001**, 11, 129.
- [8] F. Hoffmann, M. Cornelius, J. Morell, M. Fröba, *Angew. Chem. Int. Ed.* **2006**, 45, 3216.
- [9] Q. Huo, D. I. Margolese, G. D. Stucky, *Chem. Mater.* **1996**, 8, 1147.
- [10] G. S. Attard, J. C. Glyde, C. G. Göltner, *Nature* **1995**, 378, 366.
- [11] A. Monnier, F. Schüth, Q. Huo, D. Kumar, D. Margolese, R. S. Maxwell, G. Stucky, M. Krishnamurty, P. Petroff, A. Firouzi, M. Janicke, B. Chmelka, *Science* **1993**, 261, 1299.
- [12] D. Zhao, J. Feng, Q. Huo, N. Melosh, G. H. Fredrickson, B. F. Chmelka, G. D. Stucky, *Science* **1998**, 279, 548.
- [13] Q. Huo, D. I. Margolese, U. Ciesla, P. Feng, T. E. Gier, P. Sieger, R. Leon, P. M. Petroff, F. Schüth, G. D. Stucky, *Nature* **1994**, 368, 317.
- [14] Q. Huo, D. I. Margolese, U. Ciesla, D. G. Demuth, P. Feng, T. E. Gier, P. Sieger, A. Firouzi, B. F. Chmelka, F. Schüth, G. D. Stucky, *Chem. Mater.* **1994**, 6, 1176.
- [15] P. T. Tanev, T. J. Pinnavaia, *Science* **1995**, 267, 865.
- [16] S. A. Bagshaw, E. Prouzet, T. J. Pinnavaia, *Science* 1995, 269, 1242.
- [17] R. Ryoo, S. H. Joo, S. Jun, *J. Phys. Chem. B* **1999**, 103, 7743.
- [18] D. A. Loy, K.J. Shea, *Chem. Rev.* **1995**, 95, 1431.
- [19] K. J. Shea, D.A. Loy, *Chem. Mater.* **2001**, 13, 3306.

- [20] S. Inagaki, S. Guan, Y. Fukushima, T. Ohsuna, O. Terasaki, *J. Am. Chem. Soc.* **1999**, *121*, 9611.
- [21] T. Asefa, M. J. MacLachlan, N. Coombs, G. A. Ozin, *Nature* **1999**, *402*, 867.
- [22] B. J. Melde, B. T. Holland, C. F. Blanford, A. Stein, *Chem. Mater.* **1999**, *11*, 3302.
- [23] K. Nakajima, D. Lu, J. N. Kondo, I. Tomita, S. Inagaki, M. Hara, S. Hayashi, K. Domen, *Chem. Letters* **2003**, *32*, 950.
- [24] S. Guan, S. Inagaki, T. Ohsuna, O. Terasaki, *J. Am. Chem. Soc.* **2000**, *122*, 5660.
- [25] A. Sayari, S. Hamoudi, Y. Yang, I. L. Moudrakovski, J. R. Ripmeester, *Chem. Mater.* **2000**, *12*, 3857.
- [26] S. Hamoudi, Y. Yang, I. L. Moudrakovski, S. Lang, A. Sayari, *J. Phys. Chem B* **2001**, *105*, 9118.
- [27] T. Asefa, M. J. MacLachlan, H. Grondy, N. Coombs, G. A. Ozin, *Angew. Chem.* **2000**, *112*, 1878 – 1881; *Angew. Chem. Int. Ed.* **2000**, *39*, 1808.
- [28] T. Ren, X. Zhang, J. Suo, *Microporous Mesoporous Mater.* **2002**, *54*, 139.
- [29] C. Yoshina-Ishii, T. Asefa, N. Coombs, M. J. MacLachlan, G. A. Ozin, *Chem. Commun.* **1999**, 2539.
- [30] G. Temtsin, T. Asefa, S. Bittner, G. A. Ozin, *J. Mater. Chem.* **2001**, *11*, 3202.
- [31] S. Inagaki, S. Guan, T. Ohsuna, O. Terasaki, *Nature* **2002**, *416*, 304.
- [32] N. Bion, P. Ferreira, A. Valente, I. S. Goncalves, J. Rocha, *J. Mater. Chem.* **2003**, *13*, 1910.
- [33] M. P. Kapoor, Q. Yang, S. Inagaki, *J. Am. Chem. Soc.* **2002**, *124*, 15176.
- [34] A. Sayari, W. Wang, *J. Am. Chem. Soc.* **2005**, *127*, 12194.
- [35] M. Cornelius, F. Hoffmann, M. Fröba, *Chem. Mater.* **2005**, *17*, 6674.
- [36] M. P. Kapoor, Q. Yang, S. Inagaki, *Chem. Mater.* **2004**, *16*, 1209..
- [37] J. Morell, C. V. Teixeira, M. Cornelius, V. Rebbin, M. Tiemann, H. Amenitsch, M. Fröba, M. Lindén, *Chem. Mater.* **2004**, *16*, 5564.
- [38] D. Zhao, Q. Huo, J. Feng, B. F. Chmelka, G. D. Stucky, *J. Am. Chem. Soc.* **1998**, *120*, 6024.
- [39] G. J. de A. A. Soler-Illia, E. L. Crepaldi, D. Grosso, C. Sanchez, *Curr. Opin. Colloid Interface Sci.* **2003**, *8*, 109.
- [40] S. Förster, *Top. Curr. Chem.* **2003**, *226*, 1.
- [41] C. Yu, Y. Yu, D. Zhao, *Chem. Commun.* **2000**, 575.
- [42] O. Muth, C. Schellbach, M. Fröba, *Chem. Commun.* **2001**, 2032.

- [43] M. C. Burleigh, M. A. Markowitz, E. M. Wong, J.-S. Lin, B. P. Gaber, *Chem. Mater.* **2001**, *13*, 4411.
- [44] W. Guo, J.-Y. Park, M.-O. Oh, H.-W. Jeong, W.-J. Cho, I. Kim, C.-S. Ha, *Chem. Mater.* **2003**, *15*, 2295.
- [45] X. Y. Bao, X. S. Zhao, X. Li, P. A. Chia, J. Li, *J. Phys. Chem. B* **2004**, *108*, 4684.
- [46] X. Y. Bao, X. S. Zhao, X. Li, J. Li, *Appl. Surf. Sci.* **2004**, *237*, 380.
- [47] X. Y. Bao, X. S. Zhao, S. Z. Qiao, S. K. Bhatia, *J. Phys. Chem. B* **2004**, *108*, 16441.
- [48] H. Zhu, D. J. Jones, J. Zajac, J. Rozière, R. Dutartre, *Chem. Commun.* **2001**, 2568.
- [49] E. B. Cho, K. Char, *Chem. Mater.* **2004**, *16*, 270.
- [50] W. Guo, I. Kim, C.-S. Ha, *Chem. Commun.* **2003**, 2692.
- [51] J. R. Matos, M. Kruk, L. P. Mercuri, M. Jaroniec, T. Asefa, N. Coombs, G. A. Ozin, T. Kamiyama, O. Terasaki, *Chem. Mater.* **2002**, *14*, 1903.
- [52] L. Zhao, G. Zhu, D. Zhang, Y. Di, Y. Chen, O. Terasaki, S. Qiu, *J. Phys. Chem. B* **2005**, *109*, 765.
- [53] Y. Goto, S. Inagaki, *Chem. Commun.* **2002**, 2410.
- [54] W. Wang, S. Xie, W. Zhou, A. Sayari, *Chem. Mater.* **2004**, *16*, 1756.
- [55] J. Morell, G. Wolter, M. Fröba, *Chem. Mater.* **2005**, *17*, 804.
- [56] M. C. Burleigh, M. A. Markowitz, M. S. Spector, B. P. Gaber, *J. Phys. Chem. B* **2002**, *106*, 9712.
- [57] M. C. Burleigh, S. Jayasundera, C. W. Thomas, M. S. Spector, M. A. Markowitz, B. P. Gaber, *Colloid Polym Sci* **2004**, *282*, 728.
- [58] M. C. Burleigh, M. A. Markowitz, S. Jayasundera, M. S. Spector, C. W. Thomas, B. P. Gaber, *J. Phys. Chem. B* **2003**, *107*, 12628.
- [59] S. Hamoudi, S. Kaliaguine, *Chem. Commun.* **2002**, 2118.
- [60] A. Sayari, Y. Yang, *Chem. Commun.* **2002**, 2582.
- [61] W. Wang, W. Zhou, A. Sayari, *Chem. Mater.* **2003**, *15*, 4886.
- [62] W. J. Hunks, G. A. Ozin, *Chem. Commun.* **2004**, 2426.
- [63] W. J. Hunks, G. A. Ozin, *Chem. Mater.* **2004**, *16*, 5465.
- [64] L. Zhang, Q. Yang, W.-H. Zhang, Y. Li, J. Yang, D. Jiang, G. Zhu, C. Li, *J. Mater. Chem.* **2005**, *15*, 2562.
- [65] M. P. Kapoor, S. Inagaki, *Chem. Mater.* **2002**, *14*, 3509.
- [66] M. Kuroki, T. Asefa, W. Whitnal, M. Kruk, C. Yoshina-Ishii, M. Jaroniec, G. A. Ozin, *J. Am. Chem. Soc.* **2002**, *124*, 13886.
- [67] K. Landskron, B. D. Hatton, D. D. Perovic, G. A. Ozin, *Science* **2003**, *302*, 266.

- [68] K. Landskron and G.A.Ozin, *Science* **2004**, 306, 1529.
- [69] W. J. Hunks, G. A. Ozin, *Adv. Funct. Mater.* **2005**, 15, 259.
- [70] R. J. P. Corriu, A. Mehdi, C. Rey  , C. Thieuleux, *Chem. Commun.* **2002**, 1382.
- [71] R. J. P. Corriu, A. Mehdi, C. Rey  , C. Thieuleux, *Chem. Commun.* **2003**, 1564.
- [72] R. J. P. Corriu, A. Mehdi, C. Rey  , C. Thieuleux, *New J. Chem.* **2003**, 27, 905.
- [73] M. Alvaro, B. Ferrer, H. Garc  a, F. Rey, *Chem. Commun.* **2002**, 2012.
- [74] M. Alvaro, B. Ferrer, V. Forn  s, H. Garc  a, *Chem. Commun.* **2001**, 2546.
- [75] T. Asefa, M. Kruk, M. J. MacLachlan, N. Coombs, H. Grondey, M. Jaroniec, G. A. Ozin, *J. Am. Chem. Soc.* **2001**, 123, 8520.
- [76] S. Hamoudi, S. Kaliaguine, *Microporous Mesoporous Mater.* **2003**, 59, 195.
- [77] X. Yuan, H. I. Lee, J. W. Kim, J. E. Yie, J. M. Kim, *Chem. Letters* **2003**, 32, 650.
- [78] Q. Yang, J. Liu, J. Yang, M. P. Kapoor, S. Inagaki, C. Li, *J. Catal.* **2004**, 228, 265.
- [79] J. Morell, M. G  ngerich, G. Wolter, J. Jiao, M. Hunger, P. J. Klar, M. Fr  ba, *J. Mater.Chem.* **2006**, 16, 2809.
- [80] G. Kolbe, *Ph.D. Thesis*, Friedrich Schiller University Jena, Germany, **1956**.
- [81] W. St  ber, A. Fink, E. Bohn, *J. Colloid Interface Sci.* **1968**, 26, 62.
- [82] C. Kaiser, *Ph.D. Thesis*, Johannes Gutenberg University Mainz, Germany, **1996**.
- [83] C. Kaiser, K. K. Unger, *German Patent DE-195 30031 A1*, **1997**.
- [84] C. Kaiser, G. B  chel, S. L  dtke, I. Lauer, K. K. Unger, in *Characterisations of porous solids IV* (Eds: B. McEnaney, T. J. Mays, J. Rouquerol, F. Rodr  guez-Reinoso, K. S. W. Sing, K. K. Unger), Royal Society of Chemistry, Cambridge **1997**, pp.406 – 412.
- [85] Q. Huo, J. Feng, F. Sch  th, G. D. Stucky, *Chem. Mater.* **1997**, 9, 14.
- [86] G. B  chel, K. K. Unger, A. Matsumoto, K. Tsutsumi, *Adv. Mater.* **1998**, 10, 1036.
- [87] H. Giesche, *Ph.D. Thesis*, Johannes-Gutenberg University, Mainz, **1987**.
- [88] G. B  chel, M. Gr  n, K. K. Unger, A. Matsumoto, K. Tsutsumi, *Supramolecular Science* **1998**, 5, 253.
- [89] L. Qi, J. Ma, H. Cheng, Z. Thao, *Chem. Mater.* **1998**, 10, 1623
- [90] M. Gr  n, K. K. Unger, A. Matsumoto, K. Tsutsumi, *Microporous Mesoporous Mater.* **1999**, 27, 207.
- [91] K. Schumacher, M. Gr  n, K. K. Unger, *Microporous Mesoporous Mater.* **1999**, 27, 201.
- [92] K. Schumacher, C. du Fresne von Hohenesche, K. K. Unger, R. Ulrich, A. du Chesne, U. Wiesner, H. W. Spiess, *Adv. Mater.* **1999**, 11, 1194.
- [93] L. Sierra, B. Lopez, J.-L. Guth, *Microporous Mesoporous Mater.* **2000**, 39, 519.

- [94] K. K. Unger, D. Kumar, M. Grün, G. Büchel, S. Lüdtke, T. Adam, K. Schumacher, S. Renker, *J. Chromator. A* **2000**, 892, 47.
- [95] C. Bossière, A. van der Lee, A. El Mansouri, A. Labot, E. Prouzet, *Chem. Commun.* **1999**, 2047.
- [96] C. Bossière, A. Labot, E. Prouzet, *Chem. Mater.* **2000**, 12, 1937.
- [97] K. Yano, N. Suzuki, Y. Akimoto, Y. Fukushima, *Bull. Chem. Soc. Jpn.* **2002**, 75, 1977.
- [98] J. L. Blin, A. Léonard, B. L. Su, *Chem. Mater.* **2001**, 13, 3542.
- [99] K. Kosuge, P. S. Singh, *Chem. Mater.* **2001**, 13, 2476.
- [100] K. Kosuge, P. S. Singh, *Microporous Mesoporous Mater.* **2001**, 44-45, 139.
- [101] B. Pawels, G. Van Tendeloo, C. Thoelen, W. Van Rhijn, P. A. Jacobs, *Adv. Mater.* **2001**, 13, 1317.
- [102] H. B. S. Chan, P. M. Budd, T. deV. Naylor, *J. Mater. Chem.* **2001**, 11, 951.
- [103] C. Oh, S.-C. Chung, S.-I. Shin, J. C. Kim, S.-S. Im, S.-G. Oh, *J. Coll. Interf. Sci.* **2002**, 254, 79.
- [104] T. Martin, G. Galarneau, F. Di Renzo, F. Fajula, D. Plee, *Angew. Chem. Int. Ed.* **2002**, 41, 2590.
- [105] C. Petitto, A. Galarneau, M.-F. Driole, B. Chiche, B. Alonso, F. Di Renzo, F. Fajula, *Chem. Mater.* **2005**, 17, 2120.
- [106] G. V. R. Rao, G. P. López, J. Bravo, H. Pham, A. K. Datye, H. Xu, T. L. Ward, *Adv. Mater.* **2002**, 14, 1301.
- [107] K. Kosuge, T. Murakami, N. Kikukawa, M. Takemori, *Chem. Mater.* **2003**, 15, 3184.
- [108] Y. Ma, L. Qi, J. Ma, Y. Wu, O. Liu, H. Cheng, *Colloids and Surfaces A: Physicochem. Eng. Aspects* **2003**, 229, 1.
- [109] K. Yano, Y. Fukushima, *J. Mater. Chem.* **2004**, 14, 1579.
- [110] A. Lind, C. Du Fresne von Hohenesche, J.-H. Smått, M. Lindén, K. K. Unger, *Microporous Mesoporous Mater.* **2003**, 66, 219.
- [111] S. Huh, J. W. Wiench, B. G. Trewyn, S. Song, M. Pruski, V. S.-Y. Lin, *Chem. Commun.* **2003**, 2364.
- [112] S. Sadasivan, D. Kushalani, S. Mann, *J. Mater. Chem.* **2003**, 13, 1023.
- [113] V. Ganesan, A. Walcarius, *Langmuir*, **2004**, 20, 3632.
- [114] L. Beaudet, K.-Z. Hossain, L. Mercier, *Chem. Mater.* **2003**, 15, 327.
- [115] J. Ding, C. J. Hudalla, J. T. Cook, D. P. Walsh, C. E. Boissel, P. C. Iraneta, J. E. O’Gara, *Chem. Mater.* **2004**, 16, 670.
- [116] J. E. Hampsey, S. Arsenault, Q. Hu, Y. Lu, *Chem. Mater.* **2005**, 17, 2475.

- [117] M. P. Kapoor, S. Inagaki, *Chem. Letters* **2004**, 33, 88.
- [118] D.-J. Kim, J.-S. Chung, W.-S. Ahn, G.-W. Kang, W.-J. Cheong, *Chem. Letters* **2004**, 33, 422.
- [119] Y. Xia, Z. Yang, R. Mokaya, *Chem. Mater.* **2006**, 18, 1141.
- [120] G. Zhu, Q. Yang, D. Jiang, J. Yang, L. Zhang, Y. Li, C. Li, *J. Chromatogr. A* **2006**, 1103, 257.
- [121] K. Flodström, C. V. Teixeira, H. Amenitsch, V. Alfredsson, M. Lindén, *Langmuir* **2004**, 20, 4885.
- [122] K. S. W. Sing, D. H. Everett, R. A. W. Haul, L. Mouscou, R. A. Pierotti, J. Rouquerol, T. Siemieniewska, *Pure & Appl. Chem.* **1985**, 57, 603.
- [123] S. Brunauer, P. H. Emmet, E. Teller, *J. Am. Chem. Soc.* **1938**, 60, 309.
- [124] E. P. Barrett, L. G. Joyner, P. P. Halenda, *J. Am. Chem. Soc.* **1951**, 73, 373.
- [125] M. Heuer, K. Leschonski, *Part.Charact.* **1985**, 2, 7.
- [126] [www. Sympatec.com/laserdiffraction](http://www.Sympatec.com/laserdiffraction)
- [127] C. F. Bohren, D. R. Huffman, *Absorption and Scattering of Light by Small Particles*, John Wiley & Sons, New York, **1983**.
- [128] U. Stark, *Granulometrische Charakterisierung feindisperser Schüttgüter*, Praktikumsanleitung, Bauhaus-Universität Weimar, Fakultät Bauingenieurwesen, **2004**
- [129] U. Teipel, U. Förster-Barth, *Partikelcharakterisierung mittels Laserbeugungsspektrometrie und dynamischer Lichtstreuung*, **2000**, Schüttgut 6.
- [130] V. R. Meyer, *Praxis der Hochleistungsflüssigchromatographie*, Wiley-VCH, 9. Auflage, **2004**.
- [131] H. G. Maier, *Lebensmittel- und Umweltanalytik*, Steinkopff Verlag, Darmstadt, **1990**.
- [132] IUPAC Manual of Symbols and Technology, Appendix 2, Part 1, *Pure appl. Chem.* **1972**, 31, 578.
- [133] S. Kamiya, H. Tanaka, S. Che, T. Tatsumi, O. Terasaki, *Solid State Science* **2003**, 5, 197.
- [134] M. A. Wahab, I. Kim, C.-S. Ha, *J. Solid State Chem.* **2004**, 177, 3439.
- [135] M. A. Wahab, I. Imae, Y. Kawakami, C.-S. Ha, *Chem. Mater.* **2005**, 17, 2165.
- [136] S. Liu, P. Cool, O. Collart, P. Van Der Voort, E. F. Vansant, O. I. Lebedev, G. Van Tendeloo, M. Jiang, *J. Phys. Chem. B* **2003**, 107, 10405.
- [137] M. Thommes, R. Köhn, M. Fröba, *J. Phys. Chem. B* **2000**, 104, 7932.
- [138] R. Köhn, *Ph.D. Thesis*, University of Hamburg, Germany, **2001**.
- [139] G. H. Bogush, M. A. Tracy, C. F. Zukowski, *J. Non-Cryst. Solids* **1988**, 104, 95.

- [140] H. Boukari, J. S. Lin, M. T. Harris, *J. Colloid Interface Sci.* **1997**, *194*, 311.
- [141] H. Boukari, G. G. Long, M. T. Harris, *J. Colloid Interface Sci.* **2000**, *229*, 129.
- [142] D. Pontoni, T. Narayanam, A. R. Rennie, *Langmuir* **2002**, *18*, 56.
- [143] A. Van Blaaderen, A. P. M. Kentgens, *J. Non-Cryst. Solids* **1992**, *149*, 161.
- [144] K. T. Lee, J. L. Look, M. T. Harris, A. V. McCormick, *J. Colloid Interface Sci.* **1997**, *194*, 78.
- [145] H.P. Lin, C. P. Kao, C. Y. Mou, S. B. Liu, *J. Phys. Chem. B* **2000**, *104*, 7885.
- [146] H. C. Marsmann, *Chemiker-Zeitung* **1973**, *3*, 128.
- [147] W. Zhang, T. R. Pauly, T. J. Pinnavaia, *Chem. Mater.* **1997**, *9*, 2491.
- [148] M. Ocaña, R. Rodriguez-Clemente, C. J. Serna, *Adv. Mater.* **1995**, *7*, 212.
- [149] T. Sugimoto, *Adv. Colloid Interface Sci.* **1987**, *28*, 65.
- [150] E. Matijević, *Chem. Mater.* **1993**, *5*, 412.
- [151] D. Zhao, J. Sun, Q. Li, G. D. Stucky, *Chem. Mater.* **2000**, *12*, 275.
- [152] E. Hecht, H. Hoffmann, *Langmuir* **1994**, *10*, 86.
- [153] R. Cardoso da Silva, G. Oloffson, K. Schillén, W. Loh, *J. Phys. Chem. B* **2002**, *106*, 1239.
- [154] J. Jansson, K. Schillén, G. Oloffson, R. Cardoso da Silva, W. Loh, *J. Phys. Chem. B* **2004**, *108*, 82.
- [155] O. Regev, *Langmuir* **1996**, *12*, 4940.
- [156] M. Lindén, S. A. Schunk, F. Schüth, *Angew. Chem. Int. Ed.* **1998**, *37*, 821.
- [157] P. Ågren, M. Lindén, J. B. Rosenholm, R. Schwarzenbacher, M. Kriechbaum, H. Amenitsch, P. Laggner, J. Blanchard, F. Schüth, *J. Phys. Chem. B* **1999**, *103*, 5943.
- [158] S. O'Brien, R. J. Francis, A. Fogg, D. O'Hare, N. Okazaki, K. Kuroda, *Chem. Mater.* **1999**, *11*, 1822.
- [159] M. Lindén, P. Ågren, S. Karlsson, P. Bussian, H. Amenitsch, *Langmuir* **2000**, *16*, 5831.
- [160] P. Ågren, M. Lindén, J. B. Rosenholm, J. Blanchard, F. Schüth, H. Amenitsch, *Langmuir* **2000**, *16*, 8809.
- [161] A. F. Gross, E. J. Ruiz, S. H. Tolbert, *J. Phys. Chem. B* **2000**, *104*, 5448.
- [162] A. F. Gross, V. H. Le, B. L. Kirsch, S. H. Tolbert, *J. Am. Chem. Soc.* **2002**, *124*, 3713.
- [163] A. F. Gross, S. Yang, A. Navrotsky, S. H. Tolbert, *J. Phys. Chem. B* **2003**, *107*, 2709.
- [164] S. Pevzner, O. Regev, *Microporous Mesoporous Mater.* **2000**, *38*, 413.
- [165] C. C. Landry, S. H. Tolbert, K. W. Gallis, A. Monnier, G. D. Stucky, P. Norby, J. C. Hanson, *Chem. Mater.* **2001**, *13*, 1600.

- [166] A. Lind, J. Andersson, S. Karlsson, P. Ågren, P. Bussian, H. Amenitsch, M. Lindén, *Langmuir* **2002**, *18*, 1380.
- [167] M. Tiemann, V. Goletto, R. Blum, F. Barbonneau, H. Amenitsch, M. Lindén, *Langmuir* **2002**, *18*, 10053.
- [168] M. Impérator-Clerc, P. Davidson, A. Davidson, *J. Am. Chem. Soc.* **2000**, *122*, 11925.
- [169] A. Y. Khodakov, V. L. Zholobenko, M. Impérator-Clerc, D. Durand, *J. Phys. Chem. B* **2005**, *109*, 22780.
- [170] P. Kipkemboi, A. Fodgen, V. Alfredsson, K. Flodström, *Langmuir* **2001**, *17*, 5398.
- [171] B. Jönsson, B. Lindmann, K. Holmberg, B. Kronberg, *Surfactants and Polymers in Aqueous Solution*, John Wiley & Sons, Chichester, New York, Weinheim, Brisbane, Singapore, Toronto, **1998**.
- [172] K. Flodström, H. Wenneström, C. V. Teixeira, H. Amenitsch, M. Lindén, V. Alfredsson, *Langmuir* **2004**, *20*, 10311.
- [173] W. Massa, *Kristallstrukturbestimmung*, 2. Auflage, Teubner, **1996**.
- [174] D. Zhao, Q. Huo, J. Feng, B. F. Chmelka, G. D. Stucky, *J. Am. Chem. Soc.* **1998**, *120*, 6024.
- [175] Q. Huo, R. Leon, P. M. Petroff, G. D. Stucky, *Science*, **1995**, *268*, 1324.
- [176] J. N. Israelachvili, D. J. Mitchell, B. W. Ninham, *J. Chem. Soc., Faraday Trans. 2* **1976**, *72*, 1525.
- [177] J. N. Israelachvili, D. J. Mitchell, B. W. Ninham, *Biochim. Biophys. Acta* **1977**, *470*, 185.
- [178] B. P. Knight, S. P. McGrath, A. M. Chaudri, *Appl. Environ. Microbiol.* **1997**, *63*, 39.
- [179] J. J. Kelly, M. Haggblom, R. L. Tate, *Soil Biology and Biochemistry* **1999**, *31*, 1455.
- [180] E. Lombi, F. J. Zhao, G. Wieshammer, G. Zhang, S. P. McGrath, *Environ. Pollut.* **2002**, *118*, 445.
- [181] S. L. McGrowen, N. T. Basta. In H. M. Selim and D. L. Sparks (eds.): *Heavy metals release in soils*. Lewis Publishers, Florida, USA, 89.
- [182] T. Vengris, R. Binkiene, *J. Chem. Technol. Biotechnol.* **2001**, *76*, 1165.
- [183] L. M. Ottosen, H. K. Hansen, A. B. Ribeiro, A. Villumsen, *J. Haz. Mat.* **2001**, *85*, 291.
- [184] R. B. Maegher, *Curr. Opin. Plant Biol.* **2000**, *3*, 153.
- [185] P. Kotrba, *Collect. Czech. Chem. Commun.* **2000**, *65*, 1205.
- [186] H. K. Hansen, L. M. Ottosen, B. K. Kliem, A. Villumsen, *J. Chem. Technol. Biotechnol.* **1997**, *70*, 67.
- [187] J. Boisson, A. Ruttens, M. Mench, J. Vangronsveld, *Environ. Pollut.* **1999**, *104*, 225.

- [188] D. H. Ham, J. H. Lee, *Arch. Environ. Contam. Toxicol.* **1996**, *31*, 488.
- [189] J. Vangronsveld, J. Colpaert, K. Van Tichelen, *Environ. Pollut.* **1996**, *94*, 131.
- [190] M. J. Mench, A. Manceau, J. Vangronsveld, H. Clijsters, B. Mocquot, *Agronomy* **2000**, *20*, 38.
- [191] W. Friesl, E. Lombi, O. Horak, W. W. Wentel, *J. Plant Nutr. Soil Sci.* **2003**, *166*, 191.
- [192] L. Mercier, T. J. Pinnavaia, *Adv. Mater.* **1997**, *9*, 500.
- [193] L. Mercier, T. J. Pinnavaia, *Environ. Sci. Technol.* **1998**, *32*, 2749.
- [194] J. Brown, R. Richer, L. Mercier, *Microporous Mesoporous Mater.* **2000**, *37*, 41.
- [195] R. I. Nooney, M. Kalyanaraman, G. Kennedy, E. J. Maginn, *Langmuir* **2001**, *17*, 528.
- [196] A. M. Liu, K. Hidajat, S. Kawi, D. Y. Zhao, *Chem. Commun.* **2000**, 1145.
- [197] L. Bois, A. Bonhommé, A. Ribes, B. Pais, G. Raffin, F. Tessier, *Colloids and Surfaces A: Physicochemical and Engineering Aspects* **2003**, *221*, 221.
- [198] Q. Yang, J. Liu, J. Yang, L. Zhang, Z. Feng, J. Zhang, C. Li, *Microporous Mesoporous Mater.* **2005**, *77*, 25.
- [199] L. Zhang, W. Zhang, J. Shi, Z. Hua, Y. Li, J. Yan, *Chem. Commun.* **2003**, 210.
- [200] B. Lee, L.-L. Bao, H.-J. Im, S. dai, E. W. Hagaman, J. S. Lin, *Langmuir* **2003**, *19*, 4246.
- [201] [Zeolithes.ethz.ch/IZA-SC/Atlas\\_pdf/MEP.pdf](http://Zeolithes.ethz.ch/IZA-SC/Atlas_pdf/MEP.pdf)
- [202] P. I. Ravikovitch, A. Neimark, *J. Phys. Chem. B* **2001**, *105*, 6817.
- [203] M. Kruk, M. Jaroniec, *Chem. Mater.* **2000**, *12*, 1961.
- [204] K. Miyazawa, S. Inagaki, *Chem. Commun.* **2000**, 2121.
- [205] H.-Y. Wang, D. Steffens, X. Wissmeier, S. Schubert, *in preparation*.
- [206] M. Kurosawa, K. Yamashita, T. Kobayashi, *European Patent EP0867217*, **1998**.
- [207] J. D. MacDowall, D. Van de Kleut, K. M. Kleij, *WO0162367*
- [208] S. Kitagawa, R. Kitaura, S.-I. Noro, *Angew. Chem.* **2004**, *116*, 2388.
- [209] E.-Y. Choi, K. Park, C.-M. Yang, H. Kim, J.-H. Son, S. W. Lee, Y. H. Lee, D. Min, Y.-U. Kwon, *Chem. Eur. J.* **2004**, *10*, 5355.
- [210] J. H. Yun, T. Duren, F. T. Keil, N. A. Seaton, *Langmuir* **2002**, *18*, 2693.
- [211] K. Morishige, H. Fujii, M. Uga, D. Kinukawa, *Langmuir* **1997**, *13*, 3494.
- [212] M. M. L. Ribeiro Carrott, A. J. E. Candeias, P. J. M. Carrott, P. I. Ravikovitch, A. V. Neimark, A. D. Sequeira, *Microporous Mesoporous Mater.* **2001**, *47*, 323.
- [213] J. Janchen, M. Busio, M. Hintze, H. Stach, J. H. C. van Hooff, *Stud. Surf. Sci. Catal.* **1997**, *105*, 1731.
- [214] J. Janchen, H. Stach, M. Busio, J. H. M. C. van Wolput, *Thermochim. Acta* **1998**, 312, 33.

- [215] X. S. Zhao, G. Q. Lu, X. Hu, *Colloids Surf. A* **2001**, 179, 261.
- [216] Y. C. Long, T. M. Xu, Y. J. Sun, W. Y. Dong, *Langmuir* **1998**, 14, 6173.
- [217] C. Nguyen, C. G. Sonwane, S. K. Bhatia, D. D. Do, *Langmuir* **1998**, 14, 4950.
- [218] V. R. Choudhary, K. Mantri, *Langmuir* **2000**, 16, 7031.
- [219] X. Hu, S. Z. Qiao, X. S. Zhao, G. Q. Lu, *Ind. Eng. Chem. Res.* **2001**, 40, 862.
- [220] T. Boger, R. Roesky, R. Glaser, S. Ernst, G. Eigenberger, J. Weitkamp, *J. Microporous Mater.* **1997**, 6, 79.
- [221] V. Hessel, H. Löwe, A. Müller, G. Kolb, *Chemical Micro Process Engineering* **2005**, Wiley VCH.
- [222] K. Schubert, J. Brandner, M. Fichtner, G. Lindner, U. Schygulla, A. Wenka, *Microscale Thermophys. Eng.* **2001**, 5, 17.
- [223] S. Lüdtke, T. Adam, K. K. Unger, *J. Chromatogr. A* **1997**, 786, 229.
- [224] K. W. Gallis, J. T. Araujo, K. J. Duff, J. G. Moore, C. C. Landry, *Adv. Mater.* **1999**, 11, 1452.
- [225] S. Lüdtke, T. Adam, N. von Doehren, K. K. Unger, *J. Chromatogr. A* **2000**, 887, 339.
- [226] K. K. Unger, D. Kumar, M. Grün, G. Büchel, S. Lüdtke, T. Adam, K. Schumacher, S. Renker, *J. Chromatogr. A* **2000**, 892, 47.
- [227] C. Thoelen, J. Paul, I. F. J. Vankelecom, P. A. Jacobs, *Tetrahedron: Asymmetry* **2000**, 11, 4819.
- [228] F. Großmann, V. Ehwald, C. du Fresne von Hohenesche, K. K. Unger, *J. Chromator. A* **2001**, 910, 223.
- [229] J. Zhao, F. Gao, Y. Fu, W. J. Jin, P. Yang, D. Zhao, *Chem. Commun.* **2002**, 752.
- [230] T. Nassivera, A. G. Eklund, C. C. Landry, *J. Chromatogr. A* **2002**, 973, 97.
- [231] T. Salesch, S. Bachmann, S. Brugger, R. Rabelo-Schaefer, K. Albert, S. Steinbrecher, E. Plies, A. Mehdi, C. Reyé, R. J. P. Corriu, E. Lindner, *Adv. Funct. Mater.* **2002**, 12, 134.
- [232] M. Mesa, L. Sierra, B. López, A. Ramirez, J.-L. Guth, *Solid State Sciences* **2003**, 5, 1303.
- [233] T. Martin, A. Galarneau, F. Di Renzo, D. Brunel, F. Fajula, *Chem. Mater.* **2004**, 16, 1725.
- [234] J.-S. Chung, D.-J. Kim, W.-S. Ahn, J.-H. Ko, W.-J. Cheong, *Korean J. Chem. Eng.* **2004**, 21, 132.
- [235] K. D. Wyndham, J. E. O’Gara, T. H. Walter, K. H. Glose, N. L. Lawrence, B. A. Alden, G. S. Izzo, C. J. Hudalla, P. C. Iraneta, *Anal. Chem.* **2003**, 75, 6781.
- [236] W. J. van Ooij, T. F. Child, *Chem. Tech.* **1998**, 28, 26.

- [237] V. Subramanian, W. J. van Ooij, *Corrosion* **1998**, 54, 204.

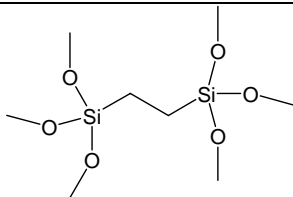
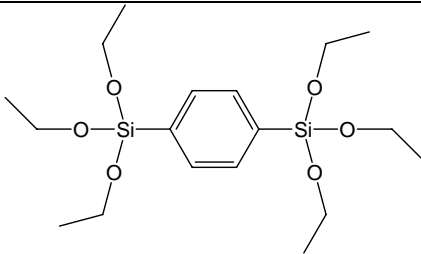
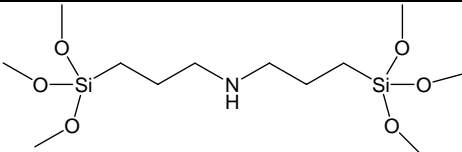
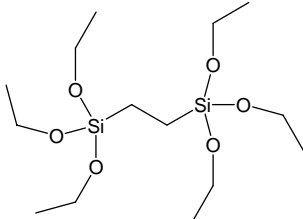
## Appendix I

### A.I.1 Applied organosilica precursors

The sample names consist of different letters and numbers. A description of the system is described below:

Capital letters stand for the organosilica precursor that was applied. The name and the organosilica precursor as well as the abbreviation that is used in this work are listed in Table A.I.1.

**Table A.I.1:** Names, structures and abbreviations of the applied organosilica precursors.

	Organosilica precursor Name	Organosilica precursor Structure	Abbreviation
A	1,2-bis(trimethoxysilyl)ethane		BTME
C	1,4-bis(triethoxysilyl)benzene		BTEB
D	<i>N,N</i> - [bis(trimethoxysilyl)propyl]amine		BTMPA
E	1,2-bis(triethoxysilyl)ethane		BTEE

### A.I.2 Applied structure-directing agents

Small letters stand for the applied structure-directing agent. The names and the abbreviations of the applied SDAs are listed in Table A.I.2.

**Table A.I.2:** Names and abbreviations of the applied SDAs.

	Structure-directing agent	Abbreviation
a	Octadecyltrimethylammonium chloride	OTAC
b	Hexadecyltrimethylammonium chloride	CTAC
d	Pluronic <sup>®</sup> P123	P123
e	Hexadecyltrimethylammonium bromide	CTAB
f	Eicosyldiethylmethylammonium bromide	C <sub>20</sub> DEMAB
j	Dodecylamine	DA
m	Brij <sup>®</sup> 76 (Polyoxyethylene-(10)-stearyl ether)	Brij <sup>®</sup> 76
o	Pluronic <sup>®</sup> F127	F127

The numbers following the letter combination do not have a special meaning and just stand for the synthesis number. Other synthesis parameters except the organosilica precursor and the SDA could not be concluded from the sample names.

## Appendix II

### A.II.1 Molar ratios of ethane- and amine-bridged samples synthesised with OTAC as SDA

The molar ratios of the ethane- and amine-bridged samples synthesised with OTAC are listed in Table A.II.1 – A.II.5.

**Table A.II.1:** Molar ratios of the samples synthesised with OTAC and  $x = 1$ ,  $y = 0$ .

	BTME (x) [mol]	BTMPA (y) [mol]	Time (stirring) [h]	Temp. (stirring) [°C]	Time (oven) [h]	Temp. (oven) [°C]	Surfactant [mol]
A1a	1	-	24	RT	24	95	0.57
A2a	1	-	24	RT	24	95	0.28
A3a	1	-	24	RT	24	95	0.85

**Table A.II.2:** Molar ratios of the samples synthesised with OTAC and  $x = 0.89$ ,  $y = 0.11$ .

	BTME (x) [mol]	BTMPA (y) [mol]	Time (stirring) [h]	Temp. (stirring) [°C]	Time (oven) [h]	Temp. (oven) [°C]	Surfactant [mol]
ADa1	0.89	0.11	24	RT	24	95	0.57
ADa28	0.89	0.11	24	RT	24	95	0.28
ADa53	0.89	0.11	24	RT	24	95	0.85
ADa38	0.89	0.11	24	RT	24	95	0.57
ADa36	0.89	0.11	24	40	24	95	0.57
ADa39	0.89	0.11	24	60	24	95	0.57
ADa43	0.89	0.11	12	RT	24	95	0.57
ADa50	0.89	0.11	12	40	24	95	0.57

**Table A.II.3:** Molar ratios of the samples synthesised with OTAC and  $x = 0.78$ ,  $y = 0.22$ .

	BTME (x) [mol]	BTMPA (y) [mol]	Time (stirring) [h]	Temp. (stirring) [°C]	Time (oven) [h]	Temp. (oven) [°C]	Surfactant [mol]
ADa35	0.78	0.22	24	RT	24	95	0.57
ADa29	0.78	0.22	24	RT	24	95	0.28
ADa30	0.78	0.22	24	RT	24	95	0.85
ADa37	0.78	0.22	24	RT	24	95	0.57
ADa35	0.78	0.22	24	40	24	95	0.57
ADa40	0.78	0.22	24	60	24	95	0.57
ADa44	0.78	0.22	12	RT	24	95	0.57
ADa49	0.78	0.22	12	40	24	95	0.57

**Table A.II.4:** Molar ratios of the samples synthesised with OTAC and  $x = 0.67$ ,  $y = 0.33$ .

	BTME (x) [mol]	BTMPA (y) [mol]	Time (stirring) [h]	Temp. (stirring) [°C]	Time (oven) [h]	Temp. (oven) [°C]	Surfactant [mol]
ADa4	0.67	0.33	24	RT	24	95	0.57
ADa31	0.67	0.33	24	RT	24	95	0.28
ADa32	0.67	0.33	24	RT	24	95	0.85
ADa45	0.67	0.33	12	RT	24	95	0.57
ADa15	0.67	0.33	12	40	24	95	0.57
ADa11	0.67	0.33	12	60	24	95	0.57
ADa4	0.67	0.33	24	RT	24	95	0.57
ADa16	0.67	0.33	24	40	24	95	0.57
ADa12	0.67	0.33	24	60	24	95	0.57

**Table A.II.5:** Molar ratios of samples synthesised with OTAC and  $x = 0.55$ ,  $y = 0.45$ .

	BTME (x) [mol]	BTMPA (y) [mol]	Time (stirring) [h]	Temp. (stirring) [°C]	Time (oven) [h]	Temp. (oven) [°C]	Surfactant [mol]
ADa5	0.55	0.45	24	RT	24	95	0.57
ADa33	0.55	0.45	24	RT	24	95	0.28
ADa34	0.55	0.45	24	RT	24	95	0.85
ADa46	0.55	0.45	12	RT	24	95	0.57
ADa17	0.55	0.45	12	40	24	95	0.57
ADa13	0.55	0.45	12	60	24	95	0.57
ADa5	0.55	0.45	24	RT	24	95	0.57
ADa18	0.55	0.45	24	40	24	95	0.57
ADa14	0.55	0.45	24	60	24	95	0.57
ADa19	0.55	0.45	24	RT	24	150	0.57
ADa20	0.55	0.45	24	RT	24	120	0.57
ADa21	0.55	0.45	24	RT	24	95	0.57
ADa22	0.55	0.45	24	RT	24	60	0.57
ADa23	0.55	0.45	24	RT	24	95	0.57
ADa24	0.55	0.45	24	RT	24	95	0.57

## A.II.2 Molar ratios of ethane- and amine-bridged materials synthesised with CTAC as SDA

The molar ratios of the ethane- and amine-bridged samples synthesised with CTAC are listed in Table A.II.6 – A.II.10.

**Table A.II.6:** Molar ratios of the samples synthesised with CTAC and  $x = 1$ ,  $y = 0$ .

	BTME (x) [mol]	BTMPA (y) [mol]	Time (stirring) [h]	Temp. (stirring) [°C]	Time (oven) [h]	Temp. (oven) [°C]	Surfactant [mol]
A1b	1	-	24	RT	24	95	0.28
A2b	1	-	24	RT	24	95	0.57
A3b	1	-	24	RT	24	95	0.85

**Table A.II.7:** Molar ratios of the samples synthesised with CTAC and  $x = 0.89$ ,  $y = 0.11$ .

	BTME (x) [mol]	BTMPA (x) [mol]	Time (stirring) [h]	Temp. (stirring) [°C]	Time (oven) [h]	Temp. (oven) [°C]	Surfactant [mol]
ADb1	0.89	0.11	24	RT	24	95	0.57
ADb23	0.89	0.11	24	RT	24	95	0.28
ADb24	0.89	0.11	24	RT	24	95	0.85

**Table A.II.8:** Molar ratios of the samples synthesised with CTAC and  $x = 0.78$ ,  $y = 0.22$ .

	BTME (x) [mol]	BTMPA (y) [mol]	Time (stirring) [h]	Temp. (stirring) [°C]	Time (oven) [h]	Temp. (oven) [°C]	Surfactant [mol]
ADb2	0.78	0.22	24	RT	24	95	0.57
ADb25	0.78	0.22	24	RT	24	95	0.28
ADb26	0.78	0.22	24	RT	24	95	0.85

**Table A.II.9:** Molar ratios of the samples synthesised with CTAC and  $x = 0.67$ ,  $y = 0.33$

	BTME (x) [mol]	BTMPA (y) [mol]	Time (stirring) [h]	Temp. (stirring) [°C]	Time (oven) [h]	Temp. (oven) [°C]	Surfactant [mol]
ADb3	0.67	0.33	24	RT	24	95	0.57
ADb27	0.67	0.33	24	RT	24	95	0.28
ADb28	0.67	0.33	24	RT	24	95	0.85

**Table A.II.10:** Molar ratios of the samples synthesised with CTAC and  $x = 0.55$ ,  $y = 0.45$ .

	BTME (x) [mol]	BTMPA (y) [mol]	Time (stirring) [h]	Temp. (stirring) [°C]	Time (oven) [h]	Temp. (oven) [°C]	Surfactant [mol]
ADb5	0.55	0.45	24	RT	24	95	0.57
ADb29	0.55	0.45	24	RT	24	95	0.28
ADb30	0.55	0.45	24	RT	24	95	0.85

### A.II.3 Nitrogen physisorption data of the samples synthesised with different OTAC concentrations

The nitrogen physisorption data of the samples synthesised with different surfactant concentrations are listed in Table A.II.11 (0.57 mol), A.II.12 (0.28 mol) and A.II.13 (0.85 mol).

**Table A.II.11:** Nitrogen physisorption data of the samples synthesised with 0.57 mol OTAC and different organosilica precursor concentrations.

sample	c(surfactant) [mol]	BTMPA [mol]	BTME [mol]	T (hydro- thermal)	BET surface [m <sup>2</sup> /g]	Pore diameter [nm]
A1a	0.57	0	1	95	1010	3.1
ADa1	0.57	0.11	0.89	95	840	3.7
ADa2	0.57	0.22	0.78	95	530	2.9
ADa4	0.57	0.33	0.67	95	400	3.1
ADa5	0.57	0.45	0.55	95	370	2.7

**Table A.II.12:** Nitrogen physisorption data of the samples synthesised with 0.28 mol OTAC and different organosilica precursor concentrations.

sample	c(surfactant) [mol]	BTMPA [mol]	BTME [mol]	T (hydro- thermal)	BET surface [m <sup>2</sup> /g]	Pore diameter [nm]
ADa47	0.28	0	1	95	350	2.8
ADa53	0.28	0.11	0.89	95	350	2.9
ADa29	0.28	0.22	0.78	95	632	3.6
ADa31	0.28	0.33	0.67	95	370	2.5
ADa33	0.28	0.45	0.55	95	200	2.6

**Table A.II.13:** Nitrogen physisorption data of the samples synthesised with 0.85 mol OTAC and different organosilica precursor concentrations.

sample	c(surfactant) [mol]	BTMPA [mol]	BTME [mol]	T (hydro- thermal)	BET surface [m <sup>2</sup> /g]	Pore diameter [nm]
ADa48	0.85	0	1	95	590	3.7
ADa53	0.85	0.11	0.89	95	750	3.3
ADa30	0.85	0.22	0.78	95	630	3.2
ADa32	0.85	0.33	0.67	95	560	2.5
ADa34	0.85	0.45	0.55	95	460	2.6

### A.II.4 Variation of the aging temperature and the aging time

The complete XRD data of all samples synthesised with a surfactant concentration (OTAC) of 0.57 mol, different aging times and temperatures are listed in Table A.II.14. The nitrogen physisorption data of these samples are listed in Table A.II.15.

**Table A.II.14:** Mesostructures of the samples synthesised with different aging times and temperatures.

Sample	BTME [mol]	BTMPA [mol]	Temp. [°C]	Stirring Time [h]	Structure
ADa1	0.89	0.11	RT	24	$Pm\bar{3}n$
ADa36	0.89	0.11	40	24	$Pm\bar{3}n$
ADa39	0.89	0.11	60	24	1 reflection
ADa43	0.89	0.11	RT	12	$Pm\bar{3}n$
ADa50	0.89	0.11	40	12	$Pm\bar{3}n$
ADa2	0.78	0.22	RT	24	1 reflection
ADa37	0.78	0.22	40	24	$Pm\bar{3}n$
ADa40	0.78	0.22	60	24	1 reflection
ADa44	0.78	0.22	RT	12	$Pm\bar{3}n$
ADa49	0.78	0.22	40	12	$Pm\bar{3}n$
ADa45	0.67	0.33	RT	12	$Pm\bar{3}n$
ADa15	0.67	0.33	40	12	$Pm\bar{3}n/p6mm$
ADa11	0.67	0.33	60	12	$p6mm$
ADa4	0.67	0.33	RT	24	$Pm\bar{3}n$
ADa16	0.67	0.33	40	24	1 reflection
ADa12	0.67	0.33	60	24	$p6mm$
ADa46	0.55	0.45	RT	12	1 reflection
ADa17	0.55	0.45	40	12	1 reflection
ADa13	0.55	0.45	60	12	1 reflection
ADa5	0.55	0.45	RT	24	$Pm\bar{3}n$
ADa18	0.55	0.45	40	24	1 reflection
ADa14	0.55	0.45	60	24	1 reflection
ADa8	0.55	0.45	60	2	$p6mm$

**Table A.II.15:** Nitrogen physisorption data of the samples synthesised with different stirring times and different temperatures during the aging step.

sample	BTME [mol]	BTMPA [mol]	Stirring temperature [°C]	stirring time [h]	BET surface [m <sup>2</sup> /g]	Pore diameter [nm]
ADa1	0.89	0.11	RT	24	840	3.8
ADa36	0.89	0.11	40	24	420	3.2
ADa39	0.89	0.11	60	24	419	3.2
ADa43	0.89	0.11	RT	12	595	3.0
ADa50	0.89	0.11	40	12	490	3.0
ADa2	0.78	0.22	RT	24	690	3.8
ADa35	0.78	0.22	40	24	220	2.8
ADa40	0.78	0.22	60	24	418	3.0
ADa44	0.78	0.22	RT	12	550	3.2
ADa49	0.78	0.22	40	12	532	3.0
ADa45	0.67	0.33	RT	12	680	3.6
ADa15	0.67	0.33	40	12	670	3.0
ADa11	0.67	0.33	60	12	630	2.8
ADa4	0.67	0.33	RT	24	400	4.1
ADa16	0.67	0.33	40	24	130	2.4
ADa12	0.67	0.33	60	24	675	2.8
ADa46	0.55	0.45	RT	12	550	2.8
ADa17	0.55	0.45	40	12	613	2.6
ADa13	0.55	0.45	60	12	640	2.6
ADa5	0.55	0.45	RT	24	370	3.8
ADa18	0.55	0.45	40	24	290	2.4
ADa14	0.55	0.45	60	24	320	Micro
ADa8	0.55	0.45	60	2	560	2.8

### A.II.5 Variation of the hydrothermal treatment temperature

The nitrogen physisorption data of the samples synthesised with a surfactant concentration of 0.57 mol (OTAC) and with different temperatures during the hydrothermal treatment step is listed in Table A.I.16.

**Table A.II.16:** Nitrogen physisorption data of the samples synthesised at different temperatures during the hydrothermal treatment step.

sample	BTME [mol]	BTMPA [mol]	Stirring temperature [°C]	stirring time [h]	BET surface [m <sup>2</sup> /g]	Pore diameter [nm]
ADa19	0.57	0.45	0.55	150	-	-
ADa20	0.57	0.45	0.55	120	152	3.7
ADa21	0.57	0.45	0.55	95	370	2.8
ADa22	0.57	0.45	0.55	60	684	2.2

### A.II.6 Nitrogen physisorption data of the ethane- and amine-bridged PMOs synthesised with CTAC as SDA

The nitrogen physisorption data of the samples synthesised with different CTAC concentrations are listed in Table A.II.17 (0.57 mol), A.II.18 (0.28 mol) and A.II.19 (0.85 mol).

**Table A.II.17:** Nitrogen physisorption data of the samples synthesised with 0.57 mol CTAC and different organosilica precursor concentrations.

sample	c(surfactant) [mol]	BTMPA [mol]	BTME [mol]	T (hydro- thermal)	BET surface [m <sup>2</sup> /g]	Pore diameter [nm]
ADb32	0.57	0	1	95	490	3.6
ADb1	0.57	0.11	0.89	95	800	3.8
ADb2	0.57	0.22	0.78	95	670	3.5
ADb3	0.57	0.33	0.67	95	480	2.3
ADb5	0.57	0.45	0.55	95	233	2.3

**Table A.II.18:** Nitrogen physisorption data of the samples synthesised with 0.28 mol CTAC and different amounts of organosilica precursors.

sample	c(surfactant) [mol]	BTMPA [mol]	BTME [mol]	T (hydro- thermal)	BET surface [m <sup>2</sup> /g]	Pore diameter [nm]
ADb31	0.28	0	1	95	690	3.2
ADb23	0.28	0.11	0.89	95	800	3.2
ADb25	0.28	0.22	0.78	95	570	2.8
ADb27	0.28	0.33	0.67	95	540	3.6
ADb29	0.28	0.45	0.55	95	550	2.4

**Table A.II.19:** Nitrogen physisorption data of the samples synthesised with 0.85 mol CTAC and different amounts of both organosilica precursors.

sample	c(surfactant) [mol]	BTMPA [mol]	BTME [mol]	T (hydro- thermal)	BET surface [m <sup>2</sup> /g]	Pore diameter [nm]
ADb33	0.85	0	1	95	510	3.2
ADb24	0.85	0.11	0.89	95	670	2.8
ADb26	0.85	0.22	0.78	95	650	2.8
ADb28	0.85	0.33	0.67	95	580	2.8
ADb30	0.85	0.45	0.55	95	660	2.4

## Appendix III

### A.III.1 Spherical ethane-bridged particles with an average particle diameter of 500 nm

The molar ratios of the samples synthesised with C<sub>20</sub>DEMAB as SDA and different synthesis parameters are listed in Tables A.III.1 and A.III.2.

**Table A.III.1:** Molar ratio of ethane-bridged Stöber PMOs synthesised C<sub>20</sub>DEMAB as SDA and with different ethanol concentrations.

	BTME [mol]	EtOH [mol]	C <sub>20</sub> DEMAB [mol]	NH <sub>3</sub> [mol]	H <sub>2</sub> O [mol]	Stirring Time [min]	Temp. [°C]
Af50	0.5	70.20	0.22	27.66	95.12	120	33
Af51	0.5	59.21	0.22	27.66	134.67	120	33
Af52	0.5	48.83	0.22	27.66	174.22	120	33
Af53	0.5	37.24	0.22	27.66	213.78	120	33
Af54	0.5	26.86	0.22	27.66	253.33	120	33
Af55	0.5	16.48	0.22	27.66	292.88	120	33
Af56	0.5	5.49	0.22	27.66	332.44	120	33
Af57	0.5	0	0.22	27.66	352.21	120	33
Af58	0.5	80.57	0.22	27.66	55.57	120	33

**Table A.III.2:** Molar ratio of ethane-bridged Stöber PMOs synthesised with C<sub>20</sub>DEMAB as SDA and different ammonia concentrations.

	BTME [mol]	EtOH [mol]	C <sub>20</sub> DEMAB [mol]	NH <sub>3</sub> [mol]	H <sub>2</sub> O [mol]	Stirring Time [min]	Temp. [°C]
Af59	0.5	36.0	0.22	11.77	166.06	120	33
Af60	0.5	36.0	0.22	17.72	178.02	120	33
Af61	0.5	36.0	0.22	23.59	189.72	120	33
Af62	0.5	36.0	0.22	29.43	201.56	120	33
Af63	0.5	36.0	0.22	35.31	213.39	120	33
Af64	0.5	36.0	0.22	47.10	237.06	120	33
Af65	0.5	36.0	0.22	58.86	260.72	120	33
Af66	0.5	36.0	0.22	70.63	284.40	120	33
Af67	0.5	36.0	0.22	81.67	308.06	120	33

### A.III.2 Nitrogen physisorption data of the samples synthesised with different ethanol concentrations

The nitrogen physisorption data of the samples synthesised with different ethanol concentrations are listed in Table A.III.3.

**Table A.III.3:** Nitrogen physisorption data of the samples synthesised with different ethanol concentrations.

Sample	c(ethanol) [mol]	BET surface [m <sup>2</sup> /g]	Pore Diameter Maximum [nm]	Pore Diameter Range [nm]
Af58	80.57	970	2.6	1 - 10
Af50	70.20	1140	2.6	1 - 10
Af51	59.21	1083	2.7	1.7 - 3.5
Af52	48.83	1190	2.7	1.7 - 3.5
Af53	37.24	1166	2.6	1.7 - 3.5
Af54	26.86	1170	2.6	1.7 - 3.6
Af55	16.48	1082	2.6	1.7 - 3.7
Af56	5.49	930	2.6	1.7 - 4
Af57	0	880	2.6; 3.1	1.7 - 4

## Appendix IV

### A.IV.1 Molar ratios of the ethane-bridged spheres in the size range of 25 – 300 $\mu\text{m}$

**Table A.IV.1:** Molar ratios of the ethane-bridged samples synthesised with different stirring speeds.

	BTEE [mol]	Ethanol [mol]	DA [mol]	HCl [mol]	H <sub>2</sub> O [mol]	Stirring Speed [rpm]	Stirring Time [min]	Temp. [°C]
Ej20	0.5	2.43	0.32	0.0061	47.59	300	60	RT
Ej21	0.5	2.43	0.32	0.0061	47.59	400	60	RT
Ej22	0.5	2.43	0.32	0.0061	47.59	500	60	RT
Ej23	0.5	2.43	0.32	0.0061	47.59	600	60	RT
Ej24	0.5	2.43	0.32	0.0061	47.59	700	60	RT
Ej25	0.5	2.43	0.32	0.0061	47.59	800	60	RT
Ej26	0.5	2.43	0.32	0.0061	47.59	900	60	RT

**Table A.IV.2:** Molar ratios of the ethane-bridged PMOs synthesised with different mixing procedures.

	BTEE [mol]	Ethanol [mol]	DA [mol]	HCl [mol]	H <sub>2</sub> O [mol]	Stirring Speed [rpm]	Stirring Time [min]	Temp. [°C]
Ej20	0.5	2.43	0.32	0.0061	47.59	300	60	RT
Ej31	0.5	2.43	0.32	0.0061	47.59	Shaking 600/min	60	RT
Ej32	0.5	2.43	0.32	0.0061	47.59	Shaking 1400/min	60	RT
Ej52	0.5	2.43	0.32	0.0061	47.59	No mixing	60	RT

**Table A.IV.3:** Molar ratios of ethane-bridged PMOs synthesised with different pH values.

	BTEE [mol]	Ethanol [mol]	DA [mol]	HCl [mol]	H <sub>2</sub> O [mol]	Stirring Speed [rpm]	Stirring Time [min]	Temp. [°C]
Ej53	0.5	2.43	0.32	0.026	47.59	400	60	RT
Ej54	0.5	2.43	0.32	0.087	47.59	400	60	RT
Ej55	0.5	2.43	0.32	0.131	47.59	400	60	RT
Ej56	0.5	2.43	0.32	0.174	47.59	400	60	RT
Ej57	0.5	2.43	0.32	0.0087	47.59	400	75	RT
Ej58	0.5	2.43	0.32	0.013	47.59	400	75	RT
Ej59	0.5	2.43	0.32	0.017	47.59	400	75	RT
Ej60	0.5	2.43	0.32	0.0043	47.59	400	75	RT
Ej61	0.5	2.43	0.32	0.0017	47.59	400	75	RT
Ej62	0.5	2.43	0.32	0	47.59	400	240	RT

**Table A.IV.4:** Molar ratios of ethane-bridged PMOs synthesised with different amounts of ethanol.

	BTEE [mol]	Ethanol [mol]	DA [mol]	HCl [mol]	H <sub>2</sub> O [mol]	Stirring Speed [rpm]	Stirring Time [min]	Temp. [°C]
Ej45	0.5	0	0.32	0.0098	53.46	300	60	RT
Ej87	0.5	2.41	0.32	0.0087	47.59	300	60	RT
Ej88	0.5	4.59	0.32	0.0076	41.71	300	60	RT
Ej89	0.5	6.89	0.32	0.0065	35.84	300	60	RT
Ej90	0.5	9.18	0.32	0.0055	29.96	300	60	RT
Ej91	0.5	11.48	0.32	0.0044	24.08	300	60	RT
Ej92	0.5	13.77	0.32	0.0033	18.21	300	60	RT
Ej93	0.5	16.06	0.32	0.0022	12.33	300	60	RT
Ej94	0.5	18.36	0.32	0.0012	6.46	300	60	RT
Ej95	0.5	20.65	0.32	0	0	300	60	RT

**Table A.IV.5:** Molar ratios of ethane-bridged PMOs synthesised with different amounts of ethanol.

	BTEE [mol]	Ethanol [mol]	DA [mol]	HCl [mol]	H <sub>2</sub> O [mol]	Stirring Speed [rpm]	Stirring Time [min]	Temp. [°C]
Ej78	0.14	2.41	0.32	0.0087	47.59	300	60	RT
Ej79	0.14	4.59	0.32	0.0076	41.71	300	60	RT
Ej80	0.14	6.89	0.32	0.0065	35.84	300	60	RT
Ej81	0.14	9.18	0.32	0.0055	29.96	300	60	RT
Ej82	0.14	11.48	0.32	0.0044	24.08	300	60	RT
Ej83	0.14	13.77	0.32	0.0033	18.21	300	60	RT
Ej84	0.14	16.06	0.32	0.0022	12.33	300	60	RT
Ej85	0.14	18.36	0.32	0.0012	6.46	300	60	RT
Ej86	0.14	20.65	0.32	0	0	300	60	RT

**Table A.IV.6:** Molar ratios of ethane-bridged PMOs synthesised with different surfactants.

	BTEE [mol]	Ethanol [mol]	DA [mol]	HCl [mol]	H <sub>2</sub> O [mol]	Stirring Speed [rpm]	Stirring Time [min]	Temp. [°C]
Edj75	0.86	2.72	0.46 + P123 [mol] 0.0018	0.0075	41.13	300	60	RT
Eoj76	0.86	2.72	0.46 + F127 [mol]	0.0075	41.13	300	60	RT
Eaj77	0.86	2.72	0.46 + OTAC [mol] 0.03	0.0075	41.13	300	60	RT

### A.IV.2 Molar ratios of the phenylene-bridged spheres in the size range of 10 – 300 $\mu\text{m}$

**Table A.IV.7:** Molar ratios of phenylene-bridged PMOs synthesised with different pH values.

	BTEB [mol]	Ethanol [mol]	DA [mol]	HCl [mol]	H <sub>2</sub> O [mol]	Stirring Speed [rpm]	Stirring Time [min]	Temp. [°C]
Cj11	0.5	4.89	0.41	0.0027	73.86	500	90	RT
Cj12	0.5	4.89	0.41	0.14	73.86	500	90	RT
Cj13	0.5	4.89	0.41	0.21	73.86	500	90	RT
Cj14	0.5	4.89	0.41	0.28	73.86	500	90	RT
Cj15	0.5	4.89	0.41	0.0068	73.86	500	90	RT
Cj16	0.5	4.89	0.41	0.0095	73.86	500	90	RT
Cj17	0.5	4.89	0.41	0.014	73.86	500	90	RT
Cj18	0.5	4.89	0.41	0.021	73.86	500	90	RT
Cj22	0.5	4.89	0.41 + 0.137 mol mesitylene	0.0068	73.68	500	120	RT

**Table A.IV.8:** Molar ratios of phenylene-bridged PMOs synthesised with different shaking procedures.

	BTEB [mol]	Ethanol [mol]	DA [mol]	HCl [mol]	H <sub>2</sub> O [mol]	Shaking [spm]	Shaking Time [min]	Temp. [°C]
Cj23	0.5	4.89	0.41	0.28	73.86	600	90	RT
Cj24	0.5	4.89	0.41	0.42	73.86	600	90	RT
Cj25	0.5	4.89	0.41	0.21	73.86	1000	90	RT
Cj26	0.5	4.89	0.41	0.21	73.86	1400	90	RT
Cj27	0.5	4.89	0.41	0.42	73.86	1400	120	RT

### A.IV.3 Ethane-bridged PMOs synthesised with different stirring rates

Optical microscopic images of the samples synthesised with different mixing rates are shown in Figure A.IV.1 a – j.

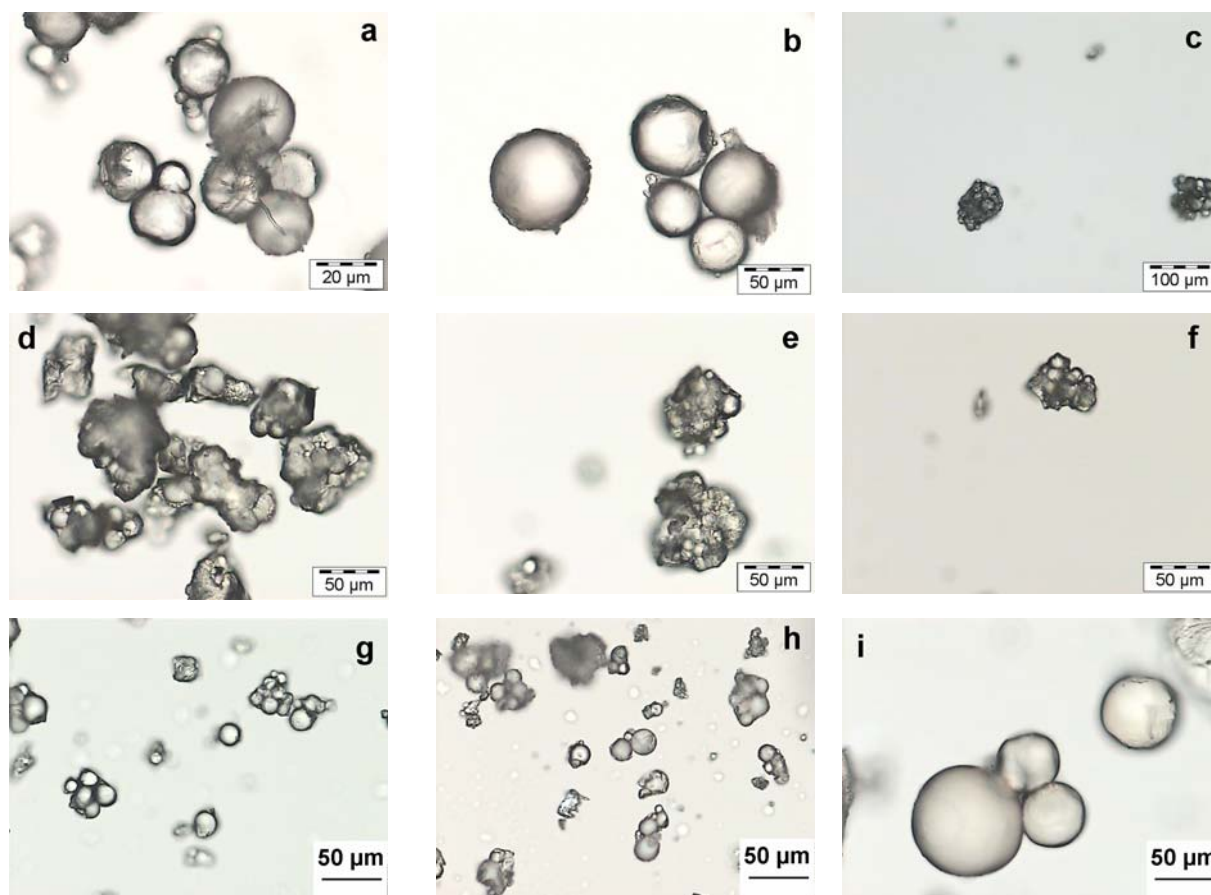


**Figure A.IV.1:** Optical microscopic images of the samples synthesised with different mixing rates (molar ratios: Table A.IV.1 + A.IV.2): 300 rpm (a); 400 rpm (b); 500 rpm (c); 600 rpm (d); 700 rpm (e); 800 rpm (f), 600 spm (g); 1400 spm (h); without mixing (i).

The nitrogen physisorption data of the ethane-bridged samples synthesised with different stirring and shaking rates are listed in Table A.IV.9.

**Table A.IV.9:** Nitrogen physisorption data of the samples synthesised with different mixing procedures and mixing rates

sample	Mixing	BET surface [m <sup>2</sup> /g]	Pore diameter [nm]	Diameter range [nm]
Ej20	Stirring (300 rpm)	888	2.5	1.3 – 17
Ej21	Stirring (400 rpm)	908	2.5	1.3 – 25
Ej22	Stirring (500 rpm)	898	2.5	1.3 – 17
Ej23	Stirring (600 rpm)	894	2.5	1.3 – 9
Ej24	Stirring (700 rpm)	879	2.5	1.3 – 9
Ej25	Stirring (800 rpm)	843	2.5	1.3 – 11.5
Ej26	Stirring (900 rpm)	927	2.5	1.3 – 17
Ej31	Shaking (600/min)	1004	2.5	1.3 – 15
Ej32	Shaking (1400/min)	922	2.5	1.3 – 16
Ej52	-	1004	2.5	1.3 – 50

#### A.IV.4 Ethane-bridged samples synthesised with different pH values

The complete nitrogen physisorption data of the ethane-bridged samples synthesised with different pH values are listed in Table A.IV.10.

**Table A.IV.10:** Nitrogen physisorption data of the samples synthesised with different pH values.

sample	c (HCl) [mol]	BET surface [m <sup>2</sup> /g]	Pore diameter [nm]	Diameter range [nm]
Ej53	0.026	965	3.3	1.3 – 10
Ej59	0.017	865	2.5	1.3 – 30
Ej58	0.013	969	2.5	1.3 – 30
Ej57	0.0087	1008	3.1	1.3 – 17
Ej60	0.0043	1028	3.5	1.3 – 17
Ej61	0.0017	987	3.5	1.3 – 17
Ej62	0	1067	2.5	1.3 – 5

### A.IV.5 Ethane-bridged samples synthesised with different co-surfactants

Optical microscopic images of the samples synthesised with different ethanol concentrations are shown in Figure A.IV.2 a – c.

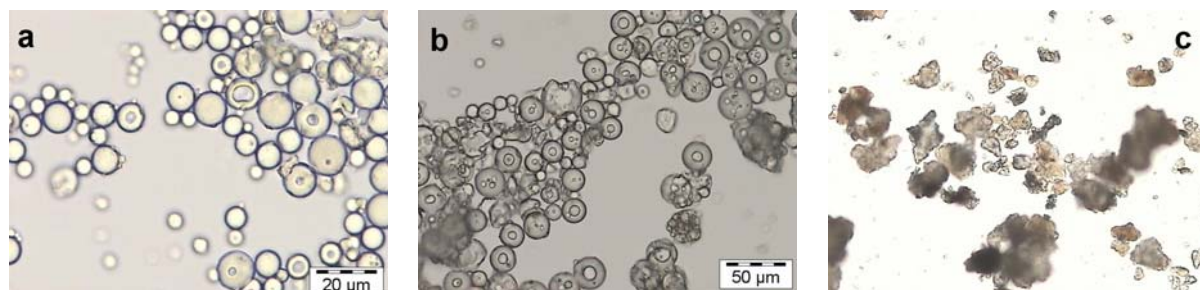


**Figure A.IV.2:** Optical microscopic images of the samples synthesised with different co-surfactants (molar ratios: see Table A.IV.8: Pluronic<sup>®</sup> P123 (a); Pluronic<sup>®</sup> F127 (b) and OTAC (c).

The nitrogen physisorption data of the ethane-bridged samples synthesised with different co-surfactants are listed in Table A.IV.11.

**Table A.IV.11:** Nitrogen physisorption data of the samples synthesised with the addition of different co-surfactants.

	Co-surfactant	BET surface [m <sup>2</sup> /g]	Pore Diameter [nm]	Diameter Range [nm]
Edj75	P123	1047	3.0	1.3 – 55
Eoj76	F127	1065	2.4	1.3 – 49
Eaj77	OTAC	998	2.4	1.3 – 80

### A.IV.6 Phenylene-bridged PMOs synthesised at different pH values

The nitrogen physisorption data of the phenylene-bridged samples synthesised at different pH values of the solution are listed in Table A.IV.12.

**Table A.IV.12:** Nitrogen physisorption data of the phenylene-bridged spheres synthesised with different pH values.

	c(HCl) [mol]	BET surface [m <sup>2</sup> /g]	Pore Diameter [nm]
Cj14	0.28	690	1.2
Cj13	0.21	770	1.3
Cj12	0.14	830	1.4
Cj18	0.021	535	1.3
Cj17	0.014	-	-
Cj16	0.0095	-	-
Cj15	0.0068	-	-
Cj11	0.0027	-	-

### A.IV.7 Phenylene-bridged PMOs synthesised with different shaking intensities

The nitrogen physisorption data of the phenylene-bridged samples synthesised with different mixing intensities are listed in Table A.IV.13.

**Table A.IV.13:** Nitrogen physisorption data of phenylene-bridged spheres synthesised with different HCl concentrations and shaking intensities.

	BTEB [mol]	HCl [mol]	Shaking [spm]	Shaking time [min]
Cj23	0.5	0.28	600	90
Cj24	0.5	0.42	600	90
Cj25	0.5	0.21	1000	90
Cj26	0.5	0.21	1400	90
Cj27	0.5	0.42	1400	120

## Appendix V

### A.V.1 Spherical phenylene-bridged PMOs in the size range of 5 to 10 $\mu\text{m}$

The complete molar ratios of all synthesised and investigated samples are listed in Table A.V.1 – A.V.4

**Table A.V.1:** Molar ratios of the samples synthesised with different hydrothermal treatment procedures.

	BTEB [mol]	P123 [mol]	CTAB [mol]	HCl [mol]	Ethanol [mol]	H <sub>2</sub> O [mol]	Hydrothermal Treatment
Cde18	0.5	0.017	0.044	1.95	14.14	163	5 h / 80 °C 12 h / 130 °C
Cde18 a	0.5	0.017	0.044	1.95	14.14	163	5 h 80 °C
Cde18 b	0.5	0.017	0.044	1.95	14.14	163	12 h 130 °C

**Table A.V.2:** Molar ratios of the samples synthesised with different pH values.

	BTEB [mol]	P123 [mol]	CTAB [mol]	HCl [mol]	Ethanol [mol]	H <sub>2</sub> O [mol]
Cde38	0.5	0.017	0.044	5.85	14.14	163
Cde37	0.5	0.017	0.044	5.20	14.14	163
Cde36	0.5	0.017	0.044	4.55	14.14	163
Cde15	0.5	0.017	0.044	3.9	14.14	163
Cde16	0.5	0.017	0.044	3.25	14.14	163
Cde17	0.5	0.017	0.044	2.60	14.14	163
Cde18	0.5	0.017	0.044	1.95	14.14	163
Cde33	0.5	0.017	0.044	1.30	14.14	163
Cde34	0.5	0.017	0.044	0.65	14.14	163
Cde35	0.5	0.017	0.044	0	14.14	163

**Table A.V.3:** Molar ratios of the samples synthesised with different ethanol concentrations.

	BTEB [mol]	P123 [mol]	CTAB [mol]	HCl [mol]	Ethanol [mol]	H <sub>2</sub> O [mol]
Cde43	0.5	0.017	0.044	1.95	0	163
Cde39	0.5	0.017	0.044	1.95	7.07	163
Cde18	0.5	0.017	0.044	1.95	14.14	163
Cde40	0.5	0.017	0.044	1.95	21.21	163
Cde41	0.5	0.017	0.044	1.95	28.28	163
Cde42	0.5	0.017	0.044	1.95	35.35	163

**Table A.V.4:** Molar ratios of the samples synthesised with different compositions of the SDAs.

	BTEB [mol]	P123 [mol]	CTAB [mol]	HCl [mol]	Ethanol [mol]	H <sub>2</sub> O [mol]
Cde44	0.5	0.017	0	1.95	14.14	163
Cde45	0.5	0	0.044	1.95	14.14	163
Cde46	0.5	0	0	1.95	14.14	163
Cde18	0.5	0.017	0.044	1.95	14.14	163

### A.V.2 Investigations of the hydrothermal treatment procedure

The optical microscopic images of the phenylene-bridged spheres synthesised with different hydrothermal treatment procedures are depicted in Figure A.V.1 a – c.

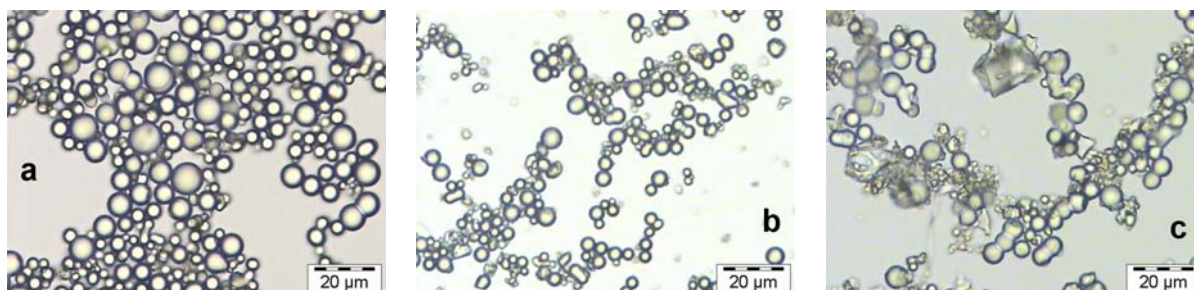


**Figure A.V.1:** Optical microscopic images of the phenylene-bridged samples synthesised with different hydrothermal treatment procedures (molar ratios: Table A.V.6): 5 h / 80 °C + 12 h / 130 °C (a); 5 h / 80 °C (b); 12 h / 130 °C (c).

The nitrogen physisorption data of the samples synthesised with different hydrothermal treatment procedure are listed in Table A.V.5.

**Table A.V.5:** Nitrogen physisorption data of the phenylene-bridged samples synthesised with different SDA contents.

	Step 1	Step 2	BET [m <sup>2</sup> /g]	Pore Diameter [nm]
Cde18	5 h / 80 °C	12 h / 130 °C	1181	5.7
Cde18 a	5 h / 80 °C	-	813	3 broad
Cde18 b	-	12 h / 130 °C	1325	6.1

### A.V.3 Phenylene-bridged spherical PMOs synthesised at different pH values

The complete nitrogen physisorption data of the samples synthesised at different pH values are listed in Table A.V.6

**Table A.V.6:** Nitrogen physisorption data of the samples synthesised at different pH values.

	n(HCl) [mol]	pH value	BET [m <sup>2</sup> /g]	Pore Diameter [nm]
Cde38	5.85	-0.16	1295	3.1 (broad)
Cde37	5.20	-0.11	1253	3.7 (broad)
Cde36	4.55	-0.05	1239	4.3 (broad)
Cde15	3.9	0.02	1080	4.8
Cde16	3.25	0.1	1227	5.3
Cde17	2.60	0.2	1230	5.7
Cde18	1.95	0.3	1181	5.7
Cde33	1.30	0.5	835	5.9
Cde34	0.65	0.8	914	5.9
Cde35	0	6.6	860	6.5 (broad)

#### A.V.4 Phenylene-bridged spherical PMOs synthesised with different ethanol concentrations

The optical microscopic images of the phenylene-bridged samples synthesised with different ethanol concentrations are shown in Figure A.V.2 a – f.

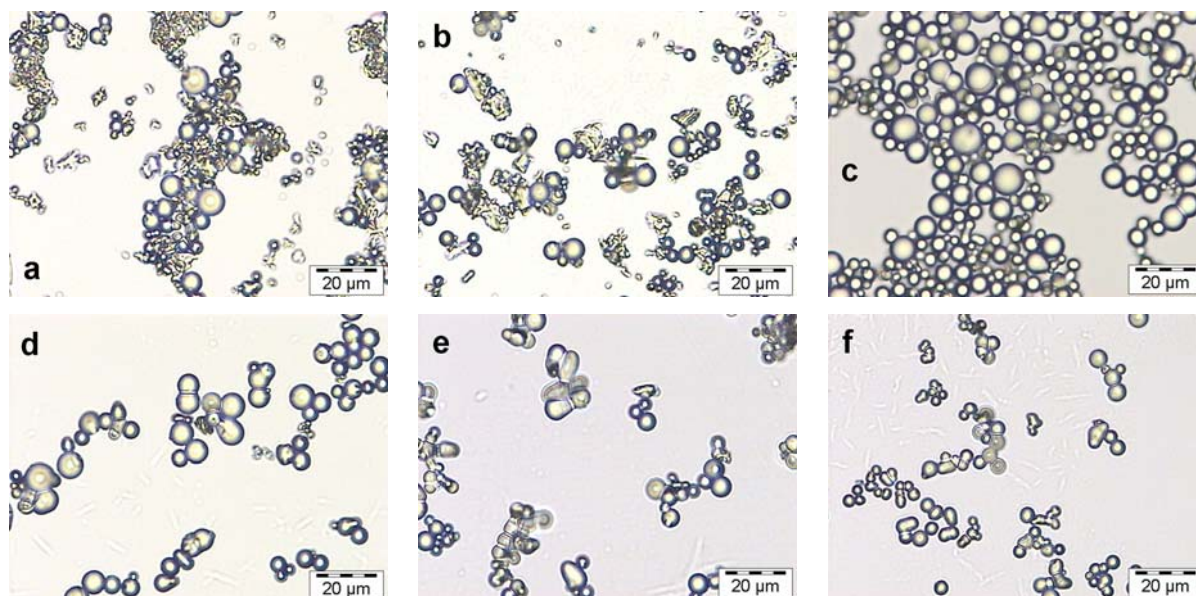


**Figure A.V.2:** Optical microscopic images of phenylene-bridged samples synthesised with different ethanol concentrations (molar ratios: Table A.V.3): 0 mol (a); 7.07 mol (b); 14.14 mol (c), 21.21 mol (d); 28.28 mol (e) and 35.35 mol (e).

The nitrogen physisorption data of the phenylene-bridged samples synthesised with different ethanol concentrations are listed in Table A.V.7.

**Table A.V.7:** Nitrogen physisorption data of the phenylene-bridged samples synthesised with different ethanol concentrations.

	Ethanol [mol]	BET [ $\text{m}^2/\text{g}$ ]	Pore Diameter [nm]
Cde43	0	220	3.5
Cde39	7.07	976	5.9
Cde18	14.14	1181	5.7
Cde40	21.21	1142	5.7
Cde41	28.28	1318	5.7
Cde42	35.35	1468	5.3

### A.V.5 Phenylene-bridged samples synthesised with different contents of both SDAs

The nitrogen physisorption data of the samples synthesised with different contents of the SDAs are summarised in Table A.V.8.

**Table A.V.8:** Nitrogen physisorption data of the phenylene-bridged samples synthesised with different SDA contents.

	n(P123)	n(CTAB)	BET [m <sup>2</sup> /g]	Pore Diameter [nm]
Cde18	0.017	0.044	1181	5.7
Cde44	0.017	-	1131	6.8
Cde45	-	0.044	1019	2 – 15
Cde46	-	-	1142	6.1 (2 – 20)

## Appendix VI

### A.VI.1 Molar ratios of the phenylene-bridged samples synthesised with Pluronic® P123 as SDA

The molar ratios of the samples synthesised for the formation studies are listed in Table A.VI.1.

**Table A.VI.1:** Synthesis conditions of phenylene-bridged PMOs synthesised with P123 as SDA.

	BTEB [mol]	P123 [mol]	HCl [mol]	H <sub>2</sub> O [mol]	Time (stirring) [min]	Temp (stirring) [°C]	Temp. hydroth. [°C]	Time hydroth. [min]
Cd1	0.5	0.038	0.66	369.06	120	40	105	1440
Cd2	0.5	0.038	0.66	369.06	120	40	-	-
Cd3	0.5	0.038	0.66	369.06	1440	40	-	-
Cd4	0.5	0.038	0.66	369.06	1440	40	105	1440
Cd14	0.5	0.038	0.66	369.06	90	40	-	-
Cd15	0.5	0.038	0.66	369.06	180	40	-	-
Cd16	0.5	0.038	0.66	369.06	360	40	-	-
Cd17	0.5	0.038	0.66	369.06	540	40	-	-

### A.VI.2 Molar ratios of the phenylene-bridged samples synthesised with Brij<sup>®</sup> 76 as SDA

The molar ratios of the samples synthesised for the formation studies are listed in Table A.VI.2.

**Table A.VI.2:** Synthesis conditions of phenylene-bridged PMOs synthesised with Brij 76 as surfactant.

	BTEB [mol]	Brij <sup>®</sup> 76 [mol]	HCl [mol]	H <sub>2</sub> O [mol]	Time (stirring) [min]	Temp (stirring) [°C]	Temp. hydroth. [°C]	Time hydroth. [min]
Cm1	0.5	0.121	0.309	171.89	120	50	-	-
Cm2	0.5	0.121	0.309	171.89	120	50	105	1440
Cm3	0.5	0.121	0.309	171.89	1440	50	-	-
Cm4	0.5	0.121	0.309	171.89	1440	50	105	1440
Cm5	0.5	0.121	0.309	171.89	120	50	-	-
Cm6	0.5	0.121	0.309	171.89	240	50	-	-
Cm7	0.5	0.121	0.309	171.89	455	50	-	-
Cm8	0.5	0.121	0.309	171.89	550	50	-	-

## Appendix VII

### A.VII.1 Experimental details of the $\text{Cu}^{2+}$ adsorption experiments

The experimental details of the  $\text{Cu}^{2+}$  adsorption experiments and the experimental details of the washing procedures are listed in Tables A.VII.1 – A.VII.6. The samples are named as follows: The PMO material containing 11 % BTMPA and 89 % BTME is named PMO-11, the PMO material containing 33 % BTMPA and 67 % BTME is named PMO-33 and the SBA-15 silica is named SBA-15.

**Table A.VII.1:** Experimental details of the  $\text{Cu}^{2+}$  adsorption experiments of PMO-11 a – j.

	Weight [mg]	$c(\text{Cu}^{2+})$ [mol/L]	$V(\text{Cu}^{2+}\text{-L.})$ [L]	$n(\text{Cu}^{2+})$ [mol]	Stirring Time [min]
PMO-11 a	200.7	0.001	0.004	$4 \cdot 10^{-6}$	120
PMO-11 b	200.3	0.005	0.004	$2 \cdot 10^{-5}$	120
PMO-11 c	200.7	0.01	0.004	$4 \cdot 10^{-5}$	120
PMO-11 d	200.5	0.05	0.004	$2 \cdot 10^{-4}$	120
PMO-11 e	200.4	0.1	0.004	$4 \cdot 10^{-4}$	120
PMO-11 f	200.5	0.01	0.004	$4 \cdot 10^{-5}$	10
PMO-11 g	200.2	0.01	0.004	$4 \cdot 10^{-5}$	30
PMO-11 h	200.3	0.01	0.004	$4 \cdot 10^{-5}$	60
PMO-11 i	200.5	0.01	0.004	$4 \cdot 10^{-5}$	120
PMO-11 j	200.4	0.01	0.004	$4 \cdot 10^{-5}$	480

**Table A.VII.2:** Experimental details of the washing procedure of the PMO-11 Cu a – j.

	Weight [mg]	$V(\text{H}_2\text{O})$ [L]	Stirring Time [h]
PMO-11 a Cu	50.3	0.005	24
PMO-11 b Cu	50.0	0.005	24
PMO-11 c Cu	50.3	0.005	24
PMO-11 d Cu	50.6	0.005	24
PMO-11 e Cu	50.5	0.005	24
PMO-11 f Cu	50.6	0.005	24
PMO-11 g Cu	50.7	0.005	24
PMO-11 h Cu	49.9	0.005	24
PMO-11 i Cu	50.8	0.005	24
PMO-11 j Cu	50.6	0.005	24

**Table A.VII.3:** Experimental details of the  $\text{Cu}^{2+}$  adsorption experiments on PMO-33 a – j.

	Weight [mg]	$c(\text{Cu}^{2+})$ [mol/L]	$V(\text{Cu}^{2+}\text{-L.})$ [L]	$n(\text{Cu}^{2+})$ [mol]	Stirring Time [min]
PMO-33 a	200.1	0.005	0.004	$4 \cdot 10^{-6}$	120
PMO-33 b	200.3	0.01	0.004	$2 \cdot 10^{-5}$	120
PMO-33 c	200.7	0.05	0.004	$4 \cdot 10^{-5}$	120
PMO-33 d	200.5	0.1	0.004	$2 \cdot 10^{-4}$	120
PMO-33 e	200.4	0.001	0.004	$4 \cdot 10^{-4}$	120
PMO-33 f	200.5	0.01	0.004	$4 \cdot 10^{-5}$	10
PMO-33 g	200.2	0.01	0.004	$4 \cdot 10^{-5}$	30
PMO-33 h	200.3	0.01	0.004	$4 \cdot 10^{-5}$	60
PMO-33 i	200.5	0.01	0.004	$4 \cdot 10^{-5}$	120
PMO-33 j	200.4	0.01	0.004	$4 \cdot 10^{-5}$	480

**Table A.VII.4:** Experimental details of the washing procedure of the PMO-33 b – j.

	Weight [mg]	$V(\text{H}_2\text{O})$ [L]	Stirring Time [h]
PMO-33 a Cu	-*	-	-
PMO-33 b Cu	50.3	0.005	24
PMO-33 c Cu	49.9	0.005	24
PMO-33 d Cu	50.0	0.005	24
PMO-33 e Cu	50.4	0.005	24
PMO-33 f Cu	50.7	0.005	24
PMO-33 g Cu	50.1	0.005	24
PMO-33 h Cu	50.5	0.005	24
PMO-33 I Cu	50.6	0.005	24
PMO-33 j Cu	50.5	0.005	24

\* broken in the centrifuge

**Table A.VII.5:** Experimental details of the  $\text{Cu}^{2+}$  adsorption experiments on SBA-15 a – j.

	Weight [mg]	$c(\text{Cu}^{2+})$ [mol/L]	$V(\text{Cu}^{2+}\text{-L.})$ [L]	$n(\text{Cu}^{2+})$ [mol]	Stirring Time [min]
SBA-15 a	50.5	0.001	0.004	$4 \cdot 10^{-6}$	120
SBA-15 b	50.5	0.005	0.004	$2 \cdot 10^{-5}$	120
SBA-15 c	50.2	0.01	0.004	$4 \cdot 10^{-5}$	120
SBA-15 d	50.0	0.05	0.004	$2 \cdot 10^{-4}$	120
SBA-15 e	50.8	0.1	0.004	$4 \cdot 10^{-4}$	120
SBA-15 f	50.1	0.01	0.004	$4 \cdot 10^{-5}$	10
SBA-15 g	50.3	0.01	0.004	$4 \cdot 10^{-5}$	30
SBA-15 h	50.4	0.01	0.004	$4 \cdot 10^{-5}$	60
SBA-15 i	50.6	0.01	0.004	$4 \cdot 10^{-5}$	120
SBA-15 j	50.4	0.01	0.004	$4 \cdot 10^{-5}$	480

**Table: A.VII.6:** Experimental details of the washing procedure of the SBA-15 silica Cu a – j.

	Weight [mg]	V (H <sub>2</sub> O) [L]	Stirring Time [h]
SBA-15 a Cu	30.9	0.005	24
SBA-15 b Cu	30.1	0.005	24
SBA-15 c Cu	30.8	0.005	24
SBA-15 d Cu	30.4	0.005	24
SBA-15 e Cu	30.3	0.005	24
SBA-15 f Cu	30.2	0.005	24
SBA-15 g Cu	30.3	0.005	24
SBA-15 h Cu	30.4	0.005	24
SBA-15 i Cu	30.4	0.005	24
SBA-15 j Cu	30.3	0.005	24

### A.VII.2 Results of the copper adsorption experiments

The results of the concentration-dependent adsorption experiments listed in Table A.VII.7 (PMO-11), A.VII.8 (PMO-33) and A.VII.9 (SBA-15). The different amounts denoted as  $n(\text{Cu}^{2+})_1$ ,  $n(\text{Cu}^{2+})_2$  and  $n(\text{Cu}^{2+})_3$  are due to the amounts in the original solution ( $n(\text{Cu}^{2+})_1$ ), the solution after  $\text{Cu}^{2+}$  adsorption ( $n(\text{Cu}^{2+})_2$ ) and the amount being adsorbed in each sample ( $n(\text{Cu}^{2+})_3$ ). The adsorption was estimated in mol/g of the substance and the percentage ratio of adsorbed  $\text{Cu}^{2+}$  amount was calculated.

**Table A.VII.7:** Results of the  $\text{Cu}^{2+}$  adsorption experiments of PMO-11 from solutions with different concentrations.

	$n(\text{Cu}^{2+})_1$ [mol]	$n(\text{Cu}^{2+})_2$ [mol]	$n(\text{Cu}^{2+})_3$ [mol]	Adsorption [mol/g]	Adsorption [%]
PMO-11 a Cu	$4 \cdot 10^{-6}$	$3.2 \cdot 10^{-8}$	$3.968 \cdot 10^{-6}$	$1.977 \cdot 10^{-5}$	99.2
PMO-11 b Cu	$2 \cdot 10^{-5}$	$6.4 \cdot 10^{-8}$	$1.9936 \cdot 10^{-5}$	$9.95 \cdot 10^{-5}$	99.68
PMO-11 c Cu	$4 \cdot 10^{-5}$	$5.1 \cdot 10^{-8}$	$3.9949 \cdot 10^{-5}$	$19.90 \cdot 10^{-5}$	99.87
PMO-11 d Cu	$2 \cdot 10^{-4}$	$3.6 \cdot 10^{-8}$	$1.99964 \cdot 10^{-4}$	$99.7 \cdot 10^{-5}$	99.982
PMO-11 e Cu	$4 \cdot 10^{-4}$	$6.1 \cdot 10^{-8}$	$3.99939 \cdot 10^{-4}$	$199.9 \cdot 10^{-5}$	99.985

**Table A.VII.8:** Results of the  $\text{Cu}^{2+}$  adsorption experiments of PMO-33 from solutions with different concentrations.

	$n(\text{Cu}^{2+})_1$ [mol]	$n(\text{Cu}^{2+})_2$ [mol]	$n(\text{Cu}^{2+})_3$ [mol]	Adsorption [mol/g]	Adsorption [%]
PMO-33 e Cu	$4 \cdot 10^{-6}$	$6.4 \cdot 10^{-8}$	$3.936 \cdot 10^{-6}$	$1.968 \cdot 10^{-5}$	98.4
PMO-33 a Cu	$2 \cdot 10^{-5}$	-*	-	-	-
PMO-33 b Cu	$4 \cdot 10^{-5}$	$3 \cdot 10^{-8}$	$3.997 \cdot 10^{-5}$	$19.99 \cdot 10^{-5}$	99.925
PMO-33 c Cu	$2 \cdot 10^{-4}$	$2.27 \cdot 10^{-7}$	$1.9977 \cdot 10^{-4}$	$99.88 \cdot 10^{-5}$	99.88
PMO-33 d Cu	$4 \cdot 10^{-4}$	$5.16 \cdot 10^{-7}$	$3.9948 \cdot 10^{-4}$	$199.74 \cdot 10^{-5}$	99.87

\* broken in the centrifuge

**Table A.VII.9:** Results of the  $\text{Cu}^{2+}$  adsorption experiments of the SBA-15 silica from solutions with different concentrations.

	$n(\text{Cu}^{2+})_1$ [mol]	$n(\text{Cu}^{2+})_2$ [mol]	$n(\text{Cu}^{2+})_3$ [mol]	Adsorption [mol/g]	Adsorption [%]
SBA-15 a Cu	$4 \cdot 10^{-6}$	$2.77 \cdot 10^{-6}$	$1.23 \cdot 10^{-6}$	$2.46 \cdot 10^{-5}$	30.75
SBA-15 b Cu	$2 \cdot 10^{-5}$	$1.79 \cdot 10^{-5}$	$2.1 \cdot 10^{-6}$	$4.2 \cdot 10^{-5}$	10.5
SBA-15 c Cu	$4 \cdot 10^{-5}$	$3.3 \cdot 10^{-5}$	$7.0 \cdot 10^{-6}$	$14.0 \cdot 10^{-5}$	17.5
SBA-15 d Cu	$2 \cdot 10^{-4}$	$1.26 \cdot 10^{-4}$	$7.4 \cdot 10^{-5}$	$148 \cdot 10^{-5}$	37.0
SBA-15 e Cu	$4 \cdot 10^{-4}$	$3.41 \cdot 10^{-4}$	$5.9 \cdot 10^{-5}$	$118 \cdot 10^{-5}$	14.75

The results of the time-dependent adsorption experiments are listed in Tables A.VII.10 (PMO-11), A.VII.11 (PMO-33) and A.VII.12 (SBA-15).

**Table A.VII.11:** Results of the time-dependent  $\text{Cu}^{2+}$  adsorption experiments of PMO-11.

	$n(\text{Cu}^{2+})$ 1 [mol]	$n(\text{Cu}^{2+})$ 2 [mol]	$n(\text{Cu}^{2+})$ 3 [mol]	Adsorption [mol/g]	Adsorption [%]
PMO-11 f Cu	$4 \cdot 10^{-5}$	$6.3 \cdot 10^{-8}$	$3.9937 \cdot 10^{-5}$	$1.992 \cdot 10^{-4}$	99.84
PMO-11 g Cu	$4 \cdot 10^{-5}$	$8.3 \cdot 10^{-8}$	$3.9917 \cdot 10^{-5}$	$1.994 \cdot 10^{-4}$	99.79
PMO-11 h Cu	$4 \cdot 10^{-5}$	$7.4 \cdot 10^{-8}$	$3.9926 \cdot 10^{-5}$	$1.993 \cdot 10^{-4}$	99.82
PMO-11 i Cu	$4 \cdot 10^{-5}$	$8.3 \cdot 10^{-8}$	$3.9917 \cdot 10^{-5}$	$1.991 \cdot 10^{-4}$	99.79
PMO-11 j Cu	$4 \cdot 10^{-5}$	$3.0 \cdot 10^{-8}$	$3.997 \cdot 10^{-5}$	$1.995 \cdot 10^{-4}$	99.93

**Table A.VII.11:** Results of the time-dependent  $\text{Cu}^{2+}$  adsorption experiments of PMO-33.

	$n(\text{Cu}^{2+})$ 1 [mol]	$n(\text{Cu}^{2+})$ 2 [mol]	$n(\text{Cu}^{2+})$ 3 [mol]	Adsorption [mol/g]	Adsorption [%]
PMO-33 f Cu	$4 \cdot 10^{-5}$	$3.7 \cdot 10^{-8}$	$3.996 \cdot 10^{-5}$	$1.997 \cdot 10^{-5}$	99.90
PMO-33 g Cu	$4 \cdot 10^{-5}$	$3.1 \cdot 10^{-8}$	$3.997 \cdot 10^{-5}$	$1.997 \cdot 10^{-5}$	99.93
PMO-33 h Cu	$4 \cdot 10^{-5}$	$4.2 \cdot 10^{-8}$	$3.996 \cdot 10^{-5}$	$1.993 \cdot 10^{-5}$	99.90
PMO-33 i Cu	$4 \cdot 10^{-5}$	$6.9 \cdot 10^{-8}$	$3.993 \cdot 10^{-5}$	$1.996 \cdot 10^{-5}$	99.83
PMO-33 j Cu	$4 \cdot 10^{-5}$	$10.7 \cdot 10^{-8}$	$3.990 \cdot 10^{-5}$	$1.994 \cdot 10^{-5}$	99.75

**Table A.VII.12:** Results of the time dependent  $\text{Cu}^{2+}$  adsorption investigations of SBA-15 silica.

	$n(\text{Cu}^{2+})$ 1 [mol]	$n(\text{Cu}^{2+})$ 2 [mol]	$n(\text{Cu}^{2+})$ 3 [mol]	Adsorption [mol/g]	Adsorption [%]
SBA-15 f Cu	$4 \cdot 10^{-5}$	$3.1 \cdot 10^{-5}$	$8.99 \cdot 10^{-6}$	$1.79 \cdot 10^{-4}$	22.4
SBA-15 g Cu	$4 \cdot 10^{-5}$	$2.93 \cdot 10^{-4}$	$10.74 \cdot 10^{-6}$	$2.15 \cdot 10^{-4}$	26.85
SBA-15 h Cu	$4 \cdot 10^{-5}$	$3.03 \cdot 10^{-5}$	$9.66 \cdot 10^{-6}$	$1.93 \cdot 10^{-4}$	24.15
SBA-15 i Cu	$4 \cdot 10^{-5}$	$2.98 \cdot 10^{-5}$	$10.21 \cdot 10^{-5}$	$2.04 \cdot 10^{-4}$	25.52
SBA-15 j Cu	$4 \cdot 10^{-5}$	$3.09 \cdot 10^{-5}$	$9.07 \cdot 10^{-5}$	$1.81 \cdot 10^{-4}$	22.68

### A.VII.3 Results of the washing procedure

Washing experiments were carried out in order to obtain information about the metal content after a 24-hour treatment with deionised water. For these experiments about 50 mg of the PMO samples and 30 mg of the SBA-15 were suspended in 5 mL of demineralised water. After a 24-hour stirring step at room temperature (23 °C) the suspension was centrifuged, the  $\text{Cu}^{2+}$  containing aqueous solution was transferred into a 50 mL vessel and filled with deionised water. The  $\text{Cu}^{2+}$  content of these solutions was measured by AAS again. The results of the samples impregnated with  $\text{Cu}^{2+}$  solution in the concentration dependent adsorption procedure are listed in Tables A.VII.13 (PMO-11), A.VII.14 (PMO-33) and A.VII.15 (SBA-15). The columns are named as follows: Weight is in this case the sample weight used for the washing experiments. The  $c(\text{Cu}^{2+})_1$  is the  $\text{Cu}^{2+}$  concentration measured by AAS. The  $c(\text{Cu}^{2+})_2$  is the  $\text{Cu}^{2+}$  concentration in 50 mL of deionised water. The adsorbed  $\text{Cu}^{2+}$  is the  $\text{Cu}^{2+}$  content in the respective sample weight resulting from the adsorption experiments described above. In the last column the  $\text{Cu}^{2+}$  contents that were washed out during this procedure is listed.

**Table A.VII.13:** Results of the washing procedure of the PMO-11 material impregnated in the concentration-dependent adsorption procedure.

	Weight [mg]	$c(\text{Cu}^{2+})_1$ [mg/L]	$c(\text{Cu}^{2+})_2$ [mol/50 mL]	Adsorbed $\text{Cu}^{2+}$ [mol/g]	$\text{Cu}^{2+}$ loss [%]
PMO-11 a o Cu	50.3	0.003	$0.2 \cdot 10^{-8}$	$9.94 \cdot 10^{-7}$	0.2
PMO-11 b o Cu	50.0	0.059	$4.6 \cdot 10^{-8}$	$4.98 \cdot 10^{-6}$	0.92
PMO-11 c o Cu	50.2	0.054	$4.3 \cdot 10^{-8}$	$9.99 \cdot 10^{-6}$	0.4
PMO-11 d o Cu	50.6	0.171	$13.5 \cdot 10^{-8}$	$5.05 \cdot 10^{-5}$	0.27
PMO-11 e o Cu	50.5	0.639	$50.3 \cdot 10^{-8}$	$1.01 \cdot 10^{-4}$	0.5

**Table A.VII.14:** Results of the washing procedure of the PMO-33 material impregnated in the concentration-dependent adsorption procedure.

	Weight [mg]	$c(\text{Cu}^{2+})$ 1 [mg/L]	$c(\text{Cu}^{2+})$ [mol/50 mL]	Adsorbed $\text{Cu}^{2+}$ [mol/g]	$\text{Cu}^{2+}$ loss [%]
PMO-33 e o Cu	50.4	0.038	$3 \cdot 10^{-8}$	$9.9 \cdot 10^{-7}$	3
PMO-33 a o Cu	-*	-	-	-	-
PMO-33 b o Cu	49.9	0.053	$4.2 \cdot 10^{-8}$	$1.0 \cdot 10^{-5}$	0.42
PMO-33 c o Cu	50.0	0.532	$41.9 \cdot 10^{-8}$	$4.9 \cdot 10^{-5}$	0.8
PMO-33 d o Cu	50.4	2.812	$221.3 \cdot 10^{-8}$	$9.9 \cdot 10^{-5}$	2.2

\* broken in the centrifuge

**Table A.VII.15:** Results of the washing procedure of the SBA-15 material impregnated in the concentration-dependent adsorption procedure.

	Weight [mg]	$c(\text{Cu}^{2+})$ 1 [mg/L]	$c(\text{Cu}^{2+})$ [mol/50 mL]	Adsorbed $\text{Cu}^{2+}$ [mol/g]	$\text{Cu}^{2+}$ loss [%]
SBA-15 a o Cu	30.9	0.047	$1.5 \cdot 10^{-8}$	$7.53 \cdot 10^{-7}$	2.4
SBA-15 b o Cu	30.1	0.015	$1.2 \cdot 10^{-8}$	$1.25 \cdot 10^{-6}$	0.96
SBA-15 c o Cu	30.8	0.016	$1.3 \cdot 10^{-8}$	$4.30 \cdot 10^{-6}$	0.3
SBA-15 d o Cu	30.4	0.19	$1.5 \cdot 10^{-8}$	$4.50 \cdot 10^{-4}$	0.03
SBA-15 e o Cu	30.3	0.28	$2.2 \cdot 10^{-8}$	$3.5 \cdot 10^{-4}$	0.06

The results of the AAS measurements of the samples impregnated with  $\text{Cu}^{2+}$  in the time-dependent adsorption procedure are listed in Tables A.VII.16 (PMO-11), A.VII.17 (PMO-33) and A.VII.18 (SBA-15).

**Table A.VII.16:** Results of the washing procedure of the PMO-11 material impregnated in the time-dependent adsorption procedure.

	Weight [mg]	$c(\text{Cu}^{2+})$ 1 [mg/L]	$c(\text{Cu}^{2+})$ [mol/50 mL]	Adsorbed $\text{Cu}^{2+}$ [mol/g]	$\text{Cu}^{2+}$ loss [%]
PMO-11 f o Cu	50.6	0.033	$2.6 \cdot 10^{-8}$	$1.01 \cdot 10^{-5}$	0.26
PMO-11 g o Cu	50.7	0.052	$4.1 \cdot 10^{-8}$	$1.01 \cdot 10^{-5}$	0.41
PMO-11 h o Cu	49.9	0.055	$4.3 \cdot 10^{-8}$	$0.99 \cdot 10^{-5}$	0.43
PMO-11 i o Cu	50.8	0.086	$6.8 \cdot 10^{-8}$	$1.01 \cdot 10^{-5}$	0.67
PMO-11 j o Cu	50.6	0.074	$5.8 \cdot 10^{-8}$	$1.01 \cdot 10^{-5}$	0.57

**Table A.VII.17:** Results of the washing procedure of the PMO-33 material impregnated in the time-dependent adsorption procedure.

	Weight [mg]	$c(\text{Cu}^{2+})$ 1 [mg/L]	$c(\text{Cu}^{2+})$ [mol/50 mL]	Adsorbed $\text{Cu}^{2+}$ [mol/g]	$\text{Cu}^{2+}$ loss [%]
PMO-33 f o Cu	50.7	0.063	$5 \cdot 10^{-8}$	$1.01 \cdot 10^{-5}$	0.49
PMO-33 g o Cu	50.1	0.013	$1 \cdot 10^{-8}$	$1.00 \cdot 10^{-5}$	0.1
PMO-33 h o Cu	50.5	0.039	$3.1 \cdot 10^{-8}$	$1.01 \cdot 10^{-5}$	0.31
PMO-33 i o Cu	50.6	0.053	$4.2 \cdot 10^{-8}$	$1.01 \cdot 10^{-5}$	0.42
PMO-33 j o Cu	50.5	0.002	$0.2 \cdot 10^{-8}$	$1.01 \cdot 10^{-5}$	0.02

**Table A.VII.18:** Results of the washing procedure of the SBA-15 material impregnated in the time-dependent adsorption procedure.

	Weight [mg]	$c(\text{Cu}^{2+})$ 1 [mg/L]	$c(\text{Cu}^{2+})$ [mol/50 mL]	Adsorbed $\text{Cu}^{2+}$ [mol/g]	$\text{Cu}^{2+}$ loss [%]
SBA-15 f o Cu	30.2	0.021	$1.7 \cdot 10^{-8}$	$5.15 \cdot 10^{-6}$	0.03
SBA-15 g o Cu	30.3	0.018	$1.4 \cdot 10^{-8}$	$6.47 \cdot 10^{-6}$	0.22
SBA-15 h o Cu	30.4	0.035	$2.8 \cdot 10^{-8}$	$5.82 \cdot 10^{-6}$	0.48
SBA-15 i o Cu	30.4	0.22	$1.7 \cdot 10^{-8}$	$6.13 \cdot 10^{-6}$	0.28
SBA-15 j o Cu	30.3	0.21	$1.7 \cdot 10^{-8}$	$5.45 \cdot 10^{-6}$	0.31

## Appendix VIII

### A.VIII.1 UV/Vis spectra of the components of the three test mixtures applied for chromatographic tests

In order to obtain information about the absorption maxima of the single substances UV/Vis spectra were recorded. The spectra of benzene, naphthalene, biphenyl and phenanthrene are shown in Figure A.VIII.1, the spectra of BHT, sorbic acid and aspartam are shown in Figure A.VIII.2 and the spectra of coumarin, vanillin and caffeine are depicted in Figure A.VIII.3.

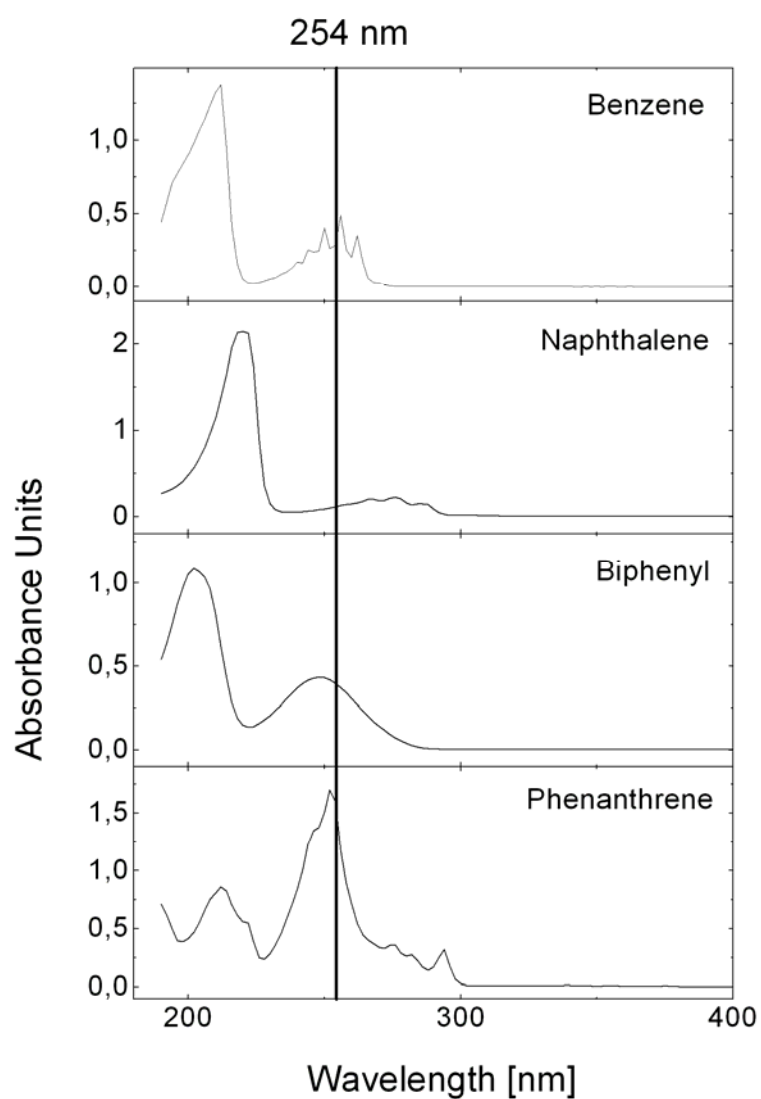


**Figure A.VIII.1:** UV/Vis-spectra of benzene, naphthalene, biphenyl and phenanthrene.

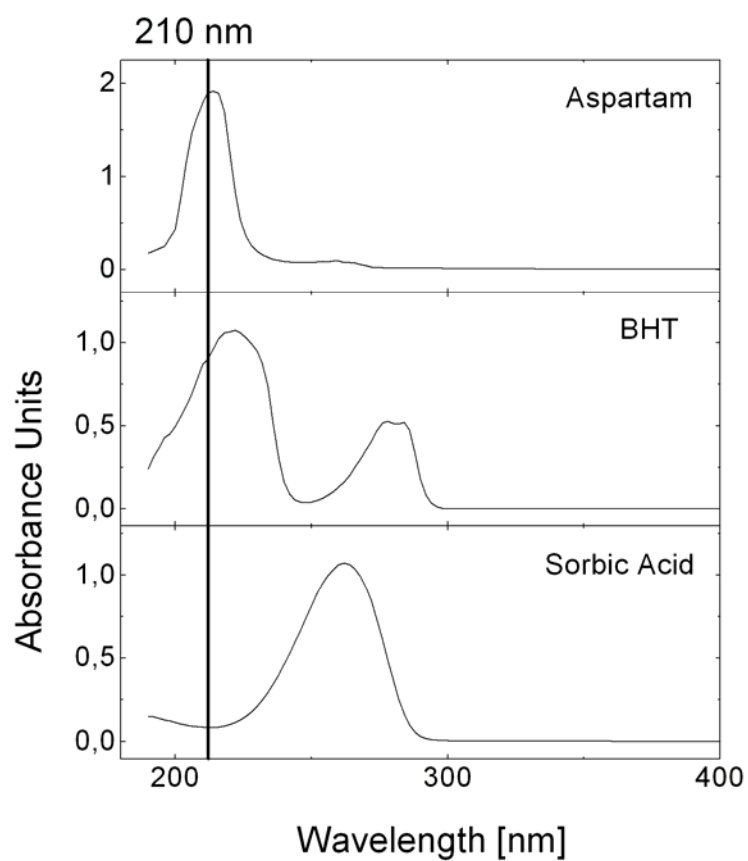


**Figure A.VIII.2:** UV/Vis-spectra of aspartam, BHT and sorbic acid.

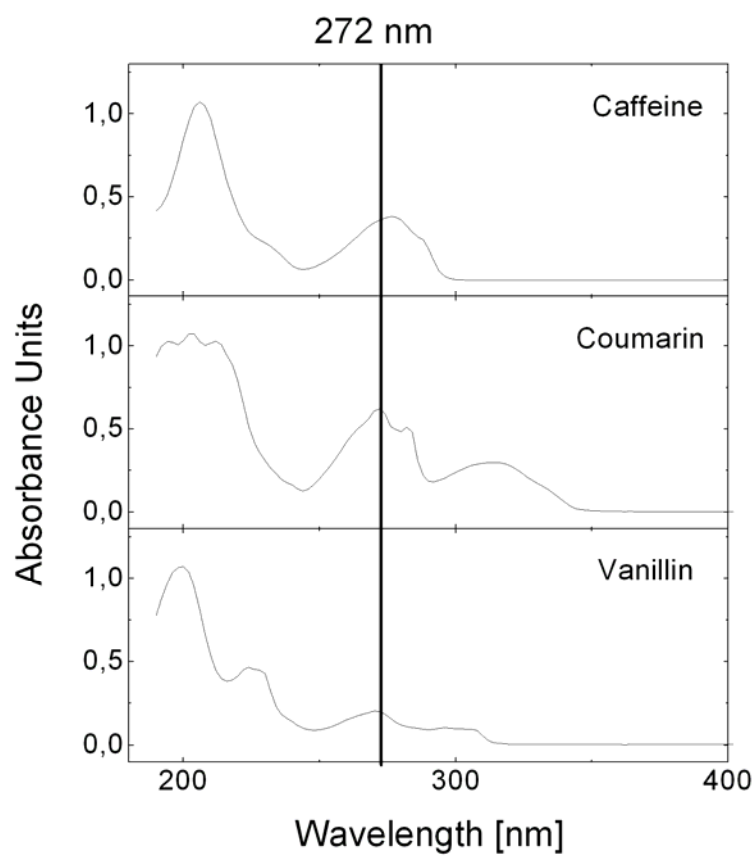


**Figure A. VIII.3:** UV/Vis-spectra of caffeine, coumarin and vanillin.

### A.VIII.2 The Elutropic Series

Different solvent properties like elution strength ( $\epsilon^0$ ), viscosity ( $\eta$ ), the refraction index ( $n_D^{20}$ ), the UV absorption limit (UV), the boiling point (bp), the dipole ( $\pi^*$ ), the basicity ( $\beta$ ) and the acidity ( $\alpha$ ) are listed in Table A.VIII.1.

**Table A.VIII.1:** Elutropic series and solvent properties.<sup>[204]</sup>

	$\epsilon^0$	$\eta$ (mPa s)	$n_D^{20}$	UV [nm]	Bp [°C]	$\pi^*$	$\alpha$	$\beta$
<i>n</i> -pentane	0.00	0.23	1.3575	195	36			
<i>n</i> -hexane	0.00	0.33	1.3749	190	69			
Isooctane	0.01	0.5	1.3914	200	99			
Cyclohexane	0.03	1.0	1.4262	200	81			
Caclopentane	0.04	0.47	1.4064	200	49			
Carbon tetrachloride	0.14	0.97	1.4652	265	77			
p-xylene	0.20	0.62	1.4958	290	138	0.81	0.00	0.19
Diisopropyl ether	0.22	0.37	1.3681	220	68	0.36	0.00	0.64
Toluene	0.22	0.59	1.4969	285	111	0.83	0.00	0.17
Chlorobenzene	0.23	0.80	1.5248	290	132	0.91	0.00	0.09
Benzene	0.25	0.65	1.5011	280	80	0.86	0.00	0.14
Diethyl ether	0.29	0.24	1.3524	205	34.5	0.36	0.00	0.64
Dichloromethane	0.30	0.44	1.4242	230	40	0.73	0.27	0.00
Chloroform	0.31	0.57	1.4457	245	61	0.57	0.43	0.00
1,2-Dichloroethane	0.38	0.79	1.4448	230	83	1.00	0.00	0.00
Triethylamine	0.42	0.38	1.4010	230	89	0.16	0.00	0.84
Acetone	0.43	0.32	1.3581	330	56	0.56	0.06	0.38
Dioxane	0.43	1.54	1.4224	220	101	0.60	0.00	0.40
Methyl acetate	0.46	0.37	1.3614	260	56	0.55	0.05	0.40
Tetrahydrofuran (THF)	0.48	0.46	1.4072	220	66	0.51	0.00	0.49
Tert. Butylmethyl ether	0.48	0.35	1.3689	220	53	0.36	0.00	0.64
Ethyl acetate	0.48	0.45	1.3724	260	77	0.55	0.00	0.45
Dimethyl sulphoxide (DMSO)	0.48	2.24	1.4783	270	189	0.57	0.00	0.43
Nitromethane	0.49	0.67	1.3819	380	101	0.64	0.17	0.19
Acetonitrile (ACN)	0.50	0.37	1.3441	190	82	0.60	0.15	0.25
Pyridine	0.55	0.94	1.5102	305	115	0.58	0.00	0.42
Isopropanol	0.60	2.3	1.3772	210	82	0.22	0.35	0.43
Ethanol	0.68	1.2	1.3614	210	78	0.25	0.39	0.36
Methanol	0.73	0.6	1.3284	205	65	0.28	0.43	0.29
Acetic acid		1.2	1.3719	260	118	0.31	0.54	0.15
Water		1.0	1.3330	< 190	100	0.39	0.43	0.18
Buffer								

$\epsilon^0$ : describes the elution strength of the solvent when it is used as mobile phase on silica gel. It is a measure for the adsorption energy of one solvent molecule per unit of area of the adsorbent.

Dipole character  $\pi^*$ : a measure for the dipole- and polarisation interactions between the solvent and a dissolved substance.

Acidity  $\alpha$ : a measure for the hydrogen bonding interactions between the solvent (hydrogen bonding donor) and a dissolved basic substance (hydrogen bonding acceptor).

Basicity  $\beta$ : A measure for the hydrogen bonding interactions between the solvent (hydrogen bonding acceptor) and a dissolved acidic substance (hydrogen bonding donor).

$\pi^*$ ,  $\alpha$  and  $\beta$  are normalised. The sum of the three values is 1 in all cases. Thus all values are relative. The correlation between the three values is shown in Figure A.VIII.4.

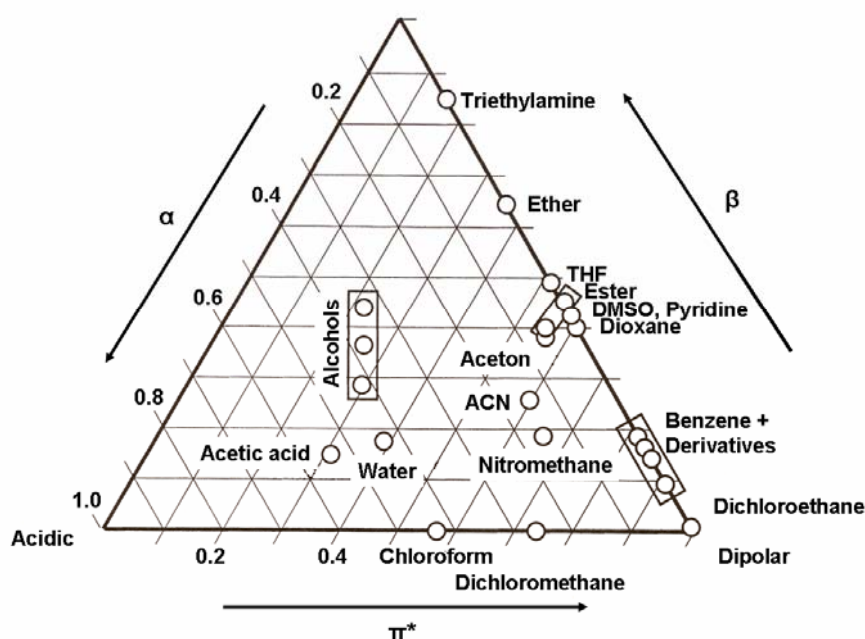


**Figure A.VIII.4:** Schematic illustration of the correlations of the acidity, basicity and dipolarity (selectivity triangle).<sup>[130]</sup>

## Appendix IX: Hazardous Chemicals

Substance	Supplier	Purity	CAS-Nr.	Hazard Category <sup>1</sup>	R-phrase <sup>2</sup> S-phrase <sup>3</sup>
Ammonia (32 %)	Merck	purum	1336-21-6	C, N	R 34-50 S 26-36/37/39-45-61
Benzene	Merck	purum	71-43-2	F, T <sup>+</sup>	R 45-11- E48/23/24/25 S 53-45
1,4-Bis(triethoxysilyl)benzene	Sigma-Aldrich	96 %	2615-18-1	-	-
1,2-Bis(triethoxysilyl)ethane	ABCR	97 %	16068-37-4	Xi	R36/37/38 S26-28-36/37/39
1,2-Bis(trimethoxysilyl)ethane	Sigma-Aldrich	96 %	18406-41-2	T	R 26/27/28 S 23-36/37/39-45
N,N-Bis[3-(trimethoxysilyl)propyl]amine	Fluka	>97 %	82985-35-1	Xn	R 20/22-36/37/38 S 26-36/37/39
Brij <sup>®</sup> 76	Sigma-Aldrich		9005-00-9	Xi	R 36 S 26-36
Carbon tetrachloride	Merck	for HPLC	56-23-5	T <sup>+</sup> , N	R23/24/25-40- 48/23-52/53-59 S 23.2-36/37-45-59
Dichloromethane	Merck	for HPLC	75-09-2	Xn	R40 S 23.2-24/25-36/37
1,4-Dioxane	Merck	for HPLC	123-91-1	F, Xn	R 11-19-36/37-40 S 9-16-36/737-46
Dodecylamine	Merck	for synthesis	124-22-1	C	R 22-35 S 26-28.1- 36/37/39-45
Ethanol	Merck	purum	64-17-5	F	R 11 S 7-16
n-Hexan	Merck	SeccoSolv	110-54-3	F, Xn, N	R 10-20/21/22 S 36/37
Hexadecyltrimethylammonium chloride	Fluka	>98%	11-02-7	Xi, N	R 36/37/38 S 26-37/39
Hexadecyltrimethylammonium bromide	Merck		57-09-0	Xn, N	R 22-36/38-50/53 S 26-39-61
Hydrochloric acid (32 %)	Merck	purum		C	R 34-37 S 26-36/37/39-45
Mesitylene	Merck		108-67-8	Xi, N	R 10-37-51/53 S 61
Methanol	Merck	for HPLC	67-56-1	F, T	R 11-23/24/25- 39/23/24/25 S 7-16-36/37-45
Sodium hydroxide	Fischer Scientific		1310-73-2	C	R 35 S26-37/39-45
Octadecyltrimethylammonium chloride	Fluka	>98 %	112-03-8	Xn	R 21/22-36/37/38 S 26-36
Pluronic <sup>®</sup> P123	Sigma-Aldrich		9003-11-6		S 23.2-25
2-Propanol	Merck	for analysis	67-63-0	F, Xi	R 11-36-67 S 7-16-24/25-26
tert.-butylmethylether	Merck	for HPLC	1634-04-4	F	R 11-66 S 16-23.2-29-33
Tetraethyl orthosilicate	Merck	for synthesis	78-10-4	Xn	R 10-20-36/37

<sup>1</sup> C (corrosive), N (dangerous for the environment), F (flammable), T<sup>+</sup> (highly toxic), T (toxic), Xi (irritant), Xn (harmful to health)

## <sup>2</sup>R-phrases

R10	Flammable
R11	Highly flammable
R19	May form explosive peroxides
R20/21/22	Harmful on inhalation, in contact with skin and if swallowed
R20/22	Harmful on inhalation and if swallowed
R22	Harmful if swallowed
R26/27/28	Very toxic on inhalation and in contact with skin
R34	Causes burns
R35	Causes severe burns
R36	Irritating to eyes
R37	Irritating to respiratory system
R36/37	Irritating to eyes and respiratory system
R36/37/38	Irritating to eyes, respiratory system and skin
R36/38	Irritating to eyes and skin
R40	Possible risks of irreversible effects
R45	May cause cancer
R48/23	Toxic, danger of serious damage to health by prolonged exposure through inhalation
R48/23/24/25	Toxic, danger of serious damage to health by prolonged exposure through inhalation, contact with skin and if swallowed
R50	Very toxic to aquatic organisms
R50/53	Very toxic to aquatic organisms and may cause long-term adverse effects in the aquatic environment
R51/53	Toxic to aquatic organisms and may cause long-term adverse effects in the aquatic environment
R52/53	Harmful to aquatic organisms and may cause long-term adverse in the aquatic environment
R59	Dangerous for the ozone layer

**<sup>3</sup>S-phrases**

S7	Keep container tightly close
S16	Keep away from sources of ignition – No smoking
S23	Do not breathe gas/fume/vapour/sprays
S25	Avoid contact with eyes
S26	In case of contact with eyes rinse immediately with plenty of water and seek medical advice
S28.1	After contact with skin wash immediately with plenty of water
S36	Wear suitable protective clothing
S36/37	Wear suitable protective clothing and gloves
S36/37/39	Wear suitable protective clothing, gloves and eye/face protection
S37/39	Wear suitable gloves and eye/face protection
S39	Wear suitable eye/face protection
S45	In case of an accident or if you feel unwell seek medical advice immediately (show the label where possible)
S46	If swallowed seek medical advice immediately and show this container or label
S53	Avoid exposure – obtain special instructions before use
S59	Refer to manufacturer/supplier for information on recovery/recycling
S61	Avoid disposal in the environment

## Appendix X: Abbreviations

a	unit cell parameter
$a_0$	effective headgroup area at the micelle surface
AEP	3-[2-(2-aminomethylamino)ethylamino]propyl
APMS	acid prepared mesoporous particles
APTS	3-aminopropyltriethoxysilane
a.u.	arbitrary units
BET	Brunauer, Emmet and Teller
BHT	butylhydroxytoluene, 2,6-di- <i>tert</i> -butyl-4-methylphenol
BJH	Barret-Joyner-Halender
p-PMO	phenylene-bridged PMO material
Brij <sup>®</sup> 56	polyoxyethylene-(10)-cetyether
Brij <sup>®</sup> 58	polyoxyethylene-(20)-cetyether
Brij <sup>®</sup> 76	polyoxyethylene-(10)-stearylether
BTME	1,2-bis(trimethoxysilyl)ethane
BTEE	1,2-bis(triethoxysilyl)ethane
BTEB	1,4-bis(triethoxysilyl)benzene
BTEBP	4,4'-bis(triethoxysilyl)biphenyl
BTET	2,5-bis(triethoxysilyl)thiophene
BTEVB	1,4-bis[( <i>E</i> )-2-(triethoxysilyl)vinyl]benzene
BTMPA	<i>N,N</i> -bis[(trimethoxysilyl)propyl]amine
C <sub>20</sub> DEMAB	eicosyldiethylmethylammonium bromide
CMK	Carbon Mesoporous of Kaist
CP	3-cyanopropyl
CPB	cetylpyridinium bromide
CPC	cetylpyridinium chloride
cps	counts per second
CTAB	hexadecyltrimethylammonium bromide
CTAC	hexadecyltrimethylammonium chloride
DA	dodecylamine
DESY	Deutsches Elektronensynchrotron
$d_{hkl}$	d-value of the diffraction peak hkl
EO	ethylene oxide

e-PMO	ethane-bridged PMO material
EtOH	ethanol
FDU	Fudan University Shanghai
F127	Pluronic <sup>®</sup> F127 (PEO <sub>106</sub> PPO <sub>70</sub> PEO <sub>106</sub> )
<i>g</i>	effective surfactant ion pair packing parameter
HASYLAB	Hamburger Synchrotronstrahlungslabor
HMS	hexagonal ordered mesoporous silica
HPC	hydroxypropyl cellulose
HPLC	high performance liquid chromatography
HRTEM	high resolution transmission electron microscopy
I <sup>+</sup>	positive charged inorganic species
I <sup>-</sup>	negative charged inorganic species
I <sup>0</sup>	non-ionic inorganic species
IR	infrared
<i>l</i>	kinetic surfactant tail length or curvature elastic energy
Log K <sub>OW</sub>	negative logarithm to the base 10 of the octanol-water partition coefficient
MAS-NMR	magic angle spinning nuclear magnetic resonance
MCM	Mobil composition of matter
MeOH	methanol
MOF	metal organic framework
MP	mercaptopropyl-
MPTS	3-mercaptopropyltriethoxysilane/3-mercaptopropyltriethoxysilane
MS	mass spectrometry
MSU	Michigan State University
N	plate number
(N)	functionalised with aminopropyltriethoxysilane
(N-N)	functionalised with [amino-ethylamino]propyltriethoxysilane
(N-N-N)	functionalised with (2-amino-ethylamino)-ethylamino]propyltriethoxysilane
N <sup>0</sup>	non-ionic triblock copolymer
NLDFT	non-local density functional theory
NP	normal phase
O <sub>A</sub>	oil phase of an oil in water in oil emulsion (O <sub>A</sub> /W/O <sub>B</sub> )
O <sub>B</sub>	oil phase of an oil in water in oil emulsion (O <sub>A</sub> /W/O <sub>B</sub> )
OEt	ethoxy-

OMe	methoxy-
OM	optical microscopy
OTAB	octadecyltrimethylammonium bromide
OTAC	octadecyltrimethylammonium chloride
P-XRD	powder X-ray diffraction
p	pressure
p <sub>0</sub>	saturation pressure of bulk fluid
P123	Pluronic <sup>®</sup> P123 (PEO <sub>20</sub> PPO <sub>70</sub> PEO <sub>20</sub> )
PEG	polyethylene glycole
PEO	polyethylene oxide
PMO	periodic mesoporous organosilica
PPO	polypropylene oxide
PTMS	phenyltrimethoxysilane
Q <sup>n</sup>	<sup>29</sup> Si-MAS-NMR signal Q <sup>n</sup> : (OH) <sub>4-n</sub> Si(OSi) <sub>n</sub> ; n = 2 – 4
RP	reversed phase
RP18	reversed phase with octadecyl chains grafted onto the surface
rpm	rotations per minute
s	1/d-value
(S)	functionalised with mercaptopropyltriethoxysilane
S <sup>+</sup>	positive charged surfactant molecule
S <sup>-</sup>	negative charged surfactant molecule
S <sup>0</sup>	non-ionic structure-directing agent
SAXS	small angle X-ray scattering
SBA	Santa Barbara
SDA	structure-directing agent
SEM	scanning electron microscopy
Sph	spherical
spm	shakes per minute
T <sup>n</sup>	<sup>29</sup> Si-MAS-NMR signal T <sub>1</sub> : (C(OH) <sub>2</sub> Si(OSi)
T <sub>2</sub>	<sup>29</sup> Si-MAS-NMR signal T <sub>2</sub> : (C(OH)Si(OSi) <sub>2</sub> )
T <sub>3</sub>	<sup>29</sup> Si-MAS-NMR signal T <sub>3</sub> : (CSi(OSi) <sub>3</sub> )
TBME	<i>tert</i> -butylmethylether
TBOS	tetrabutyl orthosilicate
TEM	transmission electron microscopy

---

TEOS	tetraethyl orthosilicate
TG	thermogravimetry
THF	tetrahydrofurane
TLCT	true liquid crystal templating
TMB	1,3,5-trimethylbenzene
TMOS	tetramethyl orthosilicate
$2\theta_{hkl}$	2 theta angle of the diffraction peak hkl
$V$	total volume of the surfactant chains plus any co-solvent organic molecules between the chains
VOAG	vibrating orifice aerosol generator
W	aqueous phase of an oil in water in oil emulsion ( $O_A/W/O_B$ )
$X^+$	positive charged mediator ion
$X^-$	negative charged mediator ion
XRD	X-ray diffraction

## Thanks

First of all I would like to thank Prof. Dr. Michael Fröba for his excellent supervision, the opportunity to work in his group and for the possibility of free creating my work, for the chance to work on projects at HASYLAB@DESY, Hamburg, Germany and ELETTRA, Trieste, Italy, and for his continuous support over the last six years.

Thanks to the members of the group for their help and profitable discussions:

Maximilian Cornelius, Jürgen Morell, Andreas Lotz, Jan Roggenbuck, Tamara Stumpf, Dr. Michael Tiemann and Thomas Waitz, especially Sven Kroker for lots of little things like pictures and help with the computers, Dr. Felix Brieler for the “apartment sharing” during the first years, lots of jokes and really good music and Dr. Frank Hoffmann for his critical view on my work, for the help with the Figures, for interesting discussions, and the corrections he made of my thesis.

Special thanks to Dr. Felix Brieler, Dr. Nadine Oberender, Ansgar Dülmer, Dr. Wolfgang Herrendorf, Dr. Michael Serafin and Dr. Olaf Muth for their help to get along with this new situation within the first months.

Thanks to Stephan Hauschild for his patience and his inquiry when all guys from Giessen need literature from the Journal of Materials' Chemistry.

I would like to thank Michaela Jakubowski and Steffen Pötz for their great support in the laboratory which helped me to reach the aim of applying nearly every material we synthesised during this long time of productive cowork. Thanks to Marie-Luise Wolff, Petra Grundmann, Georg Wolter, Hubert Wörner and Dana Jäger for lots of small favours that made life a lot easier (Nitrogen physisorption and XRD measurements, change of the gas bottles, organising different things that were spontaneous needed for special measuring setups etc., stuff for administration).

For the long ours in darkness at the TEM and lots of great pictures I want to thank Günter Koch. For SEM investigations and the possibility to escape the reality for several hours I would like to thank Dr. Holger Reinshagen, Klaus Peppler and Carina Gath. And I thank Dr. Ilia Valov for the AFM measurements.

For their collaboration I would like to thank:

- Udo Weißgüttel (Martin Luther Universität, Halle-Wittenberg) for the sieving of the spherical particles and the laser diffraction measurements.
- Dr. Jan Hanss (Universität Augsburg) for the TG measurements.
- Jiao Jian and Prof. Dr. Michael Hunger (University of Stuttgart) for recording the  $^{29}\text{Si}$  MAS NMR spectra.
- Dr. Marco Bertmer (RWTH Aachen) and Dr. Heike Hausmann (JLU Giessen) for recording the  $^2\text{H}$  NMR spectra.
- Martin Guengerich (Philipps Universität Marburg) for recording the Raman spectra.
- Dr. Torsten Henning (Forschungszentrum Karlsruhe), Martin Guengerich, Martin Schreiber and Prof. Dr. Peter Klar (all Philipps Universität Marburg) for the interesting cowork during the microreactor project.
- Prof. Dr. Diedrich Steffens and Roland Pfanschilling for the cowork during the  $\text{Cu}^{2+}$  adsorption experiments.

Special thanks to Rainer Schmidt and Dr. Erwin Röcker (both JLU Giessen) for the opportunity of working with their HPLC and their great support during this long period of time.

Also a special thanks to Dr. Sérgio Funari, Martin Dommach and Ulf Brüggmann for the help during the long nights at the beamline A2 at HASYLAB.

Special personal thanks to:

- My friend Petschi for the visits, the long discussions, the dinners and the beers
- My schoolmates Svenja and Julia for their friendship over all this years despite the distance between Hamburg, New York and Giessen.
- Bine for friendship and motivation when I lost my “aim of this work”.
- My fellow students Yee, Shirin and Ella for their friendship and their help with decisions for the future.

Last but not least I want to thank my familiy, in particular:

- My brother Oliver and my grandparents Helmut and Margarete Rebbin and Heinz Dietrich and Kerstin Herrmann for their continuous interest in my thesis.
- My sister Julia for long talks during times I thought I would never finish this work.
- And my wonderful parents for their continuous support and trust in whatever I did, my father Hans-Jürgen for the quiet and factual discussions as well as for his experience and my mother Kristin for long hours that were necessary not to give up before reaching the end.

Finally I would like to thank Holger for his love and patience with my emotional personality, especially during the last months.

## Full list of publications

### Peer-reviewed paper

Synthesis and Characterisation of Spherical Periodic Mesoporous Organosilicas (sph-PMOs) with Variable Pore Diameters

V. REBBIN, M. JAKUBOWSKI, S. PÖTZ, M. FRÖBA

*Microporous Mesoporous Mater.* **2004**, 72, 99.

*In situ* Synchrotron SAXS/XRD Study of the Formation of Ordered Mesoscopic Hybrid Materials with Crystal-like Walls

J. MORELL, C. V. TEIXERA, M. CORNELIUS, V. REBBIN, M. TIEMANN, H.

AMENITSCH, M. FRÖBA, M. LINDÉN

*Chem. Mater.* **2004**, 16, 5564.

Spherical Particles of Phenylene-bridged Periodic Mesoporous Organosilicas for High Performance Liquid Chromatography

V. REBBIN, R. SCHMIDT, M. FRÖBA

*Angew. Chem. Int. Ed.* **2006**, 45, 5210.

### In preparation

Synthesis of Periodic Mesoporous Organosilicas (PMOs) with the Incorporation of a Secondary Amine Bridge into the Framework Wall

V. REBBIN, M. JAKUBOWSKI, S. PÖTZ, M. FRÖBA

Synthesis and Characterisation of Phenylene-bridged Spherical Periodic Mesoporous Organosilicas (sph-PMOs) in the Size Range of 20 to 250  $\mu\text{m}$

V. REBBIN, M. JAKUBOWSKI, S. PÖTZ and M. FRÖBA

Two Different Formation Mechanisms of 2d Hexagonal Periodic Mesoporous Organosilicas (PMOs)

V. REBBIN, S. S. FUNARI, M. FRÖBA

Synthesis and Characterisation of Phenylene-bridged Spherical Periodic Mesoporous Organosilicas (sph-PMOs) in the Size Range of 3 to 10  $\mu\text{m}$

V. REBBIN, M. JAKUBOWSKI, S. PÖTZ, M. FRÖBA

Copper Adsorption Properties of Amine-bridged Periodic Mesoporous Organosilicas (PMOs)

V. REBBIN, R. PFANSCHILLING, D. STEFFENS, M. FRÖBA

*In situ* SAXS Investigations of the SBA-15 Silica with Pluronic P 123 as Structure-directing Agent in Different Concentrations

V. REBBIN, S. S. FUNARI, F. HOFFMANN, M. SERAFIN, M. FRÖBA

Conference proceedings

Periodic Mesoporous Organosilicas (PMOs) with Different Organic Bridging Groups: Synthesis and Characterisation

O. MUTH, V. REBBIN, M. FRÖBA

*Mat. Res. Soc. Sym. Proc.* **2002**, 726, Q8.3.1.

Periodic Mesoporous Organosilica Spheres: Novel Synthesis and Characterisation

V. REBBIN, M. JAKUBOWSKI, S. PÖTZ, M. FRÖBA

*Proc. 14<sup>th</sup> internat. Zeolite Conf.* **2004**, 568.

Selective Adsorption of Solvents in a Multiscale Device

T. HENNING, J. J. BRANDNER, L. EICHHORN, K. SCHUBERT, M. SCHREIBER, M. GUENGERICH, H. GÜNTHER, P. J. KLAR, V. REBBIN, M. FRÖBA

Proceedings of ASME ICNMM2006-9610.

Reports and extended abstracts

*In situ* SAXS Studies on the Template-directed Synthesis of the SBA-15 and Periodic Mesoporous Organosilicas (PMOs)

V. REBBIN, F. J. BRIELER, S. S. FUNARI, M. FRÖBA

*Hasylab Annual Report 2001* (Part 1), HASYLAB/DESY, Hamburg **2002**, 643.

*In situ* SAXS Studies on Amine-functionalised Periodic Mesoporous Organosilicas (PMOs)

V. REBBIN, S. S. FUNARI, M. FRÖBA

*Hasylab Annual Report 2003* (Part 1), HASYLAB/DESY, Hamburg **2004**, 327.

*In situ* SAXS Investigations of Ethane-bridged Periodic Mesoporous Organosilicas (PMOs)

V. REBBIN, S. S. FUNARI, M. FRÖBA

*Hasylab Annual Report 2003* (Part 1), HASYLAB/DESY, Hamburg **2004**, 325.

*In situ* SAXS Studies of Benzene- and Thiophene-bridged Periodic Mesoporous Organosilicas (PMOs) with Pluronic P123 as Structure-directing Agent

V. REBBIN, S. S. FUNARI, J. MORELL, M. CORNELIUS, M. FRÖBA

*Hasylab Annual Report 2003* (Part 1), HASYLAB/DESY, Hamburg **2004**, 333.

*In situ* SAXS Investigations of Phenylene-bridged Periodic Mesoporous Organosilicas (PMOs)

V. REBBIN, S. S. FUNARI, J. MORELL, M. CORNELIUS, M. FRÖBA

*Hasylab Annual Report 2004* (Part 1), HASYLAB/DESY, Hamburg **2005**, 643.

Poster presentations

*In situ* SAXS Studies on the Template-directed Synthesis of the SBA-15 and Periodic Mesoporous Organosilicas (PMOs)

V. REBBIN, F. J. BRIELER, S. S. FUNARI, M. FRÖBA

*Hasylab Users Meeting 2001*, Hamburg, Germany, January 25, **2002**.

*In situ* SAXS Investigations of Benzene- and Ethane-bridged Periodic Mesoporous Organosilicas (PMOs)

V. REBBIN, S. S. FUNARI, M. FRÖBA

*Hasylab Users Meeting 2002*, Hamburg, Germany, January 31, **2003**.

Synthesis and Characterisation of Amine-functionalised Periodic Mesoporous Organosilicas (PMOs)

V. REBBIN, M. FRÖBA

*15<sup>th</sup> German Zeolite Conference*, Kaiserslautern, Germany, March 5 – 7, **2003**.

*In situ* SAXS Studies of Benzene- and Thiophene-bridged Periodic Mesoporous Organosilicas (PMOs) with Pluronic P123 as Structure-directing Agent

V. REBBIN, S. S. FUNARI, J. MORELL, M. CORNELIUS, M. FRÖBA

*Hasylab Users Meeting 2003*, Hamburg, Germany, January 27, **2004**.

Spherical Periodic Mesoporous Organosilicas (sph-PMOs) in a Wide Particle Size Range

V. REBBIN, S. PÖTZ, M. JAKUBOWSKI, M. FRÖBA

*16<sup>th</sup> German Zeolite Conference*, Dresden, Germany, March 5 – 7, **2004**.

Spherical Periodic Mesoporous Organosilicas (sph-PMOs) in a Wide Particle Size Range

V. REBBIN, S. PÖTZ, M. JAKUBOWSKI, M. FRÖBA

*14<sup>th</sup> International Zeolite Conference*, Cape Town, South Africa, April 25 – 30, **2004**.

Novel Synthesis of Periodic Mesoporous Organosilicas (PMOs)

V. REBBIN, M. JAKUBOWSKI, S. PÖTZ, M. FRÖBA

*4<sup>th</sup> International Mesostructured Materials Symposium*, Cape Town, South Africa, May 1-4, **2004**.

*In situ* SAXS Investigations of Periodic Mesoporous Organosilicas (PMOs) in a Flow-through Capillary

V. REBBIN, S. S. FUNARI, J. MORELL, M. CORNELIUS, M. FRÖBA

*Hasylab Users Meeting 2004*, Hamburg, Germany, January 28, **2005**.

Synthesis of Spherical Phenylene-bridged Periodic Mesoporous Organosilicas (sph-PMOs) in the Size Range of 3 to 15  $\mu\text{m}$ .

V. REBBIN, M. JAKUBOWSKI, S. PÖTZ, M. FRÖBA

*17<sup>th</sup> German Zeolite Conference*, Giessen, Germany, March 2 – 4, **2005**.

Spherical Phenylene-bridged Periodic Mesoporous Organosilicas: A New Material for Chromatographic Application

V. REBBIN, M. JAKUBOWSKI, S. PÖTZ, R. SCHMIDT, M. FRÖBA

*18<sup>th</sup> German Zeolite Conference*, Hannover, Germany, March 1 – 3, **2006**.

*Oral presentations*

New Synthesis Pathways to Spherical Periodic Mesoporous Organosilicas (sph-PMOs)

V. REBBIN, M. FRÖBA

invited talk at the Merck KGaA, Darmstadt Germany, May 27, **2004**.

## Curriculum Vitae

Vivian Rebbin, born October 26, 1976 in Hamburg, Germany

1983 – 1987	Elementary School <i>Erich-Kästner Grundschule</i> in Halstenbek
1987 – 1996	Grammar School <i>Wolfgang-Borchert-Gymnasium</i> in Halstenbek
May 1996	Abitur
Oct. 1996 – Mar. 2001	Study of Food Chemistry at <i>Universität Hamburg</i>
Aug. 1998	Diplomvorprüfung
Feb. 2000 – Nov. 2000	Work on Diploma thesis: „Fütterungseinflüsse in der Rindermast: Carry-over ausgewählter Antioxidantien und deren Einfluß auf die Lipidstabilität sowie Stereosiomerenverteilung des $\alpha$ -Tocopherols in verschiedenen Rindergeweben in Abhängigkeit von der Futterzusammensetzung.“ in the research group of Prof. Dr. Dr. Hans Steinhart at <i>Universität Hamburg</i> .
Aug 2000 – Apr. 2001	“Erstes Staatsexamen” in Food Chemistry at <i>Universität Hamburg</i> .
Since May 2001	Work on Dissertation (PhD Thesis): “Spherical Periodic Mesoporous Organosilicas: Synthesis, Characterisation and Application in Chromatography” in the group of Prof. Dr. M. Fröba at the <i>Justus-Liebig-Universität Giessen</i> .
May 2001 – Sep. 2006	Employed as scientific Assistant at the <i>Justus-Liebig-Universität Giessen</i> founded by the <i>Justus-Liebig-Universität Giessen</i> .
Oct. 2006 – Mar. 2007	Employed as scientific Assistant at the <i>Justus-Liebig-Universität Giessen</i> founded by the BMBF.